THÈSE POUR OBTENIR LE GRADE DE DOCTEUR DE L'UNIVERSITÉ DE MONTPELLIER

En Physique et Astrophysique

École doctorale I2S

Unité de recherche UMR 5299

Studying γ-ray halos around pulsars using H.E.S.S. data

Présentée par Karim SABRI
Le 10 Décembre 2025

Sous la direction de Yves GALLANT
et le co-encadrement de Justine DEVIN

Devant le jury composé de

Ana PALACIOS, Astronome, LUPM	Présidente du jury
Emma DE OÑA WILHELMI, Group leader (Staff scientist), DESY	Rapporteure
Bruno KHÉLIFI, Directeur de recherche, APC	Rapporteur
Pierrick MARTIN, Chargé de recherche, IRAP	Membre du jury
Alison MITCHELL, DFG Emmy Noether Group Leader, ECAP	Membre du jury
Nukri KOMIN, Professeur, LUPM	Membre du jury
Justine DEVIN, Chargée de recherche, LUPM	Membre du jury
Yves GALLANT, Directeur de recherche, LUPM	Directeur de thèse

UNIVERSITÉ DE MONTPELLIER

Contents

Acknowledgments **4**

Abstract **6**

1 Introduction **8**
1.1 Gamma-ray astronomy 8
1.2 Radiative processes in non-thermal astrophysics 11
1.3 Cosmic rays 14
1.4 Galactic sources 18

2 Pulsar wind nebulae and pulsar halos **23**
2.1 General considerations on pulsars 23
2.2 Pulsar wind nebulae 26
2.3 The γ-ray halos observed towards middle-aged pulsars 27

3 Instruments and data analysis methods **31**
3.1 Extensive Air Showers 31
3.2 The H.E.S.S. experiment 32
3.3 The Cherenkov Telescope Array Observatory 35
3.4 Data analysis with Gammapy 36

4 Pulsar halo modeling framework **43**
4.1 Theoretical prescription 43
4.2 Building pulsar halo templates for H.E.S.S. data fitting 55

5 Search for pulsar halo candidates in the H.E.S.S. Galactic Plane Survey **61**
5.1 Pulsar halo candidates in the HGPS 62
5.2 Associations with 1LHAASO sources 64
5.3 Comparison with pulsar halo candidates in the literature 68
5.4 Non-detected HGPS sources around energetic pulsars 69
5.5 Conclusion 70

6 HESS J1831−098: Exploring a pulsar halo scenario **72**
6.1 Context 72
6.2 H.E.S.S. data analysis 73
6.3 Discussion 88

7 Characterization of pulsar halos with H.E.S.S. and CTAO **90**
7.1 General method 90
7.2 Characterization of pulsar halos with H.E.S.S. 92
7.3 Towards pulsar halos with CTAO 99
7.4 Conclusion 104

Conclusion and prospects **106**

Bibliography **109**

Thesis summary (French version) **116**

Appendix: HESS J1831−098 **122**

Acknowledgments

I would like to extend my deepest gratitude to my supervisors, Yves Gallant and Justine Devin, for their mentor-ship and all their support during the three years of my PhD. We traveled to numerous places across Europe for presentations, had countless discussions on science extending beyond the topic of this thesis, and they gave me the opportunity to travel to Namibia to conduct astronomical observations at the H.E.S.S. facility, which still does not feel real to me. Yves and Justine were ever-present, guiding me through every step. Through the opportunity they gave me, I connected with a community of scientists which has become so dear to me during this journey. The environment Yves and Justine have allowed me to work in and their pedigree as colleagues and scientists was one of my biggest motivations. I will cherish these memories forever.

Many thanks to the members of this jury, who have agreed to commit their time and effort to reviewing this work, a culmination of three years of research. Bruno Khélifi and Emma de Oña Wilhelmi accepted producing reports on the entirety of this thesis, and I highly appreciate their undertaking of this task. The discussions we've had together during H.E.S.S. and CTAO meetings and their feedback on my work was invaluable. It is a pleasure to know that they will share their expertise on the topic of this thesis as rapporteurs. I am grateful to Pierrick Martin, Alison Mitchell and Nukri Komin, who have followed the progress of this project from the start, and agreed to take the roles of examiners. I would like to thank Ana Palacios, for agreeing to take the role of president of the jury. All the members of this jury, through their expertise and contributions to the field, have directly and indirectly played a part in the completion of my and many students' theses, and their critical input on this work means everything to me.

Kirsty Feijen conducted the cross-check analysis of the HESS J1831−098 data analysis. Her expertise on Galactic sources and contributions to the developments of many of the tools used in this work made her input and insight crucial to the advancement of this project, culminating in an ICRC 2025 talk in Geneva. It was a pleasure to have worked together on this project.

Pierrick Martin has followed the advancement of my PhD since the start, participating as a member of the "Comité de Suivi Individuel". Further, his contributions to the topic of pulsar halos and pulsar wind nebulae, and the numerous discussions we've had online and in person at CTAO meetings, were instrumental in shaping the direction of this project.

Alison Mitchell conducted the review of the HESS J1831−098 data analysis, and was an organizer of the ECAP Astroparticle School 2023 in Obertrubach, which was an unforgettable experience for me. Our multiple correspondences over the data analysis, discussions at numerous H.E.S.S. Collaboration meetings, and her contributions to the field of Galactic sources were invaluable for my progress and the production of this thesis.

I am thankful to all the members of the H.E.S.S. Collaboration, a community which I hold dearly. We met in County Cavan, Bordeaux, Tübingen, Kraków and Obergurgl

for the H.E.S.S. Collaboration meetings, and I was given the opportunity of spending 4 weeks in Namibia at the H.E.S.S. site. These moments are unforgettable. Many thanks to Jonathan Mackey and Brian Reville, the conveners of our work group, for organizing the monthly Galactic sources science meetings, which have always been a pleasure to attend. I would also like to thank Quentin Rémy, for his crucial insight on data analysis, his input on my work in the H.E.S.S. Collaboration, and his participation in the development of the tools that I used in my project.

I would like to express my gratitude to the EMAC team at the LUPM, for being so welcoming and fostering an environment with a diversity of theoretical and experimental expertise. Alexandre Marcowith and Claire Guépin organized numerous team meetings where I was able to share my work with my peers, and I would like to thank them for all the discussions that we've had and their feedback on my project throughout the years. Many thanks to Frédéric Piron, who was a member of my "Comité de Suivi Individuel" and whose participation helped shape the direction of this project.

I can only look back at my time at the LUPM with fond memories with my lab-mates since I was welcomed here three years ago. Many thanks to my fellow PhD students for all the wonderful discussions during our coffee and lunch breaks, and to the entirety of the LUPM staff for giving me this opportunity.

None of this could have happened without my parents' and my siblings' love and support. All my love to my best friend, my *fellow tarnished*, who has always pushed me for the better throughout the years, and for all the moments spent together despite the physical distance between us.

Abstract

Pulsars produce emission nebulae wherein electrons and positrons are confined in a nebular magnetic field originating in the pulsar. Such pulsar wind nebulae constitute a prominent category of γ-ray sources and are possibly important contributors to the local positron cosmic-ray spectrum. Escaped electrons and positrons from middle-aged pulsars, detected at very high energies, allow the study of particle escape from pulsar wind nebulae and the late stages of their evolution. This observation is referred to as the "pulsar halo" phenomenon. Only a handful of very-high-energy sources are proposed as identified or candidate pulsar halos, and the line between older pulsar wind nebulae and pulsar halos is blurred in very-high-energy data. In this thesis, we study these so-called "pulsar halos" using data from H.E.S.S., an Imaging Atmospheric Cherenkov Telescope experiment uniquely situated in the Southern hemisphere with a view on the inner Galaxy.

We adopted a commonly used model of pulsar halos, which predicts well the morphological and spectral features of the γ-ray emission around the Geminga and Monogem pulsars in HAWC data. We used this model to build templates that can be used in spectro-morphological analyses of γ-ray data with the Gammapy library, with the goal of searching for and possibly identifying plausible halos in H.E.S.S. data. We started by searching for halo candidates in the H.E.S.S. Galactic Plane Survey catalog, which yielded 20 candidates, some of which are found to have likely ultra-high-energy counterparts as detected by the LHAASO experiment.

This search motivated the spectro-morphological analysis of the source HESS J1831 −098, where we constrained the parameters of the halo model assuming it is powered by PSR J1831−0952 or PSR J1831−0941, two energetic pulsars coincident with the very-high-energy emission region. We find the former to be a more plausible scenario owing to its higher spin-down power. The diffusion coefficient in the halo is consistent with the measurements of HAWC for the Geminga and Monogem halos, and the source shows good morphological and spectral consistency with the potential HAWC and LHAASO ultra-high-energy counterparts 3HWC J1831−095 and 1LHAASO J1831−1007u.

Finally, we simulated observations of pulsar halos over multiple model parameters with the H.E.S.S. and the CTAO instrument response functions, to study the detectability and the ability of these instruments to discriminate between the γ-ray emission features of a pulsar halo and simple 2D Gaussian components. We discuss the morphological and spectral features that the H.E.S.S. and CTAO arrays are sensitive to. The results show a drastic improvement from H.E.S.S. to CTAO in the ability to identify pulsar halos, which is very encouraging for future Galactic surveys.

French version

Les pulsars produisent des nébuleuses dans lesquelles les électrons et positrons sont confinés par le champ magnétique, qui provient du pulsar. Ces nébuleuses de vent de pulsar constituent une catégorie importante de sources en rayons γ et contribuent potentiellement de manière importante au spectre local des positrons cosmiques. Les électrons et positrons qui s'échappent de la nébuleuse ont été détectés grâce à leur rayonnement aux très hautes énergies. Ce phénomène, appelé "halo de pulsar", permet pour la première fois d'étudier l'échappement de particules d'un système ainsi que les étapes tardives de l'évolution des nébuleuses de vent de pulsars. Seul un petit nombre de sources aux très hautes énergies ont été identifiées comme halos ou sont proposées comme candidats, et la distinction entre une nébuleuse de vent de pulsar évoluée et un halo de pulsar n'est pas évidente sur le plan observationnel. Dans cette thèse, nous étudions les halos de pulsar dans les données de H.E.S.S., une expérience de télescopes à imagerie Tcherenkov atmosphérique ayant une situation unique dans l'hémisphère Sud et fournissant une vue détaillée des régions internes de la Galaxie.

Nous adoptons un modèle de halo de pulsar communément utilisé, qui reproduit adéquatement les caractéristiques morphologiques et spectrales de l'émission γ autour des pulsars de Geminga et Monogem observée par l'expérience HAWC. Nous utilisons ce modèle pour construire des "templates" pouvant être utilisées dans les analyses spectro-morphologiques en rayons γ avec la librairie Gammapy, dans le but de rechercher des candidats de halos dans les données de H.E.S.S. et possiblement de les identifier en contraignant leurs paramètres physiques.

Nous commençons par rechercher de potentiels halos dans le catalogue du relevé du plan galactique de H.E.S.S., sur la base d'associations avec des pulsars énergétiques et possiblement des sources aux ultra hautes énergies. Nous révélons 20 candidates possibles, dont certains ayant des contreparties probables aux ultra-hautes énergies détectées par l'expérience LHAASO.

Cette première recherche a mené a l'analyse spectro-morphologique détaillée de la source HESS J1831−098 dans les données H.E.S.S. Nous contraignons les paramètres du halo en supposant qu'il est alimenté par l'un des pulsars énergétiques PSR J1831−0952 ou PSR J1831−0941, tous deux coïncidant avec la région d'émission aux très hautes énergies. Sur la base de considérations énergétiques, nous trouvons que la source HESS J1831−098 est plus probablement alimentée par le pulsar PSR J1831−0952 que PSR J1831−0941. Le coefficient de diffusion correspondant est compatible avec les mesures de HAWC dans les halos de Geminga et Monogem, et les données de H.E.S.S. montrent que la source est morphologiquement et spectralement compatible avec les contreparties aux ultra-hautes énergies 1LHAASO J1831−1007u* et 3HWC J1831−095.

Finalement, nous simulons des observations de halos de pulsar pour plusieurs valeurs des paramètres du modèle avec les réponses instrumentales de H.E.S.S. et CTAO, afin d'étudier la capacité de ces instruments à détecter les halos et à les identifier comme tels (comparé à des Gaussiennes bi-dimensionnelles). Nous examinons les caractéristiques morphologiques et spectrales auxquelles H.E.S.S. et CTAO sont sensibles. Les résultats montrent une amélioration radicale de la capacité à identifier les halos de pulsars entre H.E.S.S. et CTAO, ce qui est prometteur pour de futurs relevés galactiques et augmentera vraisemblablement notre compréhension de ces objets.

Chapter 1

Introduction

Contents

1.1 Gamma-ray astronomy 8
1.2 Radiative processes in non-thermal astrophysics 11
1.3 Cosmic rays 14
1.4 Galactic sources 18

1.1 Gamma-ray astronomy

Gamma-ray astronomy probes the sky from the MeV to PeV photon energy range, which includes the electromagnetic signal emitted by Galactic and extragalactic relativistic charged particles at their acceleration sites and as they propagate. In the Milky Way, particle acceleration takes place at the shocks associated with stellar objects, magnetic reconnection events and shocks generated by colliding winds. The charged particles propagate in the Interstellar Medium (ISM), interacting with the nuclei of interstellar gas, photon fields produced by stars and interstellar dust, the Cosmic Microwave Background (CMB), and the Galactic magnetic field.

The charged relativistic particles permeating the Milky Way are known as "cosmic rays" (CRs). Their existence was established by Victor Hess in 1912, who observed that the ionization rate in the atmosphere increases with altitude up to ~ 5.2 km with balloon-based experiments. At the time, CRs were proposed as being ionizing radiation of astrophysical origin. The particle nature of this signal was discovered in 1927 by Clay, who observed that CRs experience deflection by the Earth's magnetic field, and Skobeltzyn, who observed the tracks they produce in cloud chambers. Two years after the discovery of the π^0-meson, which quickly decays into two γ rays, Hayakawa (1952) predicted the existence of a diffuse γ-ray signal due to the production of π^0 from collisions between CR and interstellar gas protons in the Galactic disk. This signal was confirmed with the OSO-3 satellite (Clark et al. 1968) at energies > 50 MeV. COS-B, the European Space Agency's first-ever satellite, probed the sky from the 50 MeV to the 5 GeV range (Hermsen 1983). Major results of the COS-B experiment include the confirmation of the spatial correlation between diffuse Galactic γ-ray emission and interstellar gas, and the production of the 2CG catalog of 25 point-like sources (i.e. with extensions $\lesssim 2.0°$), only 4 of which were identified (including the Crab and Vela pulsars). Gamma-ray emission from the Geminga pulsar would only be identified in 1991 when the ROSAT satellite

confirmed the pulsed X-ray emission (Halpern & Ruderman 1993). Fermi-LAT, launched in 2008, revolutionized the field, revealing the γ-sky in the 20 MeV to 100's of GeV range with an angular resolution better than 0.15° at energies above 10 GeV and a field of view of ~ 2 sr. The 8-year 4FGL source catalog (Abdollahi et al. 2020) contains 5064 sources, including 3130 identified blazars and 239 pulsars. 75 4FGL sources are spatially resolved (i.e. their angular extension is statistically significant).

In the Fermi-LAT energy range, typically referred to as the high energy (HE) range, γ-ray emission from hadronic interactions between CRs and interstellar nuclei dominates over the source signal in the Galactic disk, which makes this instrument suitable to study the large-scale diffuse γ-ray component of the Galaxy. As shown in Fig. 1.1 from Ackermann et al. (2012), this component is composed of γ rays from the decay of neutral pions produced through inelastic $p-p$ collisions between CR and ISM nuclei, Inverse Compton (IC) emission and bremsstrahlung emission by electrons and positrons (cf. Section 1.2).

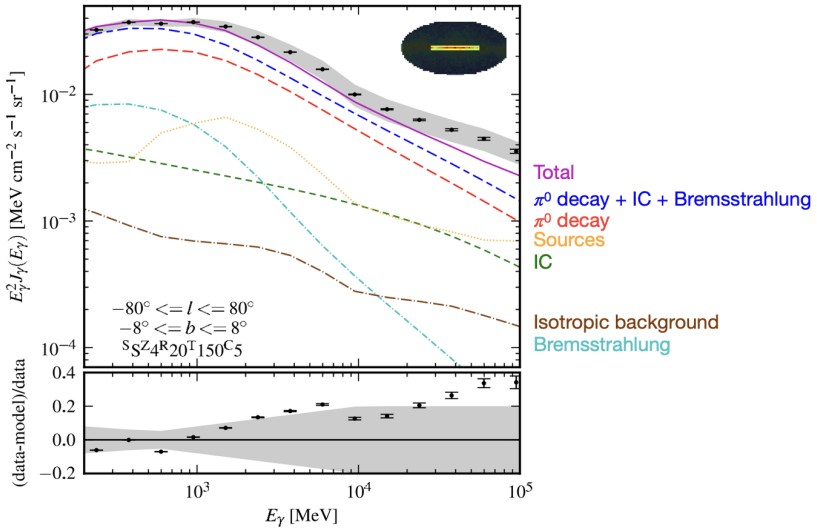

Figure 1.1: Fermi-LAT large-scale diffuse emission and GALPROP model prediction around the Galactic center ($|\ell| < 80°$, $|b| < 8°$) from Ackermann et al. (2012). The various radiation mechanisms are presented in Section 1.2. The isotropic background signal is due to extragalactic sources.

In the TeV to PeV range, much larger detector areas are required due to the decreasing photon flux and therefore observations are conducted from the ground. This revolves around the detection of the Cherenkov signal emitted by particles produced in air showers originating from γ rays and CRs entering the Earth's atmosphere. The Crab nebula was the first-ever detected source at TeV photon energies (Weekes et al. 1989), using the Whipple 10-meter telescope (Acado, Arizona) which pioneered the Imaging Atmospheric Cherenkov technique. The 2000s saw the development of major Imaging Atmospheric Cherenkov Telescope (IACT) facilities, such as VERITAS (Acado, Arizona), H.E.S.S. (Khomas Highlands, Namibia) and MAGIC (La Palma, Spain), probing the sky in the 0.1-100 TeV range, which is typically referred to as the very-high-energy (VHE) range. These observatories are arrays of 2 to 5 telescopes equipped with UV-optical cameras. The direction and energy of γ rays entering the Earth atmosphere are reconstructed from images of the Cherenkov signal created by air shower particles in the atmosphere. While the field of view of these instruments is limited to a few degrees, they provide the best angular resolution in γ-ray astronomy (few arc-minutes) in an energy range where source components are often dominant over the large-scale Galactic diffuse emission component,

making them suitable for detailed source analyses. Over the last two decades, IACT's proved that a large diversity of astrophysical sources are efficient VHE γ-ray emitters such as pulsars and their nebulae, supernova remnants, massive stellar clusters, binary systems (including micro-quasars), hadronic interactions between CRs and interstellar nuclei such as the Galactic center ridge, active galactic nuclei and γ-ray bursts. H.E.S.S. is uniquely situated in the southern hemisphere and provides a detailed view of the inner Galaxy. The H.E.S.S. Galactic Plane Survey (HGPS) catalog (H.E.S.S. Collaboration 2018d) includes a total of 78 sources at Galactic latitudes $|b| \leq 3°$, with 28 of these being firmly identified as the counterparts of pulsar wind nebulae, supernova remnants or both (i.e. composite systems). In the HGPS, the nature of the majority of sources remains unidentified, either due to source confusion or due to a lack of a multiwavelength counterpart (i.e. "dark" sources).

Direct Extensive Air Shower (EAS) observatories, such as Milagro (Smith 2005, operating between 1999 and 2008 in Los Alamos, New Mexico), HAWC (Abeysekara et al. 2013, operating since 2013 in Puebla, Mexico) and LHAASO (Aharonian et al. 2021, operating since 2016 in Sichuan, China), rely on the direct detection of air shower particles at higher altitudes. In the case of Milagro, HAWC and LHAASO's Water Cherenkov Detector Array (WCDA), this is achieved by an array of water containers equipped with detectors of the Cherenkov signal. The primary γ ray's incoming direction is reconstructed through the time of arrival of a Cherenkov signal in different containers across the array. LHAASO's Kilometer Square Array (KM2A), probing the γ-ray sky up to PeV energies with an angular resolution of 0.2° at 100 TeV (Cao et al. 2024a), relies on the detection of air shower particles using an array of plastic scintillators. The $>$ 100 TeV range is referred to as the ultra-high-energy (UHE) range. Direct EAS observatories cover nearly the entire sky (2 steradians), and their nearly full duty cycle makes them the most sensitive instruments at the highest ($\gtrsim$ 30 TeV) energies. They are most suitable for searching for extended and faint γ-ray sources and studying the large-scale Galactic diffuse emission in the multi-TeV range. They provide access to the most extreme particle accelerators, where relativistic leptons and/or protons are accelerated to PeV energies (i.e. leptonic or hadronic "PeVatrons"). 1LHAASO, the first source catalog published by LHAASO, contains 43 sources detected at energies higher than 100 TeV (half of which are spatially coincident with pulsars, although their nature remains unknown), providing an unprecedented view of the UHE sky. One of the major recent results of LHAASO was to reveal PeV photons from the Crab nebula (LHAASO Collaboration 2021), implying multi-PeV electrons accelerated within the source, and from the Cygnus Bubble, potentially implying the first detection of a hadronic PeVatron (LHAASO Collaboration 2024), although the exact acceleration site remains uncertain. Fig. 1.2 shows the LHAASO measurements of the Crab pulsar wind nebula's photon spectrum from LHAASO Collaboration (2021), accompanied by measurements from the radio to the GeV bands and the predicted synchrotron and inverse Compton (cf. Section 1.2) photon spectra from $e^{-/+}$ with different energies. The model spectra are computed using a one-zone model, i.e. the spatial electron and magnetic field distributions are assumed to be homogeneous.

A general view of the γ-ray sky in different energy bands is shown in Fig. 1.3. The top panel shows the Fermi-LAT 12 years counts map at $>$ 1 GeV, smoothed with a Gaussian kernel of 0.25° from Tibaldo et al. (2021). The middle panel is the H.E.S.S. Galactic Plane Survey map above 0.3 TeV, showing the statistical significance of excess counts above the predicted hadronic CR background. The bottom panel is the 1LHAASO survey's KM2A map above 25 TeV, showing the statistical significance of the excess counts above

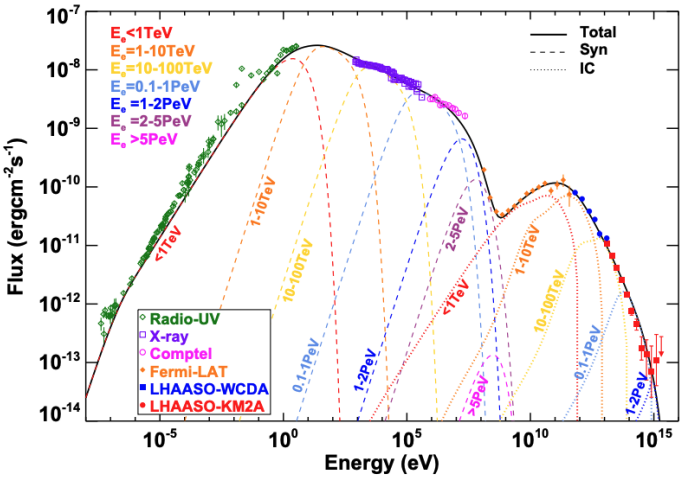

Figure 1.2: Multi-wavelength differential photon spectrum of the Crab pulsar wind nebula, from LHAASO Collaboration (2021). The green diamonds are the radio, UV, IR and optical measurements (see references therein). The purple data points are the X-ray ROSAT and BeppoSAX measurements. The magenta data points are the COMPTEL measurements. The orange data points are from Fermi-LAT measurements. The blue and red data points correspond to LHAASO's WCDA and KM2A measurements respectively. The model-predicted synchrotron and Inverse Compton spectra from $e^{-/+}$ with different energy ranges are shown as dashed and dotted lines respectively, and the solid line is the total model-predicted spectrum.

the predicted background and Galactic diffuse emission. The Fermi-LAT map features extragalactic and Galactic sources, along with the diffuse emission across the Galactic plane, which is generally spatially correlated with the distribution of interstellar gas. The HGPS map features individual sources, some of which are extended. The KM2A map features UHE sources, probing accelerated particles at the highest energies. Knowledge gained of the Galactic diffuse emission is crucial to studying sources across the HE-VHE-UHE bands, specially for extended and faint sources. The analysis of sources with the best angular resolution in the VHE band improves prospects of identifying the astrophysical scenario underlying the γ-ray emission. The extension of source observations to the highest energies in the UHE constrains the highest achievable energies by Galactic accelerators. Thus, the available wide band coverage of the γ-ray sky allows us to test astrophysical models of particle acceleration and propagation in the ambient medium.

1.2 Radiative processes in non-thermal astrophysics

This section is based on the formalism of Rybicki & Lightman (1979).

Synchrotron emission

Synchrotron emission is the beamed cyclotron radiation emitted by ultra-relativistic charged particles in a magnetic field. For electrons with constant speed v and random velocities, the observed power radiated by an electron is obtained by averaging over the pitch angle and is expressed as:

$$\dot{E} = -\frac{4}{3}\sigma_T c \beta^2 \gamma^2 U_B \tag{1.1}$$

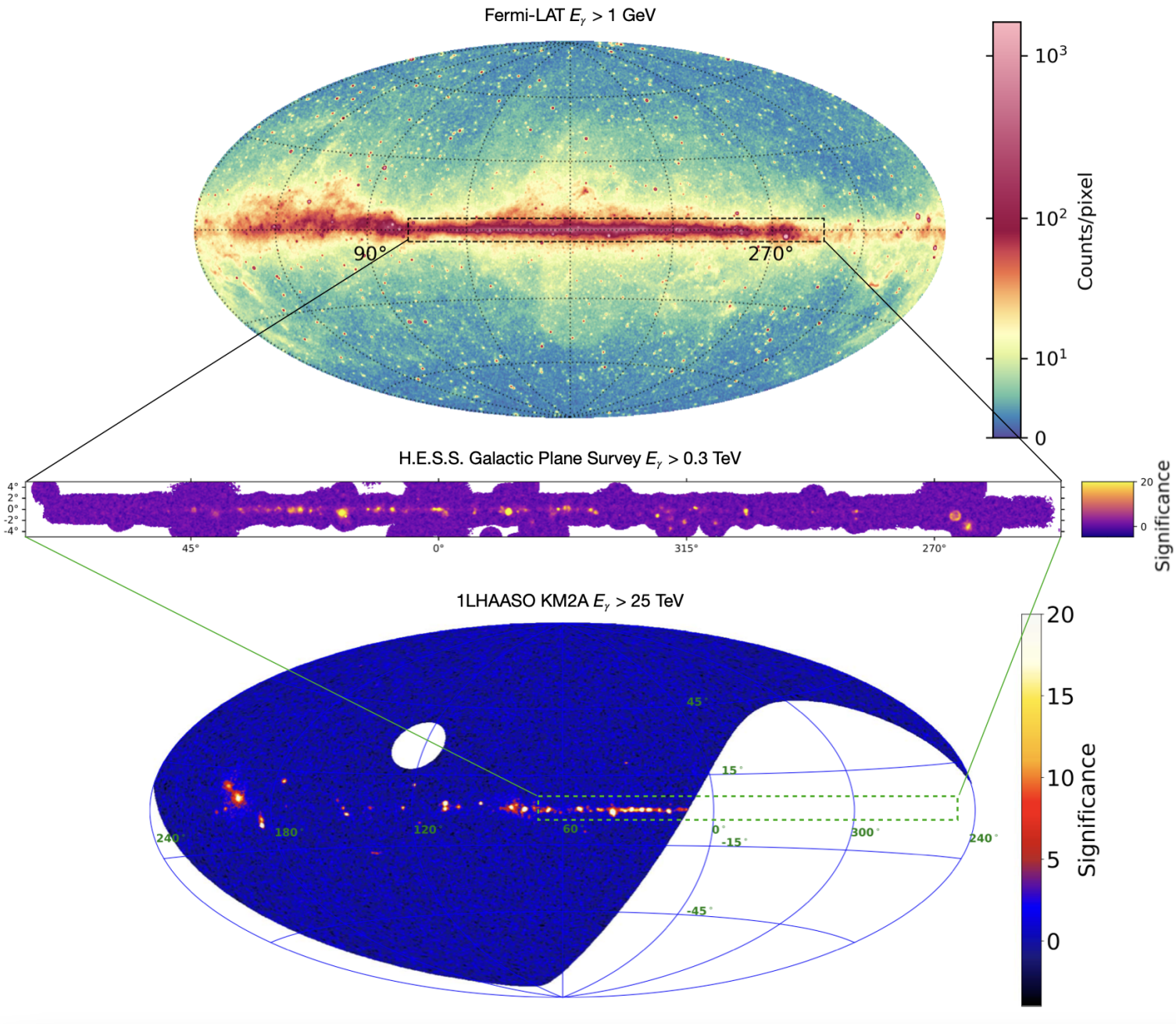

Figure 1.3: Sky maps from γ-ray observatories in different energy bands. The Galactic longitude and latitude axes of each map have different scales. **Top:** Fermi-LAT counts map above 1 GeV adapted from Tibaldo et al. (2021). **Middle:** H.E.S.S. Galactic Plane Survey significance map with a correlation radius of 0.2° above 0.3 TeV (H.E.S.S. Collaboration 2018d). **Bottom:** 1LHAASO KM2A survey map above 25 TeV centered at Galactic longitude $\ell = 60°$ (Cao et al. 2024b). The white regions in the 1LHAASO map are not visible to the LHAASO observatory.

with $\beta = v/c$, γ the Lorentz factor, σ_T the Thomson cross section and $U_B = B^2/8\pi$ the magnetic field energy density. The energy loss timescale is thus $t_{\text{cool, syn}} = -E/\dot{E} \propto \gamma^{-1}B^{-2}$. The observed continuum emission scales with the angular frequency ω as $\omega^{1/3}$ for low frequencies and peaks at $\sim 0.29\omega_c$, with ω_c the cut-off angular frequency:

$$\omega_B = \omega_L/\gamma \tag{1.2}$$

$$\omega_c = \frac{3}{2}\gamma^3 \omega_B \sin\alpha \tag{1.3}$$

with ω_L the Larmor frequency and α the pitch angle. The total radiated power can be expressed as a power law function of ω/ω_c. For a power law spectrum of ultra-relativistic electrons defined as γ^{-p}, the resulting synchrotron spectrum is a power law with spectral index $s = \frac{p-1}{2}$. Synchrotron radiation is observed from radio to MeV energies, with synchrotron emission from protons being negligible due to their much smaller gyration frequency.

Inverse Compton Scattering

Compton scattering is the process by which an incoming photon is scattered by an electron. If the photon energy is much lower than the electron rest energy, the interaction is approximately elastic and the cross-section is the Thomson scattering cross-section $\sigma_T = \frac{8\pi}{3} r_0^2 \sim 6.65 \times 10^{-25}$ cm^2 with r_0 the classical electron radius. For an electron at rest and an incident photon energy ϵ approaching or exceeding the electron rest energy, the interaction is inelastic due to relativistic kinematics. If the electron is relativistic, it loses energy in the observer frame. This is referred to as Inverse Compton scattering, the main process responsible for the very-high-energy radiation emitted by relativistic leptons. Inverse Compton scattering is treated as Compton scattering in the electron rest frame. If the incident photon in the rest frame has an energy $\epsilon \ll m_e c^2$, the resulting photon in the observer frame is boosted by a factor of order γ^2 with γ the electron's Lorentz factor. In the Thomson regime and for an isotropic photon distribution, the electron energy loss from one scattering can be expressed as

$$\dot{E} = -\frac{4}{3}\sigma_T c \beta^2 \gamma^2 U_{rad} \tag{1.4}$$

with U_{rad} the photon field's energy density. The inverse Compton energy loss timescale in the Thomson regime is $t_{\text{cool, IC}} = -E/\dot{E} \propto \gamma^{-1} U_{rad}^{-1}$. A 1 TeV electron has a cooling timescale of $\sim$ 310 kyr in a photon field with $U_{rad} = 1$ eV/cm^3. This is identical to the synchrotron cooling timescale corresponding to a magnetic field $B = 6.3$ μG. For a population of electrons described by a power law spectrum of index p, it can be shown that the resulting photon spectrum is a power law with index $s = \frac{p-1}{2}$. Hence, the synchrotron and inverse Compton spectra from a population of leptons have similar shapes (in the Thomson regime approximation). For black-body distributions of the photon field, the spectrum can be described semi-analytically (Khangulyan et al. 2014).

When $x = \epsilon/m_e c^2$ approaches or exceeds 1, the cross-section, obtained from quantum electrodynamics, is the Klein-Nishina cross-section:

$$\sigma_{KN} = \sigma_T \frac{3}{4}\left(\frac{1+x}{x^3}\left(\frac{2x(1+x)}{1+2x} - \ln(1+2x)\right) + \frac{1}{2x}\ln(1+2x) - \frac{1+3x}{(1+2x)^2}\right) \tag{1.5}$$

An approximation of the electron energy loss rate in the Klein-Nishina regime can be found in Moderski et al. (2005) and an approximation including an intermediary regime from Thomson to Klein-Nishina can be found in Delahaye et al. (2010). The reaction is less likely to occur with higher photon energies due to relativistic and quantum effects, and the observed spectrum by a population of electrons experiences a cut-off when the photon energy approaches and exceeds the electron rest energy. For an electron with an energy of 1 TeV, 10 TeV or 100 TeV, the cross-section approaches the Klein-Nishina

regime for a photon field with a temperature of 3000 K, 300 K or 30 K, respectively (i.e. the average photon's energy in the electron's rest frame is ~ 506 keV).

Relativistic electrons can scatter CMB photons, UV-optical starlight, infrared photons from dust, and the synchrotron emission they produce, in a process called synchrotron self-Compton (SSC). The latter is observed in extreme accelerators such as the Crab nebula.

Bremsstrahlung emission

Charges accelerated in the Coulomb field of nuclei emit bremsstrahlung radiation (also called free-free emission). Bremsstrahlung emission is observed from radio to γ rays and the contribution from protons is negligible relatively to that of $e^{-/+}$ due to their higher mass. In the case of cosmic rays propagating in the interstellar medium, we refer to relativistic bremsstrahlung, in which the non-thermal particle distribution is assumed to be a power law. The energy loss rate of a relativistic electron is proportional to its energy E_e and to the number density of the gas n_H:

$$\dot{E} \propto -n_H E_e \tag{1.6}$$

The spectral index of the photon spectrum is the same as the power law distribution of electrons in a weakly ionized plasma, following Blumenthal & Gould (1970).

Neutral pion decay

Inelastic proton collisions (e.g. between cosmic ray and interstellar medium nuclei) produce neutral and charged pions at roughly similar fractions. Assuming a target proton at rest, the incident proton's kinetic energy must be at least 280 MeV. Neutral pions decay into two photons, while charged pions decay into muons and neutrinos. In the produced photon spectral energy distribution (SED, $E_\gamma^2 \times$ the flux), a "bump" close to 300-400 MeV indicates irrevocable evidence for hadronic interactions. At high energies, the γ-ray spectrum has approximately a similar spectral index as the CR proton spectral distribution. The amplitude of the γ-ray spectrum is proportional to the density of the target interstellar protons and the CR protons. Generally, $E_p \sim 10 E_\gamma$ with E_p the proton energy and E_γ the produced photon energy. Approximations of the produced spectra of γ rays can be found in Kafexhiu et al. (2014).

1.3 Cosmic rays

Spectrum and composition

Cosmic rays (CRs) are observed directly with space-borne experiments ($\lesssim 1$ TeV) such as AMS-02 (Aguilar et al. 2013), DAMPE (Chang et al. 2017) and CALET (Torii 2007), balloon experiments such as CREAM (Seo et al. 2004, covering the TeV to PeV range), or on the ground through the particle showers they produce in the atmosphere such as the Pierre Auger observatory (Abraham et al. 2004, up to EeV energies). The all-particle flux, shown in Fig. 1.4 (Evoli 2025), is characterized by a power law as a function of energy with an index of -2.7 from ~ 10 GeV up to a softening at ~ 3 PeV to an index of -3.0 (the "knee"). A second softening, the "iron knee", is observed at an energy 26 times higher than the first at roughly 80 PeV (Apel et al. 2013). The spectrum softens smoothly

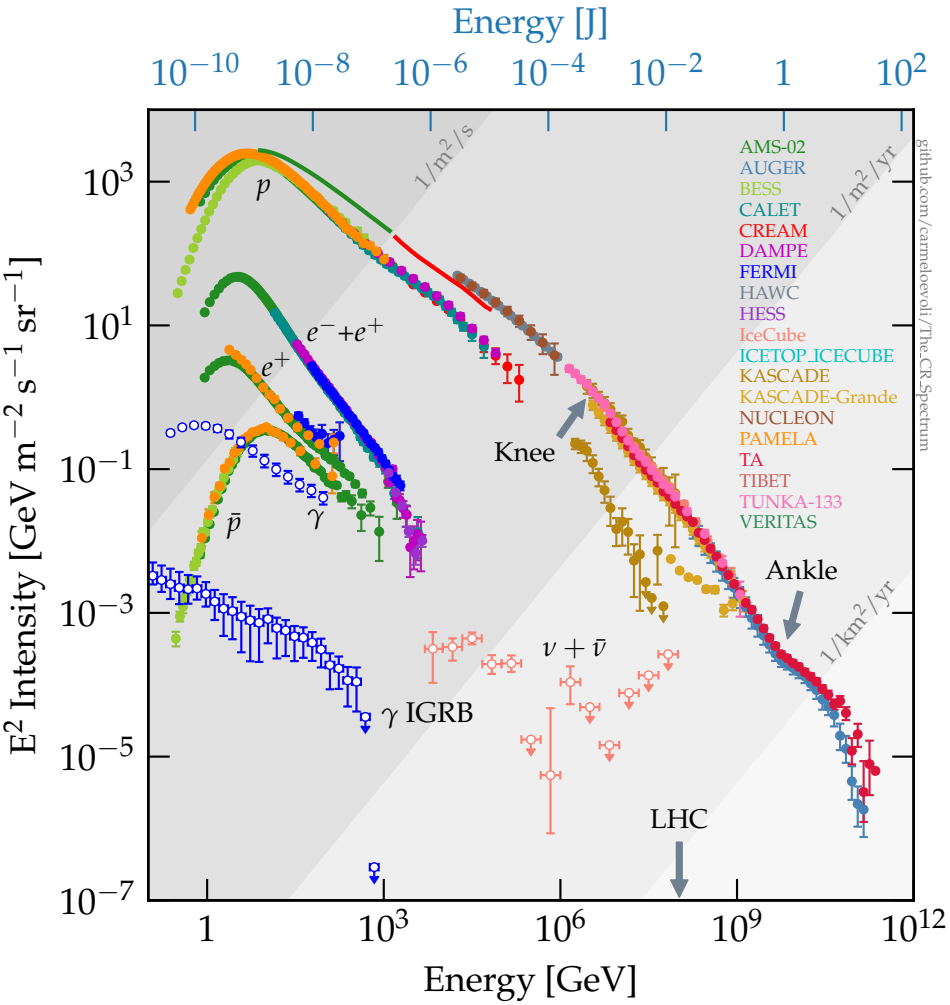

Figure 1.4: Compilation of cosmic ray intensity measurements from different experiments from Evoli (2025). The "Knee" in the all-particle spectrum refers to the softening at ~ 3 PeV. The "Ankle" refers to the hardening at ~ 3 EeV. The shown spectra include the all-particle spectrum, the proton spectrum, the total electron and positron spectrum, the positron spectrum, the antiproton spectrum, the γ-ray spectrum and the total neutrino spectrum.

between 141 and 400 PeV to an index of ~ -3.3 (Coleman 2020) before a hardening at ~ 5 EeV (the "ankle") to an index between -2.5 and -2.8 (Abbasi et al. 2008 and Aab et al. 2020). It cuts off at the Greisen-Zatsepin-Kuzmin limit of ~ 40 EeV (Fenu & Pierre Auger Collaboration 2017) due to interactions between CR protons and the Cosmic Microwave Background (CMB) in the intergalactic medium. CRs are composed primarily of protons (accounting for more than 90% of the total flux), heavier nuclei, electrons, positrons and antiprotons. The leptonic species account for $\sim 1\%$ of the total flux. The local energy density of CRs is of the order of 1 eV/cm^3, approximately in equipartition with that of interstellar gas, magnetic fields and radiation fields. Hence, they may dynamically influence the interstellar medium (ISM), regulating star formation through the ionization of molecular clouds, generating magnetic turbulence and providing pressure support which enhances the outflow of gas from the Galaxy (Ruszkowski & Pfrommer 2023).

CR electrons and positrons lose energy on much shorter time scales than CR nuclei and therefore must originate from nearby accelerators. Hence, the local CR electron and

positron fluxes provide constraints on sources within ~ 1 kpc. The electron and positron spectrum can be modeled as a power law with index ~ -3 up to ~ 1 TeV where a steepening to ~ -4 occurs (Aharonian et al. 2024). The abundance of electrons relatively to positrons indicates that the former are likely primary particles because secondary electrons and positrons are expected to have similar abundances.

Propagation in the Galaxy

As they propagate in the Galactic disk, CR nuclei interact with interstellar gas nuclei to produce secondary nuclei through spallation. This is inferred by the over-abundance of certain CR nuclei relatively with the solar system's abundances (Gaisser et al. 2016). The measure of primary-to-secondary ratios provides an estimate on the residence time of CRs in the Galaxy on the order of 1 Myr at GeV energies (Gabici et al. 2019), implying from their mean free path that they must be diffusively confined within the Galactic halo, repeatedly crossing the Galactic disk. Spatial diffusion is a stochastic process which describes the scattering of CRs by magnetohydrodynamical (MHD) waves and discontinuities in a turbulent magnetic field. The spatial diffusive component of CR transport is represented by the diffusion coefficient, which is directly related to the turbulent magnetic field's wave vector spectrum. The latter can be derived as a power law using Kolmogorov's theory of turbulence, wherein energy is injected from large-scale eddies and cascades to smaller scales until it is dissipated as heat. In the Galaxy, turbulence is injected by supernovae at a scale of roughly 100 pc, where the random field can dominate over the regular field (e.g. Jansson & Farrar 2012), resulting in in the isotropization of CR diffusion in the Galaxy. The diffusion coefficient can be expressed as a power law function of particle energy $D(E) = D_0(E/E_0)^\delta$ with E_0 the reference energy and δ the rigidity dependence (a derivation can be found in e.g. Becker Tjus & Merten 2020). From measurements of the local CR Boron-to-Carbon ratio, the average diffusion coefficient in the Galaxy is inferred to be $\sim 10^{28}$ cm^2 s^{-1} for 1 GeV $e^{-/+}$, and scales with energy as a power law of index $\delta \sim 0.33$, which is compatible with the theoretical value of 1/3 derived from Kolmogorov turbulence theory (Aguilar et al. 2016). The derived value of δ depends on the assumed CR propagation model, and has been shown to lie within the 0.3 to 0.6 range (e.g. Evoli et al. 2020). Kraichnan's incompressible MHD turbulence (Kraichnan 1965), which explicitly accounts for the presence of a magnetic field, predicts a harder rigidity dependence of $\delta = 1/2$.

Astrophysical origin

Astrophysical source classes from which CRs originate must produce the locally observed spectral features and luminosity (in addition to the energy-dependent composition and spatial distribution in the sky, which will not be discussed here). A detailed review on the origin of CRs can be found in Becker Tjus & Merten (2020). Beyond the "ankle" at ~ 5 EeV, CRs are believed to be of extragalactic origin, as no Galactic source is capable of accelerating particles to such energies. The observed softening in the spectrum between ~ 3 PeV and 400 PeV is thought to reflect on a cut-off in Galactic accelerators' spectra due to their maximum achievable energy. Acceleration of nuclei up to PeV energies might occur in supernova remnants with Diffusive Shock Acceleration under extreme conditions in terms of shock velocity and matter density (see Cristofari 2021 for a review). Conversely, none of the presently discovered PeVatrons are identified to be of hadronic origin, and known supernova remnants exhibit spectral cut-offs well below PeV energies.

Young massive stellar clusters have become a promising candidate in recent years, as shown in Aharonian et al. (2019) and LHAASO Collaboration (2024). The origin of Galactic PeV CR nuclei remains unknown, and the arrival of observatories probing the sky at photon energies above 100 TeV such as HAWC, LHAASO and later CTAO is a crucial step in shedding light on the subject.

A hardening of the ratio of positrons can be seen in AMS-02 data at $\sim$ 10 GeV (first observed by PAMELA) and can be explained as being due to nearby sources of primary positrons (such as pulsar wind nebulae) and/or a signature of dark matter interactions in the Galactic halo (Gabici et al. 2019). This observation is referred to as the GeV "positron excess" (Accardo et al. 2014). Thus, constraining the population of nearby lepton accelerators such as PWNe and their particle escape is of high interest. The contribution from pulsars and their nebulae remains an open question, with HAWC showing that $e^{-/+}$ may diffuse too slowly near pulsars to contribute significantly to the local spectrum (Abeysekara et al. 2017), while different modeling propositions in the literature have attempted to remedy this discrepancy (to be discussed in Section 2.3). Fig. 1.5 from Abeysekara et al. (2017) shows the predicted positron contribution from the Geminga pulsar to the local positron flux compared with the spectrum measured by AMS-02. Different values of the diffusion coefficient's power law index δ and the Geminga pulsar's spin-down timescale τ are tested. The latter parameter determines the historic rotational energy loss rate of the Geminga pulsar, a fraction of which is converted to $e^{-/+}$ (a more detailed discussion of pulsars is presented in Section 2.1). The plot illustrates the difficulty in reproducing the local $e^{-/+}$ spectrum if a slow diffusion between Earth and Geminga is assumed.

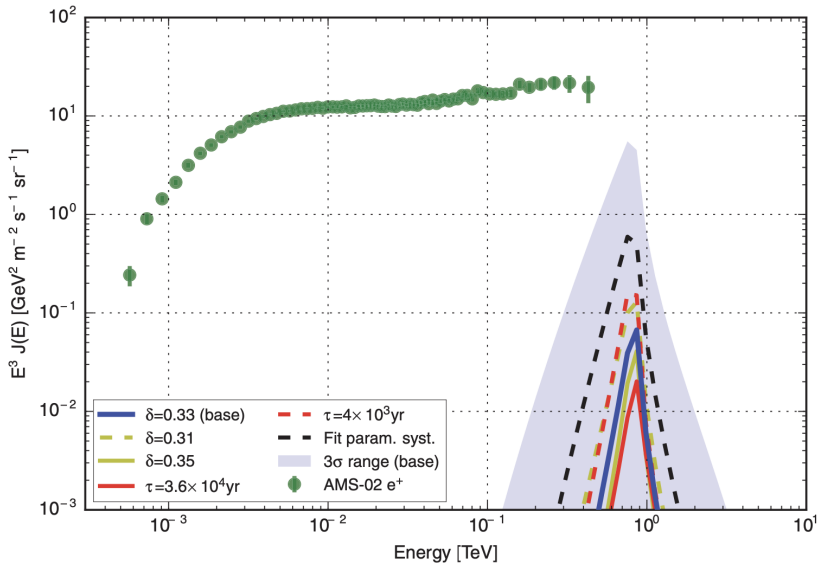

Figure 1.5: Expected local positron flux contribution from the Geminga pulsar from Abeysekara et al. (2017). The AMS-02 positron spectrum is shown in green. The predicted positron spectrum from Geminga is shown for different assumed values of the diffusion coefficient's power law index δ and for different initial spin-down timescales τ of the Geminga pulsar.

1.4 Galactic sources

VHE and UHE experiments revealed different types of sources as efficient γ-ray emitters. Along the Galactic plane, source classes include pulsar wind nebulae (PWNe), supernova remnants (SNRs), young massive stellar clusters and binary systems (including possible microquasars).

Binary systems

Binary systems that contain a compact object are characterized by environments with high magnetic and radiation energy densities. Interactions between the compact object and stellar winds produce shocks that accelerate particles to ultra-relativistic energies, and they are characterized by a γ-ray signal with high variability. The 3 binary systems in the HGPS are LS 5039, PSR B1259−63 and 1FGL J1018.6-5856 (HESS J1018−589 A). The variability of LS 5039 in H.E.S.S. data is illustrated in Fig. 1.6 from Aharonian et al. (2006), showing the 3.9-day modulation of the γ-ray emission (which corresponds to the orbital period of the binary system). Stronger absorption of the VHE photons through $\gamma - \gamma$ pair production with the stellar radiation field occurs at the superior conjunction near the periastron. The nature of the compact object remains unknown.

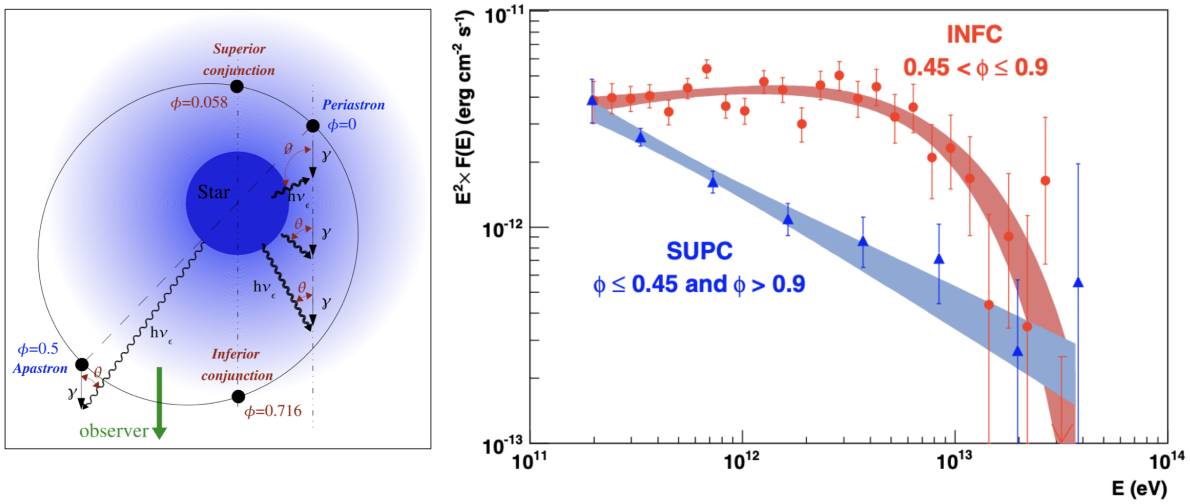

Figure 1.6: **Left:** Illustration of the geometry of LS 5039's orbit from Aharonian et al. (2006), with the star's size to scale, indicating the orbital phase ϕ at the inferior and superior conjunctions. **Right:** LS 5039 H.E.S.S. differential photon spectrum from from Aharonian et al. (2006) at the inferior (red) and superior (blue) conjunctions.

Microquasars consist of a binary system containing a black hole. The high accretion rate produces a hot disk that can be seen in X-rays, and relativistic jets that can be seen in the radio band. Particle acceleration occurs when the jet encounters the ambient medium, resulting in VHE γ rays in the form of two distinct lobes spanning up to tens of parsecs around the black hole as shown in Fig. 1.7 of the H.E.S.S. significance map of SS 433 (H.E.S.S. Collaboration 2024a). VHE emission from SS 433 was first seen by the HAWC observatory (Abeysekara et al. 2018). Microquasars can accelerate particles to PeV energies, as shown by Lhaaso Collaboration et al. (2025).

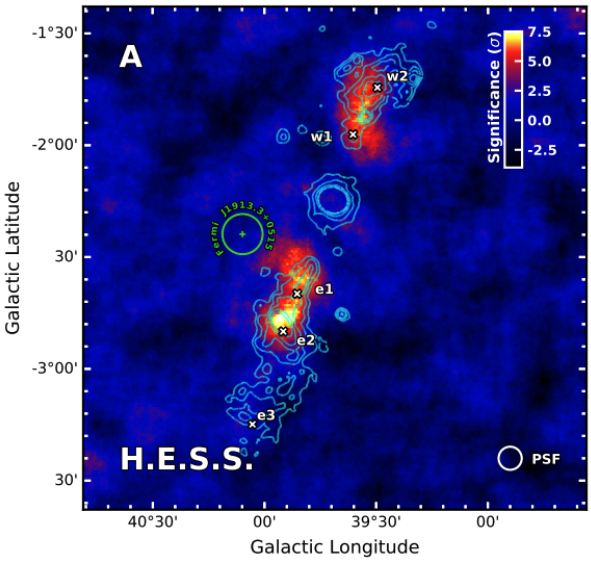

Figure 1.7: Significance map above 0.8 TeV of the SS 433 region after subtracting the predicted background from H.E.S.S. Collaboration (2024a), overlaid with blue contours representing the X-ray morphology measured with ROSAT (Brinkmann et al. 1996). Regions annotated with "e" and "w" are the jet termination regions observed in X-rays (Abeysekara et al. 2018). The compact object lies within the central X-ray contours.

Young massive stellar clusters

Massive stars exhibit high mass loss rates and strong stellar winds. In a massive stellar cluster, such as Westerlund 1 (Aharonian et al. 2022) and Cygnus OB2 in the Cygnus X star-forming region (Ackermann et al. 2011), interactions between stellar winds create shocks that could lead to particle acceleration (Aharonian et al. 2019). The collective activity of the massive stars can also create structures known as "superbubbles" which can span tens of parsecs and appear extended in the sky. A superbubble scenario, among other scenarios, is studied in the case of the VHE emission in the vicinity of Westerlund 1, known as HESS J1647−458 in the HGPS, which is shown in Fig. 1.8 from Aharonian et al. (2022). The diffuse emission extends beyond a "shell"-like structure around the cluster, but the contribution from two energetic pulsars in the region cannot be ruled out. Young massive stellar clusters are considered PeVatron candidates, and LHAASO recently detected PeV photons in the direction of the Cygnus cocoon (LHAASO Collaboration 2024).

Supernova remnants

A massive star ($\geq$ 8 $M_\odot$) undergoing core collapse at the end of its life time (core-collapse supernova), or a white dwarf exceeding the Chandrasekhar limit ($\geq$ 1.44 $M_\odot$) due to accretion of its binary companion's material (thermonuclear supernova), expels the majority of its stellar material and produces an expanding shock wave that sweeps the surrounding interstellar material. Interstellar hadrons and leptons meeting the shock front are accelerated to ultra-relativistic energies, producing γ-ray emission along a rim-like structure in the sky (the "shell"), such as SN 1006 (Acero et al. 2010), RX J1713−3946 (H.E.S.S. Collaboration 2018e) and Vela Junior (H.E.S.S. Collaboration 2018c), as shown in Fig. 1.9. In a search for such structures in the HGPS (H.E.S.S. Collaboration 2018a), two sources were identified as SNRs based on their shell-like morphology. These objects

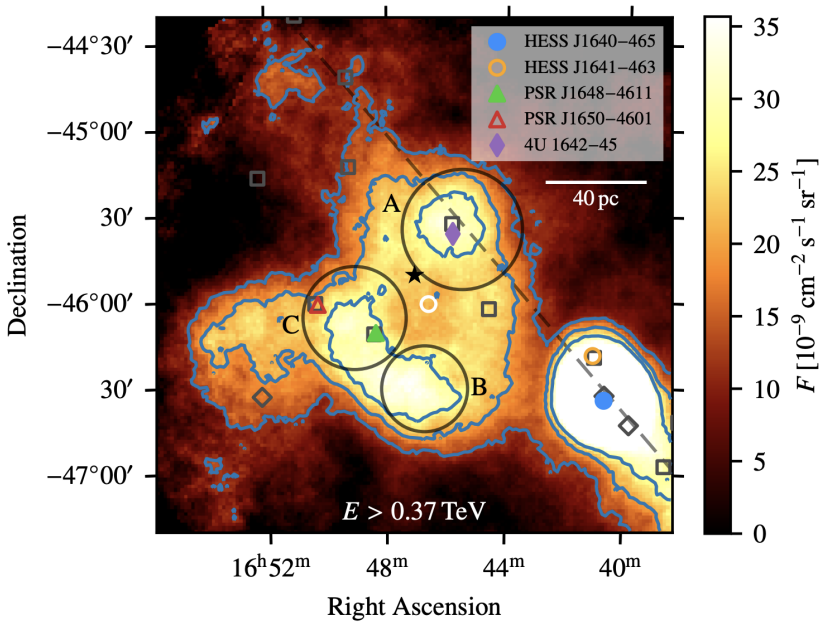

Figure 1.8: Flux map above 0.37 TeV of the emission region around Westerlund 1, smoothed with a 0.22° disk, from Aharonian et al. (2022). The black star is the position of Westerlund 1. The black circles A, B and C represent regions of enhanced emission. The 40 pc scale is given for the distance to Westerlund 1. Squares and diamonds represent sources from the 4FGL-DR2 catalog, with the diamonds indicating sources significant above 30 GeV. The dashed line represents the Galactic Plane. The position of 4U 1642−45, a Low Mass X-ray Binary, is shown along with the positions of H.E.S.S. sources and energetic pulsars in the region as indicated in the legend. The contour lines represent three different flux levels.

can extend up to tens of parsecs, shining at VHE for thousands of years. Particles escaping confinement from the SNR can also collide with nearby molecular clouds to produce γ rays, as in the case of W44 (Uchiyama et al. 2012), however this process is yet to be firmly identified in the VHE range. The rate of supernovae in the Milky Way is ~ 2 per century, potentially making SNRs the most prominent contributor to the local CR flux below the break at ~ 3 PeV. They have long been proposed as PeVatron candidates, but none of the currently detected SNRs show γ-ray emission extending up to 100's of TeV without a curvature (or cut-off). Core collapse supernovae result in the creation of a pulsar and a pulsar wind nebula which are presented below.

Pulsars and pulsar wind nebulae

As mentioned previously, pulsars and pulsar wind nebulae (PWNe) are prominent categories of γ-ray sources. Fermi-LAT's 4FGL catalog reported the detection of GeV pulsed emission from 239 pulsars. While pulsars are efficient GeV γ-ray emitters, only less than a handful (the most powerful) have been detected up to TeV energies. TeV pulsed emission from the Crab and the Vela pulsars have been detected up to 1.5 TeV and 20 TeV by MAGIC (Ansoldi et al. 2016) and H.E.S.S. (Aharonian et al. 2023) respectively. Most recently, the detection of pulsed emission up to 10 TeV from PSR J1509−5850 was announced by H.E.S.S. (Regeard et al. 2025). Young pulsars can produce emission nebulae which are observed from radio to PeV energies. The radiation is usually due to synchrotron and inverse Compton emission by $e^{-/+}$ confined in a nebular magnetic field originating in the pulsar, and can extend up to tens of parsecs in the TeV range. The

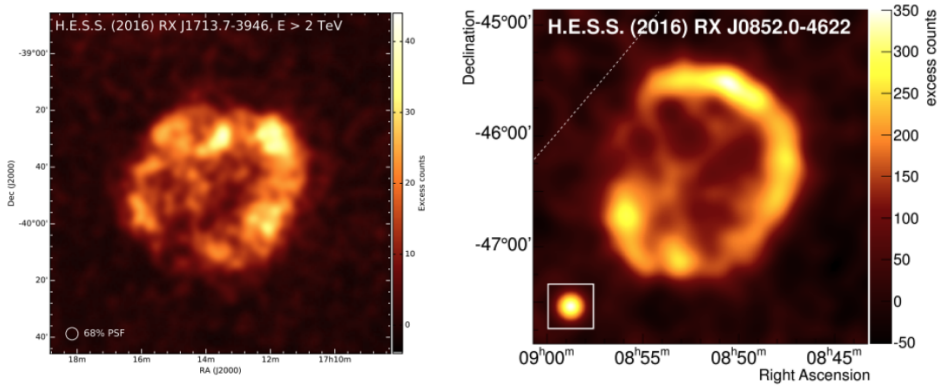

Figure 1.9: **Left:** H.E.S.S. excess counts map of RX J1713 − 3946 above 2 TeV from H.E.S.S. Collaboration (2018e). **Right:** H.E.S.S. excess counts map of Vela Junior smoothed with a 0.08°-width Gaussian function from H.E.S.S. Collaboration (2018c).

HGPS contains 12 sources that are firmly identified as PWNe, and a population study of sources spatially coincident with energetic pulsars revealed 10 plausible PWNe candidates (H.E.S.S. Collaboration 2018f). The firmly identified PWNe are known as such based on multi-wavelength evidence and/or their energy-dependent morphology. The extent of the source increases with decreasing photon energy, due to the energy loss timescale of $e^{-/+}$ as they are transported away from the pulsar. The most extended γ-ray PWN is HESS J1825−137 with a radius of $\sim$ 50 pc, powered by the pulsar PSR B1823−13 with a characteristic age of 21.4 kyr. Fig. 1.10 from H.E.S.S. Collaboration (2019b) shows the extent of the PWN in two different energy bands, clearly illustrating the energy-dependent morphology.

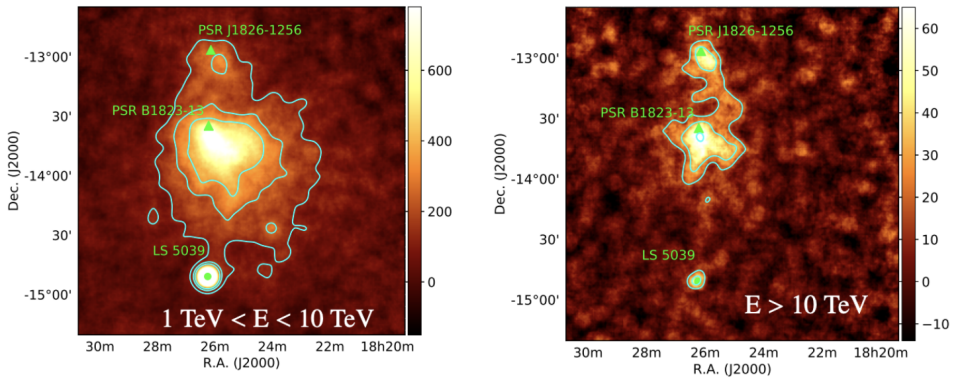

Figure 1.10: Excess counts map after subtracting the predicted background model in the HESS J1825−137 region, from H.E.S.S. Collaboration (2019b). Shown in green triangles are the pulsars in the region, with PSR B1823−13 powering the PWN, and PSR J1826−1256 possibly associated with a nearby source HESS J1826−130. The source at the bottom of the map is the binary system LS 5039. **Left:** Excess map in the 1 to 10 TeV range, with the cyan contours representing the 5-10-15σ statistical significance levels. **Right:** Excess map above 10 TeV, with the cyan contours representing the 3-5-10σ statistical significance levels.

PWNe are long-lasting sources at VHE, and extended γ-ray emission can be observed towards pulsars with characteristic ages on the order of 10^2 kyr. Evidence of VHE and UHE γ rays from $e^{-/+}$ which have escaped the nebular magnetic field has been observed towards PWNe which are powered by middle-aged ($\gtrsim$ 40 kyr) pulsars, such as the extended γ-ray emission around the Geminga pulsar (Abeysekara et al. 2017). This

observation is known as the "pulsar halo" phenomenon. The pulsar, pulsar wind nebula and pulsar halo notions are presented in more detail in the following chapter.

The Galactic Center ridge

Hosting numerous giant molecular clouds, massive stellar clusters (including the Arches, Quintuplets and the Central Cluster), SNRs, PWNe and millisecond pulsars that lie in the inner few hundreds of pc of the Galaxy, the Galactic center (GC) region encapsulates the central supermassive black hole Sagittarius A* (Sgr A*). The VHE emission has been studied extensively by H.E.S.S. (e.g. H.E.S.S. Collaboration 2018b), and is characterized by diffuse emission spanning $\sim 2°$ (the GC ridge) and a point-like component, HESS J1745−290, which is likely associated with Sgr A*. The variability of Sgr A* has been observed in the radio, infrared and X-ray bands (Genzel et al. 2010) and is considered "dormant" (i.e. its accretion rate is low). Evidence such as the detection of X-ray light echoes (Ponti et al. 2010) and the Fermi bubbles (Su et al. 2010) could suggest the presence of historic activity in the past 100 yr to 10 Myr. The latest data from H.E.S.S. is shown in Fig. 1.11 from Devin et al. (2025) as a map of the GC ridge's excess (i.e. after subtracting the contributions of G0.9+0.1, HESS J1745−290 and the diffuse Galactic emission), with the total excess above the background level shown in the inset. The cyan contours represent the Central Molecular Zone (CMZ) as traced by carbon monosulphide (CS), and the positions and extensions of all known H.E.S.S. sources in the region are shown as crosses if they are point-like or dashed circles if they are found to be extended. A scenario where CRs are continuously injected near the GC is preferred by the data, however it remains unclear whether these originate from Sgr A* or source populations in the vicinity such as the Central Cluster

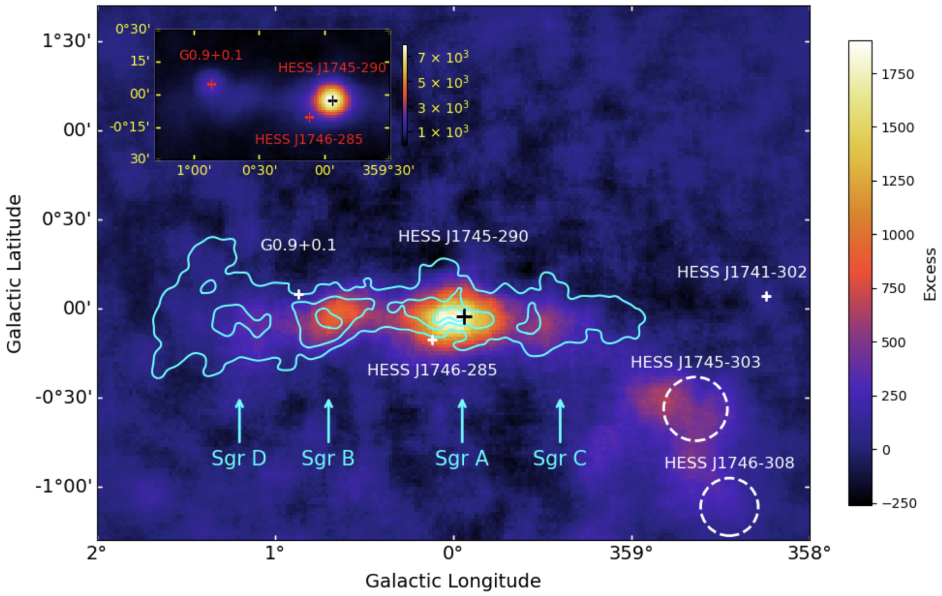

Figure 1.11: GC ridge excess map above the background level after subtracting the contributions of G0.9+0.1, HESS J1745−290 and the Galactic diffuse emission, from Devin et al. (2025). The total excess map above the background level is shown in the inset. The cyan contours represent the CMZ as traced by CS (Tsuboi et al. 1999), with the arrows indicating the positions of known molecular cloud complexes.

Chapter 2

Pulsar wind nebulae and pulsar halos

Contents

2.1 General considerations on pulsars 23

2.2 Pulsar wind nebulae 26

2.3 The γ-ray halos observed towards middle-aged pulsars . . . 27

Pulsar Wind Nebulae (PWNe) are highly efficient $e^{-/+}$ accelerators, and are possibly important contributors to the observed local $e^{-/+}$ spectra in the GeV range. They are observed from the radio band up to the highest energy γ-rays, primarily from synchrotron and inverse Compton emission. The diversity of the physical properties of the pulsars powering them and their long-lasting emission mean that PWNe are studied at different evolutionary stages. Recent important discoveries in γ-ray astronomy include the detection of PeV photons from the Crab by LHAASO (LHAASO Collaboration 2021), and the discovery of the highly extended halos towards the Geminga (PSR J0633+1746) and Monogem (PSR B0656+14) pulsars by the HAWC observatory (Abeysekara et al. 2017). The latter provided direct evidence of $e^{-/+}$ escape from PWNe, and established a new class of sources in which cosmic-ray escape and propagation into the ambient medium can be studied. Some sources in the HGPS have also been interpreted as being in a transition stage from PWN to pulsar halo, such as HESS J1809−193 (e.g. H.E.S.S. Collaboration 2023b, Martin et al. 2024 and Xian et al. 2026) and HESS J1825−137 (e.g. Lu et al. 2022, Collins et al. 2024 and Martin et al. 2024).

2.1 General considerations on pulsars

Rapidly rotating neutron stars are remnants of the gravitational collapse of a massive ($\geq 8\ M_\odot$) star's core. Atomic nuclei and electrons undergo electron capture to produce neutrons and neutrinos, forming a body primarily composed of nuclear matter and held together by neutron degeneracy pressure. The compact object has a mass $\sim 2\ M_\odot$ and is $\sim 10 - 20$ km in diameter. Due to conservation of the angular momentum and stellar magnetic flux of the progenitor, neutron stars spin with periods on the order of milliseconds to seconds, hosting a magnetic field $\sim 10^{12}$G. The resulting electric field accelerates $e^{-/+}$ to ultra-relativistic energies, radiating as they migrate to the poles and creating pair production cascades. The misalignment of the magnetic poles with the

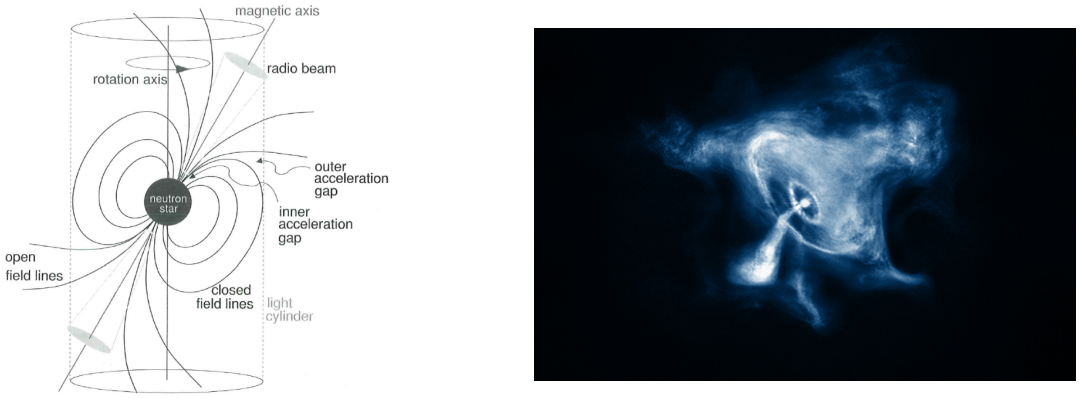

Figure 2.1: **Left:** Pulsar illustration from Lorimer & Kramer (2004). **Right:** Chandra image of the Crab nebula (Credits: NASA). The innermost ring around the central object is the wind termination where $e^{-/+}$ are re-accelerated.

rotational axis means that the beamed emission can sweep the line of sight, causing the observed highly periodic pulsations. Pulsars allow direct measurements of the period P and period evolution $\dot{P}$. In the following, we briefly summarize basic pulsar evolution relationships from Lorimer & Kramer (2004). The left panel of Fig. 2.1 from Lorimer & Kramer (2004) illustrates a simple pulsar model, where the light cylinder denotes the distance from the neutron star at which the comoving magnetic field lines rotate at the speed of light. Beyond this point, open magnetic field lines carry $e^{-/+}$ produced in the magnetosphere in a particle wind. $e^{-/+}$ are re-accelerated at the wind termination shock, the boundary with the synchrotron nebula (which can be seen in the X-ray Chandra image of the Crab nebula in the right panel of Fig. 2.1). In the so-called striped wind model, $e^{-/+}$ may also be accelerated within the wind through repeated magnetic reconnection in the presence of a current sheet (Pétri 2012).

The loss rate of the pulsar's rotational energy is

$$\dot{E} = -I\Omega\dot{\Omega} = 4\pi^2 I\dot{P}P^{-3} \tag{2.1}$$

with Ω the angular frequency and I the inertial momentum canonically taken as $I = 10^{45}$ g cm^2 in the absence of direct mass and radius measurements. The bulk of this power is converted into a relativistic wind and high-energy radiation. A rotating magnetic dipole with magnetic moment $|\mathbf{m}|$ has a radiation power

$$\dot{E}_{dipole} = \frac{2}{3c^3}|\mathbf{m}|^2\Omega^4 \sin^2\alpha \tag{2.2}$$

with α the angle between the magnetic moment and the rotation axis. Equating $\dot{E}$ and $\dot{E}_{dipole}$:

$$\dot{\Omega} = -\left(\frac{2|\mathbf{m}|^2 \sin^2\alpha}{3Ic^3}\right)\Omega^3 \tag{2.3}$$

Since the pulsar is not a pure electromagnetic dipole (due to the production of a particle wind), a generalized equation is used instead:

$$\dot{\Omega} = -K\Omega^n \tag{2.4}$$

with K assumed to be constant and n the braking index. The latter can be determined by measurements of the second derivative of the rotational frequency, although this is

a difficult measurement and has only been done for few pulsars, with $n \neq 3$ generally. Expressing Ω as a function of P, integrating Eq. 2.4 over time and assuming $n \neq 1$, the true age of the pulsar reads

$$t_{age} = \frac{P}{(n-1)\dot{P}} \left(1 - \left(\frac{P_0}{P}\right)^{n-1}\right) \tag{2.5}$$

with P_0 the pulsar's birth period. Assuming $P_0 \ll P$ and a pure magnetic dipole ($n = 3$), $\tau_c = P/2\dot{P}$ is known as the characteristic age. τ_c is not always a reliable estimate of the true pulsar's age. The characteristic magnetic field strength at the surface is

$$B_S = \sqrt{\frac{3c^3}{8\pi^2} \frac{I}{R^6 \sin^2 \alpha} \dot{P} P} \tag{2.6}$$

and is constant throughout the evolution if $n = 3$. In Faucher-Giguère & Kaspi (2006), Monte Carlo pulsar population syntheses, which were assumed to have braking index $n = 3$ (and therefore a constant surface magnetic field B_S throughout their evolution), were found to reproduce the observed B_S distribution adequately. The population syntheses of Gonthier et al. (2002) show that field decay on a timescale of $\sim 10^3$ kyr better reproduces the data. This value is an order of magnitude larger than the pulsars which will be considered throughout this thesis, and the evolution of B_S can therefore be neglected. For $n = 3$ and defining the initial spin-down age $\tau_0 = \tau_c - t_{age}$, the spin-down evolution of the pulsar can be modeled as

$$L(t) = \dot{E} \left(\frac{1 + t_{age}/\tau_0}{1 + t/\tau_0}\right)^2 \tag{2.7}$$

with t the time since the pulsar's birth.

The distances to radio pulsars are obtained using the dispersion measure DM:

$$DM = \int_0^L n_e d\ell = \langle n_e \rangle d_{PSR} \tag{2.8}$$

with L the path length along the line of sight, $\langle n_e \rangle$ the free electron number density in the medium between the observer and the pulsar, and d_{PSR} the distance to the pulsar. DM can be measured through the delay in time of arrival of pulses at different wavelengths. A derivation of the expression is shown in Shapiro & Teukolsky (1983):

$$\frac{\Delta t_A}{\Delta \omega} = -\frac{4\pi e^2}{m_e c \omega^3} DM \tag{2.9}$$

with $\Delta t_A(\omega)$ the measured time delay of different frequency (ω) components of the pulse. Typically the free electron density model of Yao et al. (2017) is used, yielding 1σ errors on the distance of $\pm 20\%$ (unless stated otherwise for specific pulsars in the paper). The most accurate pulsar distances have been measured through parallax (as is the case for Geminga) provided they are close enough.

Pulsars are generally born at low Galactic latitudes, in the spiral arms and migrate away from the Galactic plane throughout their lifetime (i.e. the pulsar population's spin-down power decreases with Galactic latitude). The "kick velocity" of the pulsar at birth, called as such because pulsars are observed to have higher velocities than their progenitors,

is possibly due to asymmetries during core collapse. In Faucher-Giguère & Kaspi (2006), the mean pulsar velocity is found to be 380^{+40}_{-60} km/s. In Hobbs et al. (2005), the highest measured transverse velocity in the sky is that of PSR B2011+38 at 1624 km/s with an error of roughly 55%. Hence, middle-aged pulsars are expected to eventually leave their parent supernova remnants or leave behind a relic pulsar wind nebula within tens to hundreds of thousands of years. Moving at supersonic speeds in the ISM, they form structures known as bow-shock PWNe, characterized by a thin lagging tail-like structure than can span multiple parsecs (e.g. the Guitar and Lighthouse nebulae).

2.2 Pulsar wind nebulae

$e^{-/+}$ are transported along the open magnetic field lines of the pulsar beyond the light cylinder, forming a relativistic wind wherein acceleration may occur through magnetic reconnection events. Particles are re-accelerated at the wind termination shock (the boundary with the synchrotron nebula) to ultra-relativistic energies and form a nebula produced by synchrotron and inverse Compton scattering (ICS) emission. The ICS emission is generally produced by cooler (i.e. lower energy) $e^{-/+}$ than those responsible for the X-ray emission because the cooling time is inversely proportional to the particle energy, and the PWN's magnetic field decreases with time and distance from the pulsar. Hence, $e^{-/+}$ responsible for the VHE emission cool down on longer timescales than those responsible for the X-ray emission, and the morphology of the source at VHE can be more extended because $e^{-/+}$ have time to diffuse away from the pulsar before cooling. In the VHE band, PWNe outlast the emission from their host SNRs due to efficient confinement of $e^{-/+}$ and can radiate for multiple tens of thousands of years as their resident pulsar's rotational power is converted into ultra-relativistic $e^{-/+}$. The PWN cools due to adiabatic losses, radiation processes and particle escape. Their evolution is generally characterized by three phases (Gelfand et al. 2009), illustrated in Fig. 2.2 from Amato & Recchia (2024). The first phase is the free expansion phase where the nebula grows adiabatically in the unshocked ejecta of the SNR. G21.5−0.9 is an example of a system in this evolutionary stage, and is observed in radio, X-rays and VHE γ rays (HESS J1833−105). The second phase begins at a few kyr, when the PWN's expansion (now with a size ~ 10 pc) is disrupted by the reverse shock of the SNR, and compression of the PWN up to an order of magnitude of its current size takes place. This begins a reverberation phase where the PWN re-expands due to the increased pressure and re-compresses by repeated interactions with the reverse shock, until a balance is reached with its surroundings. In this stage, PWN morphologies can be highly irregular, as seen in the case of Vela X (H.E.S.S. Collaboration 2019a). In the third stage, the PWN grows steadily, with the pulsar eventually leaving it due to its proper motion, resulting in a relic PWN. From one-zone models (e.g. Bucciantini et al. 2010), the injection spectrum of $e^{-/+}$ into the PWN is characterized by a break between $0.1 - 1$ TeV, with a harder index between $1.0 - 2.0$ below the break and a softer index of $2.0 - 2.5$ above the break.

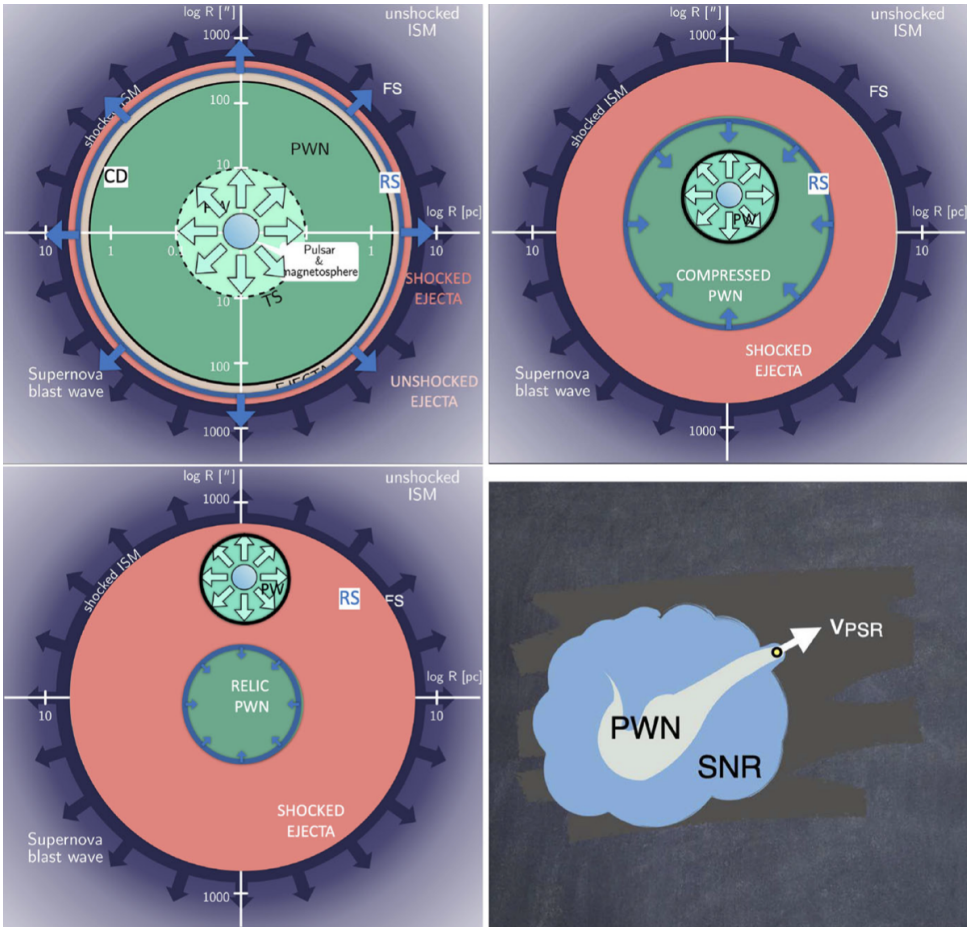

Figure 2.2: Sketch of the different phases of PWN and SNR evolution from Amato & Recchia (2024). **Top left:** The free expansion phase, showing the wind termination shock (TS), the SNR forward shock (FS) propagating in the ISM and the reverse (RS) shock which is yet to encounter the PWN. **Top right:** The reverberation phase, the PWN is disrupted by the incoming RS and undergoes repeated compression and expansion. **Lower left:** The relic stage when the pulsar has left its initial PWN and begins creating a new PWN from freshly injected particles. **Lower right:** The pulsar leaves the SNR, possibly forming a bow shock PWN.

2.3 The γ-ray halos observed towards middle-aged pulsars

HAWC data revealed two highly extended γ-ray structures around the Geminga (PSR J0633+1746) and Monogem (PSR B0656+14) pulsars (Abeysekara et al. 2017) in the $8 - 40$ TeV range. The emission around each pulsar extends to multiple degrees in the sky, as shown in Fig. 2.3. These pulsars are referred to as "middle-aged" pulsars, with characteristic ages of 342 kyr for Geminga and 110 kyr for Monogem. The Geminga pulsar, a radio-quiet pulsar detected in the X-ray and GeV energy bands, is surrounded by an X-ray nebula (Pavlov et al. 2010 and Posselt et al. 2017) spanning a few arc-minutes and featuring three distinct "tails", as observed by the Chandra X-ray observatory. Thus, given the pulsar's distance to Earth of 250 parsecs measured with parallax, the VHE emission traces $e^{-/+}$ transport at a larger ($\approx$ 20 pc) scale than the X-ray emission in the 0.3 to 7 keV range ($\lesssim$ 1 pc). The excessive difference in size is due to the different cooling time scales, with the X-ray component tracing a much younger and confined population of $e^{-/+}$ than the population responsible for the VHE emission by ICS. Given the energies

at which the TeV halos are observed, the most prominent contribution to the γ-ray SED is that of up-scattered CMB photons (due to the Klein-Nishina suppression of ICS of higher energy photons). Additionally, the ages of the pulsars are significantly higher than those of known TeV emitting PWNe, and they may have exited their SNR, with the Geminga pulsar having traveled $\sim$ 70 pc since its birth. These features warranted the distinction between PWNe and pulsar halos.

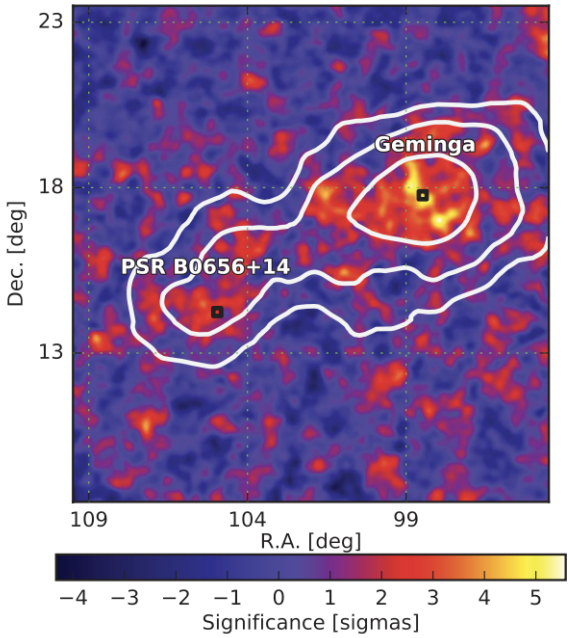

Figure 2.3: Significance map of the excess above the predicted background in HAWC data from 1 to 50 TeV from Abeysekara et al. (2017). The white contours indicate the 5-7-10σ levels.

The observations made by the HAWC Collaboration unambiguously revealed, for the first time, VHE emission from escaped $e^{-/+}$ produced in a PWN. Hence, observations of halos around nearby PWNe may further constrain their contribution to the local positron spectrum, which is crucial to determine the origin of the hardening seen in AMS-02 data (the "positron excess"). In Abeysekara et al. (2017), the γ-ray emission was spatially modeled for Geminga and Monogem by $e^{-/+}$ continuously injected from a point-like source and diffusing symmetrically, cooling due to synchrotron emission and ICS. The fitted model parameters are shown in Table 2.1. The assumed $e^{-/+}$ injection spectrum is a power law the normalization of which is a fraction (i.e. the injection efficiency) of the historic pulsar spin-down power as defined in Eq. 2.7. For Geminga and Monogem, the injection efficiency is assumed to be 40%, and 4% respectively. This yielded a measured diffusion coefficient that was found to be roughly two orders of magnitude lower ($\sim 4 \times 10^{27}$ cm^2/s at 100 TeV for Geminga) than the expected value from extrapolation of the average Galactic value. The latter ($\sim 10^{29}$ cm^2/s at 100 TeV) is obtained by extrapolating the diffusion coefficient measured from secondary to primary CR ratios, assuming that it scales as a power law function of energy. Abeysekara et al. (2017) show that $e^{-/+}$ produced by Geminga and Monogem and diffusing at a suppressed rate to Earth would weakly contribute to the local positron spectrum. Subsequently, Fang et al. (2018) showed that if diffusion is slowed in an extended region around the pulsar (possibly tens to 100 pc in size) and resumes at the average Galactic value outside the suppressed diffusion region, there could be a non-negligible contribution to the local positron flux measured

Model parameter	Geminga	PSR B0656+14
Char. age τ_c [kyr]	342	110
Period P [ms]	237	385
Distance d [pc]	250	288
Spin-down power $\dot{E}$ [10^{34} erg/s]	3.26	3.8
Initial spin-down power L_0 [10^{34} erg/s]	27.8	4.0
PL norm. N [10^{-15} TeV^{-1} cm^{-2} s^{-1}]	$13.6^{+2.0}_{-1.7}$	$5.6^{+2.5}_{-1.7}$
PL index α	2.34 ± 0.07	2.14 ± 0.23
Diff. coeff. at 100 TeV D_0 [10^{27} cm^2 s^{-1}]	$3.2^{+1.4}_{-1.0}$	15^{+49}_{-9}

Table 2.1: Assumed pulsar properties and fitted $e^{-/+}$ spatial diffusion model by HAWC. The pulsars' characteristic ages τ_c, present-day periods P, distances d and spin-down powers $\dot{E}$ are from Manchester et al. (2005). The initial spin-down power L_0 is assumed. The differential photon spectrum is modeled as a power law (PL), with N the normalization at 20 TeV and α the spectral index. D_0 is the diffusion coefficient normalization at 100 TeV, assuming $D \propto E^\delta$ with $\delta = 1/3$.

by AMS-02 as shown in Fig. 2.4 from Fang et al. (2018). The Geminga halo's positron contribution from a two-zone diffusion model (with a suppressed region of 50 pc where the diffusion coefficient is fixed to the HAWC measurement and an injection efficiency of 75%) is shown in dashed green, against the AMS-02 positron spectrum data from Accardo et al. (2014) and a model predicted secondary positron flux in dashed cyan. The injection efficiency acts as a normalization, and if it is reduced to the value used by Abeysekara et al. (2017), the model would still predict a significant contribution by Geminga to the local positron flux. Further, as will be explored in Chap. 4, the injection efficiency and the diffusion coefficient could be correlated owing to the reduced particle density when the latter is increased.

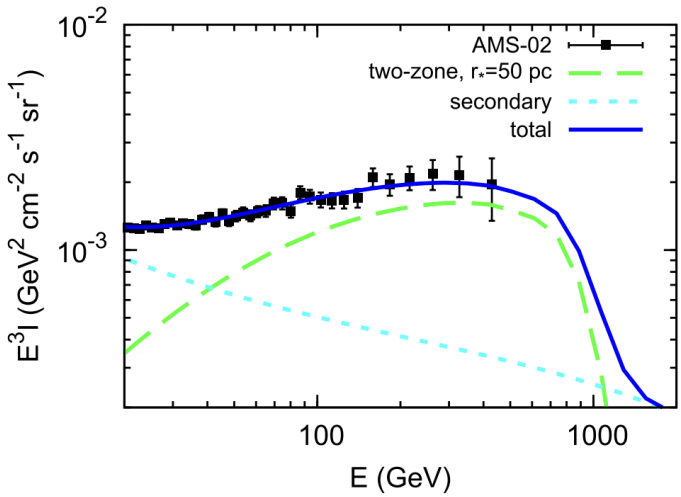

Figure 2.4: Positron contribution to the local positron flux by the Geminga halo (dashed green) under the assumption of two-zone diffusion, a suppressed diffusion region of 50 pc where the diffusion coefficient is fixed to the HAWC measurement and an injection efficiency of 75%, and by a predicted secondary positron flux from inelastic $p-p$ collisions (dashed cyan), from Fang et al. (2018). The total predicted flux is shown in solid blue. The AMS-02 data from Accardo et al. (2014) is shown in black.

In principle the local $e^{-/+}$ spectra could be used to constrain the population of nearby PWNe/pulsar halos, as was done in Martin et al. (2022) using the two-zone diffusion model of Tang & Piran (2019). The mechanism by which diffusion is slowed in the region around the pulsar remains a theoretical subject of interest, with current propositions being self-confinement by enhanced turbulence from escaped leptonic cosmic-rays, or that

the halo developed in a medium where turbulence was enhanced due to the progenitor's environment and past SNR. Understanding the mechanism behind the slowed diffusion requires knowledge of the medium in which the pairs are propagating. Giacinti et al. (2020) proposed that if the halo traces escaped $e^{-/+}$ diffusing in the ISM, their energy density should be considerably lower than that of the ISM such as they do not dynamically influence the medium. Fang et al. (2019) proposed a scenario in which the Geminga halo develops inside its SNR, the expanding shock-wave of which can provide enough energy to produce the observed enhanced turbulence level. A model which does not require a suppressed diffusion rate is proposed in Liu et al. (2019) with anisotropic diffusion of $e^{-/+}$, in which the size and asymmetry of the γ-ray morphology is determined from the alignment of the mean magnetic field with the line of sight. The difficulties of constraining models of $e^{-/+}$ transport arise from model degeneracies with respect to multiple parameters, and some assumptions must be made on pulsar parameters such as the braking index, the true age and the distance, if these are not measured. The line between PWNe and pulsar halos is blurred, with multiple sources found to possibly be in a transitional stage. Supplementing the population of identified or candidate pulsar halos could help approach the biggest questions they pose, such as their contribution to the large-scale Galactic emission as unresolved sources, their implications on the escape of $e^{-/+}$ from PWNe, and their potential as laboratories to study CR propagation near their sources.

Since the identification of the Geminga and Monogem halos, a handful of pulsar halo candidates have been proposed by H.E.S.S, HAWC and LHAASO, and in this thesis a search for candidates in the H.E.S.S. Galactic Plane Survey will be conducted in Chap. 5. The large extensions of pulsar halos mean that they are difficult to study with Imaging Atmospheric Cherenkov Telescopes if the pulsar is too close, due to the limited field of view of these instruments. The run-matching background method (Wach et al. 2024) was developed for this purpose and applied to a newly discovered halo candidate around PSR B1055−52. Otherwise, the angular resolution of IACTs allows studying halos towards more distant middle-aged pulsars, provided they are energetic enough. Evidence of escaped $e^{-/+}$ has recently been proposed in HESS J1809−193 (H.E.S.S. Collaboration 2023b) and HESS J1813−178 (H.E.S.S. Collaboration 2024b). The development of spectro-morphological analyses and template-based techniques in IACT data analysis (cf. Chap. 3) warrant revisiting the Galactic plane and the population of H.E.S.S. PWNe in search for possible pulsar halo candidates. Additionally, the availability of the recently published 1LHAASO catalog of VHE/UHE sources allows for better constraints on physical models with access to a wider energy band.

Chapter 3

Instruments and data analysis methods

Contents

3.1 Extensive Air Showers 31
3.2 The H.E.S.S. experiment 32
3.3 The Cherenkov Telescope Array Observatory 35
3.4 Data analysis with Gammapy 36

This chapter presents the detection technique of γ-ray emission in the VHE range, the experiments producing the data (or simulated data) that are used in this thesis (H.E.S.S. and CTAO) and the data analysis method based on the Gammapy package (Donath et al. 2023).

3.1 Extensive Air Showers

Shower development

Extensive air showers (EAS) are the cascade of reactions initiated upon the incidence of a γ ray or cosmic-ray particle with the Earth's atmosphere. Gamma rays entering the Earth's atmosphere undergo pair production by interacting with the Coulomb fields of atmospheric nuclei. The $e^{-/+}$ pairs in turn interact with the Coulomb fields of nuclei to produce γ rays through bremsstrahlung emission. The width of the particle shower as a function of altitude is governed by Coulomb scattering of the resulting $e^{-/+}$ pairs. Similarly, showers are produced by hadronic and leptonic cosmic-rays entering the atmosphere. These result in the creation of neutral and charged pions which decay into γ rays, muons and secondary $e^{-/+}$. The width of the shower as a function of altitude is governed by the transverse momentum transfer. The shower development stops when the losses due to ionization dominate over bremsstrahlung, which occurs at the critical electron energy of $E_c \sim 83$ MeV in air. Assuming that bremsstrahlung radiation and pair-production are the only dominant processes (i.e. the Heitler model, Heitler 1954), the characteristic amount of matter (i.e. depth) traversed by $e^{-/+}$ during a bremsstrahlung and pair production process in a given material is defined by the radiation length X_0 in g cm^{-2}, with $X_0 \sim 36.7$ g cm^{-2} in the atmosphere. The depth of shower development maximum X_{max} corresponds to the depth at which ionization losses dominate over bremsstrahlung

losses, and is defined as $X_{max} = X_0 \ln E_0/E_c$, with E_0 the primary γ ray's energy (see e.g. de Naurois 2012 for a derivation). The altitude at which shower development halts scales linearly with $-\ln\left(\ln\left(\frac{E_0}{E_c}\right)/\ln 2\right)$, and corresponds to ~ 9 km for $E_0 = 1$ TeV. A discussion on more accurate approximations of shower development, such as the semi-empirical Greisen model (Greisen 1956) which accounts for ionization losses, can be found in de Naurois (2012).

Cherenkov radiation

An electron (and other particles) may not emit a photon in a vacuum due to conservation of energy. In a medium of refractive index n, the emission of a photon is possible if the incident electron has a speed $v_1 > c/n$ with c the speed of light. This criterion can be cast as

$$E_1 > \frac{nm_ec^2}{\sqrt{n^2-1}} \tag{3.1}$$

with E_1 the incident electron's energy. At 20°C, the electron's energy must be higher than ~ 0.8 MeV in water ($n \sim 1.33$), or ~ 22.0 MeV in air ($n \sim 1.00027$). The photon is emitted at an angle ϕ such that

$$\cos\phi = \frac{E_\gamma(n^2-1)+2E_1}{2p_1cn} \tag{3.2}$$

with E_γ the photon's energy, $p_1 = \gamma m_e v_1$ the incident electron's momentum and γ its Lorentz factor. Thus, the maximum energy the photon can have is

$$E_{\gamma,max} = 2\frac{n\sqrt{E_1^2 - m_e^2c^4} - E_1}{n^2-1} \tag{3.3}$$

For $E_1 \gg m_ec^2$, $\phi_{max} \sim \arccos(1/n)$ ($\sim 41.2°$ for water and $\sim 1.3°$ for air at 20°C) and the emitted photon's wavelength is $\lambda_{min} \sim \frac{(n+1)hc}{2E_1}$. The emitted Cherenkov radiation is enveloped by a cone of semi-angle α originating from the electron's position such as $\sin\alpha = \frac{c}{nv_1}$. Thus, for a shower in the atmosphere initiated by a 1 TeV primary γ ray, the development of which halts at an altitude of ~ 9 km according to the Heitler model, the emitted Cherenkov radiation from an electron would illuminate an area of $\sim 3.3 \times 10^5$ m^2 on the ground.

3.2 The H.E.S.S. experiment

H.E.S.S. detects the Cherenkov radiation produced in the atmosphere by air showers. The H.E.S.S. array with four Davies-Cotton telescopes, which are called CT1 to CT4, of 12 m-diameter mirrors began operations in 2004, in the Khomas Highlands, Namibia. In 2012, the central fifth telescope CT5 with a larger detector and 28 m-diameter mirror was installed, making energies down to ~ 30 GeV accessible, beginning "H.E.S.S. II", or Phase 2 of operations. In 2016 the CT1-4 cameras were upgraded. The H.E.S.S. telescopes, at an altitude of 1800 m above sea level, are laid out in a square with side 120 m. The field of view of a single CT1-4 telescope is $\sim 5°$ in diameter.

Each telescope uses an alt-azimuth mount and is equipped with a mirror that focuses the Cherenkov light onto a camera containing 960 pixels for the CT1-4 telescopes and 2048 pixels for the CT5 telescope. A pixel consists of a Winston cone which focuses



Figure 3.1: H.E.S.S. site in Namibia showing the 12-meter CT1-4 telescopes and the central 28-meter CT5 telescope, from Vincent (2005).

the light onto a photo-multiplier tube (PMT) consisting of a photocathode that converts photons into photo-electrons which are passed through a set of consecutive dynodes, each producing secondary photo-electrons. Through this cascade, the initial signal is amplified. Each camera is equipped with electronics for digitizing the signal and for triggering. The camera is triggered when coincidence occurs between 3 to 5 nearby pixels, such as the signal surpasses the threshold of 5 photo-electrons (p.e.) per pixel. If two cameras are triggered simultaneously in the telescope array, confirming that stereoscopic reconstruction of the air shower parameters is possible, the image signal in each camera is digitized.

Within each mirror, two CCD cameras are installed in the center and off the axis, allowing for re-alignment of each of the 382 (875 in the case of CT5) mirror segments by achieving the clearest image of bright stars. Further, the CCD cameras are used for the computation of a pointing model which predicts mechanical pointing deviations, allowing for the correction of pointings to achieve a pointing accuracy of 20 to 30 arcseconds.

Calibration

The signal created by a shower's Cherenkov image on the camera is digitized by converting voltage into Analog-to-Digital Converter (ADC) counts, which does not give a direct measure of the collected Cherenkov light. The objective of calibration is ultimately to convert the digital signal into the number of incident Cherenkov photons on the camera, and this is done through multiple calibration processes to determine the optical efficiency of the system and the noise.

First, the pedestal for each pixel (in units of ADC counts) is determined, which correspond to the signal in the absence of Cherenkov light. It is the electronic and thermal noise of the camera, and the Night Sky Background (NSB). The latter is the diffuse optical light from scattered moonlight, zodiacal light, and starlight. The electronic pedestal (i.e. in the absence of NSB) is computed by conducting an "electronic pedestal run", wherein the telescope is stowed in its shed and the camera lids are closed. During an observation run, the total pedestal (i.e. including the NSB) is measured for pixels without incident Cherenkov light, and the NSB rate for a given pixel can be estimated by subtracting the electronic pedestal. If a pixel's signal is found to be strongly influenced by the NSB, it may be rejected from the image analysis.

To determine the conversion factor of ADC counts to p.e. (i.e. the gain), a "single photo-electron run" is conducted, wherein the telescope is stowed within its shed, and the camera lid is open. A LED unit installed in the shed repeatedly emits a pulsed 1 p.e.-equivalent signal towards each PMT, yielding an ADC count distribution for each pixel. This distribution is parameterized by assuming that the number of p.e. follows a Poisson distribution, that the ADC count distribution corresponding to 1 p.e. is a Gaussian, and that the electronic pedestal described previously follows a Gaussian distribution. The difference between the electronic pedestal's peak and the peak of the p.e. distribution corresponds to the gain. Having determined the number of p.e.'s, a correction factor is applied to account for the inhomogeneity of the quantum efficiency (i.e. the number of p.e. produced per incident photon) across the PMTs. This is done through "flat-field runs", during which the unstowed camera is uniformly illuminated by a LED unit installed in the mirror. To convert the number of p.e. into incident Cherenkov photons, the system's global optical efficiency must be known, which accounts for the loss of Cherenkov photons throughout the entire system, due to the mirrors' reflectivity, the PMTs' quantum efficiency and the Winston cones' reflectivity. This is done by using the signal from muons, because they leave a distinct ring-shaped pattern on the camera, and the energy spectrum of Cherenkov light they produce is similar to that produced by $e^{-/+}$ in photon-induced air showers. Additionally, muons close to the ground are ultra-relativistic and thus suffer negligible energy losses with respect to altitude. The produced Cherenkov image can be computed following the Frank-Tamm equation (e.g. Gaug et al. 2019, and references therein). Thus, the global efficiency of the system is computed by reconstructing the muon track and comparing it with observations.

The CCD cameras installed within the mirror are used to apply corrections due to structural deformation of the telescope, which is done by pointing the telescopes in different altitude and azimuth directions. This process is referred to as the "pointing runs".

Stereoscopic event reconstruction

The goal of event reconstruction is to reconstruct the parameters (direction and energy) of an air shower's primary photon and discriminate between photon-induced and hadron-induced air showers. In stereoscopic reconstruction, an event corresponds to the coincident triggering of multiple cameras by Cherenkov radiation from an air shower, and the direction of the incident primary γ ray is related to the geometry of the images in each camera, as shown in Fig. 3.2 from de Naurois (2012). The projection of the shower's central axis in the sky is the major axis of the image it produces on the camera. The direction of the primary γ ray in the camera frame can be obtained by intersecting the major semi-axes of the images of the air shower in multiple cameras. The projected impact point on the ground of the primary γ ray is the intersection of the planes containing each telescope and correspondingly oriented in the azimuthal direction ϕ of the air shower's major semi-axis. The distance between a telescope and the shower's impact point on the ground is called the impact parameter, the stereoscopic reconstruction of which is illustrated in Fig. 3.3 from de Naurois (2012). The energy of the shower's primary γ ray is a function of the image intensity and the impact parameter. Event reconstruction and gamma/hadron separation can be conducted by fitting template images of air showers with different zenith, azimuth, impact parameters and image intensities. These are produced from Monte Carlo simulations of air showers.

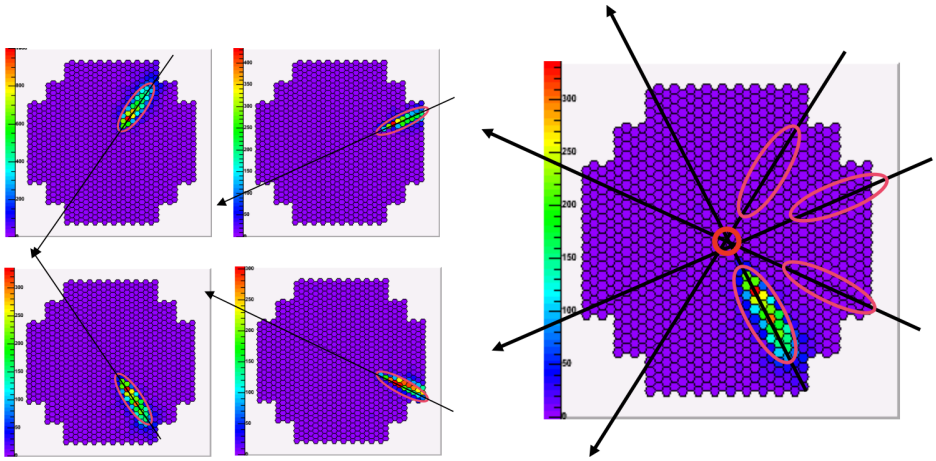

Figure 3.2: Illustration of a γ-ray induced shower intensity in 4 cameras showing the major axes of each image (left) and the stereoscopic reconstruction of the primary γ ray's direction in one camera (right), from de Naurois (2012).

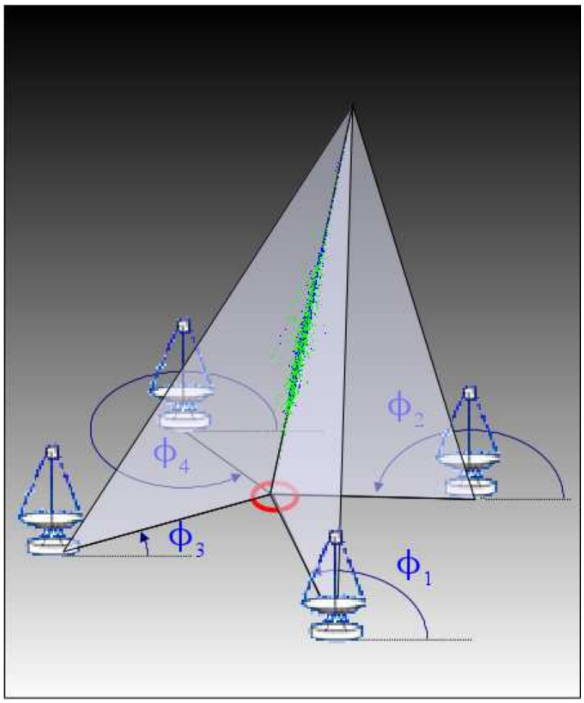

Figure 3.3: Intersection of the planes containing the telescope and orientated in the azimuthal direction ϕ of the shower image's major axis in the corresponding camera, from de Naurois (2012). The shower is shown, along with the reconstructed projected impact point of the primary photon on the ground.

3.3 The Cherenkov Telescope Array Observatory

The next generation of IACTs (currently under construction) is the Cherenkov Telescope Array Observatory (CTAO), which will have a northern hemisphere (La Palma, Spain, for which a rendition is shown in Fig. 3.4) and southern hemisphere (Atacama desert, Chile) site. The first telescope, LST-1, is currently operating. The first planned configuration ("Alpha") for the northern site is 4 LST's (23 meters, Large Size Telescope) and 9 MST's (12 meters, Medium Size Telescope), while the southern site will consist of 14 MST's and 37 SST's (4 meters, Small Size Telescope). The LST's, with a $\sim 4°$ diameter field of view

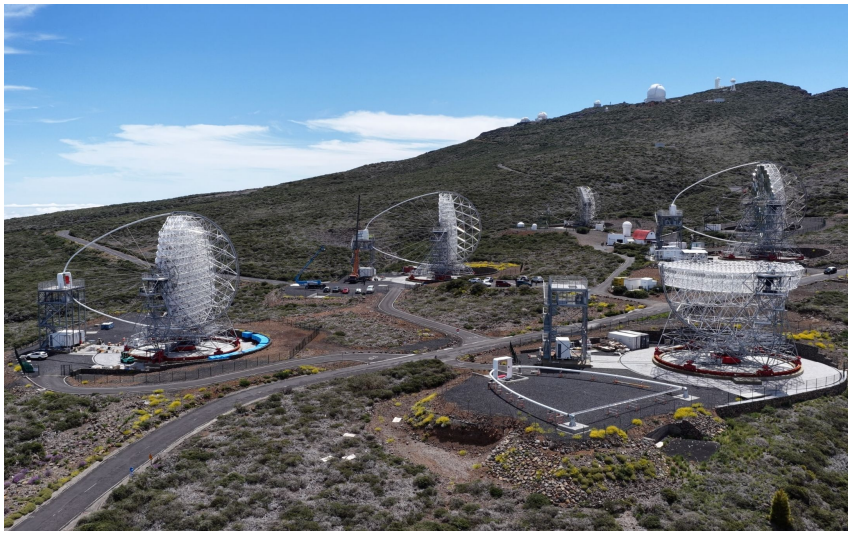

Figure 3.4: Rendition of the Large Size Telescope array in La Palma, Spain by the LST Collaboration (https://www.ctao.org/emission-to-discovery/array-sites/ctao-north/).

camera, are the array's largest IACTs allowing the detection of fainter GeV photons, while the SST array (9° field of view cameras) covers a large surface area for the purpose of probing the highest photon energies (up to 300 TeV). The MST arrays cover the central energy band, with 8° field of view cameras. The Northern hemisphere site will cover an area $\sim$ 20 times larger than the H.E.S.S. array, and the southern hemisphere site will cover an area $\sim$ 250 times larger than the H.E.S.S. array. Fig. 3.5 shows the 50-hour point source sensitivity of the CTAO North and South sites, computed with the latest simulated Instrument Response Functions (CTAO & Consortium 2021, IRFs), compared with currently operating γ-ray observatories and the planned Southern Wide-field Gamma-ray Observatory. An order of magnitude of sensitivity is expected, along with an angular resolution improved by a factor 2.

3.4 Data analysis with Gammapy

A reconstructed event passing the gamma/hadron separation process is referred to as a γ-like event, characterized by the reconstructed energy and direction of the incoming primary γ ray. During an observation, the majority of γ-like events are residual hadronic CR shower-induced events, which must be estimated from the data using a background model. In this work, version 1.2 of the Gammapy python library (Donath et al. 2023; Acero et al. 2024) is used for the reduction and analysis of IACT γ-like event data. Specifically, we use a 3D analysis method, wherein a three-dimensional counts cube with two spatial axes and one energy axis is defined. The γ-like events are binned into said cube according to their reconstructed energy and direction. Thus, we may define spectro-morphological models which predict the spectral and spatial distribution of the γ-ray emission.

The goal of an analysis is to quantify the statistical preference, by the data, of a model which predicts counts in excess of the predicted background counts. This is done through hypothesis testing, by comparing the likelihood of a model which contains the background and a γ-ray source component with the likelihood of a background-only model. The parameter values of the source component that best reproduce the data

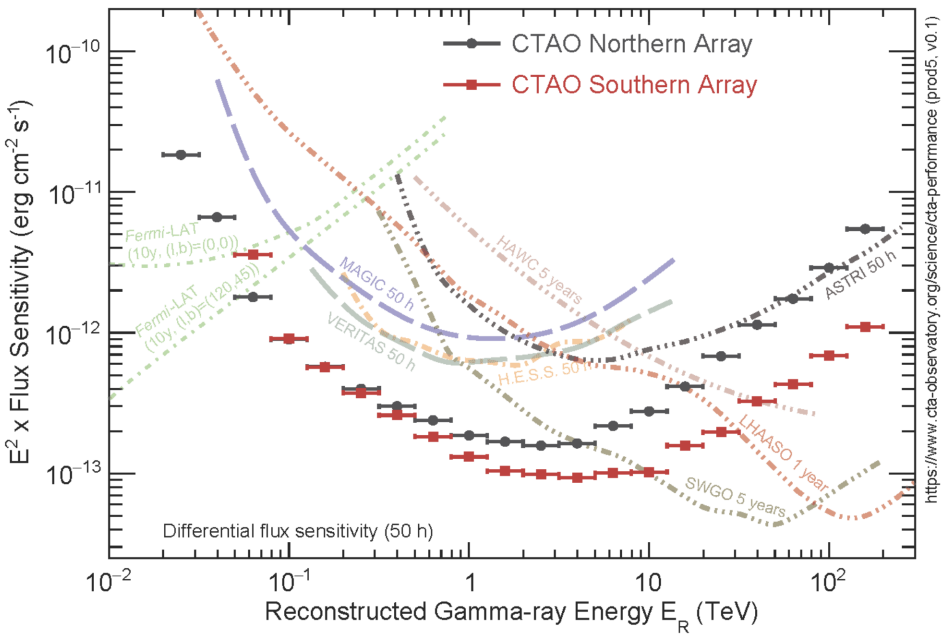

Figure 3.5: CTAO North and South expected 50 hours point-source sensitivities computed using the latest Instrument Response Function simulations (CTAO & Consortium 2021), compared with other γ-ray observatories, from https://www.ctao.org/for-scientists/performance/.

are estimated by maximizing the likelihood of the background + source model, i.e. by conducting a maximum likelihood fit. The entire analysis procedure is detailed in this section.

3.4.1 Spectro-morphological modeling

γ-ray emission modeling

Gammapy models are factorized into a spectral and spatial component in units of TeV^{-1} cm^{-2} s^{-1} and sr^{-1} respectively. Spatial components can be point-like or extended. Extended sources are typically modeled with a 2D Gaussian spatial component generally expressed as

$$G(\ell, b) = \frac{1}{2\pi\sigma^2} \exp\left(-\frac{1}{2}\frac{\theta^2}{\sigma^2}\right) \tag{3.4}$$

with (ℓ, b) corresponding to galactic coordinates and θ the angular separation between the Gaussian's central position (ℓ_0, b_0) and (ℓ, b). If the 2D Gaussian is "elliptical", then σ is replaced with

$$\sigma_{eff}(\ell, b) = \sqrt{(\sigma_M \sin(\Delta\phi))^2 + (\sigma_m \cos(\Delta\phi))^2} \tag{3.5}$$

with σ_M and σ_m the major and minor semi-axes respectively, and $\Delta\phi$ the difference in position angles between (ℓ_0, b_0) and (ℓ, b). Examples of other geometric spatial distributions include shells (H.E.S.S. Collaboration 2018a) or disks. Spatial templates based on multi-wavelength data can also been used. This is, for example, done to model the large-scale Galactic diffuse emission using tracers of interstellar gas, such as the Planck Dust Optical Depth map at 353 GHz (Planck Collaboration 2011), or to model γ-ray sources (e.g. using the X-ray spatial distribution for a PWN). Custom energy-dependent and/or physically motivated spatial models can also be defined (cf. Chap. 4.2.2).

The spectral components are typically modeled as power laws:

$$\frac{dN}{dE} = N_0 \left(\frac{E}{E_0} \right)^{-\alpha} \tag{3.6}$$

with or without an exponential cut-off factor $\exp(-E/E_c)$. E_0 is the reference energy in TeV, N_0 the amplitude in TeV^{-1} cm^{-2} s^{-1}, and α the spectral index. Other spectral models exist (e.g. log-parabola) or custom models can be defined.

Template hadronic background modeling

Gamma-like events include hadronic CR-induced events misclassified as γ rays during the gamma/hadron rejection process. They represent the residual hadronic cosmic-ray shower background, which must be estimated using the data. For extended sources and crowded regions in the sky, the template background method is used to predict the amount of residual hadronic cosmic-ray events.

The method is presented in Mohrmann et al. (2019). For H.E.S.S. analyses, the background model templates are constructed from H.E.S.S. extragalactic observations (masking the extragalactic source) where no diffuse γ-ray emission is expected. The background templates are computed for two azimuth angles due to deviation of CRs from Earth's magnetic field (the east-west effect). The rate of hadronic events is highly dependent on zenith angle, hence the background model is constructed for multiple zenith angle values. An average background rate as a function of primary particle energy and offset from the camera is computed over observations grouped in zenith and azimuth bins. The model is refined by interpolation in zenith angle, offset from the camera center and energy. The model is also corrected by a linear function to account for its correlation with the transparency coefficient, a measure of the atmosphere's transparency to Cherenkov light impacted by the presence of aerosols.

In the data analysis procedure, for a list of γ-like events from an observation, the background model is interpolated at the observation's zenith and azimuth angles. Analyses using the Field of View method are done above the energy at which the background model peaks, such that it can be re-adjusted using a power law in energy with the observation's binned events in regions devoid of γ-ray emission. This is done using a maximum likelihood fit.

3.4.2 The maximum likelihood method

The analysis of γ-ray data is done using a hypothesis testing approach, wherein an optimized model of the background signal (the null hypothesis) is compared with an optimized model of the background + source signal (the test hypothesis) using the ratio of each model's associated likelihood. The optimization of a model is conducted by minimizing its negative log-likelihood. This allows the computation of the source signal's statistical significance.

Analyses of regions near the Galactic plane and possibly subject to source confusion are best approached using the 3D analysis method, wherein the spectra and the morphologies of the components in a flux model are constrained simultaneously. The events of an observation are binned in reconstructed position and energy. The number of events in a bin i of the data cube is a Poisson-distributed random variable with an expected value equal to the sum of the predicted excess (i.e. source) and background events. For

a flux model M containing source components and a background component, the Cash statistic (Cash 1979) is used, and is expressed as

$$2\ln(L(M)) = 2\sum_i n_{excess,i} + n_{bkg,i} - n_{counts,i}\ln\left(n_{excess,i} + n_{bkg,i}\right) \tag{3.7}$$

where $L(M)$ is the likelihood of model M, $n_{excess,i}$ is the predicted number of events from the source components, $n_{bkg,i}$ is the predicted number of events from the background component and $n_{counts,i}$ is the total number of events in bin i. With the Gammapy package, we use the MINUIT backend (James & Roos 1975) with the MIGRAD algorithm for the minimization. MIGRAD is based on the Davidon-Fletcher-Powell variable-metric method (Fletcher & Powell 1963). The confidence intervals on the estimated model parameters are computed from the covariance matrix.

To estimate the statistical preference of a test hypothesis (model M) over the null hypothesis (the background-only model M_{bkg}), a ratio test is conducted:

$$\lambda = \frac{\max L(M)}{\max L(M_{bkg})} \tag{3.8}$$

According to Wilk's theorem (Wilks 1938), if the models are nested, and the number of statistics approaches infinity, $\Delta TS = -2\ln\lambda$ asymptotically approaches a χ^2 distribution with degrees of freedom equal to the additional free parameters in the test hypothesis, with $TS = -2\ln(\max L(M))$ corresponding to the Test Statistic associated to model M.

If the models are not nested, the Akaike Information Criterion (e.g. Cavanaugh & Neath 2019) can be used. An AIC score is associated to an optimized model M such as $AIC_M = 2k_M + TS_M$ with k_M the model's number of degrees of freedom and TS_M its associated TS. For two models M_1 and M_2, the model with the lower AIC score is the "better" model. The ΔAIC indicates the probability of loss of information when rejecting the "worse" model. Assuming $AIC_{M_1} < AIC_{M_2}$, $\Delta AIC = AIC_{M_2} - AIC_{M_1}$. Often, a ΔAIC higher than 8 is considered good enough to reject a model in favor of another.

3.4.3 H.E.S.S. Instrument Response Functions

The Instrument Response Functions (IRFs) map the true γ-ray signal from an astrophysical source to the reconstructed signal with the H.E.S.S. array. Given a spectro-morphological counts model $\Phi(p_{true}, E_{true})$ (in TeV^{-1} cm^{-2} s^{-1} sr^{-1}) with p_{true} the position in the sky and E_{true} the photon energy, the predicted number of events with reconstructed energy $[E; E + dE]$ and position $[p; p + dp]$ is

$$N(p, E)dpdE = t_{obs}\int_{E_{true}} dE_{true}\int_{p_{true}} dp_{true} R(p, E|p_{true}, E_{true})\Phi(p_{true}, E_{true}) \tag{3.9}$$

with t_{obs} the observation time and R the IRF. The IRF is approximated as the product of the Point Spread Function $PSF(p|p_{true}, E_{true})$ (i.e. the angular resolution), the energy dispersion $E_{disp}(E|p_{true}, E_{true})$ and the effective area $A_{eff}(p_{true}, E_{true})$.

$$R(p, E|p_{true}, E_{true}) = E_{disp}(E|p_{true}, E_{true}) \times PSF(p|p_{true}, E_{true}) \times A_{eff}(p_{true}, E_{true}) \tag{3.10}$$

PSF is the probability of measuring p given p_{true} and E_{true}. E_{disp} is the probability of measuring E given p_{true} and E_{true}. A_{eff} is the detector's effective area which depends on the detector efficiency at p_{true} and E_{true}.

Image analysis with H.E.S.S.

To recap the current state of the art on event reconstruction and γ/hadron separation used within the H.E.S.S. Collaboration, we present two pipelines based on the H.E.S.S. Analysis Package (HAP), namely HAP-Fr (Khelifi et al. 2015) and HAP's ImPACT-based pipeline (Parsons & Hinton 2014). The high-level dataset of the analysis presented in Chap. 6 was produced using HAP-Fr, while the results have been cross-checked using a dataset produced with HAP ImPACT. The first step of image analysis is the reduction of raw data using the calibration products, resulting in DST files (1 per observation). The images are then cleaned by rejecting pixels that may be strongly influenced by the NSB. In the following, the reconstruction of event parameters and the γ/hadron discrimination process from the cleaned images are described briefly.

HAP-Fr The first and second moments of the cleaned images are used to derive the Hillas parameters, i.e. the length, width, total charge, distance of the barycentre from the camera center and the main axis direction of the ellipses shown in e.g. Fig. 3.2. Images are selected following cuts on the Hillas parameters: the total charge, the number of pixels and the distance of the barycentre from the camera borders (the latter criterion is to avoid γ/hadron misclassification due to truncation effects). The event direction and impact parameter are then computed as shown in Fig. 3.2 and Fig. 3.3. The Hillas parameters are used as initial parameters of a 3D-photosphere model of the shower's Cherenkov photons, assumed to be Gaussian-distributed along the three axes, with its length taken along the shower's main axis. As described in Becherini et al. (2011), the 3D model is described by 8 parameters: the direction (two parameters) and impact parameter of the primary γ ray, the photosphere's length and transverse width, the depth of the shower maximum and the number of Cherenkov photons produced by $e^{-/+}$. The parameters are estimated by fitting the model-predicted Cherenkov images to the cleaned images using a maximum likelihood method. Reconstruction of the primary γ ray's energy makes use of the Hillas parameters, as follows. Cleaned images are simulated to create Look-up Tables (LUTs) of the total charge as a function of the impact parameter. An LUT is created for a combination of different values of the following parameters: The γ ray's true energy, the observation's zenith angle, the mirror efficiency, the γ ray's true direction with respect to the camera center, and the reconstructed shower maximum depth. For a real image, the Hillas parameters are reconstructed and the observational parameters are known. LUTs with the nearest two simulated values for each parameter are used. Thus, there are 2^5 simulated parameter value combinations (i.e. LUTs) each associated with a simulated primary γ ray energy. For each one, a weight is computed from the distance between the reconstructed and/or observational parameter values and the simulated ones (see Becherini et al. 2011 for the detailed computation). Then, the reconstructed energy is computed as the weighted mean between the 2^5 simulated true energies. This is done for each telescope, and the final reconstructed energy is the charge-weighted mean between each telescope. In the following, we describe the discriminating parameters used for γ/hadron separation. Using the previously mentioned LUTs, a similar method as for the energy reconstruction is employed to compute a weighted mean length and width of the real image, which serve as estimates of the deviations between the real image and the predicted image from simulations. From the 3D model fit, three parameters are used as discriminators: the 3D width, its error, and the depth of the shower maximum. A further three discriminating parameters are defined by computing the image predicted by

the 3D model. These correspond to the deviations between the reconstructed direction, energy and total charge from the Hillas parameters obtained from the real image vs. those predicted by the 3D model. γ/hadron discrimination is conducted through multivariate analysis using a Boosted Decision Tree algorithm, described in detail in Becherini et al. (2011).

ImPACT The ImPACT method (short for Image Pixel-wise fit for Atmospheric Cherenkov Telescopes) relies on a likelihood fit of image templates generated from Monte Carlo shower simulations using the CORSIKA code and ray-tracing optics using the *sim_telarray* code. The latter takes as input the simulated Cherenkov photons from CORSIKA. A detailed description of the method can be found in Parsons & Hinton (2014). *sim_telarray* allows one to simulate predicted images by tracing Cherenkov photons through the system (i.e. the segmented mirrors and the Winston cones) and the production of photo-electrons by the PMTs (including the NSB) for different atmospheric conditions. The image templates are generated for different zenith angles, azimuth angles, true photon energies, impact parameters and depths of shower maximum. γ/hadron separation is conducted, similarly to HAP-Fr, using discriminating Hillas parameters through a Boosted Decision Tree algorithm.

For illustrative purposes, Fig. 3.6 shows the point spread function, effective area and energy dispersion as a function of energy for two different observations that will be used in the data analysis of Chap. 6 using the HAP-Fr pipeline. These are the observations with ID 20879 and 20822, with zenith angles $z = 17°$ and $z = 31°$ respectively, and shown with solid and dashed lines respectively. For observation 20879, the IRFs are shown for two values of the offset from the camera center $\theta = 0°$ and $\theta = 1°$. The top left panel shows the bias of the energy dispersion. It corresponds to the fractional difference between E_{true} and the expected value of E. The energy resolution corresponds to the root mean square of E_{disp}, and is shown in the inset. The top right panel shows the effective area. The bottom panel shows the angular resolution, here illustrated as the 68% containment radius of the PSF.

3.4.4 Data analysis procedure

An analysis starts with the selection of H.E.S.S. observations. This is typically done by defining a cone towards the sky and taking all observations in a "Data Level 3" (DL3) production with pointings included in the cone. Cuts can be made on the zenith angle ($\leq 45°$ typically) to reduce uncertainties related to the atmosphere's transparency. An observation from a DL3 production is a list of events and their corresponding IRFs in FITS format. Each observation has an associated background model template with similar observational conditions. Cuts on the event selection are defined, to be applied for all observations. Events are selected if they fall within a defined distance, typically of 2°, from the camera center. This is done because the acceptance varies strongly near the edge of the camera due to truncated shower images, introducing large errors on its estimation. The acceptance, computed from Monte Carlo simulations, is the probability that a γ-like event triggers the system, is reconstructed and passes the event selection cuts. Events are selected with energies above a minimal threshold. This is typically such that the effective area is $10 - 20\%$ of the maximum effective area. The next step is to define the geometry of the 3D dataset into which events will be binned. This corresponds

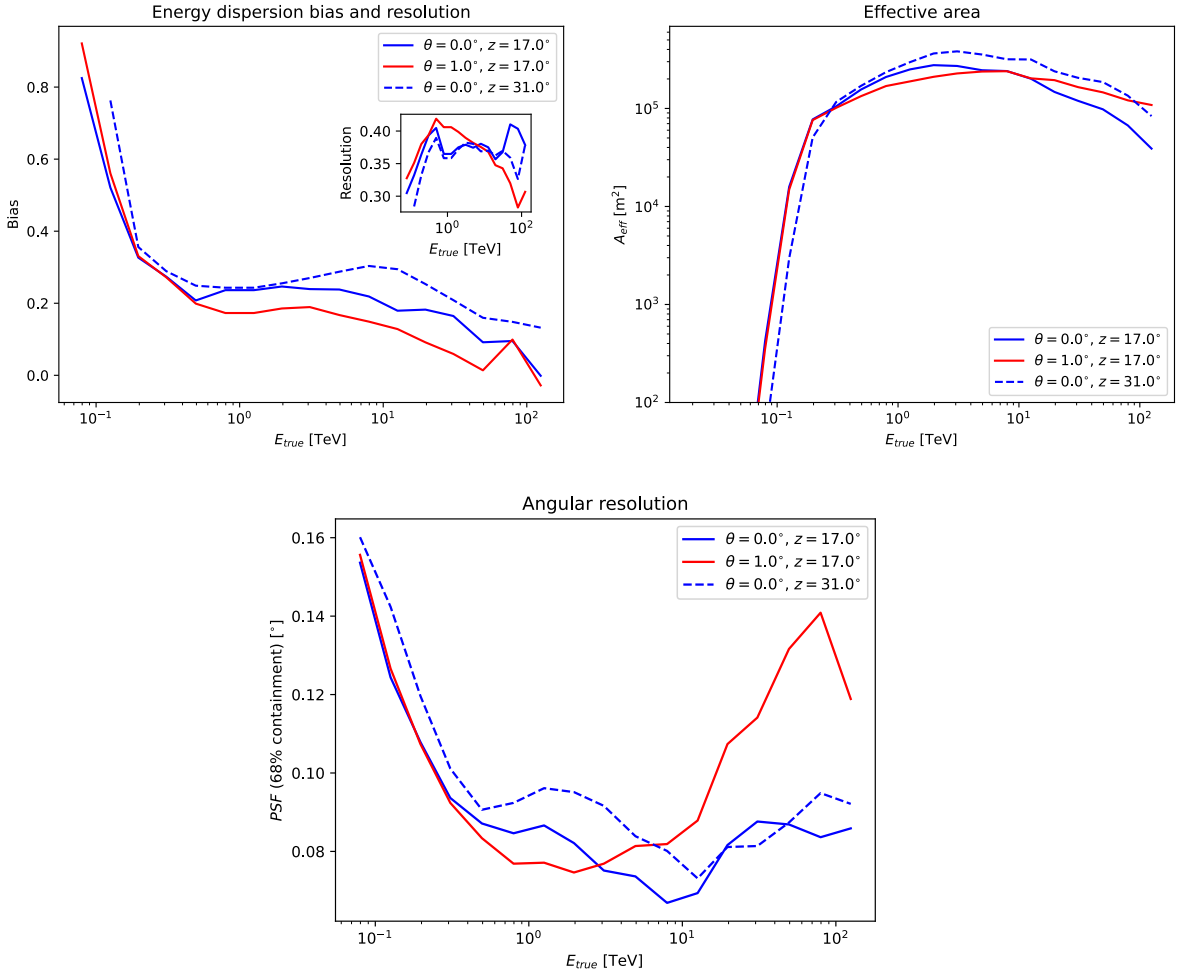

Figure 3.6: H.E.S.S. instrument response functions from the HAP-Fr pipeline. The solid lines correspond to observation 20879 with a zenith angle $z = 17°$, and the dashed line to observation 20882 with $z = 31°$. The blue lines corresponds to an offset of $\theta = 0°$ from the camera center, and the red line to an offset of $\theta = 1°$. **Top left:** Energy bias and energy resolution (in the inset) as a function of energy. **Top right:** Effective area as a function of energy. **Bottom:** Angular resolution as a function of energy.

to the width of the cube in degrees, the spatial binning in degrees and the binning of the reconstructed energy axis (usually around 10 bins per decade). A true energy axis for the IRF cubes is also defined. To adjust the template background model's spectrum, a mask must be defined, corresponding to a region where γ-ray emission is expected (e.g. sources and the Galactic plane). This region will be excluded when fitting the background model. The events of an observation are then binned into a cube with the defined geometry, the corresponding IRF cube is created, and the spectrum of the background template is re-adjusted to the observation. This is done on a run-by-run basis. Finally, the dataset cubes of each observation are stacked (i.e. the events and background cubes are summed and the IRFs are averaged). A defined model may be fitted to the stacked dataset. During the model fit, the stacked background model is re-normalized (typically with a power law function of energy) to account for systematic uncertainties introduced from stacking.

Source modeling is an iterative procedure, wherein source components are "accepted" if they improve the TS by more than 5σ. Spectral or morphological features of a given source, such as a spectral cut-off or ellipticity of a 2D Gaussian, are accepted if they improve the TS by more than 3σ.

Chapter 4

Pulsar halo modeling framework

Contents

4.1 Theoretical prescription 43

4.2 Building pulsar halo templates for H.E.S.S. data fitting . . 55

Particle transport in the Geminga and Monogem halos (and other candidate halos) has been described in the literature using an isotropic diffusion model with synchrotron and Inverse Compton losses, which predicts the γ-ray morphology and spectrum well. In this chapter, we present the model, and the method by which the γ-ray emission templates are created for data analyses with Gammapy.

4.1 Theoretical prescription

Following the characteristics of the Geminga and Monogem halos presented in section 2.3, we define pulsar halos as follows.

$e^{-/+}$ produced in the magnetosphere of the pulsar, which are further accelerated in the wind through magnetic reconnection and/or at the wind termination shock, travel away along magnetic field lines in the PWN, where the particle transport is primarily dominated by advection powered by the pulsar's rotation (Amato & Recchia 2024). They later escape into the ISM and diffuse along the ISM magnetic field lines. The halo is thought to emerge at the late stages of the Pulsar-PWN-SNR system's evolution, when particle escape becomes easier either due to the disruption of the PWN by its interplay with the SNR, or when the pulsar has left the SNR owing to the kick velocity due to the progenitor supernova explosion's asymmetry, producing a bow shock PWN. This scenario is illustrated in Fig. 4.1, adapted from (Giacinti et al. 2020). We adopt a pulsar halo model where $e^{-/+}$ are continuously injected by a PWN of negligible size (point-like) compared to the extent of the VHE emission from ICS, and assume that $e^{-/+}$ are diffusing in the ISM having escaped the PWN. The ISM environment is described by a diffusion coefficient assumed to be isotropic and homogeneous, a uniform magnetic field, and the ICS target radiation fields.

The transport in spherical coordinates of $e^{-/+}$ can be described by the continuity equation with radiative losses and a continuous point-like source term:

$$\frac{\partial N(E,\mathbf{r},t)}{\partial t} - \nabla[D(E)\nabla N] + \frac{\partial}{\partial E}[b(E)N] = Q(E,t)\delta(\mathbf{r}-\mathbf{r_s}) \tag{4.1}$$

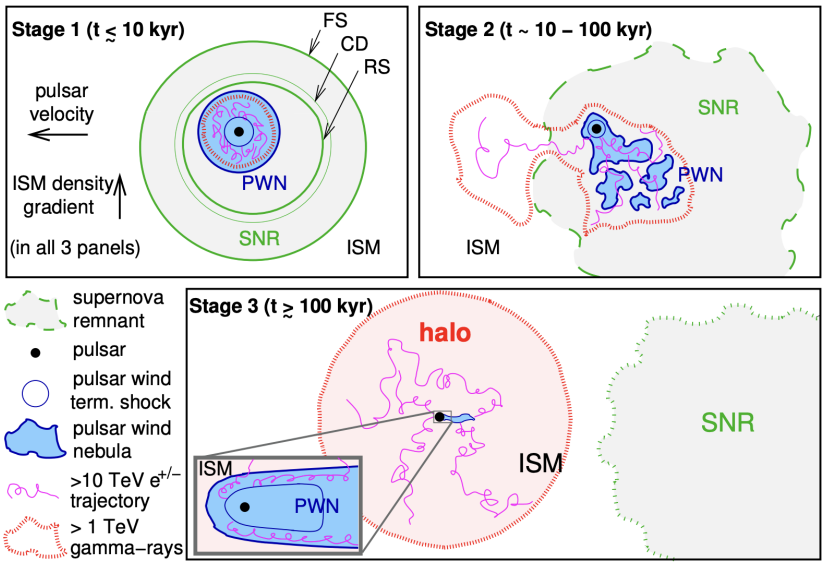

Figure 4.1: Illustration of a pulsar halo scenario involving $e^{-/+}$ escaping into the ISM, from Giacinti et al. (2020). **Top left:** Early stage with $e^{-/+}$ confined within the PWN inside the SNR before contact with the reverse shock (RS, shown in solid green). The forward shock (FS, solid green) and contact discontinuity (CD, dashed green) between the ejecta and the shocked ISM are shown. **Top right:** The PWN is disrupted by the reverse shock, with $e^{-/+}$ beginning to escape into the SNR and ISM. **Bottom:** The pulsar has exited the SNR due to its kick velocity. At supersonic speed, it forms a bow shock PWN from which $e^{-/+}$ escape into the ISM and produce an ICS halo.

where N is the differential particle number density at some energy E, time t after the pulsar birth, and position $\mathbf{r}$. $D(E) = D_0 \left(E/E_0\right)^{\delta}$, where E_0 is the reference energy, D_0 is the diffusion coefficient normalization, $b = -\partial E/\partial t$ is the particle cooling rate (from ICS and synchrotron radiation), Q is the particle injection spectrum and $\mathbf{r_s}$ is the pulsar's position.

4.1.1 Particle injection

Following the pulsar evolution model outlined in section 2.1, the pulsar's spin-down evolution is defined as:

$$L(t) = L_\star \left(\frac{1 + t_{age}/\tau_0}{1 + t/\tau_0}\right)^2 \tag{4.2}$$

with a braking index $n = 3$, t_{age} the pulsar's true age, τ_0 it's initial spin-down timescale, $L_\star$ its present-day spin-down power, and t the time since the pulsar's birth. The particle injection term $Q(E,t)$, which follows a power-law with exponential cutoff E_c and index Γ, is normalized such that the total energy in $e^{-/+}$ per unit time is equal to some fraction η (the injection efficiency) of the pulsar's spin-down power.

$$Q(E,t) = Q_0(t) \left(\frac{E}{E_0}\right)^{-\Gamma} \exp\left(\frac{-E}{E_c}\right) \tag{4.3}$$

$$Q_0(t) = \frac{\eta L(t)}{\int_{E_{min}}^{E_{max}} E \left(\frac{E}{E_0}\right)^{-\Gamma} \exp\left(\frac{-E}{E_c}\right) dE} \tag{4.4}$$

We set $E_{min} = 0.1$ TeV, since we are interested in studying pulsar halos in the H.E.S.S. energy band, and $E_{max} = 1$ PeV. As such, η represents the injection efficiency of pairs

with energy $E \geq 0.1$ TeV. Bucciantini et al. (2010) found that the injection spectra of $e^{-/+}$ into PWNe are characterized by a break between 0.1 to 1 TeV. In Martin et al. (2022) and Eckner et al. (2023), a broken power law with exponential cut-off is assumed, with $E_b = 0.1$ TeV and $E_{min} = 1$ GeV. Zhang et al. (2021) assumed an exponential cut-off power law without a break. In our halo model, we assumed $E_b = E_{min} = 0.1$ TeV, and we describe the injection spectrum by a power law with exponential cut-off E_c.

4.1.2 Particle cooling rate

$e^{-/+}$ propagating at TeV energies are predominantly subject to ICS and synchrotron radiation losses. Following H.E.S.S. Collaboration (2023a), we use the method of Delahaye et al. (2010) for the computation of energy losses due to ICS, where the authors numerically derive an "intermediate" regime between the Thomson and Klein-Nishina regimes. This method is only applicable to radiation fields parameterized as (diluted) black-bodies. Popescu et al. (2017) published the spectral energy densities of Interstellar Radiation Fields (ISRF) which they derive by applying a galactocentric radial radiative transfer model to astronomical data. To reproduce the data in Popescu et al. (2017) for every position (R, z) in galactocentric coordinates, we extrapolate the starlight spectral energy distributions (SEDs) to higher wavelengths λ and add the dust SEDs. Fig. 4.2 is a reproduction of the SEDs shown in Popescu et al. (2017).

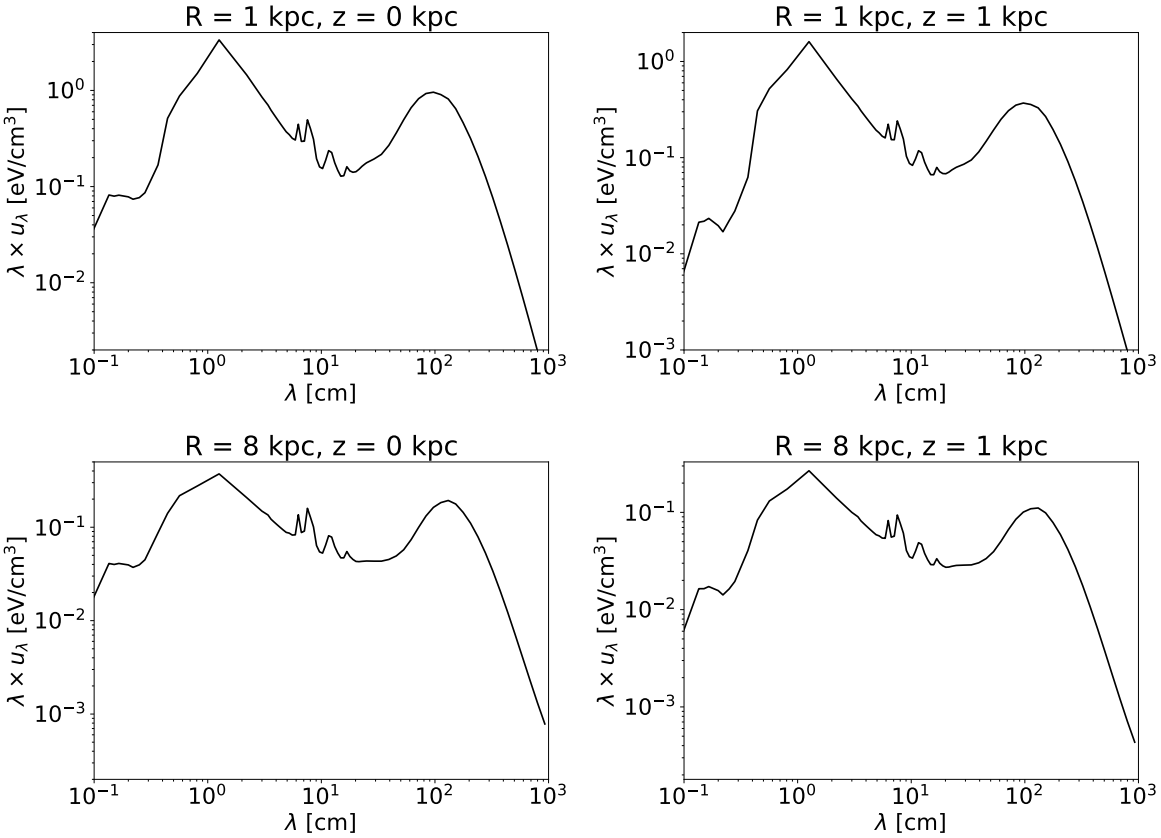

Figure 4.2: Reproduction of Figure 9 in Popescu et al. (2017), showing the ISRF SEDs as a function of wavelength λ at different galactocentric coordinates (R, z), assuming a distance of 8 kpc to the galactic center.

Given the astronomical coordinates of a pulsar and its distance to Earth, we sampled

the ISRF SED data at the pulsar's galactocentric position, and fitted the sum of three (optical, near infrared and far infrared) diluted black-body components, each represented by a Planck distribution:

$$B_{\lambda,diluted} = \frac{8\pi}{hc\lambda^5} \frac{W}{e^{\frac{hc}{\lambda k_B T}} - 1} \tag{4.5}$$

where T is the temperature and W the dilution factor. The contribution of ICS against ultraviolet photons was found to be negligible and thus not accounted for in this model. Fig. 4.3 illustrates an example of a sampled SED (purple dots) and the fitted black-body components' sum (green). The fit was done using Sherpa Python package (Siemiginowska et al. 2024), where we minimize the χ^2 statistic using the Levenberg-Marquardt algorithm.

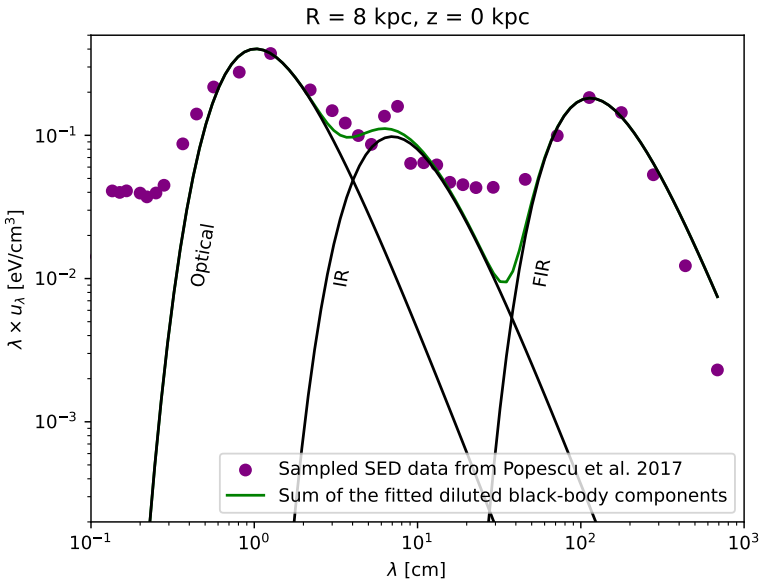

Figure 4.3: Sampled SED from the lower left panel of Fig. 4.2, with the fitted sum of three diluted black-body components (optical, infrared and far infrared).

We also computed the values at $R = 4$ kpc and $z = 0$ kpc to compare with the values reported by Zhang et al. (2021) who used a similar method for the ISRFs, as shown in Table 4.1.

Reference	Optical	IR	FIR
This work	$T = 3253$ K $U_{rad} = 2.3$ eV/cm^3	$T = 547$ K $U_{rad} = 0.5$ eV/cm^3	$T = 39$ K $U_{rad} = 1.1$ eV/cm^3
Zhang et al. (2021)	$T = 3500$ K $U_{rad} = 1.9$ eV/cm^3	$T = 500.0$ K $U_{rad} = 0.4$ eV/cm^3	$T = 40$ K $U_{rad} = 1.0$ eV/cm^3

Table 4.1: Comparison of the temperature and photon energy density values found at $R = 4$ kpc and $z = 0$ kpc in our work and Zhang et al. (2021) using the Popescu et al. (2017) data.

To validate our usage of the Delahaye et al. (2010) computation of the ICS cooling rate, we reproduced the cooling rates as a function of $e^{-/+}$ of H.E.S.S. Collaboration (2023a) in Fig. 4.4.

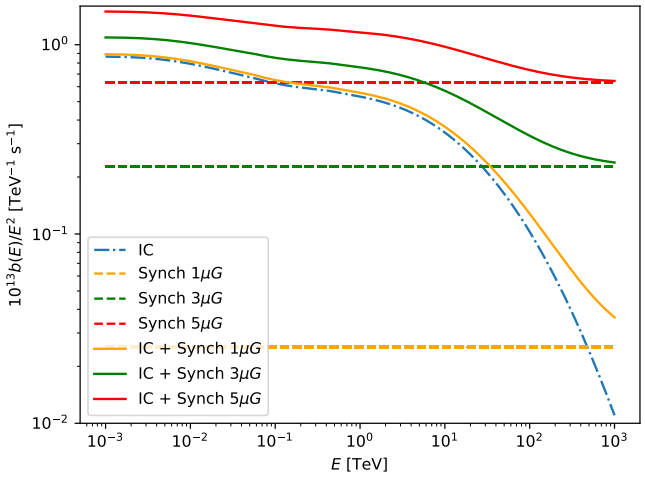

Figure 4.4: Cooling rate (divided by E^2) as a function of $e^{-/+}$ energy due to ICS and synchrotron radiation, reproduced from H.E.S.S. Collaboration (2023a) using the prescription in Delahaye et al. (2010).

4.1.3 Semi-analytical solution

Following Syrovatskii (1959), by defining the particle diffusion length scale λ and the time since injection t_{cool} as

$$\lambda^2(E, E') = 4 \int_E^{E'} \frac{D(E'')}{b(E'')} dE'' \tag{4.6}$$

$$t_{cool} = t - t' = \int_E^{E'} \frac{dE''}{b(E'')} \tag{4.7}$$

where $E'(E, t')$ is the particle's energy when injected at a time t' after the pulsar's birth (the pulsar's birth corresponds to $t' = 0$), and assuming an infinite boundary, we can use the Green's function method to find a semi-analytical solution to Eq. 4.1:

$$N(E, r, t) = \int_0^t dt' \frac{b(E')}{b(E)} Q(E', t') \frac{e^{-\frac{|\mathbf{r}-\mathbf{r}_s(t')|^2}{\lambda^2(E,E')}}}{\pi^{3/2}\lambda^3(E, E')} \tag{4.8}$$

We set the origin of the reference frame ($\mathbf{r} = \mathbf{0}$) at the pulsar's present-day position. In the case where the pulsar is stationary, we set $\mathbf{r}_s(t') = \mathbf{0}$ and N is spherically symmetric about the pulsar's position. Otherwise, we may incorporate the pulsar's transverse velocity in the sky $\mathbf{V}_{PSR}$ (perpendicular to the line of sight) by defining $\mathbf{r}_s$ in the $-\mathbf{V}_{PSR}$ direction with $r_s(t') = (t - t')V_{PSR}$. In Zhang et al. (2021), it was found that the proper motion's line of sight component had a negligible effect on the halo's morphology if the pulsar is much farther than the distance it traveled since its birth. The pulsar halos explored in this work must be far enough so that they are observable by H.E.S.S. (i.e. at kpc distances), while the distances traveled by middle-aged pulsars are on the orders of tens to hundreds of parsecs at most. As such, we only consider the transverse component of the proper motion. The solution assumes a cylindrical symmetry about the axis in the $\mathbf{V}_{PSR}$ direction. In cylindrical coordinates with the unit vectors $\mathbf{u}_\rho$ taken along

the cylinder's radius and $\mathbf{u}_z$ taken along the transverse velocity axis (i.e. the cylinder's height):

$$\begin{aligned} |\mathbf{r} - \mathbf{r}_s(t')|^2 &= |\rho\mathbf{u}_\rho + z\mathbf{u}_z - (t-t')V_{PSR}\mathbf{u}_z|^2 \\ &= (z - (t-t')V_{PSR})^2 + \rho^2 \\ &= z^2 + (t-t')^2V_{PSR}^2 - 2z(t-t')V_{PSR} + \rho^2 \end{aligned}$$

Particle cooling rate and diffusion length scale

We compute $N(E, \mathbf{r}, t = t_{age})$, where t_{age} depends on τ_c and the unknown initial period P_0. We use `scipy.optimize.fsolve` to compute E' for every t' and E by solving $t_{age} - t' - t_{cool} = 0$. This is only possible if the maximum cooling time

$$t_{cool,max} = \int_E^{+\infty} \frac{dE''}{b(E'')} \tag{4.9}$$

satisfies $t_{cool,max} > t_{age} - t'$. In other words, the time it takes a particle injected with energy E' at time t' to cool down to an energy E at the present time t_{age} is limited by $t_{age} - t'$. We show this in Fig. 4.5: The required injection energy E' goes to infinity with increasing E for some time since injection. The injection spectrum $Q(E', t')$ in the integrand of N thus falls to zero. Conclusively, when computing N for some energy E, we integrate over t' from $t_{age} - t_{cool,max}(E)$ to t_{age}. As will be shown later, this feature of the model, which is completely controlled by the system's age and the cooling rate, has an important impact on the cooled particle SED and the resulting photon SED.

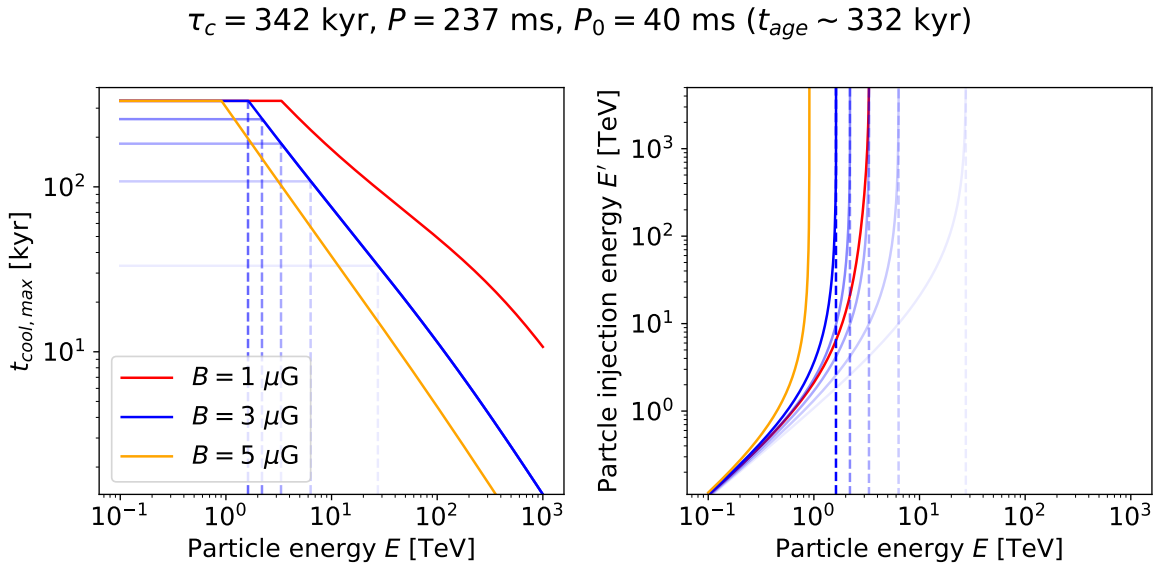

Figure 4.5: **Left:** Maximum cooling time $t_{cool,max}$. **Right:** Particle injection energy E'. In both figures, we assume the Geminga pulsar's τ_c, P and set $P_0 = 40$ ms. Different values of the magnetic field strength B are shown. For $B = 3\ \mu$G (in blue), the fainter lines represent smaller values of t' (from 0 to 299 kyr), and the dotted lines illustrate the energy E for which $t_{cool,max} = t_{age} - t'$.

The particle diffusion length scale $\lambda(E, E')$ as it cools down from E' to E depends on the diffusion coefficient D and the cooling rate b. Therefore, the energy dependence of the γ-ray emission morphology is predominantly governed by the parameters D_0, the

magnetic field intensity B, and t_{age} (or the initial period P_0), as shown in Fig. 4.6. λ changes linearly with $\sqrt{D_0}$, as shown by comparing the solid blue and green curves. The particle diffusion length scale peaks at the energy where $t_{cool,max} = t_{age} - t'$. Thus, for some cooling time t_{cool}, there exists a diffusion dominated regime for energies below $E(t_{cool,max} = t_{age} - t')$ in which $e^{-/+}$ don't have time to cool down, and a cooling dominated regime above $E(t_{cool,max} = t_{age} - t')$ where the diffusion radius is limited by the much shorter cooling time. When varying B, the peak of the diffusion length scale occurs at different $e^{-/+}$ energies. Higher energy particles diffuse farther for lower B because their cooling rate is lower and $D \propto E^{\delta}$.

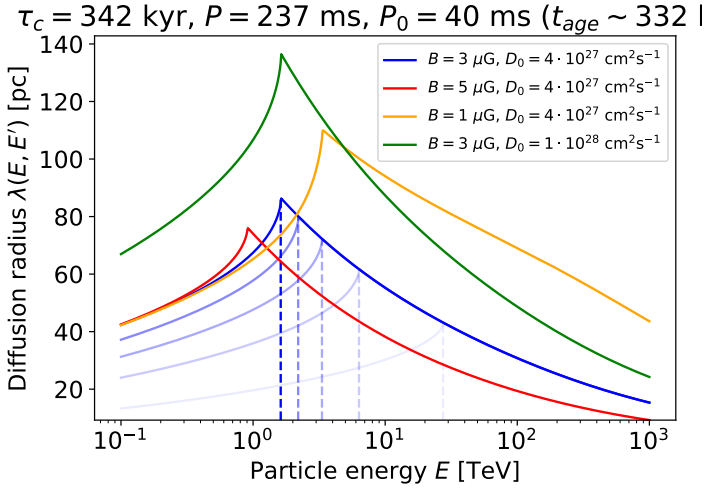

Figure 4.6: Particle diffusion length scale for different values of the magnetic field strength B and the diffusion coefficient normalization D_0. We assume the Geminga pulsar's τ_c, P and set $P_0 = 40$ ms. For $B = 3\ \mu$G and $D_0 = 4 \cdot 10^{27}$ cm^{2}s^{-1} (in blue), the fainter lines represent smaller values of t' (from 0 to 299 kyr), and the dotted lines illustrate the energy E for which $t_{cool,max} = t_{age} - t'$.

2D projection of the particle distribution

To compute the γ-ray intensity as seen from Earth, we project the differential particle density distribution N onto the sky assuming a distance d_{PSR} between Earth and the pulsar, by integrating over the line of sight ℓ. In the spherically symmetric case, $|\mathbf{r}|^2 = r^2 = \theta^2 d_{PSR}^2 + \ell^2$, where θ is the angular separation from the pulsar's position in the sky. Since we are considering pulsars at distances of multiple kpc ($\theta \ll 1$), we assume the lines of sight for all θ are parallel. The projected $e^{-/+}$ distribution per unit energy per steradian reads

$$\begin{aligned} P(E, \theta, t_{age}) &= 2d_{PSR}^2 \int_0^{+\infty} d\ell N(E, \mathbf{r}, t_{age}) \\ &= 2d_{PSR}^2 \int_0^{+\infty} d\ell \int_0^{t_{age}} dt' \frac{b(E')}{b(E)} Q(E', t') \frac{e^{-\frac{\theta^2 d_{PSR}^2}{\lambda^2(E,E')}} e^{-\frac{\ell^2}{\lambda^2(E,E')}}}{\pi^{3/2}\lambda^3(E, E')} \\ &= d_{PSR}^2 \int_0^{t_{age}} dt' \frac{b(E')}{b(E)} Q(E', t') \frac{e^{-\frac{\theta^2 d_{PSR}^2}{\lambda^2(E,E')}}}{\pi\lambda^2(E, E')} \end{aligned} \tag{4.10}$$

In the cylindrically symmetric case, $z = \theta d_{PSR}$ and $\rho^2 = \psi^2 d_{PSR}^2 + \ell^2$ (by taking $\mathbf{u}_z$ and $\mathbf{u}_\rho$ perpendicularly to the line of sight), and similarly to Eq. 4.10:

$$P(E, \theta, \psi, t_{age}) = d_{PSR}^2 \int_0^{t_{age}} dt' \frac{b(E')}{b(E)} Q(E', t') \times \frac{\exp\left(-\frac{\theta^2 d_{PSR}^2 + \psi^2 d_{PSR}^2 + (t-t')^2 V_{PSR}^2 - 2\theta d_{PSR}(t-t') V_{PSR}}{\lambda^2(E,E')}\right)}{\pi \lambda^2(E, E')} \tag{4.11}$$

P is computed over a geometrically spaced spatial grid from 0.1 to 200 pc with 50 points (in the cylindrical case, this is done for both directions along the pulsar's transverse velocity, and in the direction perpendicular to the pulsar's transverse velocity) and a logarithmically spaced particle energy grid from 0.1 to 1000 TeV with 30 points. The spatial kernel in the integrand (i.e. the factor that contains the dependence on space and λ) goes to 0 when $\lambda \to 0$ (or $t' \to t_{age}$), however it also peaks at $\lambda = r$. Therefore, at small distances to the pulsar, the spatial kernel can vary strongly in a very narrow t' to t_{age} range. To properly account for this behavior, one can use adaptive quadrature methods (e.g. `scipy.integrate.quad`), however this substantially increases the computation time, which is not suitable when we require the model to be computed over a large parameter space. Instead, we used an "inverted logarithmic" t' grid, with a sufficient number of points such that there is no loss of integration accuracy compared to an adaptive quadrature method. The integration is done using `scipy.integrate.trapezoid`. All other integrations involved in the computation (e.g. in the computation of E' and t_{cool}) make use of `scipy.integrate.quad`.

At each position θ (or (θ, ψ) if the proper motion is included), we compute the differential photon spectrum due to ICS from the particle distribution P using the Naima Python package (Zabalza 2015) and the ISRF black-body components at the pulsar's position. This yields the γ-ray intensity $I(E_\gamma, \theta)$ (or $I(E_\gamma, \theta, \psi)$) with E_γ the photon energy. By integrating I over space, we obtain the total differential photon distribution $\frac{d\phi}{dE_\gamma}$ ($\mathrm{TeV}^{-1}\mathrm{cm}^{-2}\mathrm{s}^{-1}$). Similarly, by integrating P over space, we obtain the differential particle density N_e (TeV^{-1}).

Impact of parameter variations on the γ-ray emission

For the Geminga pulsar, we looked at the impact of the model parameters on the spectrum and morphology of the γ-ray emission. We define a "baseline" model with the parameter values shown in Table 4.2. The diffusion coefficient's index δ is fixed to 1/3, thus assuming Kolmogorov scaling of the turbulence energy spectrum, the braking index n is fixed to 3, and the injection efficiency $\eta = 10\%$ acts as a normalization, which we do not vary.

The model particle SED is shown for different parameter values in Fig. 4.7. The green curves show changes with respect to P_0 (or t_{age}), the magenta curves show changes with respect to Γ, the yellow and red curves show changes with respect to B, and the blue dotted curve shows changes with respect to E_c.

As discussed previously, the limitation of the maximum particle cooling time manifests in the particle SEDs as a break in the spectrum, roughly at the energy for which $t_{cool,max} = t_{age}$. When P_0 decreases (or t_{age} increases), the SED increases below this energy as the contribution by $e^{-/+}$ injected at earlier times increases. Above this energy, the only contribution is that of the most recently injected particles. When the cooling rate changes through B, $E(t_{cool,max} = t_{age})$ changes and thus the break in the particle SED is shifted.

Model parameter	Value
Distance to pulsar d_{PSR}	250 pc
Characteristic age τ_c	342 kyr
Braking index n	3
Injection efficiency η	0.1
Present-day period P	237 ms
Initial period P_0	40 ms
Injection index Γ	2.0
Injection cut-off energy E_c	1 PeV
Magnetic field strength B	3 μG
ISRF energy densities (Optical, IR, FIR)	0.54, 0.16, 0.25 eV/cm^3
Diffusion coefficient at 100 TeV D_0	$2.36 \cdot 10^{27}$ cm^{2}s^{-1}
Rigidity dependence δ	1/3

Table 4.2: Baseline model parameter values.

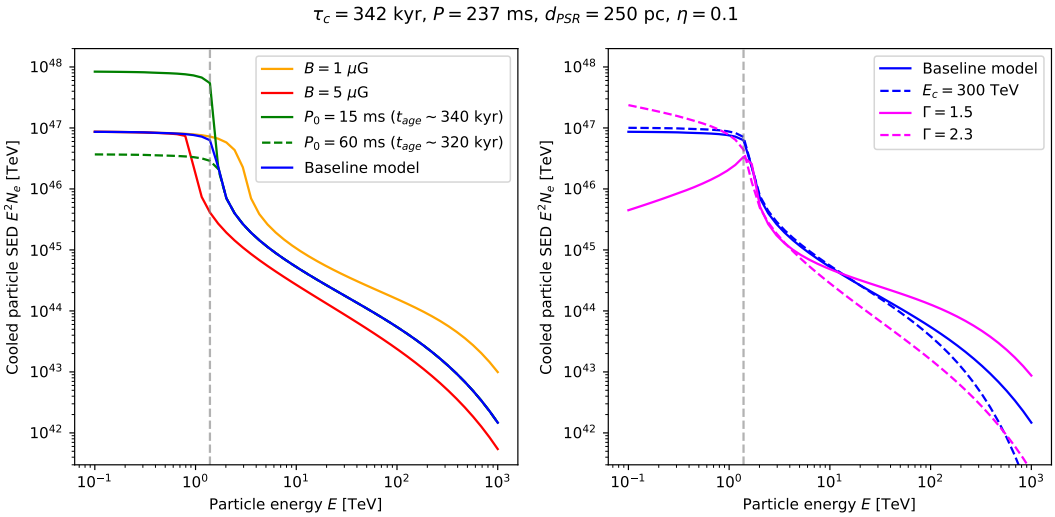

Figure 4.7: Particle SEDs assuming the Geminga pulsar's τ_c and P, an injection efficiency $\eta = 10\%$, and a braking index $n = 3$, for different model parameter values. The dashed vertical line represents $E(t_{cool,max} = t_{age})$ for the baseline model. The SEDs are displayed in two different plots for clarity.

The differential photon spectrum is shown in Fig. 4.8. We also show the fitted power-law photon spectrum and surface brightness profile measured by Abeysekara et al. (2017). Similarly to the particle SED, B considerably modifies the amplitude of the photon spectrum and the break energy, and variations with respect to P_0 govern the contribution by relic $e^{-/+}$ below the break. For younger systems, $E(t_{cool,max} = t_{age})$ is higher and therefore the break in the particle SEDs and photon spectra occurs at a higher energy. In the context of studying pulsar halos with H.E.S.S., the field of view of which is on the order of the full extent of the Geminga halo detected by HAWC, we must search for candidate halos towards farther pulsars, which will require pulsars with a higher spin-down luminosity. This implies that detectable pulsar halos in H.E.S.S. data will likely occur around pulsars younger than the Geminga pulsar. For a pulsar ten times as distant as Geminga, $\dot{E}/d_{PSR}^2$ must be ~ 100 times higher. For $n = 3$, $\dot{E}$ scales inversely with $\tau_c P^2$. Requiring that the pulsar be at least "middle-aged" with $\tau_c \sim 40$ kyr, the period P must be roughly 3 times lower than that of the Geminga pulsar. For a hypothetical pulsar with $P_0 = 40$ ms, $P = 80$ ms and $\tau_c = 40$ kyr, the true age is $t_{age} \sim 30$ kyr and $E(t_{cool,max} = t_{age}) \sim 28$ TeV. Hence, halos around younger pulsars would produce a

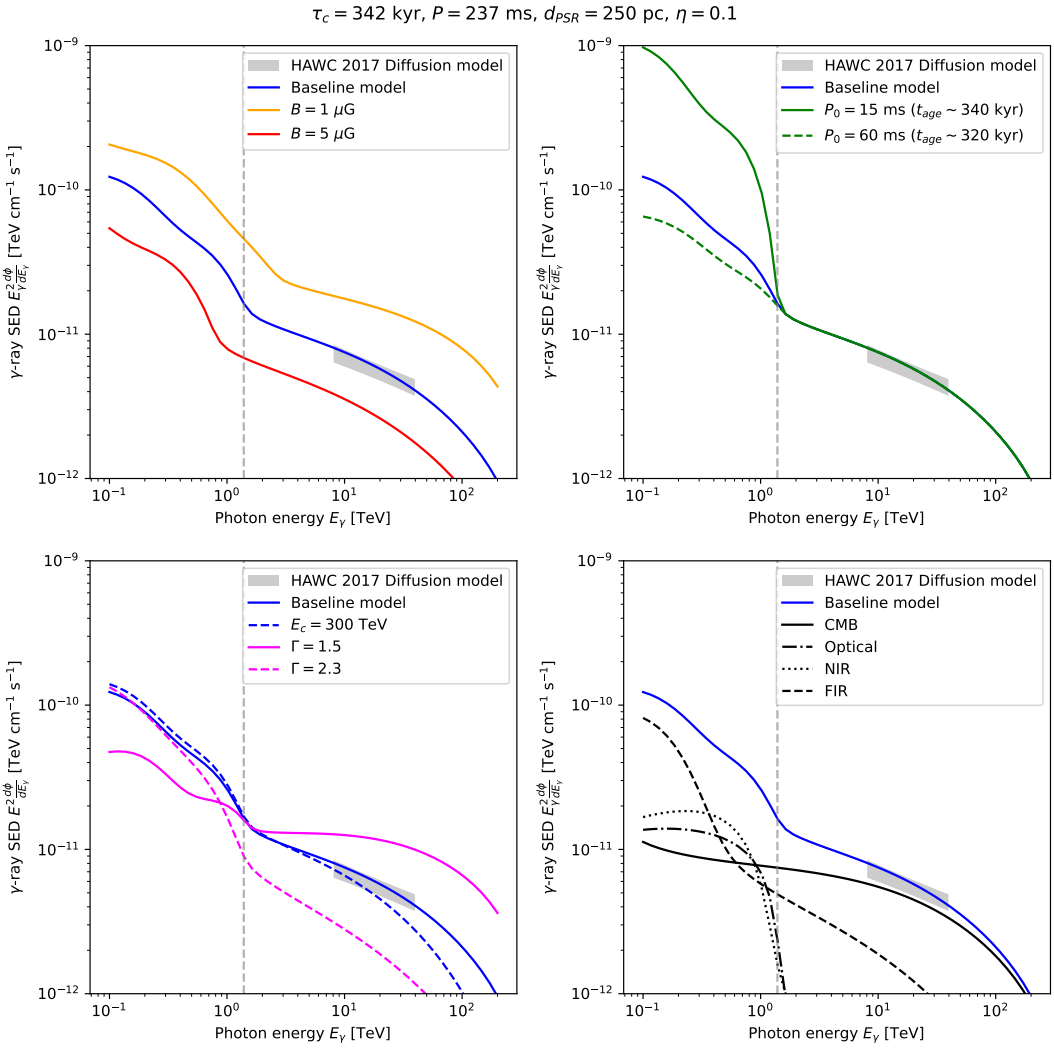

Figure 4.8: Differential photon spectra for different model parameter values assuming the Geminga pulsar's τ_c and P, for a distance $d_{PSR} = 250$ pc, an injection efficiency $\eta = 10\%$ and a braking index $n = 3$. The dotted vertical line represents $E(t_{cool,max} = t_{age})$ for the baseline model. The lower right panel shows the contribution of up-scattered photons from the different ISRFs in the baseline model. The shaded grey band is taken from Abeysekara et al. (2017). The spectra are displayed in four different plots for clarity.

photon spectrum with a break that occurs at significantly higher energies than the one predicted for Geminga. The true age of the pulsar has a significant impact on the shape of the spectrum in the H.E.S.S. band and could be constrained if the values of n and B are assumed.

As for the parameters of the injection spectrum Q (in the bottom left panel of Fig. 4.8), the variation of Γ affects the amplitude of the photon spectrum at $E_\gamma \sim 1$ TeV and its tilt, while E_c affects the cut-off at higher energies. The latter could be constrained with H.E.S.S. should the source be significant enough at higher energies.

Finally, in the bottom right panel of Fig. 4.8, we show that a dominant ICS contribution results from infrared (NIR and FIR) photons from interstellar dust, the lack of precise knowledge of which is therefore a source of systematic uncertainty.

As for the pulsar halo's morphology, the surface brightness profiles and the data from Abeysekara et al. (2017) are shown in Fig. 4.9. The top left panel shows variations of B

have a significant impact on the the Geminga halo's predicted surface brightness in the $8-40$ TeV band. In the lower left panel, variations in D_0 affect the surface brightness due to the variation in particle density. A lower D_0 yields a more peaked profile, while a higher D_0 yields a weaker surface brightness profile near the pulsar but a stronger tail. The panels on the right show variations with respect to Γ in the HAWC band (upper right) and in a larger $0.5-40$ TeV band (lower right). In both energy bands, a higher Γ (i.e. softer injection spectrum) results in a weaker surface brightness profile, due to the weaker contribution by higher energy, recently injected $e^{-/+}$ which are more concentrated near the pulsar. We found that the true age of the pulsar doesn't affect the surface brightness in the HAWC band where there is no contribution by relic $e^{-/+}$, and therefore we only show its impact in the 0.5-40 TeV band in the lower right panel, where an older pulsar produces a more extended halo.

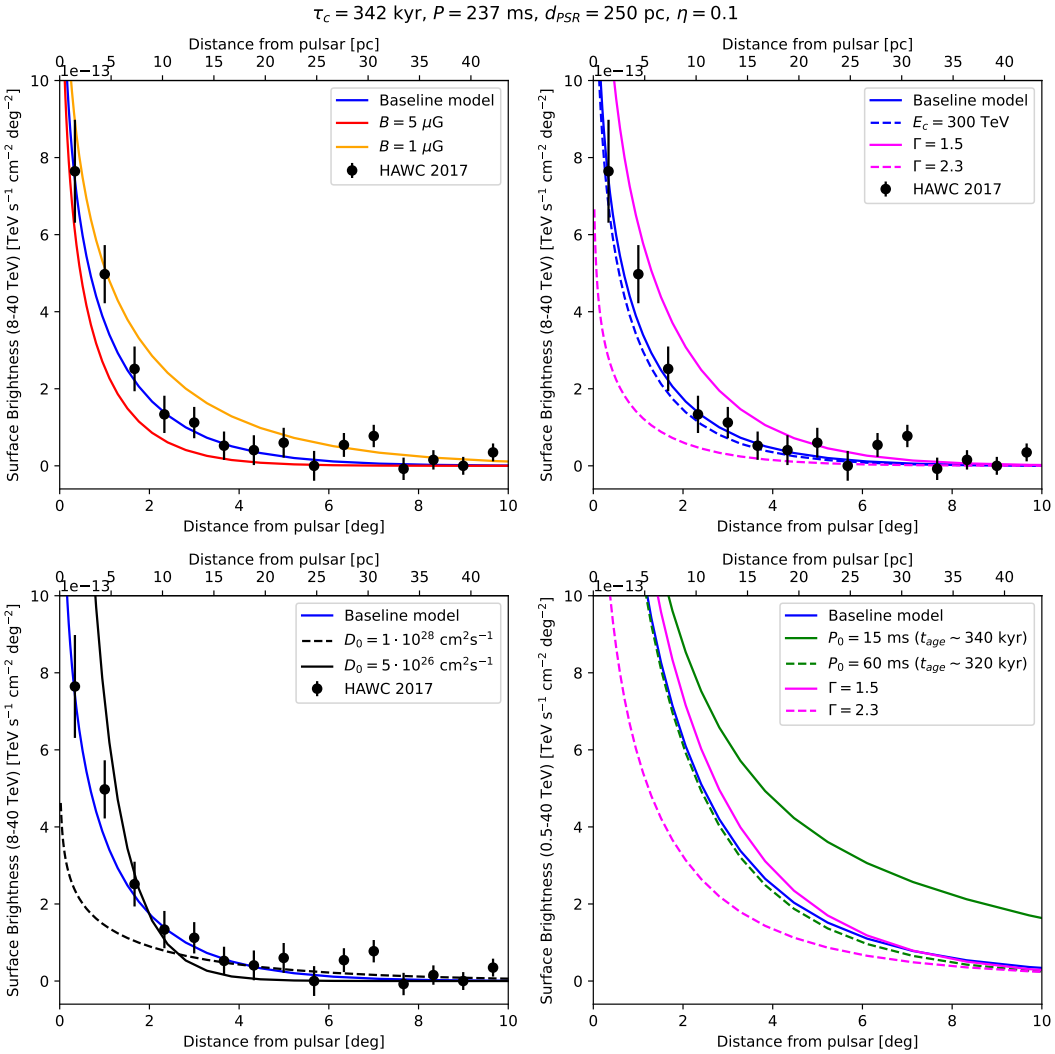

Figure 4.9: Surface brightness profiles assuming the Geminga pulsar's τ_c and P, for a distance $d_{PSR} = 250$ pc, an injection efficiency $\eta = 10\%$ and a braking index $n = 3$. The data points are taken from Abeysekara et al. (2017). The lower right panel shows the surface brightness profiles from 0.5 to 40 TeV, and the other panels from 8 to 40 TeV (corresponding to the energy band used in Abeysekara et al. (2017)). The profiles are displayed in four different plots for clarity.

Finally, we note that the diffusion coefficient normalization D_0 (and the pulsar's proper motion V_{PSR}) has little to no effect on the differential γ-ray spectrum and is

fully constrained by the spatial distribution alone. Throughout this thesis, a rigidity dependence $\delta = 1/3$ is assumed for the diffusion coefficient (following the predicted value from Kolmogorov turbulence theory). Variations of δ are expected to impact the surface brightness profile and the energy dependence of the halo's morphology. $\delta = 1/3$ is assumed for direct comparison with a multitude of works in the literature, for it's compatibility with the AMS-02 Boron-to-Carbon measurements, and because it is not a parameter that we can constrain in the data analysis of Chap. 6 as this would require a higher number of statistics.

Impact of the pulsar's proper motion

In Hobbs et al. (2005), the authors find that a population of 233 young pulsars have proper motions that follow a Maxwellian distribution with mean velocity $\sim$ 300 km/s, and the study includes a highest proper motion velocity of $\sim$ 1600 km/s. Thus, middle-aged pulsars can feasibly travel a distance similar or higher than the diffusion length scale. To account for the asymmetries and offsets observed in the HGPS PWN population (H.E.S.S. Collaboration 2018f), we incorporated the pulsar proper motion in the model, which causes a "tail-like" feature at lower energies, as shown in Fig. 4.10 where we reproduce the pulsar halo model in Zhang et al. (2021), where the pulsar is at a distance of $d_{PSR} = 2$ kpc from Earth. For the sake of reproduction, we used the ICS cooling rate given in Moderski et al. (2005). The results are only marginally different when using the cooling rate following Delahaye et al. (2010). Relic electrons which have cooled throughout the pulsar's evolution produce a secondary peak in the low energy intensity profile ($E_\gamma = 10$ GeV). At $E_\gamma = 1$ TeV, the intensity remains asymmetric. The peak at the pulsar's present-day position is due to recently injected (cooled) $e^{-/+}$. The "tail-like" structure produced by relic $e^{-/+}$ which lag behind the pulsar emerges because the diffusion length scale λ is smaller than the distance traveled by the pulsar. The pulsar's velocity governs the elongation of the γ-ray morphology in the proper motion direction, unlike D_0 which governs the isotropic extent of the morphology. As such, the model is likely not degenerate with respect to these two parameters. The impact of the pulsar's proper motion on the halo's morphology in H.E.S.S. data is studied in Chap. 7.

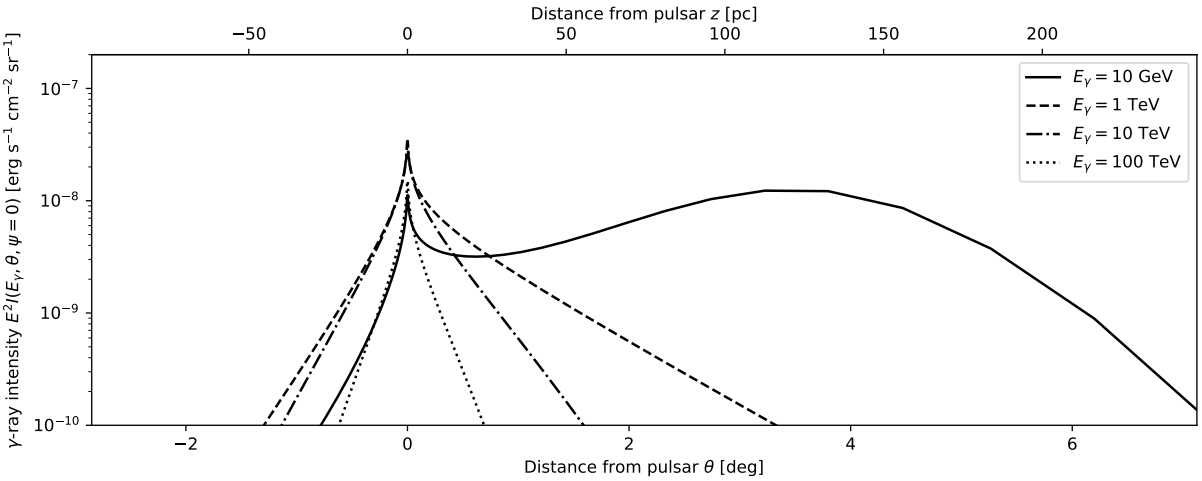

Figure 4.10: Gamma-ray halo ICS intensity $I(E_\gamma, \theta, \psi = 0)$ at different photon energies for $\psi = 0°$, reproduced from Zhang et al. (2021). The pulsar is at a distance $d_{PSR} = 2$ kpc, with $t_{age} = 327$ kyr and $V_{PSR} = 400$ km/s and the diffusion coefficient normalization $D_0 = 4.64 \times 10^{27}$ cm^{2}s^{-1} at 100 TeV. The origin $\theta = 0$ deg corresponds to the pulsar's present day position.

In this section, we proposed six parameters which could be constrained with H.E.S.S. data only if assumptions are made on d_{PSR} (the estimates of which are highly dependent on the assumed free e^- model), B, n and δ: the diffusion coefficient normalization D_0, the proper motion direction and magnitude $\mathbf{V}_{PSR}$, the injection index Γ, the initial period (or true age) P_0, the injection efficiency η (which acts as a normalization) and E_c. A thorough analysis of our ability to constrain these parameters is conducted in the pulsar halo observation simulations Chap. 7.

4.2 Building pulsar halo templates for H.E.S.S. data fitting

The pulsar halo model described previously can be fitted directly to H.E.S.S. data in a 3D data analysis, by creating spatial and spectral templates of the γ-ray emission and using them in the Gammapy (Donath et al. 2023) modeling framework. To that end, assuming measured pulsar properties (d_{PSR}, τ_c, and P) and fixed values for n, B, δ and E_c, we computed the model for different combinations of the values of the parameters we are interested in fitting (D_0, Γ, V_{PSR} and P_0). The γ-ray intensity is proportional to η and this term will be the norm of the γ-ray SED during the fit. The proper motion direction $V_{PSR,\theta}$ is a rotation of the template in the sky which is computed during the fit. In this section, we describe in detail this procedure: the creation of the templates, the usage with Gammapy, and the observation simulations used to validate the method.

4.2.1 Pulsar halo templates

We defined grids for the free parameters D_0, Γ, V_{PSR} and P_0 as follows:

- D_0 at 100 TeV: 17 points geometrically spaced from $D_{0,min} = 3 \cdot 10^{25}$ cm^{2}s^{-1} to $D_{0,max} = 2 \cdot 10^{28}$ cm^{2}s^{-1}.
- Γ: linear grid from $\Gamma_{min} = 0.5$ to $\Gamma_{max} = 3.0$ with 17 points;
- V_{PSR}: linear grid from $V_{PSR,min} = 10$ km/s to $V_{PSR,max} = 2000$ km/s with 17 points;
- P_0: linear grid from $P_{0,min} = 10$ ms to $P_{0,max} = P$ with 18 points (the model is null at $P_{0,max}$).

The number of points for the grids was chosen so the subsequent interpolation between the templates, and the fit of the model onto a simulated pulsar halo (which shall be described later), yield accurate results in a reasonable computing time. In practice, we do not fit the pulsar proper motion and the injection index at the same time for computational reasons. The model with pulsar proper motion contains an additional spatial grid (θ and ψ) compared to the symmetric model (θ), and is slower to compute over all parameter combinations. In the likelihood fitting process, an expansive parameter space is scanned, where at each step an interpolation of the templates is computed. If the number of parameters is too high, the fitting process can take an excessive amount of time (and computational resources). Thus, when the proper motion is used the model is only computed for one value of Γ and the latter is not fitted.

The Gammapy modeling framework for spectro-morphological fitting employs count models factorized as a spatial component (in units of steradians^{-1}) and a spectral component (in units of TeV^{-1}cm^{-1}s^{-1}). Consequently, we computed a normalized spatial template and the corresponding γ-ray SED for every parameter combination. Integrating the product of the spatial and spectral models and convolving with the IRFs yields the predicted number of counts.

In the following, we describe the case when the proper motion is included. For each parameter combination $\{D_0, V_{PSR}, P_0\}_i$, the intensity $I_i(E_\gamma, \theta, \psi)$ and the γ-ray differential spectrum $\phi_i(E_\gamma) = \int\int d\theta d\psi I_i$ are computed for the energy and spatial grids described in the previous section. The normalized spatial template is $I_{i,norm}(E_\gamma, \theta, \psi) = I_i(E_\gamma, \theta, \psi)/\phi_i(E_\gamma)$. The Gammapy energy-dependent spatial model is evaluated by interpolation in energy, space, D_0, P_0 and V_{PSR}. The spectral model is evaluated by interpolation in energy, D_0, P_0 and V_{PSR}. The spatial and spectral models share the parameters D_0, P_0 and V_{PSR} such that they are always evaluated for the same parameter values. For the system with no proper motion, Γ replaces V_{PSR} and the intensity depends only on θ.

4.2.2 Validation using simulated H.E.S.S. observations

To assess the accuracy of the modeling and fitting approach, we simulated observations of pulsar halos, conducted a likelihood fit of the model templates, and compared the estimated parameter values with those of the simulated model. We refer to this process as one realization. The first H.E.S.S. public data release* includes $\sim$ 8.4 hours of observations targeting the SNR MSH 15−52 and a list of off-region events which we use for the construction of the residual cosmic-ray background model. The MSH 15−52 observations are replicated 5 times to get a total of $\sim$ 42 hours of observation. The IRFs corresponding to the MSH 15−52 observations were selected because they are representative of an observation strategy dedicated to an individual extended source in the Galactic plane (in terms of wobble offset and the position of the source in the sky). To simulate one observation, we took the pointing information, the duration of the pointing, and the IRFs (PSF, energy dispersion, and effective detector area) of one MSH 15−52 observation. The counts from the pulsar halo model are generated and Poisson fluctuated. The cuts on the event selection are defined as 2° around the camera center, and a minimum energy threshold which is at least higher than the background peak energy and such that the effective area is at least 10% of the maximum effective area. The data reduction algorithm is performed to create the IRF and dataset cubes. The dataset geometry is a 4° × 4° cube centered on the position of MSH 15−52 with a spatial bin size of 0.02° and a reconstructed energy axis from 0.3 to 100 TeV (8 bins per decade). The true energy axis is defined from 0.1 to 200 TeV (20 bins per decade). We used the Field of View background method by defining a mask on γ-ray emitting regions. The background model is optimized in the region outside the mask by re-normalizing the expected counts with a power law with free normalization. This is done for the entire set of (replicated) observations, and all the generated datasets are stacked together. We defined the model of pulsar halo templates associated to multiple parameter combinations, and fit it to the stacked dataset. The simulations do not include an interstellar emission component. We produced 160 realizations for 120 different parameter combinations of the simulated halo.

*This work made use of data from the H.E.S.S. DL3 public test data release 1 (HESS DL3 DR1, H.E.S.S. collaboration, 2018) https://www.mpi-hd.mpg.de/hfm/HESS/pages/dl3-dr1/

The pulsar parameters are $P = 80$ ms, $\tau_c = 100$ kyr, $n = 3$, $d_{PSR} = 3$ kpc and the simulated parameter combinations are the following:

- $\Gamma = 1.0$ or 2.0
- $E_c = 100$ TeV or 1 PeV
- $D_0 = 1.27 \cdot 10^{26}$, $4.298 \cdot 10^{26}$, $9.688 \cdot 10^{26}$, $2.184 \cdot 10^{27}$ or $4.923 \cdot 10^{27}$ cm^{2}s^{-1}
- $V_{PSR} = 0.0$, 320.9 or 942.8 km/s
- $P_0 = 28.3$ or 68.9 ms (corresponding to $t_{age} \sim 85.7$ or 25.8 kyr, respectively).
- $\eta = 3\%$ (or 7% when $\Gamma = 1.0$ and $E_c = 1$ PeV, see explanation below)
- $B = 3$ μG

These parameter values are chosen such that they are not among the values in the grids over which the pulsar halo templates used for fitting are computed.

In Fig. 4.11, we show the γ-ray SEDs for $\eta = 3\%$ and different values of Γ, E_c and P_0. The red lines represent the $P_0 = 28.3$ ms (older) case, and the blue lines represent the $P_0 = 68.9$ ms (younger) case. The vertical dotted lines represent the energy at which the particle cooling time is equal to t_{age}. The solid lines represent the $\Gamma = 1$ case, and the dashed lines represent the $\Gamma = 2$ case. The left panel corresponds to $E_c = 100$ TeV, and the right panel corresponds to $E_c = 1$ PeV. A harder injection spectrum implies a higher proportion of $e^{-/+}$ injected at higher energies, and thus the γ-ray SED becomes more sensitive to variation in the injection cutoff energy. For a higher E_c, more of the pulsar's rotational power goes into the injection of particles that will contribute less γ-rays in the H.E.S.S. energy band. This is illustrated in Fig. 4.11 by comparing the solid curves in the left panel with those of the right panel (while the dashed curves are comparably unaffected by a change in E_c). This results in a less significant source where it's difficult to study the observational impact of varying E_c. As such, for $\Gamma = 1.0$ and $E_c = 1$ PeV, we increased η from 3% to 7%, such as the significance of the source remains roughly similar to the $\Gamma = 1.0$ and $E_c = 100$ TeV case.

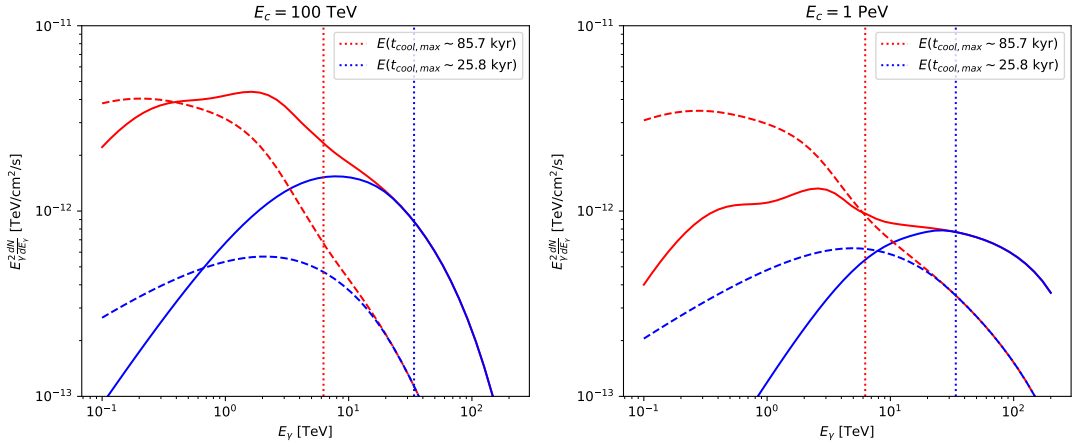

Figure 4.11: **Left:** γ-ray SEDs of the simulated pulsar halo model with $E_c = 100$ TeV. **Right:** γ-ray SEDs of the simulated pulsar halo model with $E_c = 1$ PeV. Red is for the older case ($P_0 = 28.3$ ms) and blue for the younger case ($P_0 = 68.9$ ms). The solid lines correspond to $\Gamma = 1.0$ and the dashed lines to $\Gamma = 2.0$. The vertical dotted lines indicate $E(t_{cool,max} = t_{age})$.

The chosen initial period values are representative of an old (evolved) system and a young system. The ISRFs are taken for an arbitrary position ($\ell = 317.89$ deg and $b = -1.79$ deg in galactic coordinates and $d_{PSR} = 3$ kpc). The ISRFs energy densities at this position correspond to: Optical (3312 K) 1.17 eV/cm^3, IR (551 K) 0.31 eV/cm^3 and FIR (35 K) 0.54 eV/cm^3, following Popescu et al. (2017). Fig. 4.12 shows an example model intensity (I) map at different photon energies. In the upper left panel at $E_\gamma = 0.3$ TeV, a double-peaked structure is seen, with γ-rays concentrated near the pulsar and also forming a secondary, more extended structure near the pulsar's birth position. In the upper right panel at $E_\gamma = 1.51$ TeV, the secondary structure near the pulsar's birth place is less pronounced, but still visible. At higher energies in the lower panels, the γ-ray emission is concentrated near the pulsar's present-day position. Only a slight asymmetry can be seen in the lower left panel for $E_\gamma = 13.25$ TeV. Fig. 4.13 shows the simulated dataset's excess significance map in the $0.3 - 100$ TeV band on the left and the surface brightness profiles at different photon energies on the right. The profiles are computed at the axis of the pulsar's transverse motion in the sky ($\psi = 0$). The model is computed for $D_0 = 2.184 \cdot 10^{27}$ cm^{2}s^{-1}, $V_{PSR} = 942.813$ km/s, $E_c = 100$ TeV and $\Gamma = 1$. The pulsar birth position is shown in a cyan diamond or cyan dashed line. A prominent "tail-like" structure of γ-rays from relic particles can be observed.

For each of the simulated 120 parameter combinations, we checked that the fit of the halo templates yields parameter estimates that are within one standard deviation of the simulated parameter values. We refer to this as the "parameter recovery". In Fig. 4.14, we show an example of parameter recovery for three different simulated parameter combinations with $D_0 = 2.184 \cdot 10^{27}$cm^{2}s^{-1}, $P_0 = 28.3$ ms, $\eta = 0.03$ and $E_c = 100$ TeV and different values of Γ and V_{PSR} in each row. The histograms represent the density of the estimated value in each realization. The red line represents the simulated value and the yellow line is a normal distribution with the mean and standard deviation of the estimated value across the realizations. When the source is not too significant, some of the realizations do not converge successfully in the fit, and these realizations are excluded from the statistics. The mean Test Statistic of the halo fit across all realizations ($TS_{\mathrm{halo,\,i}}$) is indicated for each simulated parameter combination i. The template fitting procedure yields convenient estimations of the simulated parameter values.

4.2.3 Conclusion

Using a particle transport model (injection, propagation and losses) that adequately reproduces the HAWC results on Geminga and Monogem, we created spectro-morphological templates of pulsar halos for different values of the diffusion coefficient normalization at 100 TeV, the initial period of the pulsar, the $e^{-/+}$ injection spectrum index, the $e^{-/+}$ injection efficiency and the pulsar's proper motion transverse velocity. The templates were then used to create Gammapy models for the purpose of 3D analyses of H.E.S.S. data (and more generally of IACT data). We created mock datasets for different pulsar halo parameter values by simulating H.E.S.S. observations using the publicly available IRFs. This approach was validated by fitting the template-based pulsar halo models on simulated datasets, ensuring that the estimated parameters are statistically compatible with the simulated ones. These templates can therefore be used for fitting IACT data in order to attempt to detect and characterize pulsar halos (see Chap. 7 for a comprehensive study using H.E.S.S. and CTAO simulations), and to constrain physical parameters related to $e^{-/+}$ transport in halos (see Chap. 6 for an application on HESS J1831−098).

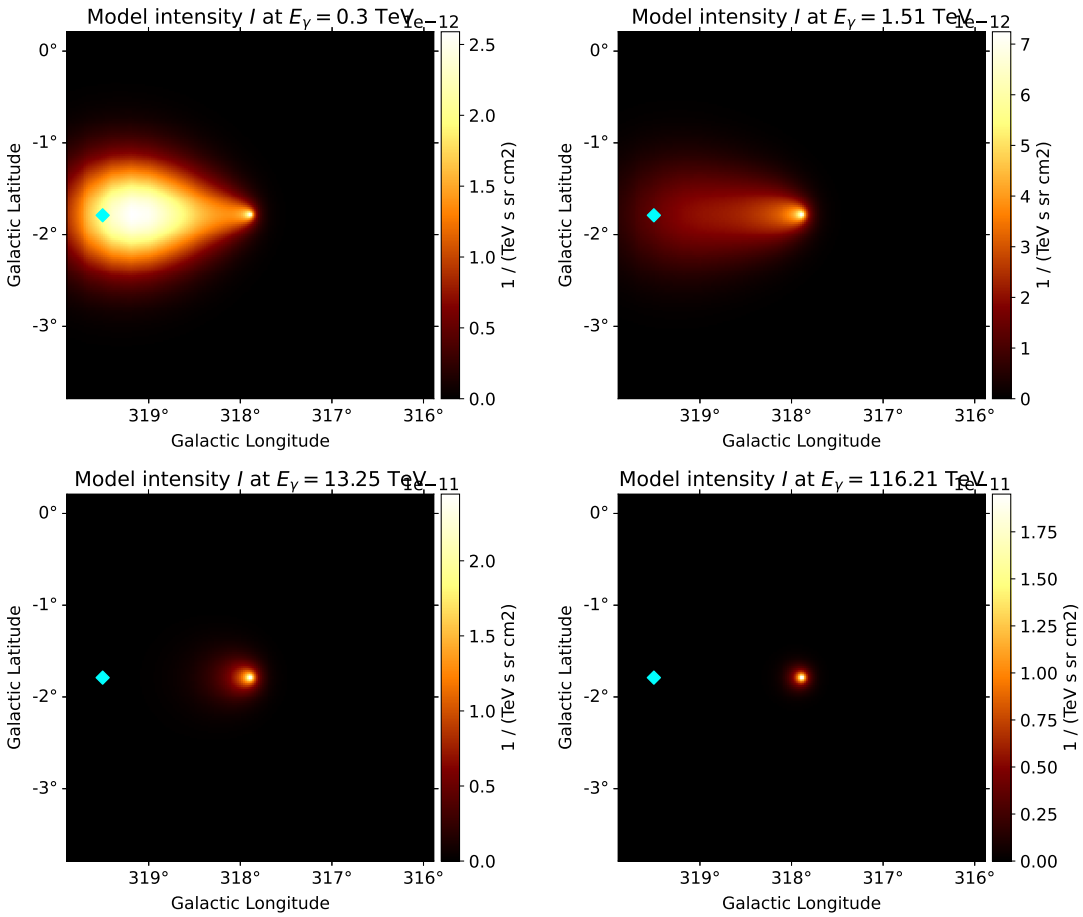

Figure 4.12: Intensity maps $I(E_\gamma, \ell, b)$ of an example pulsar halo model used for the simulations. The model parameters are $D_0 = 2.184 \cdot 10^{27}$ cm^{2}s^{-1}, $V_{PSR} = 942.8$ km/s, $E_c = 100$ TeV, $\Gamma = 1$. The pulsar's birth position is shown with a cyan diamond.

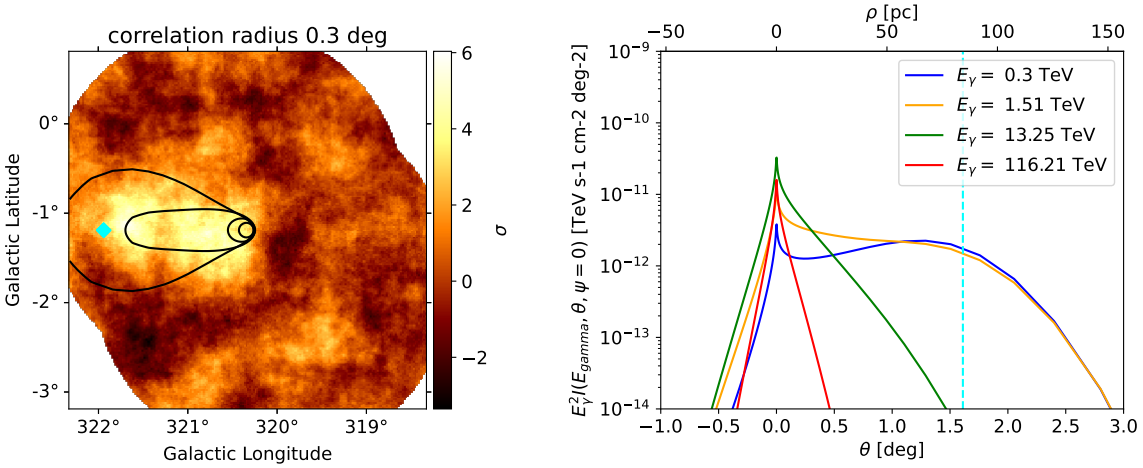

Figure 4.13: **Left:** Example excess significance map from 0.3 to 100 TeV with a correlation radius of 0.3° for the same parameters as Fig. 4.12. The contours represent the 20% of the peak $E_\gamma^2 I$ for different values of E_γ. **Right:** $E_\gamma^2 I(E_\gamma, \theta, \psi = 0)$ intensity profile of the model used for the same simulations. In both figures, the cyan diamond and the dashed vertical line represent the pulsar's birth position.

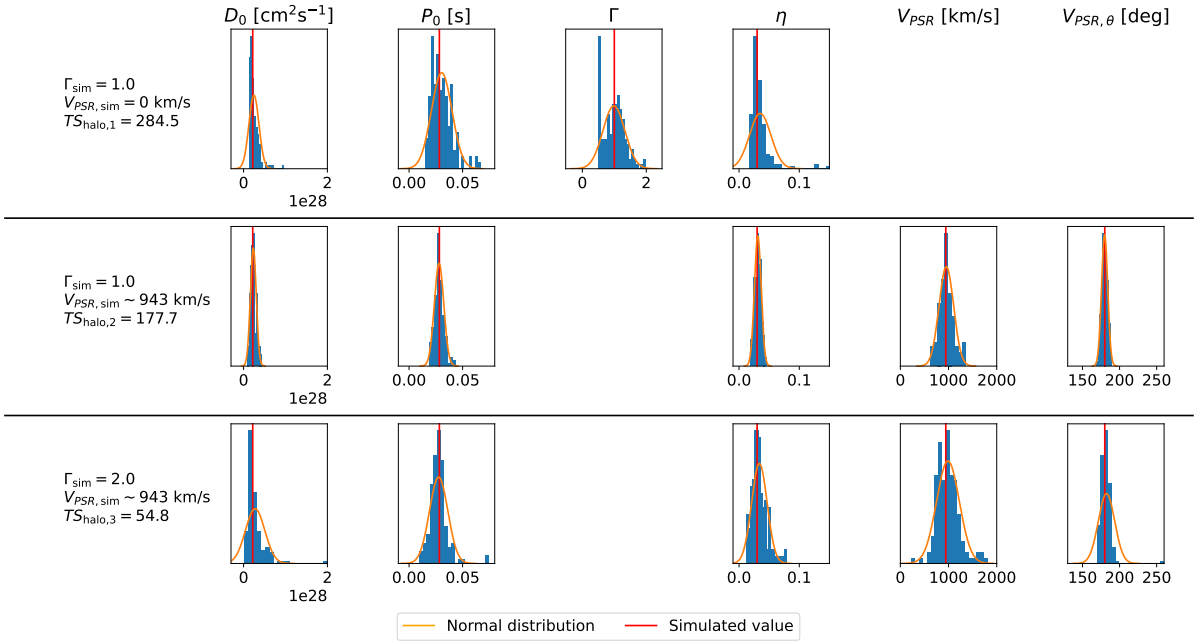

Figure 4.14: Parameter recovery for three different parameter combinations, each corresponding to one row. The histograms are the density distributions of the estimated values across all realizations. $TS_{\mathrm{halo,i}}$ corresponds to the average Test Statistic of the fitted halo model across all realizations of the i-th parameter combination. The red line indicates the simulated value, and the yellow distribution is a normalized Gaussian with the mean and standard deviation of the estimated values across all realizations. For all three rows, $D_0 = 2.184 \cdot 10^{27}\mathrm{cm}^2\mathrm{s}^{-1}$, $P_0 = 28.3$ ms, $\eta = 0.03$ and $E_c = 100$ TeV.

Chapter 5

Search for pulsar halo candidates in the H.E.S.S. Galactic Plane Survey

Contents

5.1 Pulsar halo candidates in the HGPS 62
5.2 Associations with 1LHAASO sources 64
5.3 Comparison with pulsar halo candidates in the literature . 68
5.4 Non-detected HGPS sources around energetic pulsars . . . 69
5.5 Conclusion 70

The presence of an energetic middle-aged pulsar (i.e. with a characteristic age $\tau_c \gtrsim$ 40 kyr) inside an extended region of very-high-energy emission hints at the possibility of a pulsar halo scenario. The HGPS catalog contains 12 sources that are considered firmly identified as PWNe based on multiwavelength evidence and/or their energy-dependent morphology. A further 10 associations are considered "highly-rated", based on their consistency with the observational properties of the identified PWNe. Additionally, it contains 11 unidentified sources that were not found to be associated with multi-wavelength counterparts (except possibly with Fermi-LAT sources), which we refer to as "dark" sources. The latter are of relevance in the context of relic PWNe and pulsar halos because the absence of known synchrotron X-ray or radio counterparts could indicate that the detected VHE emission is predominantly produced by relic $e^{-/+}$ (i.e. a population of $e^{-/+}$ older than that expected to emit visible X−ray radiation), or by $e^{-/+}$ outside of the nebular magnetic field.

Since the publication of the HGPS catalog, there have been important theoretical and experimental developments in the topic of pulsar-powered VHE sources, including the discovery of halos around middle-aged pulsars that are significantly older than the firmly identified PWNe in H.E.S.S. data. In this chapter, we look for pulsar halo candidates in the HGPS by searching for spatial coincidences with middle-aged pulsars in the Australian Telescope National Facility (ATNF) catalog* (Manchester et al. 2005). Further, the search is extended with the inclusion of components from the recently published 1LHAASO catalog (Cao et al. 2024b) of VHE/UHE sources. Owing to its duty cycle and field of view, LHAASO is very well suited for searching for extended and faint sources that could be pulsar halos. The goal is to determine a list of targets in H.E.S.S. data that

*https://www.atnf.csiro.au/research/pulsar/psrcat/

merit re-investigation in a dedicated analysis, in particular using the 3D likelihood and template-based approach as described in the Chapters 3 and 4.

5.1 Pulsar halo candidates in the HGPS

We considered pulsars in version 2.5.1 of the ATNF pulsar catalog. The search starts with loosely defined association criteria:

- $\frac{\dot{E}}{d_{PSR}^2} \geq 3 \times 10^{33}$ erg/s/kpc^2
- The positional offset between the HGPS source and the pulsar is $\leq 1.5 \times R_{Spec}$
- $\tau_c \leq 10^4$ kyr, to avoid the inclusion of millisecond pulsars

with $\dot{E}$ the pulsar's spin-down power, d_{PSR} its distance to Earth and τ_c its characteristic age. The first criterion follows from Carrigan et al. (2008) and H.E.S.S. Collaboration (2018f), where it was shown that the number of spatial coincidences between ($\dot{E}/d_{PSR}^2 \geq 10^{34}$ erg/s/kpc^2) pulsars and VHE components in H.E.S.S. data is significantly higher than the expected number of chance coincidences, meaning that such pulsars are generally able to produce VHE emission detectable by H.E.S.S. Since pulsar halos are generally expected to exist at later ages relatively to PWNe, a slightly lower threshold of 3×10^{33} erg/s/kpc^2 was chosen to possibly account for more evolved systems than the H.E.S.S. PWN population, without introducing too many associations that would require an implausibly high $\dot{E}$ to γ-ray luminosity conversion efficiency. The second criterion defines the spatial containment of the pulsar within the VHE emission region. For a given HGPS source, R_{Spec} corresponds to the spectral extraction region that was used in the HGPS analysis pipeline, and corresponds generally to the 70% containment (or ~ 1.5 times the source's 2D Gaussian 1σ extension). Here, we required that the pulsar be within $1.5 \times R_{Spec}$ of the source's position. This choice was made because in Chap. 7, it will be established that pulsar halos can be highly asymmetric and/or offset from the pulsar position in H.E.S.S. data due to the pulsar's proper motion and the contribution by relic $e^{-/+}$ (the 2D Gaussian models used in the HGPS analysis are strictly symmetric). From the resulting list of associations, we discarded the HGPS sources in Table 5.1 because they are firmly identified as other types of sources (supernova remnants, massive stellar clusters, etc.). HESS J0852−463 (Vela Junior, associated with PSR J0855−4644 in this search) is identified as a supernova remnant, and HESS J1640−465 (G338.3−0.0, associated with PSR J1640−4631 in this search) is identified as a composite system, however we do not exclude them from this selection because the former, characterized by multiple Gaussian components, harbors a resolved PWN candidate around the associated pulsar (Aharonian et al. 2026), and the latter because it is found to be a highly rated PWN candidate in H.E.S.S. Collaboration (2018f).

Finally, we discarded the list of firmly identified PWNe of H.E.S.S. Collaboration (2018f), and imposed a characteristic age $\tau_c \geq 40$ kyr. The resulting list of 12 associations is shown in the first and second sections of Table 5.2, where the first section groups sources best modeled with a 2D Gaussian morphology (10 associations), and the second section groups HGPS sources that are best modeled with a shell morphology following H.E.S.S. Collaboration (2018a) (i.e. SNR candidates, 2 associations). Two "dark" sources are found in this search: HESS J1745−303 which is spatially coincident with PSR B1742−30, and HESS J1458−608 which is spatially coincident with PSR J1459−6053. Additionally,

HGPS name	Identified context
HESS J1302−638	PSR B1259−63 (γ-ray binary)
HESS J1646−458	Westerlund 1 (massive stellar cluster)
HESS J1713−397	RX J1713.7−3946 (SNR)
HESS J1745−290	Galactic center, Sgr. A*
HESS J1747−281	G0.9+0.1 (composite)
HESS J1747−248	Terzan 5 (globular cluster)
HESS J1801−233	W28 (SNR/molecular cloud)
HESS J1834−087	W41 (SNR/molecular cloud)

Table 5.1: HGPS sources discarded from the preliminary selection due to firm identification as a non-pulsar halo astrophysical context (except for HESS J1746−285, see text).

HGPS	PSR	P [ms]	τ_c [kyr]	$\dot{E}$ [10^{35} erg/s]	d_{PSR} [kpc]
2D Gaussian morphology					
HESS J0852−463	J0855−4644	64.7	141	10.59	5.6
HESS J1026−582	J1028−5819	91.4	90	8.32	1.4
HESS J1458−608	J1459−6053	103.2	65	9.09	1.8
HESS J1718−385	J1718−3825 (1)	74.7	90	12.49	3.5
HESS J1745−303	B1742−30 (1)	367.4	546	0.08	0.2
HESS J1746−308	B1742−30 (2)	367.4	546	0.08	0.2
HESS J1809−193	J1809−1917	82.8	51	17.78	3.3
HESS J1813−126	J1813−1246	48.1	43	62.42	2.6
HESS J1841−055	J1838−0549	235.3	112	1.01	4.1
HESS J1852−000	J1853−0004	101.4	288	2.11	5.3
Shell morphology					
HESS J1614−518	B1607−52	182.5	559	0.34	2.9
HESS J1912+101	J1913+1011	35.9	168	28.83	4.6
Discarded components					
HGPSC 015^{L} (1)	J1406−6121	213.1	62	2.2	7.3
HGPSC 015^{L} (2)	J1413−6205	109.7	63	8.3	2.2
HGPSC 037^{S}	J1643−4505	237.4	118	0.94	4.7
HGPSC 041^{L}	J1702−4128	182.1	55	3.4	4.0
HGPSC 046^{L} (1)	J1715−3903	278.5	118	0.68	3.7
HGPSC 046^{L} (2)	J1718−3825 (2)	74.7	90	12.49	3.5
HGPSC 051^{L}	B1742−30 (3)	367.4	546	0.08	0.2
HGPSC 063^{L} (HESS J1813−178)	J1815−1738	198.4	40	3.9	4.9
HGPSC 072^{S} (HESS J1831−098) (1)	J1831−0941	300.9	56	1.2	4.2
HGPSC 072^{S} (HESS J1831−098) (2)	J1831−0952	67.3	128	11.0	3.7
HGPSC 091^{L}	J1857+0143	139.8	71	4.5	4.6

Table 5.2: Selection of pulsar associations with HGPS sources that could be pulsar halo candidates. The table is divided into three sections, with the second section grouping SNR candidates, and the third section grouping discarded HGPS components (labeled HGPSC). ^{L}: HGPS "Discarded Large". ^{S}: HGPS "Discarded Small".

the associations found for HESS J1809−193 and HESS J1718−385 are considered highly rated PWNe candidates in H.E.S.S. Collaboration (2018f), with the former having been interpreted as possibly comprising a component of escaped $e^{-/+}$ (H.E.S.S. Collaboration 2023b).

The HGPS resulted in 20 components that were discarded from the source catalog due to them not being significant in the cross-check analysis (labeled "Discarded Small"), or due to their large size and low surface brightness making them possible artifacts or a mismodeling of the large-scale Galactic diffuse emission with a latitudinal Gaussian template (labeled "Discarded Large"). This search includes these components (labeled "HGPSC" in Table 5.2) with the motivation that they may pass the cross-check process in a dedicated analysis (possibly with higher exposure), and/or that a large extension and low surface brightness could be characteristics of pulsar halos. The "Discarded Large" components in Table 5.2, indicated by the ^{L} superscript, are 2D Gaussians with 1σ extensions

ranging between 0.3° and 0.6°, which is similar to the extensions of the simulated halos (cf. Chap. 7). The search yielded 10 associations of discarded components with middle-aged energetic pulsars (three of these components are associated with two pulsars). The 2HGPS, the second H.E.S.S. Galactic Plane Survey catalog which is built using the Field of View background method and 3D analyses, is currently in progress within the H.E.S.S. collaboration and preliminary versions are available internally. Notably, in the current version of the upcoming 2HGPS catalog, HGPSC 015 is resolved into two components spatially coincident with the associated pulsars in Table 5.2, while HGPSC 041, 046 and 091 are detected in the 2HGPS with similar morphologies as in the HGPS. This is an interesting occurrence because the 2HGPS is based on a spectro-morphological analysis and models the large-scale Galactic diffuse emission using templates constructed from a cosmic-ray propagation and interaction model. It also uses more observation time than the HGPS. HGPSC 072 is labeled as HESS J1831−098 in Table 5.2, a source discovered by Sheidaei et al. (2011), and will be the subject of a dedicated analysis in Chap. 6.

Some components in Table 5.2 are found to be spatially coincident with pulsars younger than 40 kyr:

- **HESS J1841−055** is a complex region, with the source comprising two 2D Gaussian components and the presence of a younger and more energetic PSR J1841−0524 (30.3 kyr).
- **HGPSC 063** is spatially coincident with PSR J1813−1749 (5.5 kyr) of the firmly identified PWN HESS J1813−178. This "Discarded Large" component (with a 1σ extension of $\sim 0.3°$) was recently re-analyzed and interpreted as possibly resulting from the contribution of escaped particles from the identified PWN (H.E.S.S. Collaboration 2024b). Thus, in this work we consider HGPSC 063 to be a component of the firmly identified PWN HESS J1813−178 (as indicated in Table 5.2).
- **HGPSC 015** is coincident with the additional two younger and more energetic pulsars J1410−6132 (24.8 kyr) and J1413−6141 (13.6 kyr). A more detailed view on this complex region has been explored in the H.E.S.S. analysis of Chambéry et al. (2024).
- **HGPSC 051** is coincident with the younger (25.5 kyr) and more energetic PSR J1747−2958.
- **HGPSC 091** is coincident with PSR B1853+01 (20.3 kyr) of the SNR W44. HGPSC 091 is not morphologically compatible with W44, the study of which is an on-going project in the H.E.S.S. Collaboration.

5.2 Associations with 1LHAASO sources

Since it began operation, the LHAASO observatory has shown that pulsar-powered sources contribute to the UHE γ-ray sky, such as the case of the Crab PWN (LHAASO Collaboration 2021). The recent 1LHAASO catalog (Cao et al. 2024b) comprises 90 sources, 43 of which are significant above 100 TeV. Additionally, one half of the UHE sources (21) are associated with energetic pulsars. Our motivations for searching for pulsar associations with 1LHAASO sources are the following:

- Find extended components that were not detected in the HGPS, which could be produced by escaped $e^{-/+}$.
- Motivate dedicated analyses of sources detected over a large energy band (VHE to UHE), allowing for stronger constraints on physical models.
- Motivate additional H.E.S.S. observations towards 1LHAASO components without HGPS counterparts and coincident with energetic pulsars.
- Search for potential spatial associations between 1LHAASO components and the discarded components in the HGPS.

We conducted a search for spatial coincidences of ATNF pulsars with 1LHAASO components detected by the Kilometer Squared Array (KM2A, which surveys the sky at energies $\gtrsim$ 50 TeV). For a given KM2A-detected source, we searched for pulsars within 1.5 times the reported symmetric 2D Gaussian 1σ extension (roughly corresponding to the 68% containment). For unresolved sources, we used 1.5 times the reported 95% confidence interval upper limits on the extension. We restricted the search to pulsars with $\dot{E}/d_{PSR}^2 \geq 10^{34}$ erg/s/kpc^2, because 1LHAASO components can be highly extended, which could result in a large number of coincidences with a lighter constraint. In the region overlapped by both the HGPS and the 1LHAASO survey ($|b| \leq 3°$ and $10° \leq \ell \leq 65°$), there are 31 such pulsars. The search resulted in 21 KM2A sources that are spatially coincident with at least 1 energetic pulsar (8 of them are spatially coincident with 2 pulsars, 2 of them are spatially coincident with 3 pulsars, and one of them is spatially coincident with 5 pulsars). 15 of these are significant above 100 TeV. Table 5.3 shows the KM2A components that are spatially coincident with a pulsar which is in turn associated with a firmly identified or highly rated candidate H.E.S.S. PWN. The spectral compatibility between the KM2A and HGPS components is assessed by plotting the reported best-fit power law spectra in both catalogs. This is done to provide evidence supporting the associations. A spectral and positional compatibility indicates that the 1LHAASO component is probably the UHE counterpart of the H.E.S.S. PWN.

1LHAASO	HGPS	PSR	τ_c [kyr]	Spectral/Position compatibility
J1809−1918u	HESS J1809−193	J1809−1917	51.5	Yes/Yes
J1814−1719u	HESS J1813−178†	J1813−1749	5.6	Yes/Yes
J1814−1636u	"	"	"	No/No
J1825−1418	HESS J1825−137†	B1823−13	21.4	Yes/Yes
J1825−1337u	"	"	"	Yes/No
J1831−1028	HESS J1833−105†	J1833−1034	4.9	No/No
J1837−0654u	HESS J1837−069†	J1838−0655	22.7	Yes/Yes
J1848−0001u	HESS J1849−000†	J1849−0001	43.1	Yes/Yes
J1908+0615u	HESS J1908+063	J1907+0602	19.5	Yes/Yes
J1928+1813u	HESS J1930+188	J1930+1852	2.9	No/No

Table 5.3: KM2A sources associated with energetic pulsars and H.E.S.S. firmly identified (†) or highly rated candidate PWNe. If a KM2A source is associated with more than one pulsar, the pulsar shown in the table is the one associated to a H.E.S.S. firmly identified or highly-rated candidate PWN (H.E.S.S. Collaboration 2018f).

In Table 5.4, we show the HGPS halo candidates from section 5.1 that are visible to LHAASO, along with the KM2A components that are found to be spatially coincident with the corresponding pulsars. 1LHAASO components that are spectrally/positionally

compatible with a firmly identified H.E.S.S. PWN (cf. Table 5.3) are not considered. The HGPS catalog does not provide spectral information on the discarded components, therefore we cannot assess their spectral compatibility with the 1LHAASO components. An exception is made for HGPSC 072 (HESS J1831−098), for which the spectrum is taken from a dedicated analysis (Sheidaei et al. 2011). Thus, 4 of the 7 HGPS halo candidates that are visible to LHAASO are associated and spectrally/positionally compatible with a KM2A component. As for PSR J1838−0549 / HESS J1841−055, we note that the source 1LHAASO J1841−0519 is coincident with the younger pulsar PSR J1841−0524 (30.3 kyr) mentioned in the previous section. HGPSC 091, 1LHAASO J1852+0050u and 1LHAASO J1857+0203u are highly extended components with positions that are offset by $\gtrsim 1.0°$, and thus we do not consider these as reliable associations.

HGPS	PSR	τ_c [kyr]	1LHAASO	Spectral/Position compatibility
HESS J1809−193	J1809−1917	51	J1809−1918u	Yes/Yes
HESS J1813−126	J1813−1246	43	J1813−1245	Yes/Yes
HESS J1841−055	J1838−0549	112	*	
HESS J1852−000	J1853−0004	288	*	
HESS J1912+101	J1913+1011	168	J1912+1014u	Yes/Yes
Discarded components				
HGPSC 072^{S} (HESS J1831−098) (1)	J1831−0941	56	*	
〃	J1831−0952	128	J1831-1007u	Yes/Yes
HGPSC 091^{L} (1)	J1857+0143 (1)	71	J1852+0050u	-/No
〃	〃	〃	J1857+0203u	-/No

Table 5.4: HGPS pulsar halo candidates visible to LHAASO and the spatially coincident 1LHAASO KM2A components. The table is separated between HGPS sources and discarded components. ^{L}: HGPS "Discarded Large". ^{S}: HGPS "Discarded Small". *: No 1LHAASO spatial coincidence with the pulsar.

Figure 5.1 shows the regions in the publicly available HGPS significance map (with a correlation radius of 0.2°) of the sources in Table 5.4 which are found to have a 1LHAASO counterpart. The maps are overlaid with the spatial components of the KM2A sources (green) and the HGPS sources (blue), and the pulsar positions (magenta). The shaded bands correspond to the 68% confidence on the 1σ extensions, and the circles/ellipses correspond to the 95% confidence on the centroid positions. For unresolved KM2A components, the 95% upper limit on the extension is shown in dashed circles. We also show the best-fit spectral models reported in the HGPS and the 1LHAASO catalogs for each source on the right. The HGPS spectra are plotted in the energy ranges reported in H.E.S.S. Collaboration (2018d) and Sheidaei et al. (2011) for HGPSC 072 / HESS J1831−098, while the 1LHAASO spectra start at the reference energy of 50 TeV. The 1σ statistical uncertainty is represented by a shaded band. The HGPS spectra shown are the ones extracted in the R_{Spec} region defined in H.E.S.S. Collaboration (2018d), and the HGPSC 072/HESS J1831−098 spectrum was extracted in a 0.3° region around the source's position in Sheidaei et al. (2011). For HESS J1912+101, the KM2A component of 1LHAASO J1913+1014u coincides with the shell's radius and we considered it positionally compatible as indicated in 5.4.

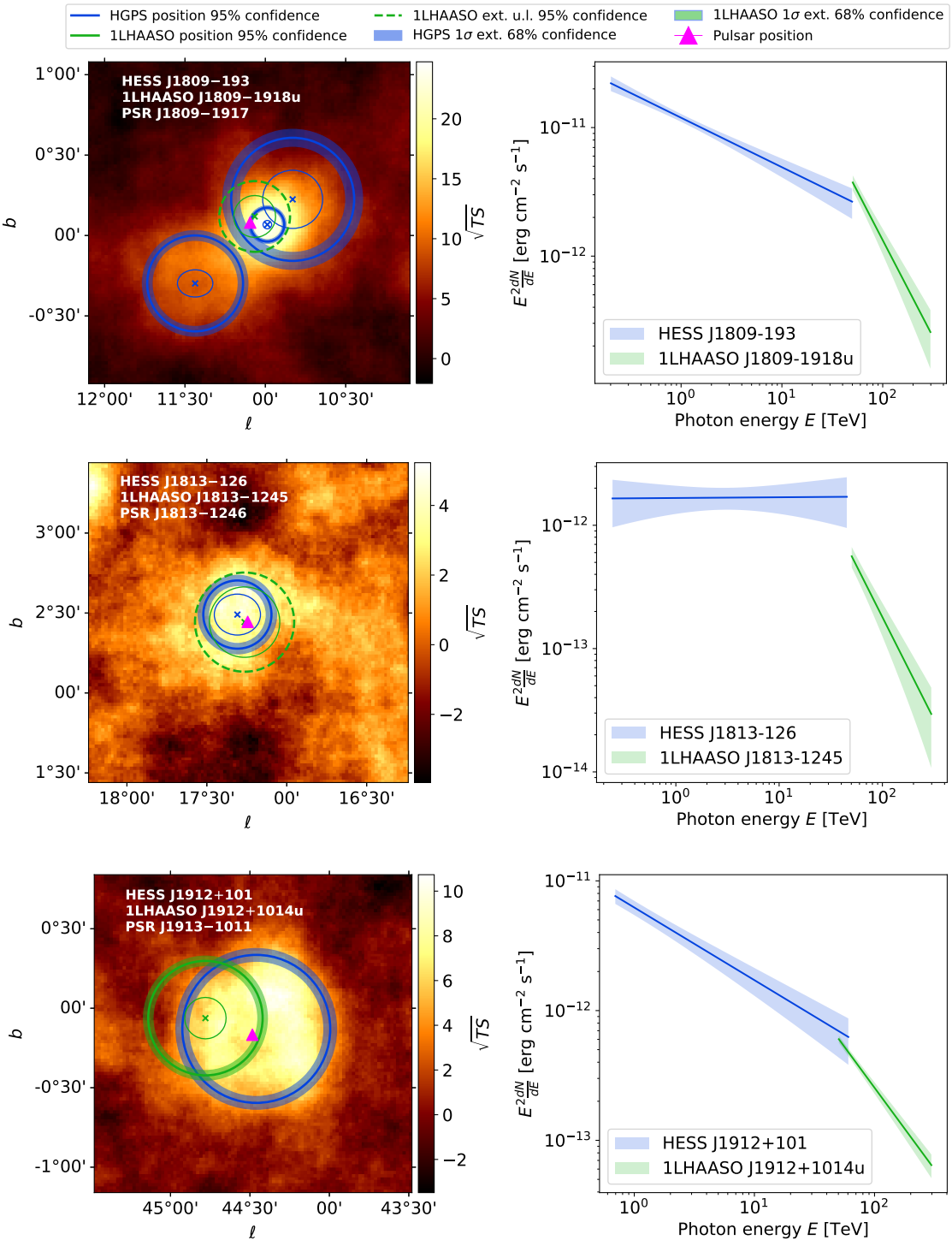

Figure 5.1: **Left:** HGPS 0.2° correlation radius significance map, overlaid with the HGPS (blue) and 1LHAASO KM2A (green) source components. The associated pulsars' positions are shown in magenta. Multiple HGPS components are shown if the source is modeled as such. The shaded bands represent the 68% confidence intervals of the 2D Gaussians' 1σ extensions. The circles/ellipses represent the 95% confidence on the positions. If the 1LHAASO component is unresolved, the 95% upper limit of the extension is shown with dashed lines. The blue HESS J1912+101 component's shaded band corresponds to the 68% confidence interval of the shell's radius. **Right:** HGPS (blue) and 1LHAASO KM2A (green) power law spectral models. The shaded band represents the 1σ statistical uncertainty. **Top to bottom:** HESS J1809−193, HESS J1813−126, HESS J1912+101, HGPSC 072 "Discarded Small"/HESS J1831−098 (continued).

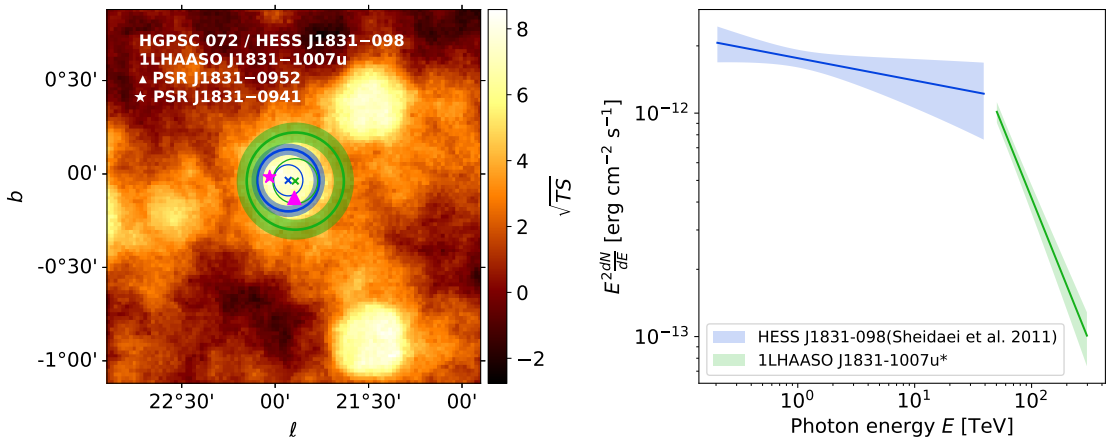

Figure 5.1 (continued): The H.E.S.S. SED shown for HGPSC 072/HESS J1831−098 was taken from Sheidaei et al. (2011).

5.3 Comparison with pulsar halo candidates in the literature

In Table 5.5, we compiled a list of pulsar halo candidates sorted by characteristic age, along with the Geminga and Monogem halos, that were published in dedicated analyses by the HAWC, LHAASO or H.E.S.S. collaborations. Fig. 5.2 shows τ_c vs. P for the

Pulsar name	Reference	P [ms]	τ_c [kyr]	d_{PSR} [kpc]
B0656+14	HAWC (Monogem)	385.0	111.0	0.29
J0633+1746	HAWC (Geminga)	237.0	342.4	0.25
J0248+6021	LHAASO J0248+6021 (Cao et al. 2025)	217.1	62.4	2.00
J0359+5414	HAWC (Albert et al. 2023)	79.4	75.2	
J0622+3749	LHAASO J0621+3755 (Aharonian et al. 2021)	333.2	207.7	
B0540+23	HAWC J0543+233 (Riviere et al. 2017)	246.0	252.7	1.60
B1055−52	H.E.S.S. (Wach & Mitchell 2025)	197.1	534.9	

Table 5.5: Pulsar halo candidates published in dedicated analyses by the HAWC, LHAASO and H.E.S.S. Collaborations. The table distinguishes between the canonical halos of the Monogem and Geminga pulsars, and the candidate halos proposed in the literature.

H.E.S.S. firmly identified and highly rated candidate PWNe in blue, the HGPS pulsar halo candidates (cf. Table 5.2) as triangles, and the compiled halo candidates from the literature as diamonds, among all the pulsars in the ATNF catalog in the HGPS coverage ($260° \leq \ell \leq 65°$). If multiple pulsars are associated to the same HGPS halo candidate component, they are all shown. The present-day periods P of the candidates that resulted from our search are generally smaller than the halo candidates proposed in the literature (mostly by HAWC and LHAASO), and hence have a higher spin-down power $\dot{E}$. This is expected for two reasons. Firstly, in the context of a survey, H.E.S.S. can only detect pulsar halos that are sufficiently distant so that their extension is smaller than the instrument's field of view. This requires that the halos be brighter and associated with more powerful, younger pulsars. The second reason is that the pulsar halo candidates in Table 5.5 are determined as such based on their similarities with the two canonical halos around the Geminga and Monogem pulsars (through pulsar halo modeling), and based on the absence of multi-wavelength counterparts that could explain the emission.

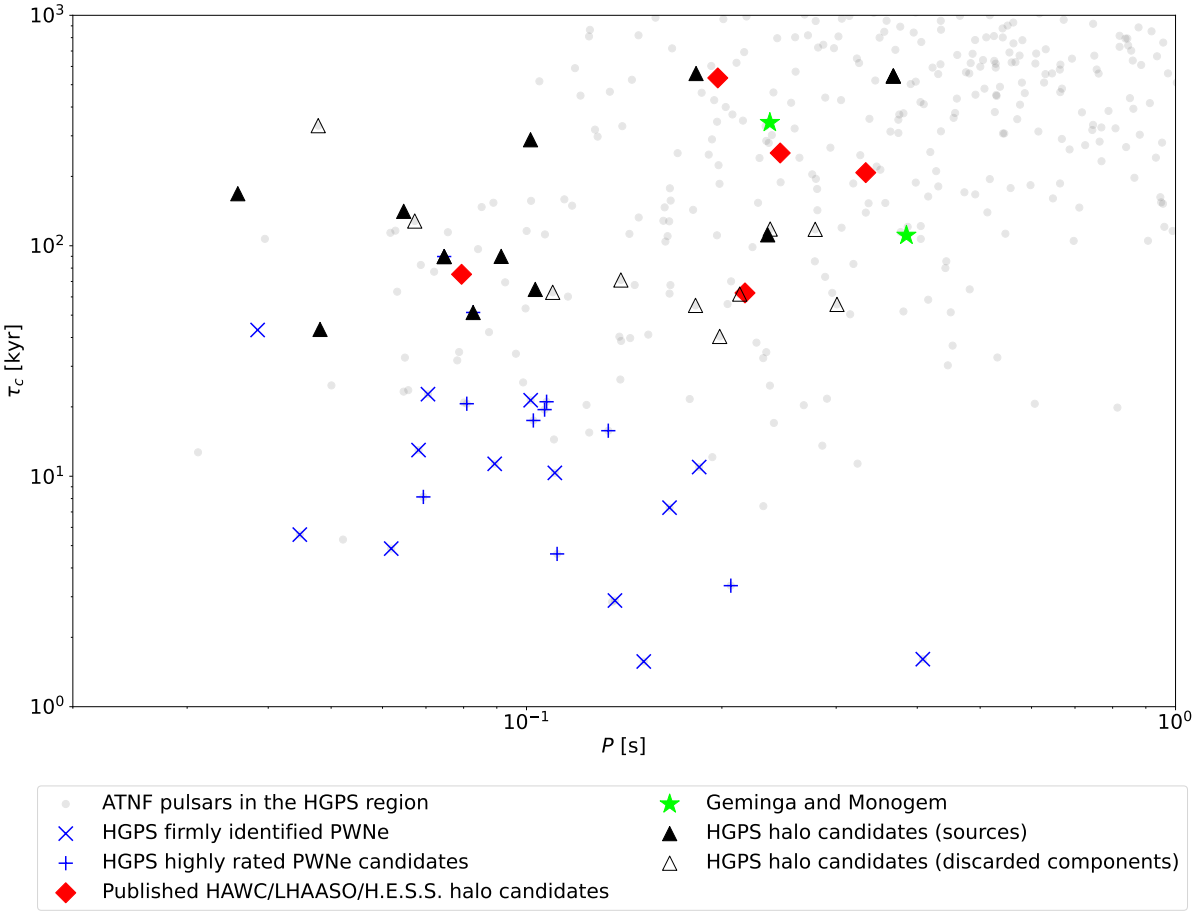

Figure 5.2: Characteristic age τ_c and present-day period P of the firmly identified HGPS PWNe (X), highly rated PWN candidates (+), known (lime stars) and candidate (diamonds) halos in the literature (diamonds), and the result of our HGPS search (triangles). The grey dots represent all ANTF catalog pulsars in the HGPS coverage.

5.4 Non-detected HGPS sources around energetic pulsars

We used the latest FITS H.E.S.S. data production, which contains observations from 2003 to 2021, with Gammapy version 1.2 to compute the acceptance-corrected live time Obs_t averaged in a 0.5° region around middle-aged pulsars ($\tau_c \geq 40$ kyr) with $\dot{E}/d_{PSR}^2 \geq 10^{34}$ erg/s/kpc^2 and $d_{PSR} \geq 1$ kpc. In Table 5.6, we show Obs_t for those that were not spatially coincident with any HGPS component (including discarded ones), and for which the acceptance-corrected live time is less than 40 hours. The cut on the pulsar distance was chosen because the halos of nearby pulsars may be too extended for the H.E.S.S. field of view. The 1LHAASO KM2A spatial coincidences resulting from the search in section 5.2 are indicated if they exist. In Eckner et al. (2023), the sensitivity of CTAO to pulsar halos was explored in detail. The last column of the table indicates their findings on the shown pulsar. "D" indicates that the potential halo could be detectable by CTAO, "M" indicates that an energy-dependent morphology could be detectable, E means that the detected extension of the halo is above 30 pc, and "C" means that the measured extent of the source is significantly different if the diffusion coefficient of the assumed halo is increased by 50%.

Pulsar name	P [ms]	τ_c [kyr]	$\dot{E}$ [10^{35} erg/s]	d_{PSR} [kpc]	Obs$_t$ [hr]	1LHAASO	Eckner et al. (2023)
B0740−28	166.8	157.1	1.4	2.0	4		DM
J0905−5127	346.3	220.7	0.2	1.3	10		D
B0906−49	106.8	112.0	4.9	1.0	27		DMEC
J1105−6107	63.2	63.2	24.8	2.4	28		DMEC
J1151−6108	101.6	156.7	3.9	2.2	13		DMC
J1429−5911	115.8	60.2	7.7	2.0	15		DMEC
J1437−5959	61.7	113.8	14.4	8.5	33		DMEC
J1925+1720	75.7	114.5	9.5	5.1	19	J1924+1609 (1)	DMEC
〃	〃	〃	〃	〃	〃	J1928+1813u (1)	〃
J1928+1746	68.7	82.6	16.0	4.3	21	J1924+1609 (2)	DMEC
〃	〃	〃	〃	〃	〃	J1928+1813u (2)	〃
〃	〃	〃	〃	〃	〃	J1928+1746u	〃
J1938+2213	166.1	62.0	3.7	3.5	23	J1937+2128	DMEC
B1951+32	39.5	107.2	37.4	3.0	1	*	DMEC
J1954+2836	92.7	69.4	10.5	2.0	12	*	DMEC

Table 5.6: Acceptance-corrected live time averaged in a 0.5° region around middle-aged pulsars with $\tau_c \geq 40$ kyr, $\dot{E}/d_{PSR}^2 \geq 10^{34}$ erg/s/kpc^2 and $d_{PSR} \geq 1$ kpc that were not spatially coincident with an HGPS component (including discarded components). Only pulsars with Obs$_t \leq 40$ hr are shown. *: Visible to LHAASO but not spatially coincident with a 1LHAASO KM2A component according to the search in section 5.2.

A noteworthy candidate, J1928+1746, which is spatially coincident with 1LHAASO J1928+1746u, was found to be a significant hotspot in the H.E.S.S. analysis presented in Abdalla et al. (2021). The extensions of 1LHAASO J1928+1813u and J1937+2128 are $\gtrsim 1°$, meaning they are subject to high systematic uncertainties due to the modeling of the Galactic diffuse emission and more information on these sources is required to assess their coincidence with the corresponding pulsars in Table 5.6. PSR B0740−28, J0905−5127, J1429−5911 and J1954+2836 are under investigation to be included in the proposals for the upcoming years of H.E.S.S. operation.

5.5 Conclusion

We searched for pulsar halo candidates among HGPS components through spatial coincidence with middle-aged energetic pulsars, having discarded H.E.S.S. sources that are firmly associated with non-pulsar halo scenarios, and built a comprehensive list of 20 HGPS sources which deserve deeper investigation through dedicated spectro-morphological analyses. The search includes components which were discarded in the HGPS analysis. Additionally, we found 4 viable associations between HGPS halo candidates, middle-aged pulsars and 1LHAASO KM2A components. A recent analysis was conducted in the case of HESS J1809−193 (H.E.S.S. Collaboration 2023b), suggesting that a halo of escaped $e^{-/+}$ may be the origin of a newly discovered elliptical component. A similar case was also found for HESS J1813−178 (H.E.S.S. Collaboration 2024b), where an extended component (HGPSC 063, which is a "Discarded" component in the HGPS) was re-analyzed and interpreted as possibly resulting from escaped leptons from the PWN. The HGPS pulsar halo candidates are generally younger than the halo candidates proposed in the literature by HAWC and LHAASO (but similar to the generic pulsar simulated in Chap. 7).

We highlighted 13 middle-aged pulsars with high enough distances and spin-down fluxes and without spatial coincidence with an HGPS component that could potentially be detectable by H.E.S.S. should they be allocated additional observation time.

Recently, a spectro-morphological analysis helped disentangle between the SNR shell and a candidate PWN component in HESS J0852−463/Vela Junior (Aharonian et al. 2026). Additionally, we propose HESS J1026−582 (in close proximity with Westerlund 2),

HESS J1718−385 (in close proximity with RX J1713.7−3947) and HESS J1745−303/HESS J1746−308 (in close proximity with the Galactic Center) as possible pulsar halo candidates, although their crowded regions and proximity with highly significant sources may render a dedicated analysis difficult. Conversely, HESS J1458−608, HESS J1852−000, HGPSC 072 (a.k.a. HESS J1831−098) and HESS J1813−126 are found in a relatively clean field of view. The latter two are likely associated with 1LHAASO J1831−1007u and 1LHAASO J1813−1245 based on their spectral and positional compatibility, and present the opportunity to constrain pulsar halo models in a wide energy band. In the next chapter, the results of a dedicated analysis of HESS J1831−098 using the pulsar halo template method (cf. Chap. 4) will be presented.

Chapter 6

HESS J1831−098: Exploring a pulsar halo scenario

Contents

6.1 Context **72**

6.2 H.E.S.S. data analysis **73**

6.3 Discussion **88**

6.1 Context

HESS J1831−098 is a very-high-energy (VHE) γ-ray source first detected by H.E.S.S. in 2011 with an extension of $\sim 0.15^\circ$ (Sheidaei et al. 2011). The source is coincident with a powerful middle-aged radio pulsar PSR J1831−0952 (Hobbs et al. 2004) with a characteristic age $\tau_c = 128$ kyr and a period $P = 67$ ms ($\dot{E} = 1.1 \times 10^{36}$ erg/s). More recently, a new radio pulsar PSR J1831−0941 (Turner et al. 2024) with $\tau_c = 56$ kyr and $P = 300$ ms ($\dot{E} = 1.2 \times 10^{35}$ erg/s) was discovered in VHE emission region. Both of these pulsars could plausibly power HESS J1831−098 through the creation of a pulsar wind nebula (PWN). Additionally, the 3HWC (Albert et al. 2020) and 1LHAASO (Cao et al. 2024b) catalogs contain sources spatially associated with the H.E.S.S. source. The source was first proposed as a pulsar halo candidate in Fang et al. (2022).

Due to a discrepancy in its detection significance between the main and the cross-check analysis chains, HESS J1831−098 was not included in the H.E.S.S. Galactic Plane Survey (HGPS) catalog as a new TeV source (H.E.S.S. Collaboration 2018d). It is a "Discarded Small" component named HGPSC 072 (cf. Chap. 5). We reanalyzed HESS J1831−098 using the following methods with the Gammapy library (Donath et al. 2023; Acero et al. 2024): a template background approach (Mohrmann et al. 2019), spectro-morphological likelihood analysis, and using templates of gas tracers to account for the large-scale Galactic diffuse emission. These methods are appropriate for extended (and possibly confused) sources near the Galactic plane.

Given the characteristic age of PSR J1831−0952 and according to the definition in Giacinti et al. (2020) of a pulsar halo, we propose an interpretation of the VHE emission as Inverse Compton Scattering (ICS) of electrons and positrons escaping the PWN and diffusing in the interstellar medium (ISM). To that end, we adopted a commonly used

model of the Geminga and Monogem (PSR J0633+1746 and PSR B0656+14) pulsar halos (and other candidates) within the Gammapy modeling framework.

The region around HESS J1831−098 is shown in Fig. 6.1 with the significance map of the HGPS overlaid with the HGPS source components (and the Discarded Small component HGPSC 072). The left panel shows the names of different HGPS components in the field of view. The right panel shows the positions of the pulsars associated with HESS J1831−098. The 68% confidence intervals on the source extensions are shown in shaded bands and the 95% confidence intervals on their positions (crosses) are shown as ellipses.

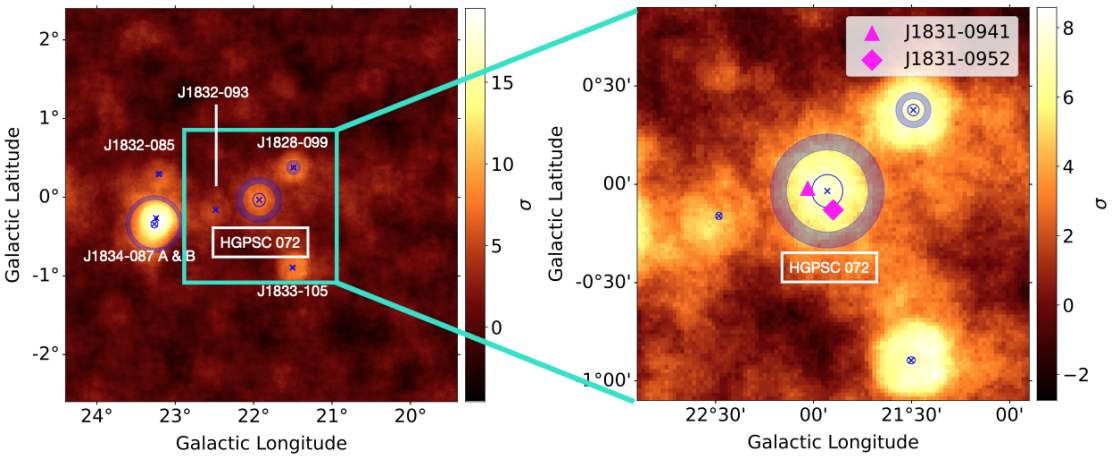

Figure 6.1: HGPS significance map with a correlation radius of 0.2° showing HESS J1831−098 (or HGPSC 072) in the HGPS. The panel on the left shows the HESS sources in the region that will included in the model and fitted. The panel on the right is a zoom-in on HESS J1831−098, showing the positions (magenta) of PSR J1831−0952 (diamond) and PSR J1831−0941 (triangle). In both panels, the shaded bands represent the 68% confidence intervals on the extensions of the sources in the HGPS, and the ellipses represent the 95% confidence intervals on the source positions (crosses).

6.2 H.E.S.S. data analysis

6.2.1 Observation selection and run-wise background normalization

The analysis was conducted using the DL3 data production HAP-FR Prod 4 (ash-stereo calibration) with the Background model v3. We selected H.E.S.S. observations taken between 2003 and 2016 in a 3° radius around the position of PSR J1831−0952 ($\ell = 21.9°$, $b = -0.1°$), and excluded observations with zenith angles $> 45°$. These runs correspond to HESS I runs taken before the camera upgrades. Events are selected such that they fall within 2° of the pointing direction, with an energy such that effective area is above 20% of the maximum effective area, or higher than the background rate peak energy. The events of each observation are binned in a $4° \times 4°$ event cube with a pixel size of 0.02° and a reconstructed energy axis from 0.5 TeV to 100 TeV (8 bins per decade). The true energy axis covers 0.1 TeV to 200 TeV (20 bins per decade). The Field of View background method is used, such that the residual hadronic cosmic-ray (CR) background is modeled with templates built from off-source regions (using extragalactic observations), and re-normalized with background events in each observation following the method in

Mohrmann et al. (2019) outside a masked region which includes known HGPS sources and the Galactic plane. The background is re-normalized with a power law function of energy with free norm and tilt. The distribution of the fitted PL norms and tilts for all observations is shown in Fig. 6.2, where the mean and standard deviation are indicated. Only observations with a fitted background norm between 0.7 and 1.5 and a fitted background tilt between -0.3 and 0.3 are included in the analysis (a total of 7 observations were excluded because of this criterion). Observations around $\ell = 19°$ targeting HESS 1826−130 were excluded. This yields a total of 123 observations, with an effective on-source live time of $\sim$ 45 hours within a 0.5° radius from the position of PSR J1831−0952.

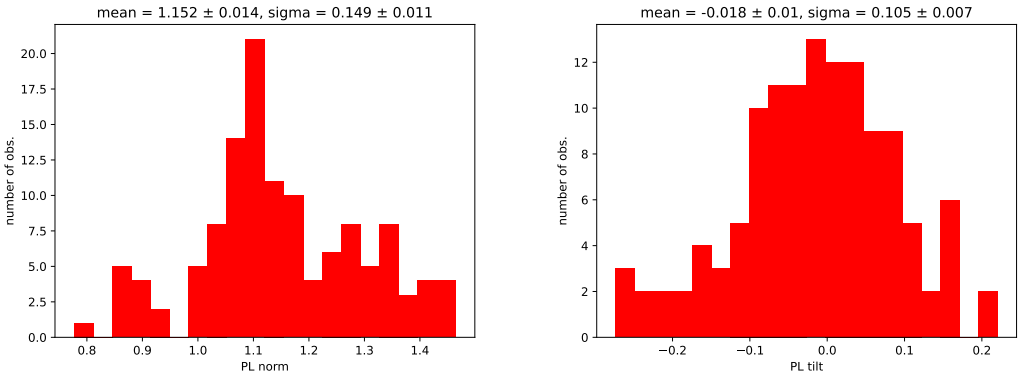

Figure 6.2: Fit results of the run-wise background normalization for all observations. **Left:** Distribution of the fitted PL norm . **Right:** Distribution of the fitted PL tilt.

The event cubes of each observation are then stacked together by averaging the Instrument Response Function (IRF) cubes and summing the background cubes. This dataset encompasses a 6° × 6° region with a pixel size of 0.02°, covering reconstructed event energies from 0.5 TeV to 100 TeV (8 bins per decade), and true energies from 0.1 TeV to 200 TeV (20 bins per decade). The spatial residual significance map of the background fit is shown in Fig. 6.3. The background is globally well reproduced, and the spatial residuals were checked in different energy ranges.

6.2.2 Spectro-morphological modeling

We conducted a 3D likelihood analysis (in space and energy) by optimizing a spectro-morphological multi-component model. Assuming a constant CR density across the FoV, the large-scale Galactic diffuse emission due to neutral pion decay traces interstellar gas. We used the Planck Dust Opacity at 353 GHz map (Planck Collaboration 2011), shown in Fig. 6.4, as a proxy of the spatial gas distribution, multiplied by a spectral power law (PL):

$$\frac{dN}{dE} = N_0 \left(\frac{E}{E_0}\right)^{-\alpha} \tag{6.1}$$

with the normalization N_0 in $\mathrm{TeV}^{-1}\ \mathrm{cm}^{-2}\ \mathrm{s}^{-1}$ and the index α free to vary. We note that all of the results shown (i.e. HESS J1831−098 modeled as a 2D Gaussian or with a pulsar halo model involving PSR J1831−0952 with and without proper motion) are statistically consistent when using the CO map of Dame et al. (2001) instead of the dust opacity map, as shown in Fig. A.1 of the appendix. To account for systematic uncertainties introduced

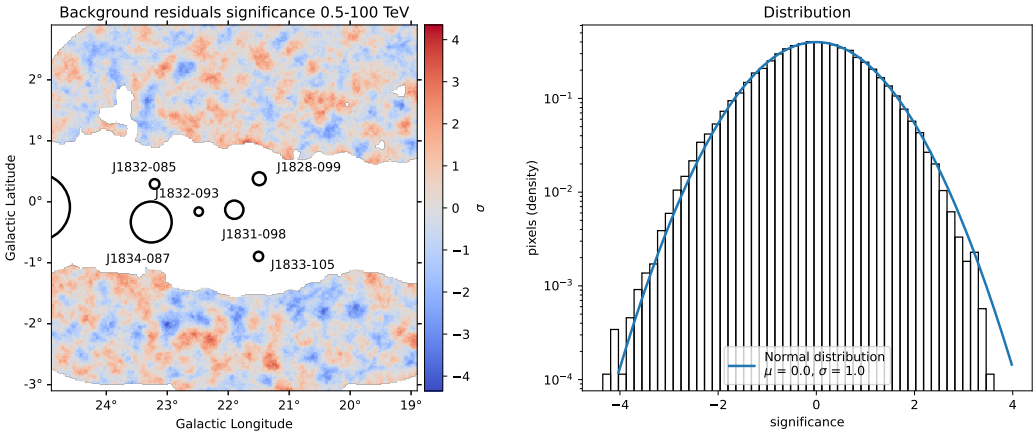

Figure 6.3: **Left:** Background fit residual significance map outside the exclusion mask in the 0.5−100 TeV band with a correlation radius of 0.15°. The spectral extraction radii used in the HGPS for the sources in the FOV are shown as circles (for HESS J1831−098, we show the extension reported by Sheidaei et al. (2011)). **Right:** Residuals distribution.

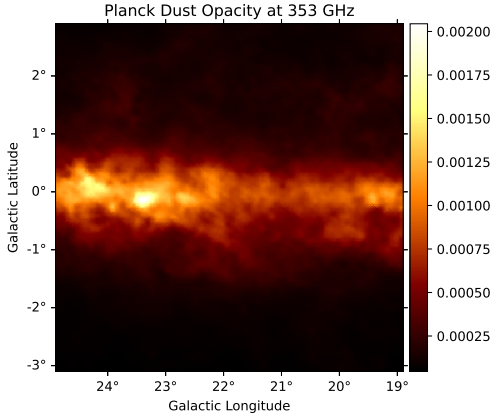

Figure 6.4: Planck dust opacity map at 353 GHz (Planck Collaboration 2011).

by stacking the background cubes, the background model is re-normalized using a piece-wise correction up to the 8.13 TeV energy bin, such as a normalization is independently fitted in each energy bin, and then a power law with free normalization and tilt up to 100.0 TeV (all normalization and tilt values are shown in Table A.1 of the appendix). The region of interest contains 5 known sources from the HGPS catalog in addition to HESS J1831−098, which we modeled spectrally with PLs and spatially with Gaussian or point-like models as indicated in Table 6.1. Adding an extension to sources that are modeled as point-like was found to be statistically insignificant, and the corresponding ΔTS values are shown in Table A.2 of the appendix.

HESS J1837−069 (towards the left side of the field of view) is masked and excluded from the fit. The spatial and spectral parameters of all components were simultaneously fitted, together with the hadronic residual background component and the large-scale Galactic diffuse emission. The optimization of the model is done by minimizing the associated Test Statistic (Cash 1979). The significance of HESS J1831−098 can be computed through hypothesis testing using Wilks' theorem (Wilks 1938). The results of the fit for all model components are shown in Table 6.2, and all sources' detection significance are shown in Table A.3 of the appendix.

Source name	Spatial model
HESS J1834−087 A	2D Gaussian
HESS J1834−087 B	2D Gaussian
HESS J1832−085	Point-like
HESS J1832−093	Point-like
HESS J1833−105	Point-like
HESS J1831−098	2D Gaussian
HESS J1828−099	2D Gaussian

Table 6.1: Spatial model for each source component in the field of view.

Component	N_0	α	σ [°]	ℓ [°]	b [°]
J1831−098	$(1.31 \pm 0.15) \times 10^{-12}$	2.15 ± 0.09	$0.204^{+0.034}_{-0.030}$	21.86 ± 0.03	-0.14 ± 0.03
J1828−099	$(5.82 \pm 0.78) \times 10^{-13}$	2.35 ± 0.13	$0.066^{+0.016}_{-0.014}$	21.50 ± 0.01	0.38 ± 0.02
J1833−105	$(3.31 \pm 0.48) \times 10^{-13}$	2.32 ± 0.15	-	21.509 ± 0.002	-0.89 ± 0.01
J1832−093	$(1.53 \pm 0.40) \times 10^{-13}$	2.35 ± 0.13	-	22.470 ± 0.001	-0.16 ± 0.01
J1832−085	$(2.27 \pm 0.51) \times 10^{-13}$	2.38 ± 0.22	-	23.22 ± 0.01	0.32 ± 0.01
J1834−087 A	$(3.97 \pm 0.68) \times 10^{-13}$	2.49 ± 0.14	0.005 ± 0.003	23.24 ± 0.01	-0.267 ± 0.001
J1834−087 B	$(2.28 \pm 0.18) \times 10^{-12}$	2.54 ± 0.08	0.160 ± 0.010	23.25 ± 0.02	-0.38 ± 0.02
Dust template	$(2.95 \pm 0.12) \times 10^{-11}$	2.43 ± 0.04	-	-	-

Table 6.2: Best-fit spatial and spectral parameters of the components included in the model (with the reference energy E_0 fixed to 1 TeV). N_0 is in units of $\mathrm{TeV}^{-1}\ \mathrm{cm}^{-2}\ \mathrm{s}^{-1}$. σ represents the radial extension of the 2D Gaussian components.

In Fig. 6.5, the significance map of the excess after subtracting all components except HESS J1831−098 is shown. The map is computed in the 0.5 − 100 TeV range with a correlation radius of 0.15°. In the left panel, the fitted positions of point-like sources are shown with white crosses, while sources modeled with 2D Gaussian components are shown with white circles corresponding to the 1σ extensions. The right panel is the same map zoomed in on HESS J1831−098, showing the coincident pulsars' positions and overlaid with the fit results of the HESS J1831−098 and HESS J1828−099 spatial components in magenta. The shaded bands represent the components' 68% confidence interval (C.I.) on the extension and the ellipses represent the 95% C.I. on the components' positions (shown in crosses). A similar map to the right panel is shown for different energy bands in Fig. A.2 of the appendix. The spatial residual map and its distribution are shown in Fig. 6.6. The spatial residual distribution shows that the data is well reproduced and variations are consistent with the expectation from statistical fluctuations. HESS J1831−098 is detected with a significance of 7.7σ with 5 degrees of freedom (3 for the 2D Gaussian and 2 for the PL spectrum). Different spectral shapes (exponentially cut-off PL and log-parabola) for HESS J1831−098 were found not to significantly improve the likelihood, as shown in Table A.4 of the appendix.

A small anti-correlation is found between the extensions of HESS J1831−098 and HESS J1828−099 depending on the analysis chain that was used for the event reconstruction (in this case HAP-FR versus HAP-HD ImPACT). This is shown in more detail in Fig. A.4 of the appendix. Therefore, the errors on the extension shown in Table 6.2 and Fig. 6.5 for these two sources are computed by computing a likelihood profile instead of taking the values from the covariance matrix. For a given source, this involves re-fitting all model components' parameters for different values of the source's extension. The 68% C.I. on the scanned parameter (i.e. the extension) is such that the ΔTS worsens by less than $\sqrt{\Delta TS} = 1$. The profiles for the scans on the extensions of HESS J1831−098 and HESS J1828−099 are shown in Fig. 6.7. The vertical dashed grey lines (*inf* and *sup*)

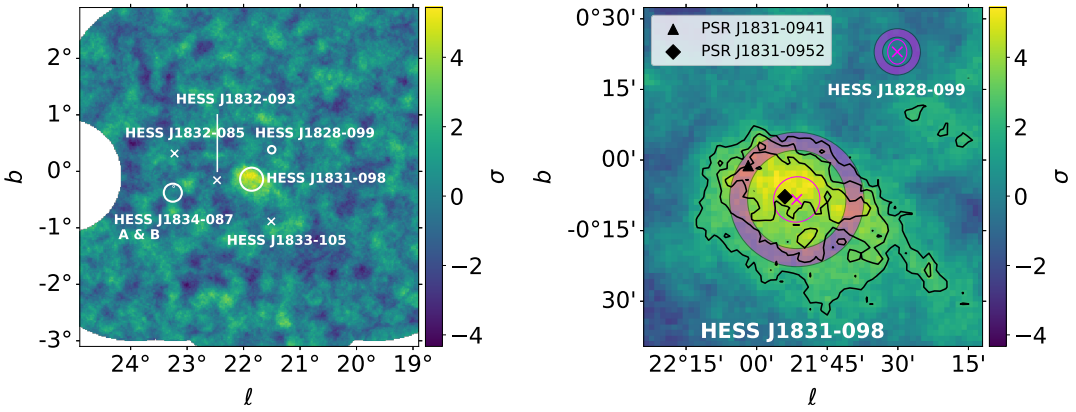

Figure 6.5: **Left:** H.E.S.S. significance map ($0.5 - 100$ TeV) with a correlation radius of $0.15°$ after subtracting a model containing the background, diffuse emission and all HESS sources apart from HESS J1831−098. Circles represent the 1σ extent of the 2D Gaussians, and crosses represent the positions of point-like sources. The masked left-most region excludes HESS J1837−069. **Right:** Zoom of the left panel, showing the coincident pulsars. The magenta bands represent the 68% confidence interval on the extensions, and the magenta circles the 95% confidence interval on the positions shown with crosses. The black contours are the 2-3-4 H.E.S.S. significance levels.

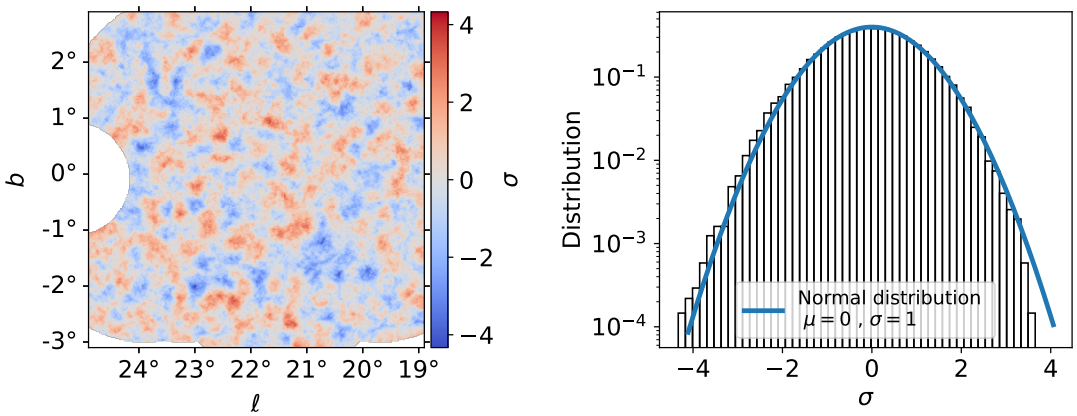

Figure 6.6: **Left:** Significance residual map ($0.5 - 100$ TeV) with a correlation radius of $0.15°$. **Right:** Normalized distribution of the map values on the left, compared with the expectation from statistical fluctuations (i.e. a standard normal distribution).

show the intersection between the profile and $\Delta TS = 1$ (i.e. the difference between the TS of the scanned value and the optimal value). The red dots represent scanned values where the fit did not formally converge, i.e. we are given Failure flag by the optimizer, but the resulting TS value and the profile are reasonable. The 68% C.I. on the extensions found with the likelihood profiles, which accounts for parameter (anti-)correlations, are significantly larger than those found through the covariance matrix (shown as black error bars in Fig. 6.7), which approximates the 68% confidence interval from the local curvature of the likelihood around the optimal value.

6.2.3 Comparison with the HGPS

We compared the spatial and spectral parameters of all source components with those found in the HGPS to check for consistency with previously published results. A map displaying the 68% C.I.'s of the extensions (shaded bands) and the 95% C.I.'s on the

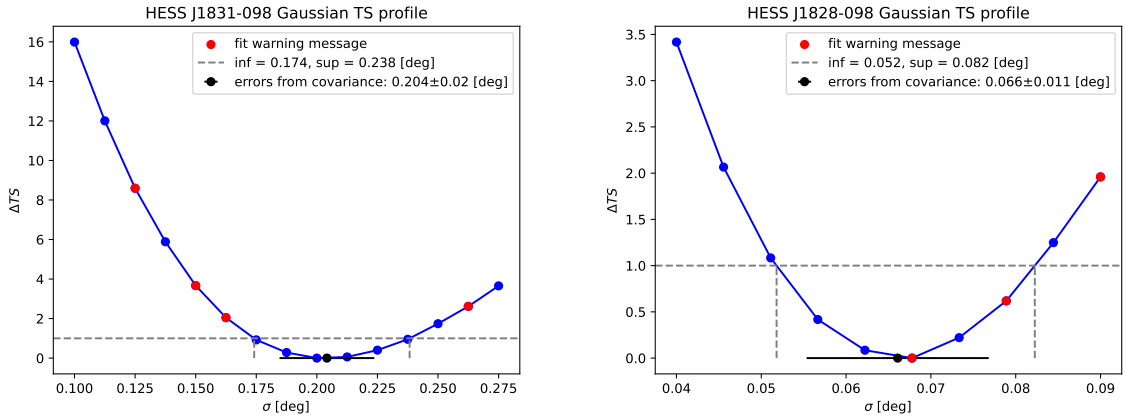

Figure 6.7: Likelihood profiles from scanning over the extensions of HESS J1831−098 (left) and HESS J1828−099 (right). *inf* and *sup* are shown with the vertical dashed lines correspond to the values at which the likelihood worsens by 1 compared with the optimal value. The red points correspond to scanned values where the fit did not converge properly. The black horizontal error bar represents the 68% confidence interval estimated from the covariance matrix (i.e. uncertainty propagation).

positions (crosses and ellipses) is shown in Fig. 6.8.

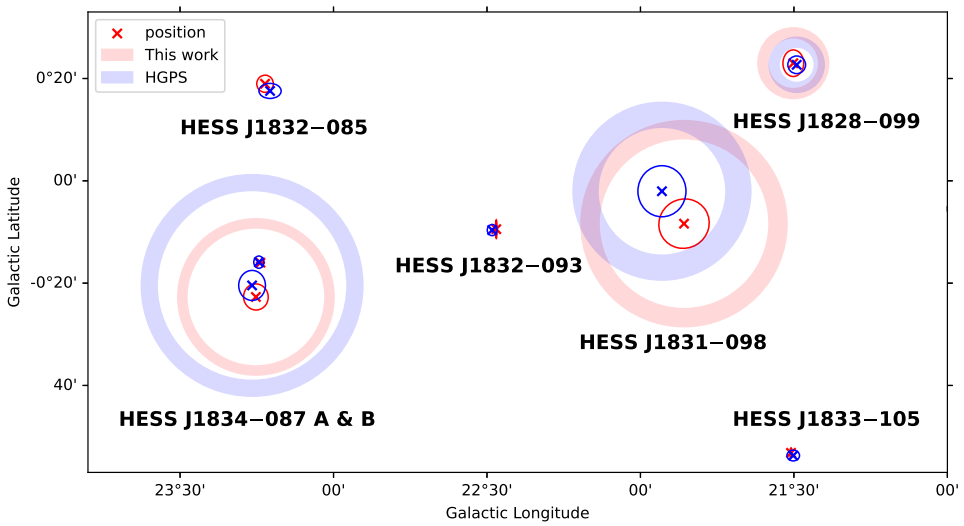

Figure 6.8: Comparison of all source components' spatial parameters between this analysis (red) and the HGPS (blue). The extension and position of HESS J1831−098 are compared with those of HGPSC 072. The shaded bands represent the 68% confidence on the source extensions (for 2D Gaussian components). The ellipses represent the 95% confidence on the positions (shown with crosses).

We explain the difference found between the HGPS and this work for the extended component of HESS J1834−087 (B) as being due to the differences in modeling the large-scale Galactic diffuse emission in our analysis and that of the HGPS. The latter uses a latitudinal Gaussian profile across the filed of view, while we use a gas tracer map as a proxy of γ rays from neutral pion decay between CR and interstellar gas nuclei. A peak in both the Planck dust opacity map and the CO map of Dame et al. (2001) can be found within the HGPS extension of HESS J1834−087 B (the more extended component). This

is also clear in the dedicated H.E.S.S. and Fermi-LAT analysis of this source in H.E.S.S. Collaboration et al. (2015), where it is shown that a peak in the Galactic Ring Survey ^{13}CO data (Jackson et al. 2006) lies at the same position as the peaks in the dust and CO maps we used. This is illustrated in Fig. 6.9 of the dust and CO maps, zoomed in at the position of HESS J1834−087 and overlaid with the HGPS (blue) and this analysis' (red) fitted spatial components. We also compared the best-fit spectral energy distribution

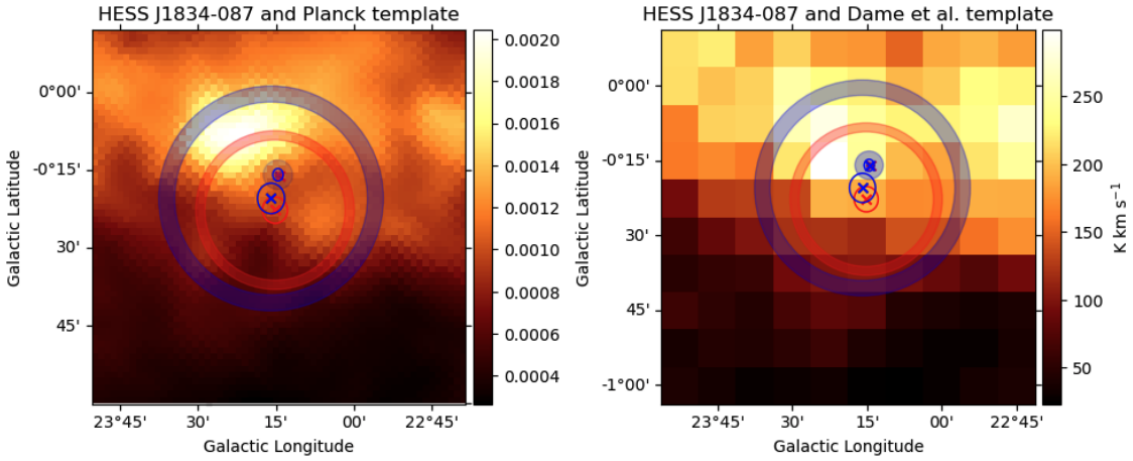

Figure 6.9: Planck dust opacity map at 353 GHz (left) and Dame et al. (2001) CO map (right) overlaid with the spatial components of HESS J1834−087 from the HGPS (blue) and this analysis (red). A peak can be seen in the gas and dust maps, which leads to a less extended source since this peak is accounted for by the template that is used in the fit.

(SED) obtained in this analysis for all the components in the region with that of the HGPS in Fig. 6.10. Each panel represents the fitted power law of a given source, with the grey bands showing the 68% confidence interval. The flux points are extracted by re-normalizing the fitted power law in each energy bin. The vertical error bars represent the 1σ error on the flux points. The upper limits are given at the 2σ level. Thus, the results in this analysis are statistically consistent with the results of the HGPS.

6.2.4 Halo template fitting

An alternative physically-motivated pulsar halo model involving PSR J1831−0952 was then tested, assuming that the VHE emission is fully due to ICS of pairs diffusing in the ISM, injected by a point-like PWN. The ISM environment is described by a constant magnetic field intensity and the ICS target radiation fields. We obtained the latter by fitting black-body components to the data provided in Popescu et al. (2017) at the pulsar's galactocentric position (cf. Table 6.3), as described in Chap. 4.

Optical	Near IR	Far IR
$T = 3252.76$ K	$T = 546.50$ K	$T = 38.92$ K
$U_{rad} = 2.30$ eV/cm^3	$U_{rad} = 0.54$ eV/cm^3	$U_{rad} = 1.06$ eV/cm^3

Table 6.3: Radiation field parameters at PSR J1831−0952's position computed using the data from Popescu et al. (2017).

We used a pulsar halo template as described in Chap. 4.2.2. The free parameters are the diffusion coefficient normalization D_0, the injection index Γ, the injection efficiency

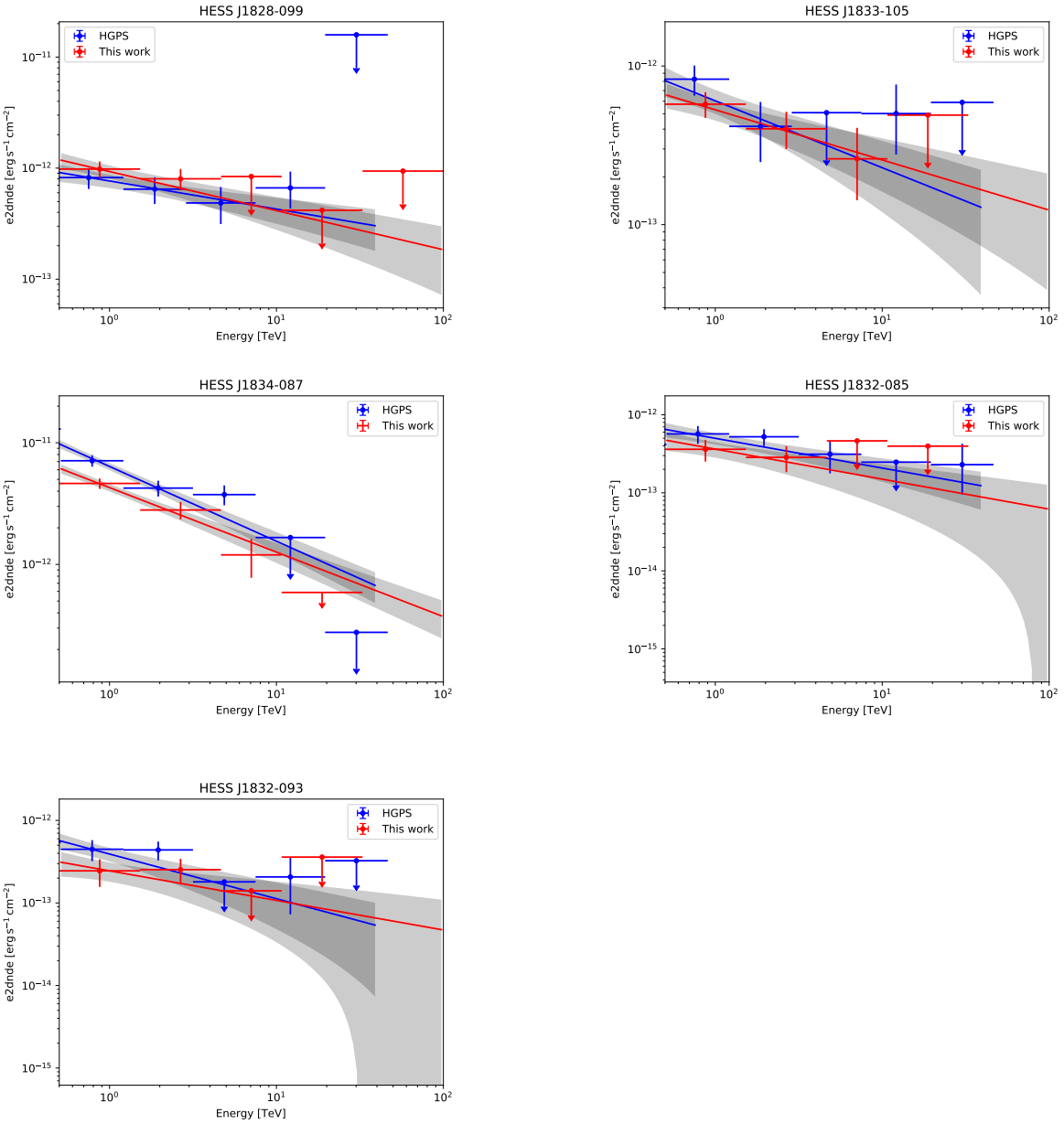

Figure 6.10: Comparison of source components' spectral parameters between this analysis (red) and the HGPS (blue). Each panel shows the fitted power law, the 68% confidence interval in grey shaded bands, and the extracted flux points with the vertical lines showing the 1σ error. The upper limits are given at the 2σ level.

η (which acts as a normalization) and the pulsar's birth period (i.e. initial period) P_0, which parametrizes the pulsar's true age. The position of the pulsar is fixed during the fit. The model templates are computed up to 200 pc away from the pulsar position. Table 6.4 summarizes the pulsar halo model parameters. The pulsar's measured parameters in the ATNF pulsar catalog are fixed. These are the present-day period P, the characteristic age τ_c, and the pulsar distance d_{PSR} which is estimated with the dispersion measurement and the free electron model of Yao et al. (2017). We assumed $\delta = 1/3$, $n = 3$, $B = 3$ μG, and $E_c = 1$ PeV. A scan will be conducted over E_c to attempt to constrain it. The addition of the proper motion to the pulsar is tested subsequently.

Model parameter	Value
Initial period P_0	Free [10 ms, P]
Injection index Γ	Free [0.5, 3.0]
Diffusion coefficient at 100 TeV D_0	Free [$1 \cdot 10^{26}$ cm^{2}s^{-1}, $9 \cdot 10^{28}$ cm^{2}s^{-1}]
Injection efficiency η	Free
Distance to pulsar d_{PSR}	3.7 kpc
Characteristic age τ_c	128 kyr
Braking index n	3
Present-day period P	67.0 ms
Injection cut-off energy E_c	1 PeV
Magnetic field strength B	3 μG
Rigidity dependence δ	1/3

Table 6.4: Pulsar halo model parameters for PSR J1831−0952. For the free parameters D_0, Γ and P_0, the number of points over which the templates are interpolated is indicated.

The pulsar halo model is fitted simultaneously with the other model components. Since the pulsar halo model's parameters are highly correlated, statistical errors are estimated at a 1σ confidence level from likelihood profiles of each parameter. To assess the statistical preference of the HESS J1831−098 pulsar halo model compared to a Gaussian × PL model, we used the Akaike Information Criterion. For two models $M1$ and $M2$, and assuming $M2$ has a better (lower) AIC score, $\Delta AIC_{M1,M2} = AIC_{M1} - AIC_{M2} = 2(k_{M1} - k_{M2}) + (TS_{M1} - TS_{M2})$ with k the number of degrees of freedom of the corresponding model.

The spatial residual significance map and its distribution after fitting the pulsar halo template is shown in Fig. 6.11 in the 0.5−100 TeV energy band with a correlation radius of 0.15°. The maps are overlaid with the source components' spatial models as black crosses for point-like sources and black circles for extended sources. The three dashed rectangles in the $0.5 - 100$ TeV map represent the regions from which the spectral residuals will be extracted. The north and south rectangles allow us to assess the quality of the fit in the "OFF" regions where no sources of γ-ray emission are expected, and the middle rectangle allows us to assess the quality of the fit in the "ON" region containing all the sources. The spectral residuals in the region within the middle rectangle are shown in the bottom panel of Fig. 6.11. The spatial and spectral residuals show that the model reproduces the data well. The number of predicted counts from the background model and the dust template model are compared to the total counts in the "ON" region in Fig. A.5 of the appendix.

The use of a pulsar halo template instead of a 2D Gaussian morphology for HESS J1831−098 does not impact the morphology and spectrum of the other sources in the region of interest. The fit results for all source components, for all the models we tested for HESS J1831−098, are shown in Tables A.5, A.6 and A.7 of the appendix. The best-fit parameters of the HESS J1831−098 pulsar halo are shown in Table 6.5 and are compared to those found for Geminga and Monogem by HAWC (Albert et al. 2024). We converted the HAWC D_0 values to a reference energy of 100 TeV.

A comparison of the differential photon spectra in the pulsar halo case (grey spectrum) and the 2D Gaussian × PL case (blue spectrum) of HESS J1831−098 is shown in Fig. 6.12. The spectrum of the spatially associated 1LHAASO J1831−1007u source (orange spectrum) is also shown. The shaded grey band associated with the pulsar halo photon SED corresponds to combinations of the free parameter values for which the model's likelihood is within 1σ of the optimal values. The likelihood for each pulsar halo

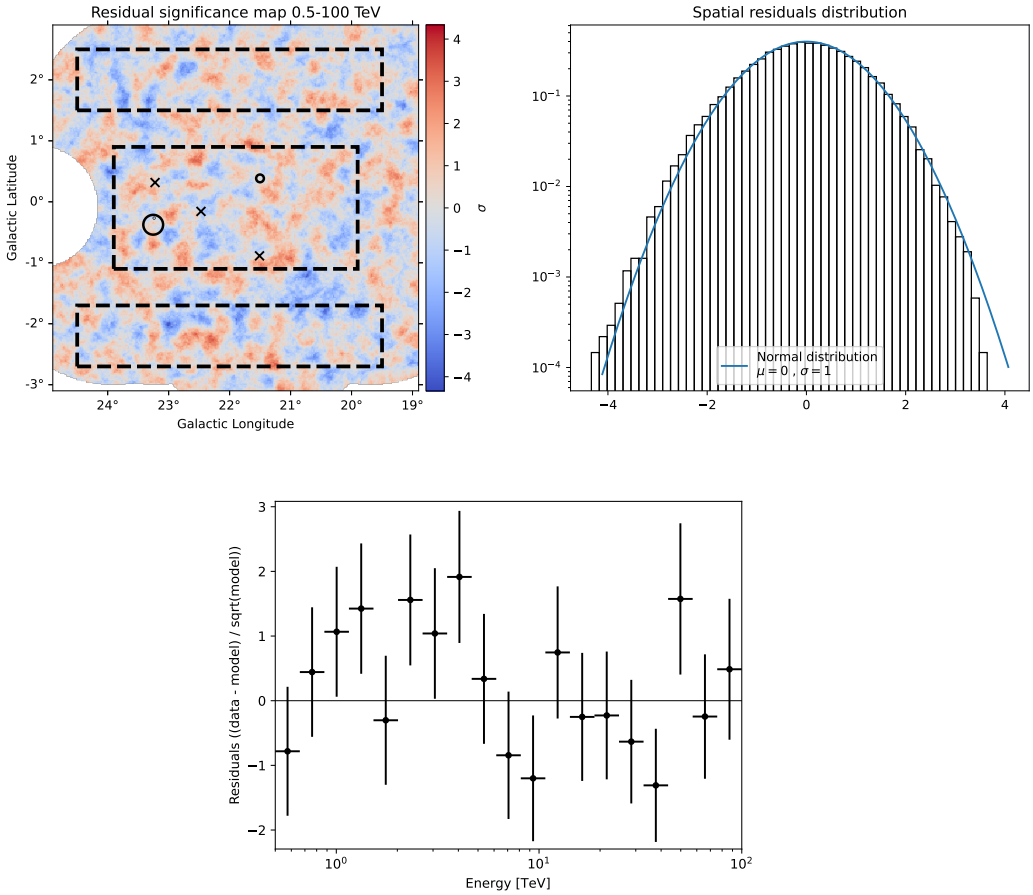

Figure 6.11: **Top left:** Residuals significance map (0.5−100 TeV, 0.15° correlation radius) of the model with HESS J1831−098 modeled as a pulsar halo. Crosses represent the positions of point-like sources. Circles represent the extensions (in 2D Gaussian σ) of extended sources. The dashed rectangles represent the regions from which the spectral residuals are extracted. **Top right:** Spatial residuals distribution, overlaid with a normal distribution which is expected from statistical fluctuations. **Bottom:** Spectral residuals extracted in the middle region shown in the top left panel.

Parameter	HESS J1831−098 (this work)	Geminga	Monogem
D_0 [10^{27} cm^{2}s^{-1}]	$3.35^{+7.66}_{-1.78}$	$4.97^{+3.38}_{-2.0}$	$6.82^{+6.97}_{-3.39}$
Γ	$1.90^{+0.38}_{-0.32}$	0.95 ± 0.32	1.06 ± 0.14
η	$0.043^{+0.141}_{-0.015}$	0.066 ± 0.025	0.051 ± 0.027
P_0 [ms]	$42.9^{+17.1}_{-15.9}$	-	-

Table 6.5: Fit results for HESS J1831−098 modeled as a pulsar halo, compared with HAWC's results for Geminga and Monogem (Albert et al. 2024). The statistical errors are given as the 68% confidence interval. For the HAWC results, we cite the systematic uncertainties because they are larger than the statistical uncertainties.

parameter combination is computed by re-fitting all model components' spectral parameters, while spatial parameters are kept frozen to the optimal values (this was done for computational efficiency). The pulsar halo model (4 degrees of freedom, $M2$) has a better (lower) AIC score than the Gaussian × PL model (5 degrees of freedom, $M1$), with $\Delta AIC_{M1,M2} \sim 2.1$, which is not high enough to reject the Gaussian × PL model model in favor of the halo model. We do not have enough statistics to discriminate between the surface brightness profile predicted by the Gaussian × PL model and the pulsar halo model, as shown in Fig. A.6 of the appendix.

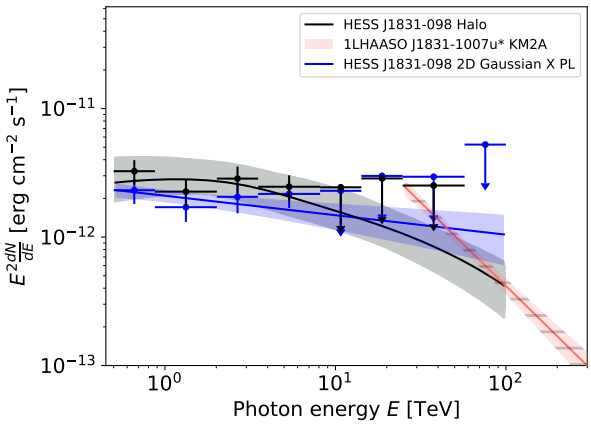

Figure 6.12: Fit photon SED and derived flux points of the pulsar halo model and the 2D Gaussian model for HESS J1831−098, and 1LHAASO J1831−1007u. The shaded bands represent the 1σ uncertainty on the fitted spectrum. The error bars are the 1σ uncertainty on the flux points. The upper limits are given at the 2σ level.

The pulsar halo model's parameters are highly correlated, as illustrated in Fig. 6.13, which shows the change of the likelihood (in Gaussian σ) from the optimal value with respect to two pulsar halo model parameters. These contours are computationally extensive to produce and therefore we computed them with a relatively low resolution. We note that not all of the points yielded a successful convergence of the fit, although for each panel this occurs in less than 27% of the points. Each point corresponds to a fit of all model components' parameters, maintaining the two scanned halo parameters fixed. The correlation between P_0 and D_0 is expected: a longer P_0 corresponds to a shorter true age, requiring a higher diffusion coefficient to reach the same size. The correlation between P_0 and η is also expected: a shorter P_0 means more energy injected (in the un-cooled part of the spectrum), requiring a lower efficiency to reach the same flux. It is unclear whether the correlation between η and D_0 can similarly be explained physically, or simply results from the correlations of P_0 with both η and D_0. The correlation between Γ and η is due to the normalization of the injection spectrum as evoked in Chap. 4. The likelihood profiles for each parameter are shown in Fig. 6.14, and the 68% C.I. on each of the pulsar halo parameters shown in Table 6.5 is computed accordingly.

6.2.5 Ultra-high-energy counterparts

The left panel of Fig. 6.15 represents the fitted components in this analysis when modeling HESS J1831−098 as a 2D Gaussian overlaid on a significance map of the excess after subtracting only the background and dust opacity template predicted counts. Point-like sources are shown as **x** symbols and extended sources are shown with black shaded bands and crosses representing the 68% confidence on the extensions and 95% confidence on the positions respectively. The map shows counterparts from the 3HWC and 1LHAASO catalogs. The position 3HWC J1831−095 (Albert et al. 2020) is shown as a blue cross and the 2D Gaussians of the 1LHAASO components in the field of view are shown as shaded bands and crosses (Cao et al. 2024b). These are 1LHAASO J1831−1007u's WCDA (purple) and KM2A (orange) components and 1LHAASO J1831−1024 which has a KM2A only. The derived photon SED of the pulsar halo is shown in the right panel of Fig. 6.15 and compared with those of the 1LHAASO components. The H.E.S.S., HAWC

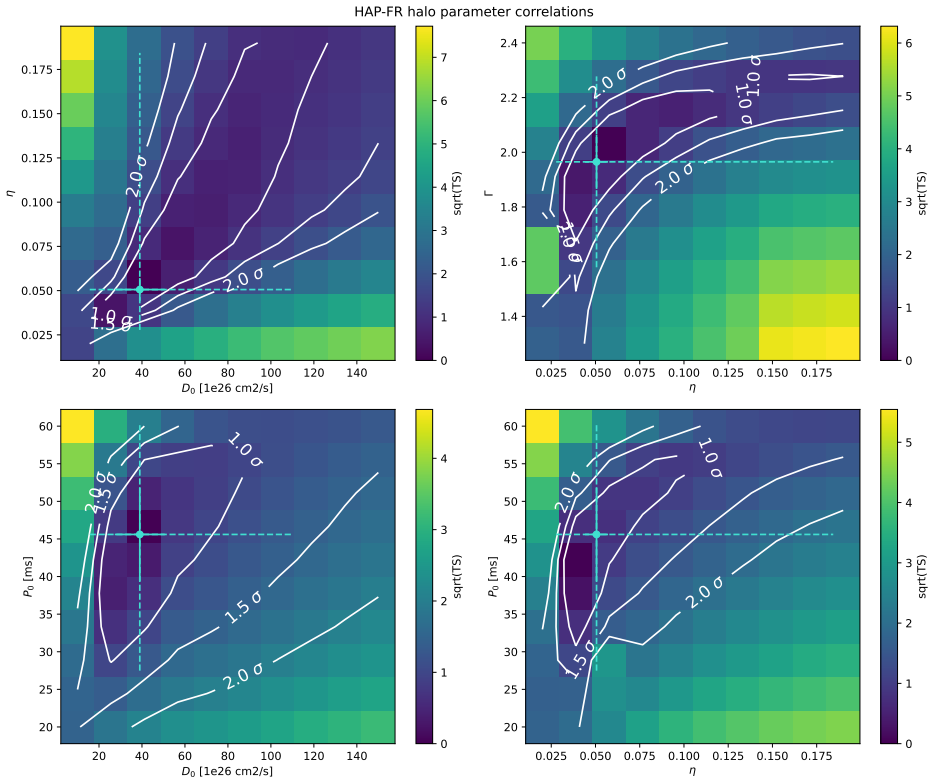

Figure 6.13: 2D confidence contours (1σ and 2σ levels) with respect to parameters that are found to be correlated. The cyan crosses represent the 68% confidence intervals approximated from the covariance matrix (solid) and those approximated from the likelihood profiles (dashed). **Upper left:** η vs. D_0. **Upper right:** Γ vs. η. **Lower left:** P_0 vs. D_0. **Lower right:** P_0 vs. η.

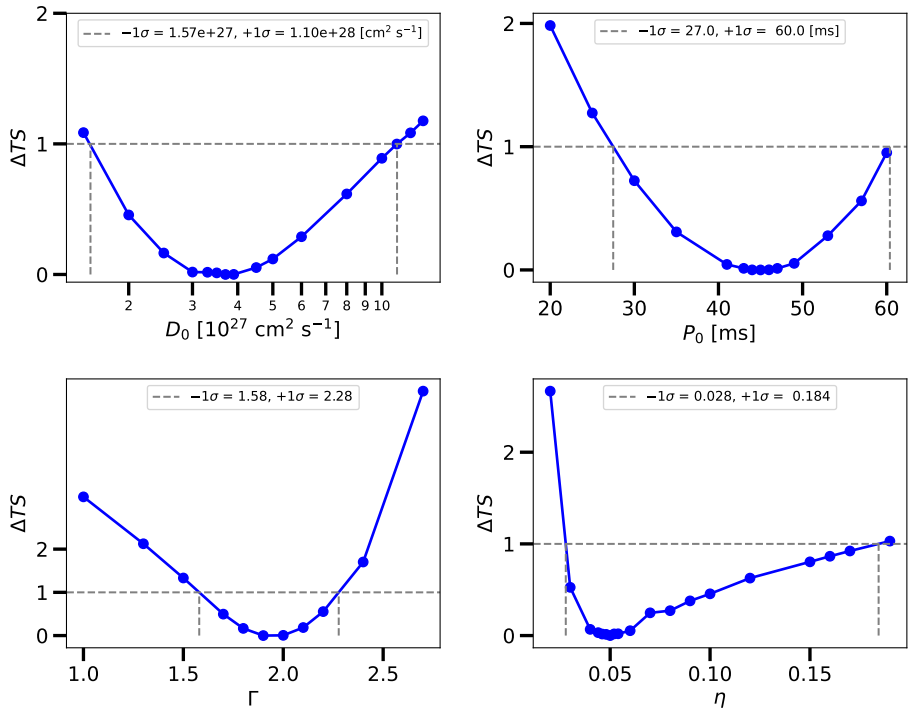

Figure 6.14: Likelihood profile scans for each free pulsar halo parameter. During the scan, the parameters of all model components except the one being scanned are free.

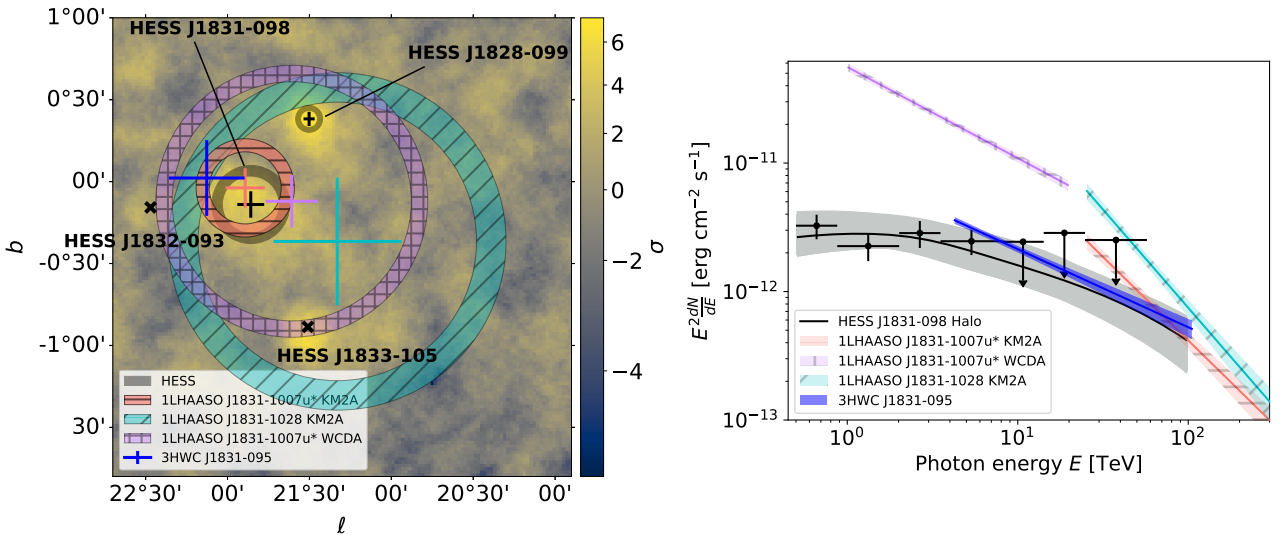

Figure 6.15: **Left:** H.E.S.S. significance map from $0.5 - 100$ TeV after subtracting a model containing the background and diffuse emission only, overlaid with our best-fit components and those reported in the 1LHAASO and 3HWC catalogs. The crosses indicate the 95% confidence interval on the positions. Shaded and hatched bands represent the 68% confidence interval on the Gaussian's 1σ extent. The **x** symbols are the H.E.S.S. point-like sources' positions. **Right:** Fit photon SED and derived flux points of the pulsar halo model, the 1LHAASO components and 3HWC J1831-095. The shaded bands represent the 1σ uncertainty. The upper limits are given at the 2σ level.

and LHAASO components are consistent both spectrally and spatially.

In the following sections, we present the constraints on the injection cut-off energy, the pulsar's proper motion, and a pulsar halo scenario involving PSR J1831−0941. These results are not yet cross-checked nor reviewed within the H.E.S.S. collaboration.

6.2.6 Constraints on the pulsar halo injection cut-off energy

The pulsar halo model was tested with different values of E_c: 30, 50, 100 and 300 TeV. The model is refitted for E_c fixed to each of these values. We find that the fit worsens by $\sim 1\sigma$ from the optimal value for $E_c = 30$ TeV. E_c seems to be correlated with Γ. Fig. 6.16 shows the best-fit values of Γ for different values of E_c and the corresponding TS of the halo model. The error bars on Γ represent the 68% confidence intervals estimated from the covariance matrix, and not the likelihood profile, and therefore may be larger in reality. The other free pulsar halo parameters are found to be statistically consistent for different values of E_c. Therefore, we find a lower limit of ~ 30 TeV on E_c at the 1σ level.

6.2.7 Halo template fitting with the pulsar proper motion

We tested the model with the pulsar proper motion $\mathbf{V}_{PSR}$. For computational reasons, this is done by scanning over different values of Γ instead of fitting Γ and $\mathbf{V}_{PSR}$ simultaneously. E_c is fixed to 1 PeV. The scan was done for $\Gamma = 1.9$, 2.0, 2.1, and 2.3. The best-fit value was found to be 2.0, and the optimal value is between 2.0 and 2.1. For $\Gamma = 2.0$, the parameters of other model components (i.e. other sources) are statistically consistent with the case without the proper motion. The addition of the proper motion improves

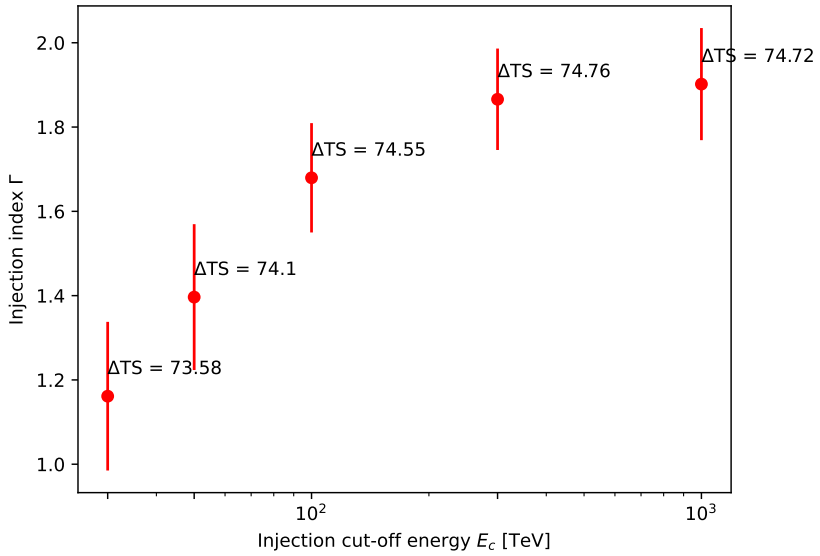

Figure 6.16: Fitted value of the injection index Γ for different values of the injection cut-off E_c. The best TS is found for $E_c = 300$ TeV, and the fit worsens by $\gtrsim 1\sigma$ at $E_c = 30$ TeV.

the likelihood by 2.1σ (Wilk's theorem with two degrees of freedom), and is therefore not very significant. We found $V_{PSR} = 377.5 \pm 188.0$ km/s and $V_{PSR,\theta} = -1.7° \pm 23.2°$, with $V_{PSR,\theta}$ taken clockwise from the increasing Galactic longitude direction. The other pulsar halo model parameters are statistically consistent with the case without proper motion. When compared with the symmetric 2D Gaussian case, when including the proper motion in the halo model, amounting to 6 degrees of freedom, we find $\Delta AIC = 4.9$ with the halo model having the better (lower) AIC score. Fig. 6.17 shows the spatial residual significance map and its distribution of the fit with the proper motion, and Fig. 6.18 shows the intensity map of the best-fit halo model with proper motion at three different photon energies (0.5, 1.0 and 10.0 TeV). A 2D Gaussian with ellipticity was tested, however this was found to be insignificant compared to a symmetric 2D Gaussian, only improving the likelihood by a value of 2.3.

6.2.8 PSR J1831−0941 scenario

PSR J1831−0941 (Turner et al. 2024) has a characteristic age $\tau_c = 56$ kyr, a present-day period $P = 300$ ms (making it roughly ten times less powerful than PSR J1831−0952) and a distance of $d_{PSR} = 4.2$ kpc from Earth. We fit the pulsar halo templates (with proper motion, to account for the offset of the emission centroid with the pulsar) with the values of τ_c, distance and the present-day period P in Turner et al. (2024) for PSR J1831-0941 (at Galactic coordinates $l = 22.03°$, $b = -0.02°$) and $E_c = 1$ PeV. We conducted a parameter scan to find the best-fit value of the injection index Γ, for values of [1.0, 1.5, 2.0, 2.2]. We found that among these values, the best-fit case ($\Gamma = 2.2$) corresponds to an injection efficiency η close to 100%, and thus do not test higher values of this parameter. The required injection efficiency makes the pulsar halo scenario (strictly assuming this model) unlikely for this pulsar because of its lower spin-down flux of 7.1×10^{33} erg/s/kpc^2. For the best-fit case that we tested ($\Gamma = 2.2$), the ΔAIC versus the 2D-Gaussian×PL model is 7.9. The TS of the halo model for different values of Γ and the fitted values of η

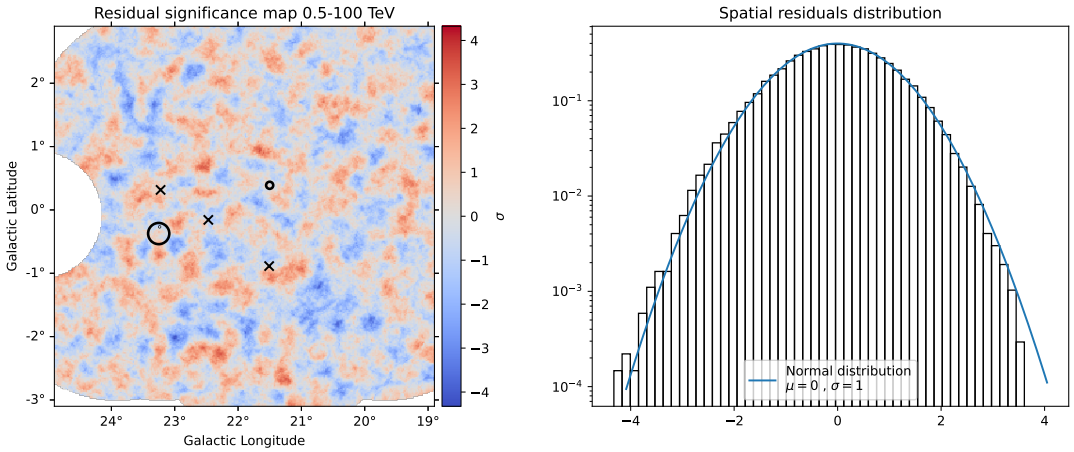

Figure 6.17: **Left:** Residuals significance map (0.5−100 TeV, 0.15° correlation radius) of the model with HESS J1831−098 modeled as a pulsar halo including the pulsar's proper motion transverse velocity. Crosses represent the positions of point-like sources. Circles represent the extensions (in 2D Gaussian σ) of extended sources. The dashed rectangles represent the regions from which the spectral residuals are extracted. **Right:** Spatial residuals distribution, overlaid with a normal distribution which is expected from statistical fluctuations.

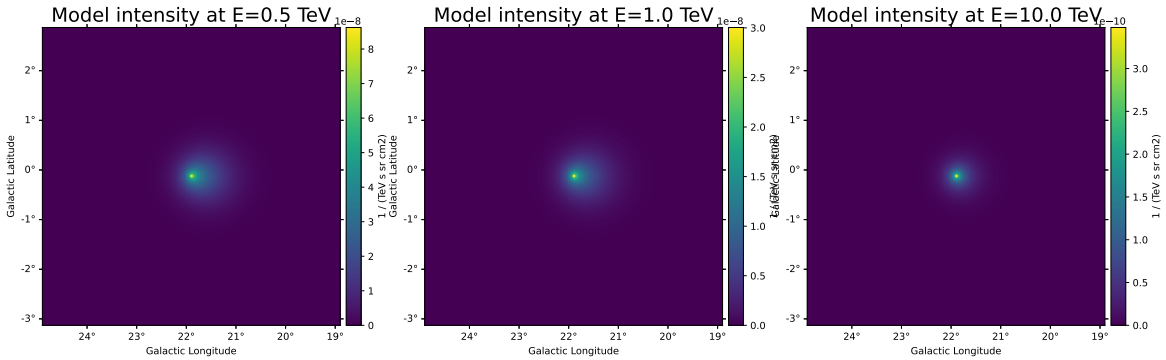

Figure 6.18: Best-fit pulsar halo model with proper motion intensity maps at 0.5, 1.0 and 10.0 TeV.

is shown in Fig. 6.19. The photon SED of the $\Gamma = 2.2$ case is shown in Fig. 6.20. Table 6.6 shows the fitted pulsar halo model values for the $\Gamma = 2.2$ case. We note, importantly,

Parameter	Value
D_0 [10^{27} cm^{2}s^{-1}]	5.46 ± 2.12
Γ	2.2 (frozen)
η	0.855 ± 0.142
P_0 [ms]	193.0 ± 12.0
V_{PSR} [km/s]	1284.3 ± 210.5
$V_{PSR,\theta}$ [deg]	31.2 ± 7.6

Table 6.6: Fit results for HESS J1831−098 modeled as the pulsar halo of PSR J1831−0941. The statistical errors are given as the 68% confidence interval.

that the assumed value of $E_c = 1$ PeV is higher than the allowed Hillas criterion limit of ~ 630 TeV derived in de Oña Wilhelmi et al. (2022), and testing different values of E_c, which might also yield lower injection efficiencies, is currently in progress.

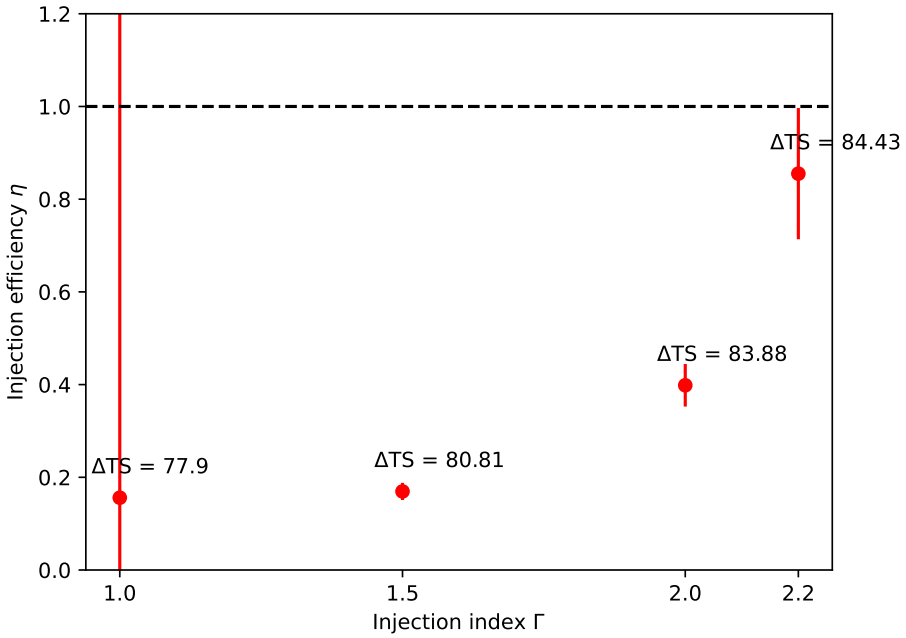

Figure 6.19: Fitted values of η and the TS values for different values of Γ for the pulsar halo scenario with PSR J1831−0941. The error bars represent the 68% confidence intervals computed from the covariance matrix. The horizontal dahsed line represents $\eta = 100\%$.

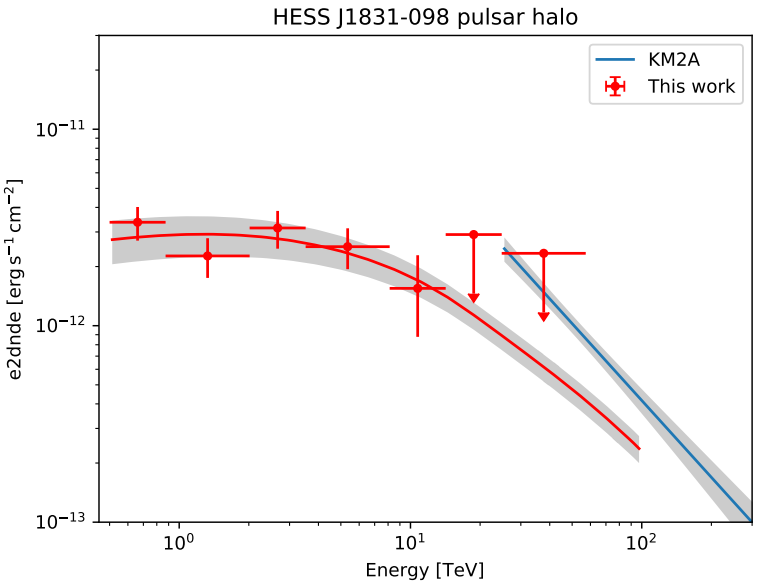

Figure 6.20: PSR J1831−0941 halo model photon spectrum for $\Gamma = 2.2$.

6.3 Discussion

The γ-ray emission can be well described by a pulsar halo model powered by PSR J1831−0952, although it is not significantly preferred over a Gaussian × PL model with a $\Delta AIC = 2.1$ in favor of the symmetric halo model fit. The best-fit diffusion coefficient of HESS J1831−098 is similar to that of the Geminga and Monogem pulsar halos. The estimated injection

efficiency, η, is plausible for a pulsar-powered source. The weaker constraint on the upper bound ($\sim 3 - 20\%$) of this parameter is due to its correlation with P_0. The true age of the pulsar, which we estimated as $75.5^{+31.7}_{-50.2}$ kyr (68% C.I.), determines the contribution to the photon SED by relic $e^{-/+}$. Consequently, P_0 strongly impacts the photon SED at energies roughly below the energy where the particle cooling time is equal to the pulsar's true age. For the optimal value of P_0, this energy corresponds to ~ 7.5 TeV. The difference in the values of the injection index Γ between HESS J1831−098 and those of Geminga and Monogem could be due to a correlation with the injection cut-off, which is different in the HAWC analysis ($E_c = 100$ TeV). The inclusion of the proper motion in the model was not significant, improving the likelihood by 2.1σ (with 2 degrees of freedom).

When the injection cut-off of the halo (powered by PSR J1831−0952) is assumed to be $E_c = 1$ PeV, we found a very good spatial and spectral consistency between between HESS J1831−098 and the KM2A component of 1LHAASO J1831−1007u*, which is reportedly significant above 100 TeV. Further, considering the systematic uncertainties discussed in Albert et al. (2020) in this region, 3HWC J1831−095 could be spatially compatible with HESS J1831−098.

We computed the average energy density in $e^{-/+}$ derived from the fitted halo model. For the optimal values, the average in a volume corresponding to the fitted Gaussian's 68% containment (for comparison with Giacinti et al. (2020)) is 0.24 eV cm^{-3}. This value is higher than the magnetic field's energy density, however a lower injection cut-off energy could yield a lower particle energy density. In the $E_c = 100$ TeV case, the predicted average energy density is 0.19 eV cm^{-3}.

We also investigated the case in which the less energetic PSR J1831-0941 is powering a halo. Our preliminary results suggest the pulsar might not be powerful enough to produce the observed γ-ray emission, requiring a large injection efficiency of $e^{-/+}$ up to possibly 100%, however more tests must be conducted, such as testing lower cut-off energy values.

Chapter 7

Characterization of pulsar halos with H.E.S.S. and CTAO

Contents

7.1 General method 90
7.2 Characterization of pulsar halos with H.E.S.S. 92
7.3 Towards pulsar halos with CTAO 99
7.4 Conclusion 104

Our goal is to assess the capability of the H.E.S.S. and southern CTAO arrays to search for and identify the TeV halos around middle-aged pulsars. To that end, we conducted simulations of observations with the IRFs of these instruments to quantify the precision with which we can characterize pulsar halos, and discriminate between the physically motivated halo model and a simple 2D Gaussian×PL model. The sensitivity of CTAO to pulsar halos has previously been studied in Eckner et al. (2023). Additionally, the observational impact of the pulsar's proper motion on the halo's morphology has been studied in Zhang et al. (2021).

7.1 General method

We simulated datasets $\sim$ 42 hours of H.E.S.S. and CTAO observations of halos using the model in Chap. 4 with numerous (120 in total) morphological and spectral parameter combinations (identical to the ones used in the validation section 4.2.2), as shown in Table 7.1.

We generated 160 stacked datasets (i.e. realizations) for each parameter combination of the simulated pulsar halo following the same method in section 4.2.2. The background model in each realization is optimized against the simulated binned-events cube outside the exclusion mask, and re-normalized (multiplied by a power law with free amplitude) during the model fitting step. For each dataset, the pulsar halo template model is fitted onto the simulated dataset to compute the Test Statistic (hereafter TS_{halo}). The fitted parameters are D_0, Γ or $\mathbf{V}_{PSR}$, P_0 and η (i.e. the model has 4 or 5 degrees of freedom depending on whether we fit Γ or $\mathbf{V}_{PSR}$). If we fit $\mathbf{V}_{PSR}$, then Γ is fixed to the value used for the dataset simulation. The halo model parameters that are not fitted are fixed to the same values used for the dataset simulation. Then, we removed the pulsar halo model, and we fitted the dataset with a model consisting of a 2D Gaussian spatial

Model parameter	Values
Initial period P_0	28.3 ms or 68.9 ms ($t_{age} \sim 85.7$ or 25.8 kyr)
Diffusion coefficient at 100 TeV D_0	1.3×10^{26} to 4.9×10^{27} cm^{2}s^{-1} (5 points)
Injection index Γ	1 or 2
Injection cut-off energy E_c	100 TeV or 1 PeV
Injection efficiency η	3% (or 7% if $\Gamma = 1$ and $E_c = 1$ PeV, cf. Section 4.2.2)
Distance to pulsar d_{PSR}	3 kpc
Characteristic age τ_c	100 kyr
Braking index n	3
Present-day period P	80 ms
Magnetic field strength B	3 μG
Rigidity dependence δ	1/3

Table 7.1: Parameter values of the simulated pulsar halo.

component (3 degrees of freedom) and a power-law spectrum (2 degrees of freedom), hereafter the "Gaussian model", and computed its Test Statistic $TS_{Gauss,1}$. For some parameter values of the simulated halo, the optimization of the Gaussian component can get stuck in a local minimum. To deal with this, we conducted the fit multiple times starting with different initial spatial parameter values and we take the model with the best $TS_{Gauss,1}$. We added and fitted a second Gaussian component on top of the first (adding 5 degrees of freedom to the Gaussian model), to test an energy-dependent morphology is detectable, and we computed $\Delta TS_{Gauss,2-1} = TS_{Gauss,1} - TS_{Gauss,2}$, which is the TS difference between the double Gaussian and single Gaussian model. If $\Delta TS_{Gauss,2-1}$ is higher than the detection threshold of 5σ ($\Delta TS_{Gauss,2-1} \geq 37$), the secondary Gaussian is accepted. The eccentricity and position angle of the larger 2D Gaussian are then freed if the simulated pulsar halo has a non-zero proper motion. The ellipticity of the larger Gaussian is accepted if it improves the fit by $\Delta TS_{2AS-2} \geq 12$ (corresponding to a threshold of 3σ for 2 d.o.f.). If the second symmetric Gaussian was not significant enough ($\Delta TS_{Gauss,2-1} < 37$), the elliptical second Gaussian is accepted if it improves the fit by $\Delta TS_{2AS} \geq 42$ versus the single Gaussian model (the detection threshold of 5σ for 7 d.o.f.). Finally, for the CTAO simulations only, an exponential cut-off in the fitted power-law spectrum of the Gaussian model is tested. If the model contains two Gaussian components, the exponential cut-off is tested for the component with the harder spectrum, because this component predominantly accounts for the γ-ray emission by the highest energy $e^{-/+}$. The exponential cut-off is accepted if it improves the fit by 3σ ($\Delta TS_{PL \to ECPL} \geq 9$ for 1 d.o.f.).

The Gaussian and pulsar halo models are not nested and do not satisfy the conditions of Wilk's theorem. To determine if we can reject one in favor of the other, we used the Akaike Information Criterion (AIC). An AIC score is assigned to an optimized model M following $AIC_M = 2k_M + TS_M$ with k_M the number of d.o.f. of model M and TS_M its Test Statistic. AIC_{halo} is defined as the AIC score of the fitted pulsar halo template model, and AIC_{Gauss} as that of the Gaussian model (which may contain multiple Gaussian components). The difference in the AIC scores between the two models is $\Delta AIC = AIC_{Gauss} - AIC_{halo} = 2(k_{Gauss} - k_{halo}) + (TS_{Gauss} - TS_{halo})$, such as a negative ΔAIC implies that the 2D Gaussian model has a better AIC score than the halo model. Here, we arbitrarily consider $\Delta AIC \geq 10$ as the threshold to reject the 2D Gaussian model in favor of the pulsar halo model.

The above procedure described for one realization is done with both the H.E.S.S. and CTAO IRFs for all realizations and all simulated parameter combinations. For

each simulated parameter combination, the mean and standard deviation over the 160 realizations of the estimated halo and Gaussian parameters, the TS, ΔTS, and ΔAIC values are recorded.

7.2 Characterization of pulsar halos with H.E.S.S.

7.2.1 Illustrative case

Figures 7.1 and 7.2 show example realizations for $P_0 = 28.3$ ms (the older system) and $P_0 = 68.9$ ms (the younger system) respectively, with $\Gamma = 1$, $E_c = 100$ TeV, different values of D_0 (4.3×10^{26} cm^2/s in the top row and 2.2×10^{27} cm^2/s in the bottom row) and three values of V_{PSR}, for ~ 42 hours of observation time. The maps correspond to the significance of the excess after subtracting the model containing only the background component, from 0.3 to 100 TeV and with a correlation radius of 0.15°. Each panel corresponds to a specific realization. The best-fit component(s) of the Gaussian model of the realization are overlaid, with the magenta component corresponding to the one with the harder PL spectrum if the model contains two components. In that case, we indicate $\Delta TS_{Gauss,2-1}$, ΔTS_{2AS-2} or ΔTS_{2AS} depending on the acceptance or not of an elliptical secondary Gaussian. The ΔAIC values are the comparison between the best Gaussian model versus the pulsar halo template fit. If $V_{PSR} \neq 0$, the pulsar birth position is shown as a blue diamond.

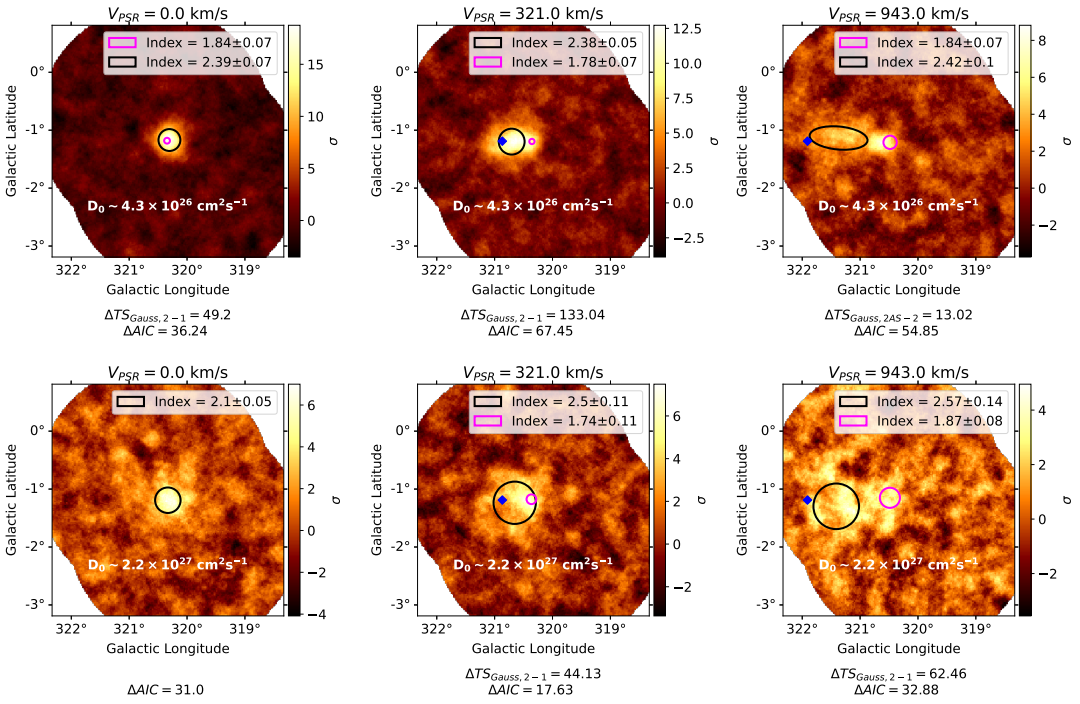

Figure 7.1: Example significance maps of simulated datasets (i.e. realizations) overlaid with the best-fit Gaussian components, for different values of the proper motion and the diffusion coefficient and for ~ 42 hours of observation time. **Top row:** $D_0 \sim 4.3 \times 10^{26}$ cm^2/s. **Bottom row:** $D_0 \sim 2.2 \times 10^{27}$ cm^2/s. All panels correspond to the older scenario ($P_0 = 28.3$ ms), with $\Gamma = 1$ and $E_c = 100$ TeV. If the proper motion is not null, the pulsar's birth position is shown as a blue diamond. If two Gaussian components are detected, ΔAIC indicates the difference in the AIC score between a model with 2 Gaussian components and a model with a fitted pulsar halo. The magenta component corresponds to the one with the harder power-law spectrum.

In Fig. 7.1 (the older pulsar scenario), adding a secondary Gaussian×PL component significantly improved the fit by $\Delta TS_{Gauss,2-1} \sim 44.1$ in the lower middle panel, up to $\Delta TS_{Gauss,2-1} \sim 133.0$ in the upper middle panel, but is not significant in the lower left panel with $D_0 \sim 2.2 \times 10^{27}$ cm^2 s^{-1} and $V_{PSR} = 0$. In the upper right panel with $V_{PSR} \sim 943.0$ km/s, there is an elongated feature stretching towards the pulsar birth position. The addition of ellipticity to the secondary Gaussian component significantly improves the fit by $\Delta TS_{Gauss,2AS-2} \sim 13.0$, while for the same V_{PSR} with higher diffusion coefficient in the lower right panel the emission appears more diffuse and symmetric so the elliptical Gaussian is not significantly preferred. We can statistically reject the Gaussian model in favor of the halo model for all of the realizations of the older case, despite the addition of a secondary Gaussian. The more compact component which is centered on the present-day pulsar position has a significantly harder PL index than the secondary, more extended component. The softer component accounts for the γ-ray emission by un-cooled relic $e^{-/+}$ that produce a "tail-like" structure when the proper motion is high enough. Thus, an energy-dependent morphology can be detected with simple geometric Gaussian models.

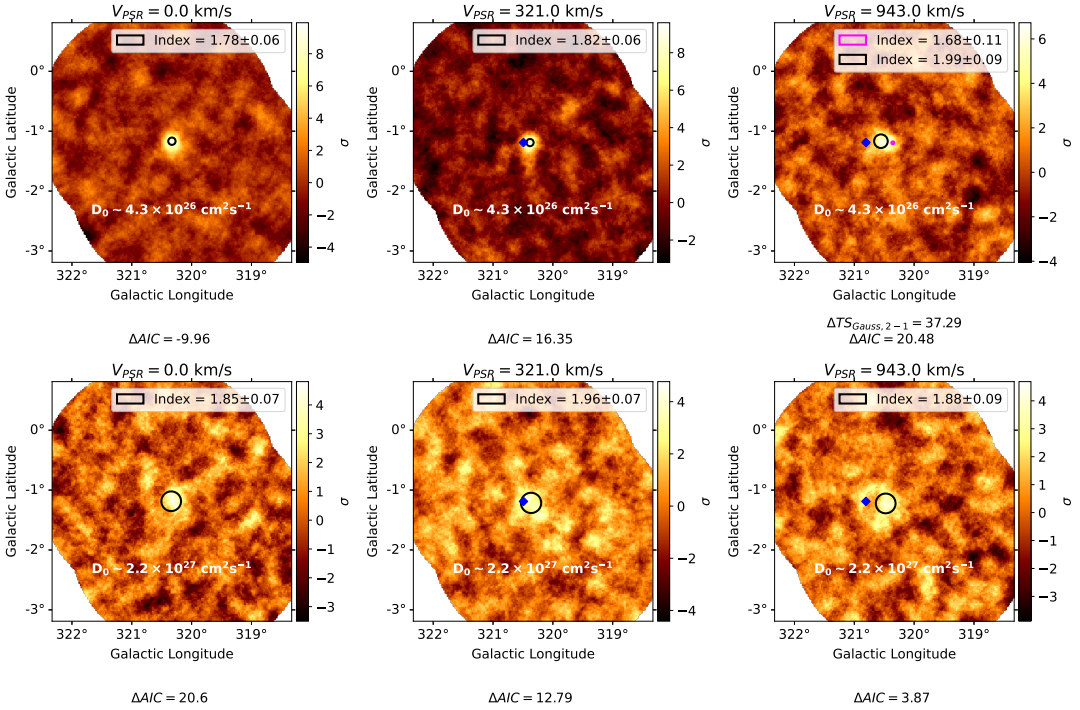

Figure 7.2: Same as Fig. 7.1 but for $P_0 = 68.9$ ms.

In Fig. 7.2 with the younger pulsar scenario, the source is generally less significant and more compact, and a secondary component is only detected for a high pulsar velocity and low diffusion coefficient ($D_0 \sim 4.3 \times 10^{26}$ cm^2 s^{-1} and $V_{PSR} \sim 943$ km/s in the upper right panel). The spectral indices in every realization are similar to those of the compact component shown for the older pulsar scenario in Fig. 7.1. This is because for a younger pulsar, the contribution from relic $e^{-/+}$ is weaker, as particles have been cooling for a shorter period, and the observed γ-ray emission is predominantly due to the population of cooled (recently injected) $e^{-/+}$. Lower ΔAIC values are found in the younger pulsar case than in the older pulsar case, which is due to the source being less significant because of the weaker signal in the H.E.S.S. energy band, and due to

the more compact emission which can often be appropriately reproduced by a simple Gaussian model. For $D_0 \sim 4.3 \times 10^{26}$ cm^2 s^{-1} and $V_{PSR} = 0$, the Gaussian model has a significantly better AIC score with $\Delta AIC \sim -10.0$, and for $D_0 \sim 2.2 \times 10^{27}$ cm^2 s^{-1} and $V_{PSR} \sim 943$ km/s we cannot reject the Gaussian model in favor of the halo model with $\Delta AIC \sim 3.9$.

We further explore the points made above from a spectral standpoint in Fig. 7.3, in which the fitted power laws corresponding to the Gaussian model's components in the realizations of Fig. 7.1 and Fig. 7.2 are shown, with $D_0 \sim 2.2 \times 10^{27}$cm^{2}s^{-1}, $V_{PSR} \sim 321.0$ km/s, $\Gamma = 1.0$ and $E_c = 100$ TeV. The sum of the components' spectra , the γ-ray SEDs of the simulated pulsar halo model, and that of the fitted halo model are shown. The shaded bands represent the 68% confidence intervals. The dotted vertical lines represent the particle energy at which the cooling timescale is equal to the pulsar's true age. The left panel shows the older pulsar scenario, and the right panel the younger pulsar scenario. In the former, the harder component's fitted PL is shown in magenta. The softer component accounts for the contribution by relic $e^{-/+}$, below the dotted vertical line at ~ 6.25 TeV. This illustrates that for this realization a secondary component is required to account for the contribution by the older particle population from a spectral standpoint. Finally, the figure shows that the simulated model SED is poorly reproduced by PL spectra. In the older case, the simulated bump in the $1 - 10$ TeV range is not reproduced by the sum of the power laws, and the simulated SED is overestimated in the $\lesssim 1$ TeV and $\gtrsim 20$ TeV ranges. In the younger case the power law underestimates the simulated SED below ~ 30 TeV. These spectral factors contribute to the preference of the halo template over the model employing Gaussian(s), on top of the morphological factors, if their emission is modeled with power laws. More complex spectral models, such as a Log Parabola, would likely help obtaining a better spectral fit for the Gaussians. The simulated SED is properly reproduced by the fitted halo template SED.

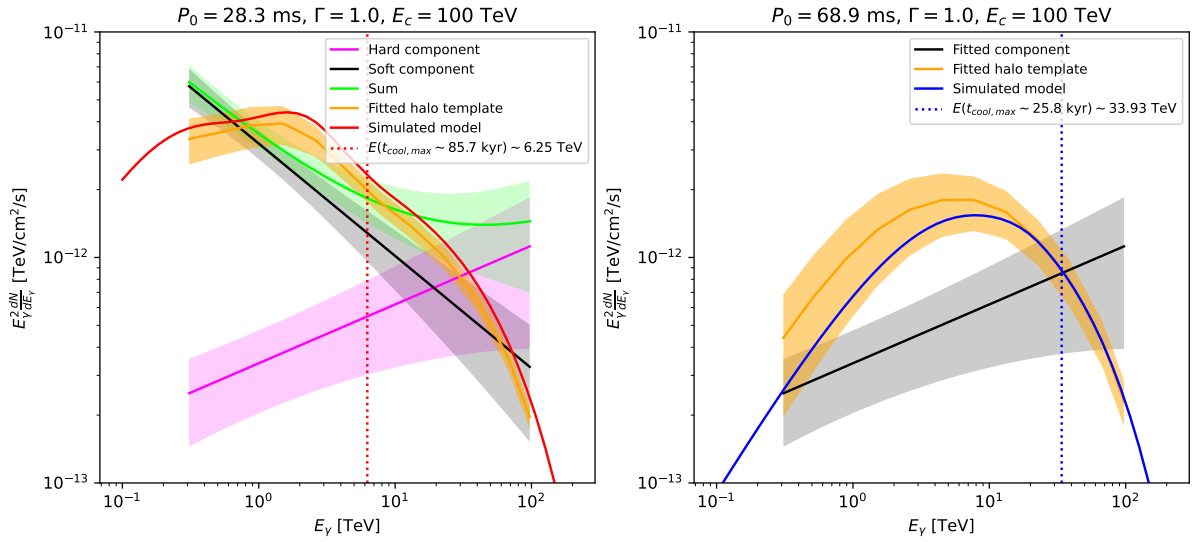

Figure 7.3: Fitted power-law spectra associated to the two Gaussian components shown in the lower middle panels of Fig. 7.1 (left) and Fig. 7.2 (right) with the H.E.S.S. IRFs, for ~ 42 hours of observation time. The red and blue solid lines corresponds to the spectra of the simulated pulsar halos. The orange curves represent the fitted pulsar halo template. The error bands represent the 68% confidence interval, and the lime spectrum corresponds to the sum of the components. The dotted red and blue line correspond to the energy at which the particle cooling rate is equal to the pulsar's true age.

7.2.2 Parameter space scan

In this section we present an overview of the results in the entire parameter space. First, we examined the fit of one 2D Gaussian component with a power-law spectrum across all parameter combinations with the H.E.S.S. IRFs. Then we looked at the ΔAIC between the pulsar halo template fit and the best-fit Gaussian model (i.e. 1 Gaussian, 2 Gaussians, or 2 Gaussians with an elliptical one).

We explored the morphology and detection significance of the γ-ray emission across the entire parameter space. Fig. 7.4 shows the TS when fitting one Gaussian with a power-law spectrum to the H.E.S.S. datasets of simulated halos with different parameter values and $E_c = 100$ TeV. The reported TS value for each parameter combination corresponds to the mean over all successful realizations. Regions below the detection threshold of 5σ for 5 d.o.f. ($TS < 37$) are hatched. The lowest and highest values of the fitted Gaussian's average extension (1σ in degrees, corresponding to the 39% containment) are indicated in red. The average offset from the pulsar position (taking into account the direction) is shown as black lines. The black lines and the sizes of the dots are scaled to the mean offsets and extensions respectively. The results are similar for the $E_c = 1$ PeV case, which is because H.E.S.S. is not sensitive to variations in the injection cut-off energy between $E_c = 100$ TeV and 1 PeV.

The source's significance is lower when the diffusion coefficient and the proper motion are higher, because of the reduced surface brightness due to the decrease in particle density. This trend is seen across all four panels. In the top left panel, with $\Gamma = 1$ and $P_0 = 28.3$ ms, the source is detected with a TS that varies from ~ 76.6 ($D_0 \sim 4.9 \times 10^{27}$ cm^{2}s^{-1}, $V_{PSR} \sim 942.8$ km/s) up to ~ 1795.1 ($D_0 \sim 1.27 \times 10^{26}$ cm^{2}s^{-1}, $V_{PSR} = 0$). The source's extension increases strongly in the increasing D_0 direction, from $\sim 0.07°$ ($D_0 \sim 1.27 \times 10^{26}$ cm^{2}s^{-1}, $V_{PSR} = 0$) up to $\sim 0.37°$ ($D_0 \sim 4.9 \times 10^{27}$ cm^{2}s^{-1}, $V_{PSR} \sim 942.8$ km/s). The offset between the Gaussian centroid and the pulsar position does not vary consistently from the $V_{PSR} \sim 320.0$ km/s and ~ 943.0 km/s cases between the lowest and highest D_0 values. It increases with V_{PSR} for the higher values of D_0, and decreases with V_{PSR} for the lower values of D_0. This is because at $\Gamma = 1$, there's a prominent γ-ray contribution by recently injected $e^{-/+}$, the transport of which is dominated by their cooling time. Thus, this contribution is concentrated near the pulsar position, and consequently, the measured Gaussian centroid offset reflects on the competition between the pulsar's velocity and the particles' diffusion coefficient. In the upper right panel with the younger pulsar ($P_0 = 68.9$ ms), the significance of the source drops, with the most significant case only reaching $TS \sim 445.8$. This remains a very significant source, but much less than for the older case. For the highest values of D_0 and V_{PSR}, the source is detected with $TS \sim 57.2$. The drop in significance is, as demonstrated in the illustrative cases (Fig. 7.3), due to the lower amount of relic $e^{-/+}$. In the bottom left panel with $\Gamma = 2$ and $P_0 = 28.3$ ms, the contribution by relic $e^{-/+}$ is much higher than that of the recently injected, cooled population. Thus, the offset between the pulsar and the Gaussian centroid is significantly higher than in the $\Gamma = 1$ case of the upper left panel, with a maximum of 1.27° (or 52 pc for $d_{PSR} = 3$ kpc) for the highest value of V_{PSR}. As expected, the offset always increases with the proper motion due to the distance between the pulsar and the relic γ-ray component. It increases with decreasing D_0 because the relic emission is more concentrated near the pulsar's birth position. The source reaches an extension of 0.6° for the highest value of D_0. Finally, in the bottom right panel with $\Gamma = 2$ and $P_0 = 68.9$ ms, the source has very little detection significance. It is on average

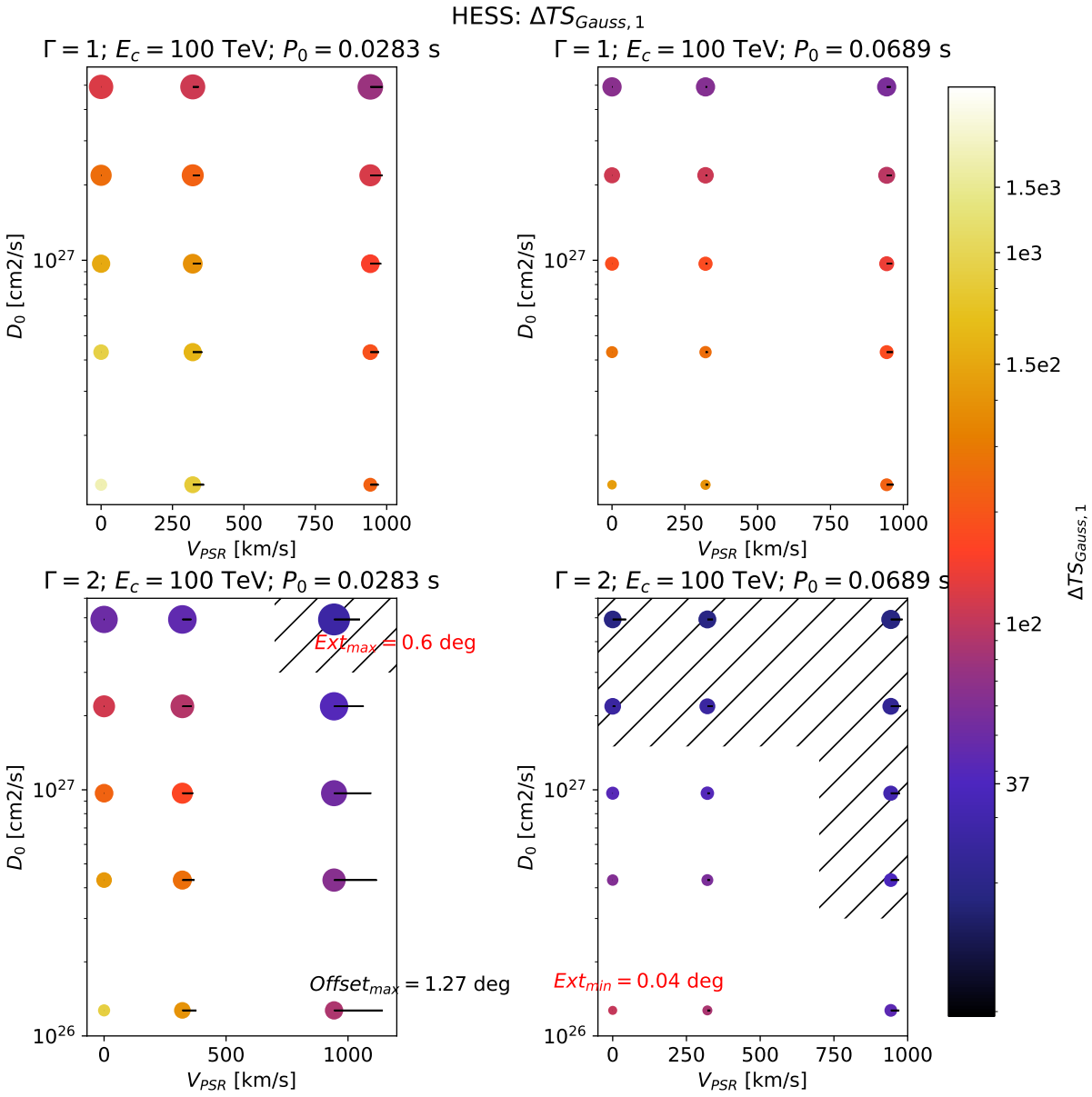

Figure 7.4: Average TS of a Gaussian fitted on a halo for $E_c = 100$ TeV in the H.E.S.S. simulations. The sizes of the dots are proportional to the average extension of the fitted Gaussian across all realizations. The horizontal lines are proportional to the offset between the Gaussian centroid and the pulsar's position (taking into account the direction). The hatched region corresponds to $TS < 37$. The lowest (0.04°) and highest (0.6°) average extensions are indicated in red, and the highest offset (1.27°) is indicated in black.

not detected for $D_0 \geq 2 \times 10^{27}$ cm^{2}s^{-1}. The compounded effect of a lack of relic $e^{-/+}$ and a softer injection spectrum make it so that the source is not detectable with $\eta = 3\%$ unless its surface brightness is high enough.

We draw the following conclusions from Fig. 7.4:

- A lower diffusion coefficient and lower pulsar transverse velocity produce a more compact source which is therefore more significant;
- Older systems are easier to detect than younger systems due to the contribution by relic $e^{-/+}$ in the H.E.S.S. band;

- A lower injection index is easier to detect than a higher injection index, although this could be due to keeping the injection efficiency constant at $\eta = 3\%$.

These results suggest that a pulsar halo with a significantly lower present-day period than the Geminga (237 ms) and Monogem (385 ms) halos and similar parameter values to the estimates in Albert et al. (2024) should be detectable by the H.E.S.S. array at a distance of 3 kpc.

We explored the identifiability of the pulsar halo in Fig. 7.5, showing the ΔAIC for the different pulsar halo parameter values ($E_c = 100$ TeV). ΔAIC corresponds to the comparison between the pulsar halo template and the best-fit Gaussian model (i.e. single Gaussian, two Gaussians, or a Gaussian and an elliptical Gaussian). The negative ΔAIC values mean that on average, the Gaussian model has a lower (better) AIC score. The hatched region represents $\Delta AIC < 10$. For $\Gamma = 1$, $P_0 = 28.3$ ms (upper left panel), 46.5% of all the realizations yield a significant secondary Gaussian. The pulsar halo template is strongly preferred over the Gaussian model, with a ΔAIC ranging from ~ 14.4 (at highest D_0 and $V_{PSR} = 0$) up to ~ 95.1. With decreasing D_0, the Gaussian model's performance becomes worse. Since D_0 has no effect on the γ-ray SED, the reason is possibly because the source is more significant and simple power law spectra cannot adequately reproduce the data. The ΔAIC increases with the pulsar proper motion, because of the prominent asymmetric tail-like feature which can not be adequately reproduced by a symmetric or elliptical Gaussian profile. These trends are seen across all four panels. For the younger pulsar with $\Gamma = 1.0$ (upper right panel), only 5.9% of all realizations yield a detected secondary Gaussian component. It becomes harder to differentiate between the Gaussian model and the halo template, with a ΔAIC ranging from ~ 4.5 to ~ 40.8. As shown in the illustrative cases, this is due to the absence of a significant energy dependent morphology due to the dominance of a single cooled $e^{-/+}$ population. For the relic-dominated case with $\Gamma = 2.0$ and an older pulsar (lower left panel), 25.6% of all the realizations resulted with a detected secondary Gaussian component. The Gaussian model performs better than the $\Gamma = 1.0$ case because of the decrease in source significance and the dominance of the relic component over the cooled component. The ΔAIC ranges from ~ 2.5 to ~ 34.0. Finally, The pulsar halo model is mostly indistinguishable from the best fit Gaussian model when $\Gamma = 2$ and $P_0 = 68.9$ ms in the lower right panel, where the highest ΔAIC value is ~ 10.8 and the lowest is -4.4. The ΔAIC is negative for the 5 parameter combinations: $V_{PSR} \leq 320.0$ km/s with $D_0 \geq 2.2 \times 10^{27}$ cm^2 s^{-1}, and $V_{PSR} \sim 943.0$ km/s with $D_0 \sim 4.9 \times 10^{27}$ cm^2 s^{-1}. There are no realizations where a secondary Gaussian is detected. As mentioned previously, this is likely because the γ-ray emission can be adequately reproduced with a simple power-law and a Gaussian, and mostly due to the on-average insignificant source detection (cf. dashed blue curve in Chap. 4: Fig. 4.11).

Thus, we found high enough ΔAIC values to reject the Gaussian model for a halo with a period significantly shorter than that of Geminga (237 ms) and Monogem (385 ms), but otherwise statistically similar to the results of Albert et al. (2024). We also found that a secondary Gaussian is accepted in a significantly higher proportion of realizations in the older pulsar scenario case than in the younger pulsar scenario case, which shows that H.E.S.S. could discriminate between the cooled and un-cooled $e^{-/+}$ populations in some cases. The following can be said regarding the identification of pulsar halos with H.E.S.S.:

- A lower diffusion coefficient results in a higher ΔAIC;

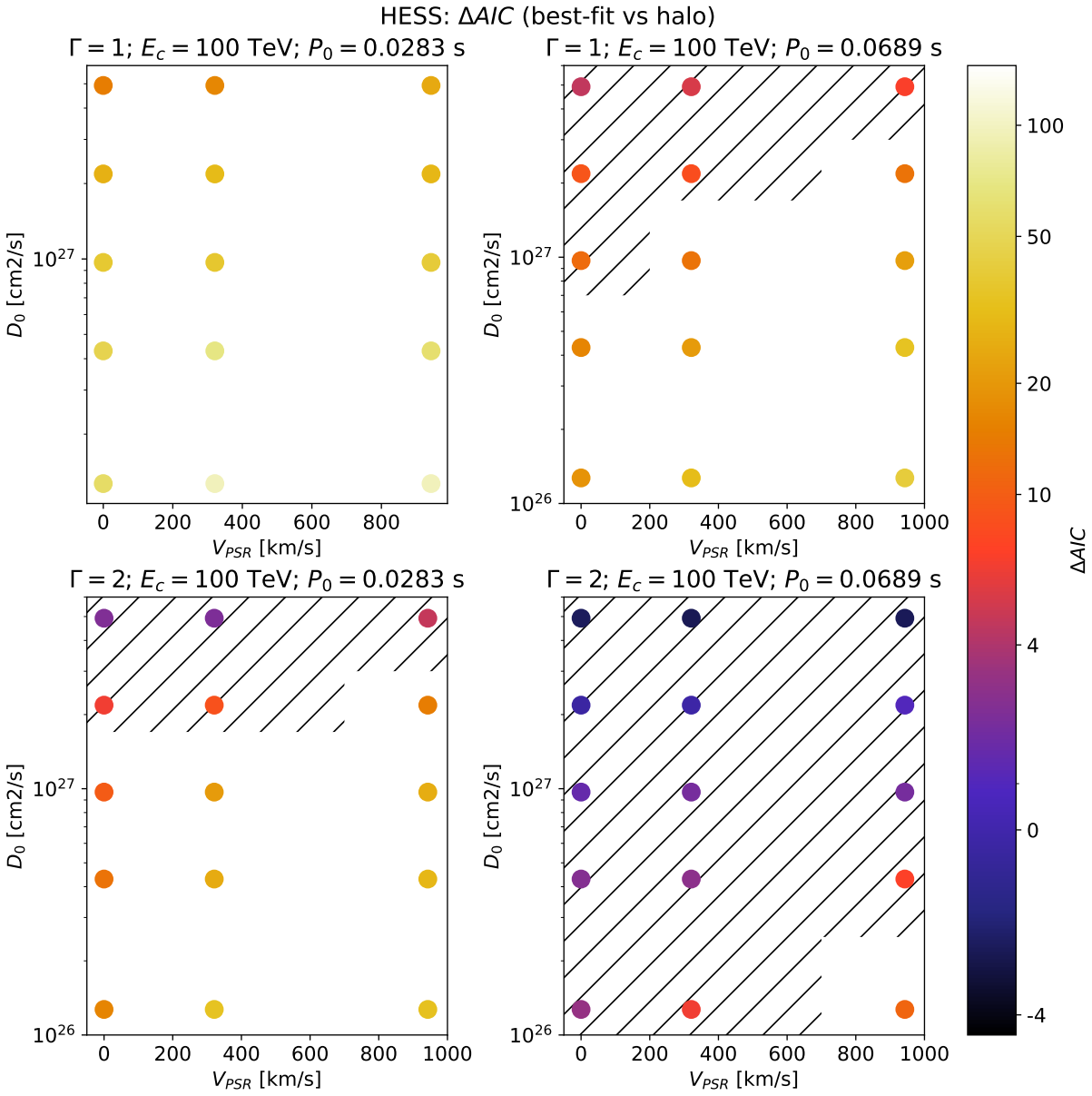

Figure 7.5: ΔAIC between the Gaussian model fit and the pulsar halo model fit for $E_c = 100$ TeV in the H.E.S.S. simulations. The diagonal back hatched regions represent $\Delta AIC < 10$.

- A higher pulsar transverse velocity results in a higher ΔAIC, even though the source is less significant;
- An older system has a higher ΔAIC than a younger system;
- A harder injection index results with a higher ΔAIC than a softer injection index;

In the cases of Fig. 7.5, H.E.S.S. can statistically reject the Gaussian model most of the time and despite the detection of a secondary Gaussian component, except when $P_0 = 68.7$ ms and $\Gamma = 2.0$. The results for $E_c = 1$ PeV follow the same trends.

D_0 and V_{PSR} are expected to have very little effect on the γ-ray SED. In Fig. 7.6, we show the means and standard deviations of the fitted power law indices over all D_0 and V_{PSR} values corresponding to a given Γ, P_0 (in blue or red) and E_c (triangle or circle) combination. The left panel represents the fitted power-law index when only one

component in the Gaussian model is found to be significant. For a given value of the injection index Γ, the measured PL index is softer on average when the pulsar is older. We show the measured PL indices when two Gaussians are detected in the middle and right panel for the older pulsar case, because for the younger case, a negligible amount of realizations result in a significant secondary Gaussian component. The trends for both the hard and the soft component are similar to those found for a single component. A difference of ~ 0.6 can be expected between the PL indices of the harder and softer Gaussian components.

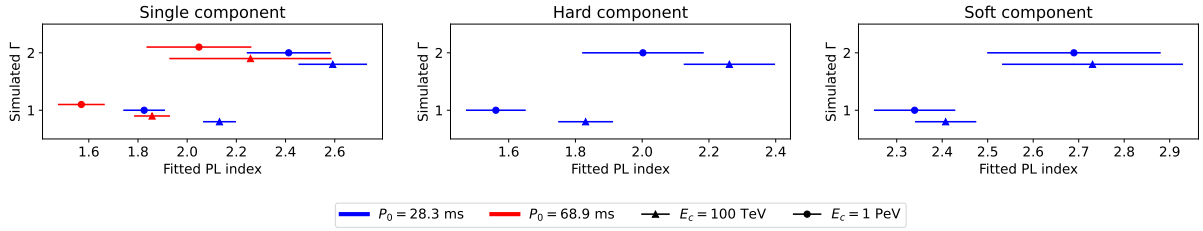

Figure 7.6: **Left:** Mean and standard deviation of the measured power-law indices for realizations where only one Gaussian component is significant. **Middle:** Mean and standard deviation of the measured power-law indices of the hard component when a secondary Gaussian is significant, for $P_0 = 28.3$ ms (older case). **Right:** Mean and standard deviation of the measured power-law indices of the soft component when a secondary Gaussian is significant, for $P_0 = 28.3$ ms (older case).

7.3 Towards pulsar halos with CTAO

The analysis configuration for the datasets simulated using the CTAO IRFs is the same as in the H.E.S.S. case, except that events are selected within 3.5° of the camera center instead of 2.0°. We used the IRFs corresponding to the Alpha configuration (14 MSTs) of Prod 5 v0.1 (CTAO & Consortium 2021). Specifically, we used the MST-South sub-array optimized for 50 hours, an average azimuth angle, and a zenith angle of 40°. In this section, we conduct the same analysis that was shown for the H.E.S.S. case using the CTAO South MST sub-array, with the addition of testing for the significance of an exponential cut-off in the fitted power-law SED of the Gaussian model. If the latter contains two components, the cut-off is tested for the component with the harder power-law index because it accounts predominantly for the γ-ray emission by the highest energy $e^{-/+}$. Identically to the H.E.S.S. study, the observation time for each realization is $\sim$ 42 hours.

7.3.1 Illustrative case

Fig. 7.7 and Fig. 7.8 show the significance maps (0.3 to 100 TeV, correlation radius of 0.15°) from simulations of a pulsar halo with $P_0 = 28.3$ ms and $P_0 = 68.9$ ms respectively, obtained using the IRFs of the CTAO South MST sub-array. The realizations shown correspond to the same pulsar halo model parameters as Fig. 7.1 and Fig. 7.2. The resulting best-fit Gaussian model is overlaid, with the harder component in magenta and the softer component in black, and the pulsar's birth position is shown with a blue diamond if $V_{PSR} \neq 0$. We indicate $\Delta TS_{Gauss,2-1}$, ΔTS_{2AS-2} or ΔTS_{2AS}, which are explained in the previous section. A spectral exponential cut-off is tested for the best-fit Gaussian model's harder component. If the addition of an exponential cut-off improves

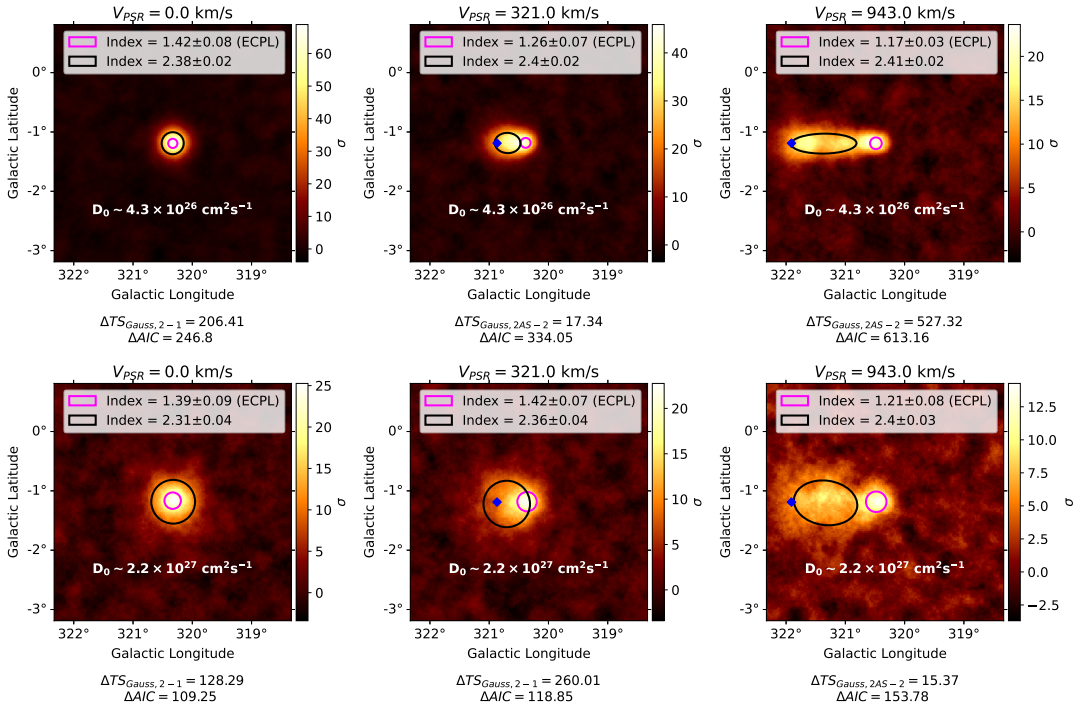

Figure 7.7: Same as Fig. 7.1 but with the CTAO South MST sub-array IRFs. "ECPL" in the label indicates the 3σ detection of a spectral exponential cutoff. $P_0 = 28.3$ ms, $\Gamma = 1$ and $E_c = 100$ TeV.

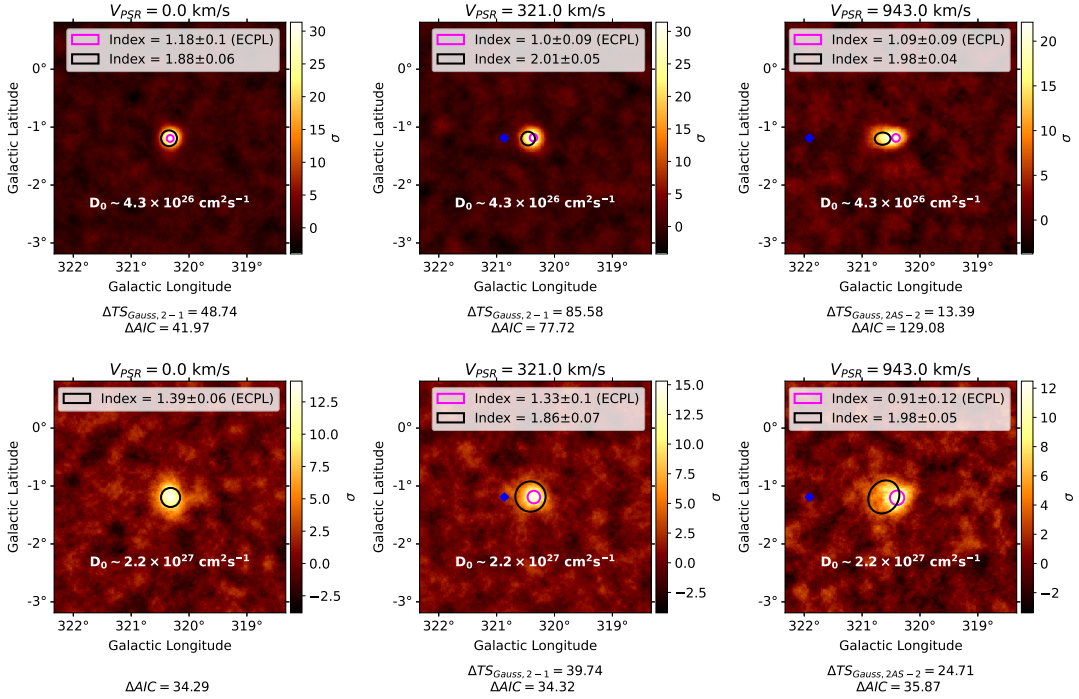

Figure 7.8: Same as Fig. 7.7 but with $P_0 = 68.9$ ms. $\Gamma = 1$ and $E_c = 100$ TeV.

the fit by $\Delta TS \geq 9$ (corresponding to a detection threshold of 3σ for one d.o.f.), "ECPL" is indicated in the legend. In the older pulsar case (Fig. 7.7), the addition of a secondary Gaussian is found to be significant in all the shown realizations. The ΔAIC ranges from ~ 109.3 for $D_0 \sim 2.2 \times 10^{27}$ cm^{2}s^{-1} and $V_{PSR} = 0.0$ (lower left panel), up to $\Delta AIC \sim 613.2$ for $D_0 \sim 4.3 \times 10^{26}$ cm^{2}s^{-1} and $V_{PSR} \sim 943.0$ km/s (upper right panel). In the

latter, the ellipticity of the larger component is highly significant, with $\Delta TS_{Gauss,2AS-2} \sim 527.3$. However, it does not properly reproduce the asymmetry of the relic halo "tail", resulting in a high ΔAIC in favor of the halo model. Fig. 7.8 shows realizations of the same parameters except for $P_0 = 68.9$, where all but one ($D_0 \sim 2.2 \times 10^{27}$ cm^{2}s^{-1} and $V_{PSR} = 0.0$ in the lower left panel) realizations result in a significantly detected secondary Gaussian component. Similarly to the older case, we may reject the Gaussian models in favor of the pulsar halo model. The addition of ellipticity to the larger Gaussian in both $V_{PSR} \sim 943.0$ km/s realizations is significant. An exponential cut-off with the harder component is significant in all the shown realizations in both Fig. 7.7 and Fig. 7.8. Therefore, for these realizations, CTAO detects more often the two Gaussian component (except for one case) as compared to H.E.S.S., even for the younger system, and the halo model is always favored.

In Fig. 7.9, we show the fitted spectral models corresponding to the lower middle panels of Figures 7.7 and 7.8 ($V_{PSR} \sim 321$ km/s, $D_0 \sim 2.2 \times 10^{27}$ cm^{2}s^{-1}, $\Gamma = 1.0$, $E_c = 100$ TeV). The fitted power-laws and their sum from the best-fit Gaussian model and the fitted halo template SED are shown, along with the simulated SED. The significance of the exponential cutoff in the hard component's spectrum is $\sim 7.7\sigma$ in the older pulsar case (left panel), and $\sim 4.5\sigma$ in the younger pulsar case (right panel). The estimation of simulated SED with power laws is improved in comparison to the H.E.S.S. study (cf. Fig. 7.3) because of the inclusion of the exponential cut-off, however it remains inadequately reproduced, which explains the preference of the halo model and the detection of a second component in the younger case ($\Delta AIC \sim 118.9$ for the older pulsar case, and $\Delta AIC \sim 34.3$ for the younger pulsar case). We note however that the use of other spectral models (Log parabola or ECPL) to the relic component in the Gaussian model could help better reproduce the simulated pulsar halo SED.

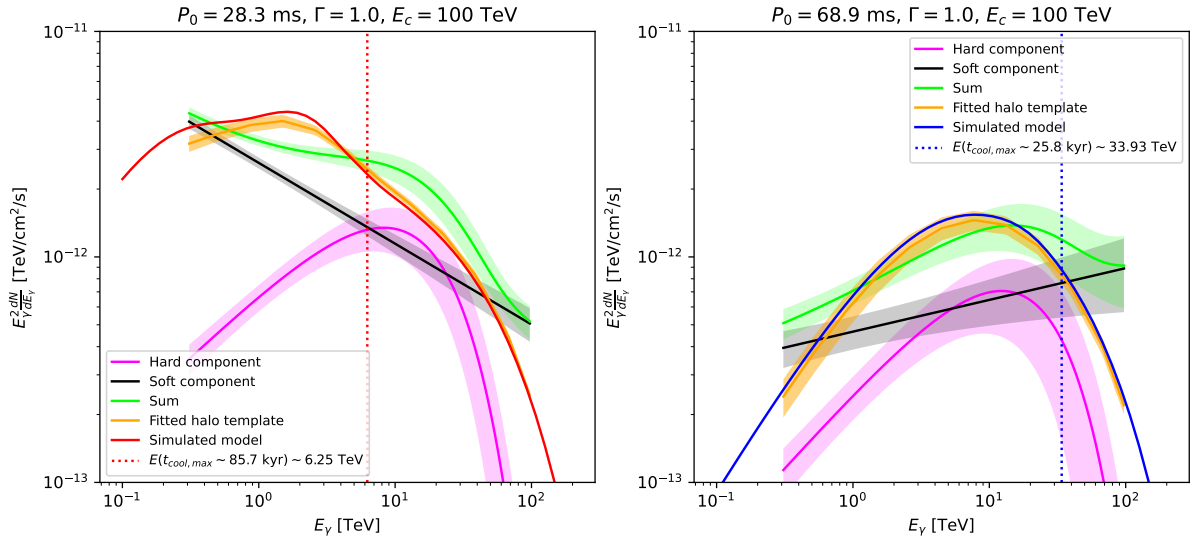

Figure 7.9: Fitted power-law spectra associated to the two Gaussian components shown in the lower middle panels of Fig. 7.7 (left) and Fig. 7.8 (right) with the MST-South IRFs. The red and blue solid lines corresponds to the spectra of the simulated pulsar halos. The error bands represent the 68% confidence interval, and the lime spectrum corresponds to the sum of both components. The dotted red and blue line correspond to the energy at which the particle cooling rate is equal to the pulsar's true age.

7.3.2 Parameter space scan

We examined the results across the entire parameter space. The source is significantly detected (when fitting only one Gaussian component, similarly to Fig.7.4 in the H.E.S.S. study) across all the different parameter combinations, and the TS of the Gaussian is dramatically improved when compared to the H.E.S.S. simulations (the corresponding figure is not shown here). We also find the same trends (Gaussian morphology, offset and TS vs. simulated halo parameters) as the ones shown for the H.E.S.S. IRFs. Consequently, in this subsection we only focus on the identifiability of the halo.

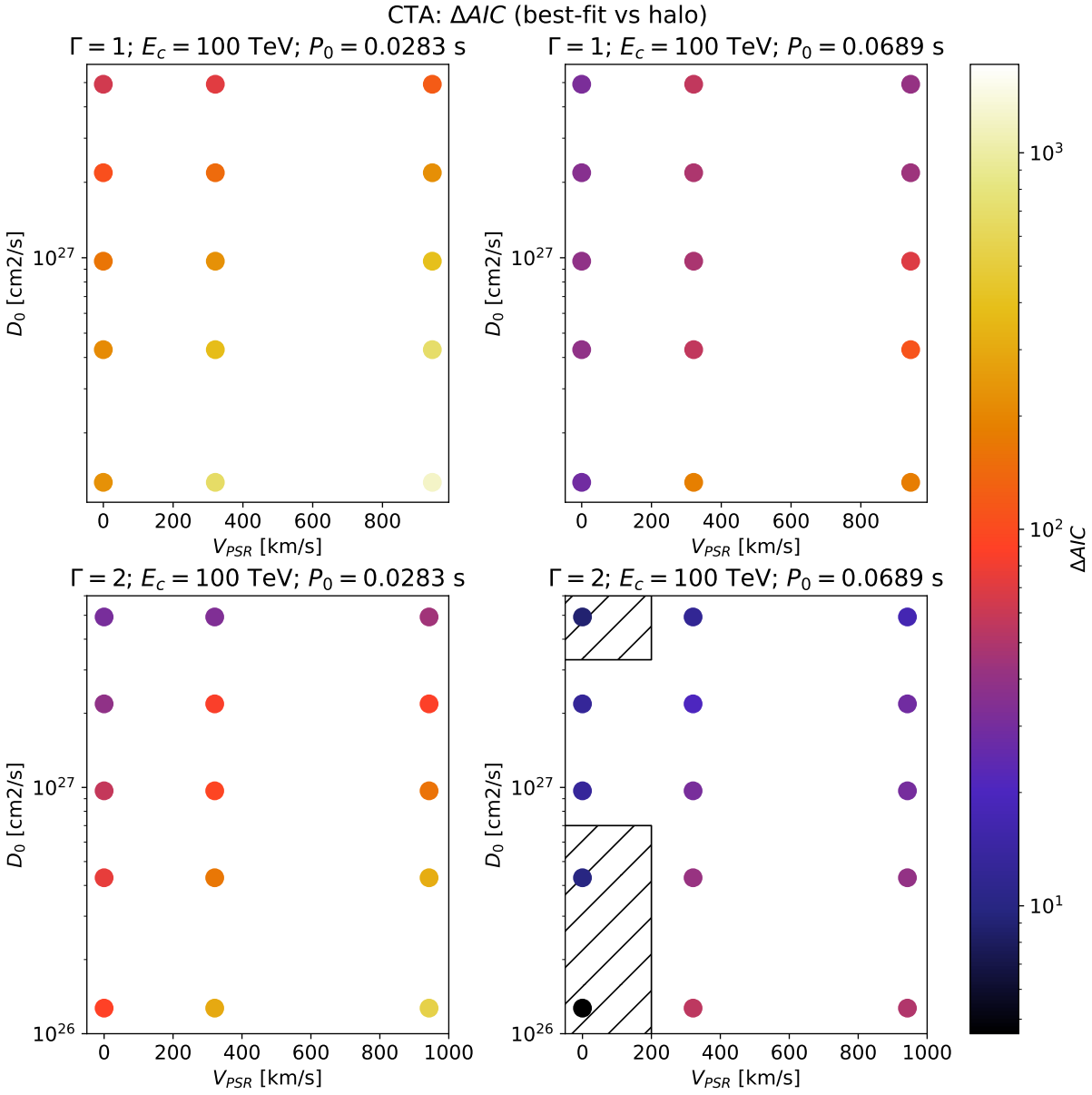

Figure 7.10: ΔAIC between the best Gaussian model fit and the pulsar halo model fit for $E_c = 100$ TeV in the CTAO simulations. The diagonal back hatched regions represent $\Delta AIC < 10$.

We computed the average ΔAIC values for the CTAO-South MST simulations, as shown in Figure 7.10. The ΔAIC corresponds to the comparison between the fitted pulsar halo template model and the best-fit Gaussian model (single Gaussian, double Gaussian or Gaussian and elliptical Gaussian). An exponential spectral cut-off is also

included in the best-fit Gaussian model's harder component if it improves the fit by 3σ. The black hatches represent $\Delta AIC < 10$. Fig. 7.10 corresponds to the $E_c = 100$ TeV case. For $\Gamma = 1$ and $P_0 = 28.3$ ms (upper left panel), the ΔAIC is generally the highest with respect to variations in Γ and P_0. The lowest value is found for $D_0 \sim 4.9 \times 10^{27}\mathrm{cm}^2\mathrm{s}^{-1}$ and $V_{PSR} = 0$, with $\Delta AIC \sim 64.0$, and increases to ~ 1217.0 at $D_0 \sim 1.27 \times 10^{26}$ cm^{2}s^{-1} and $V_{PSR} = 943.0$ km/s. The secondary Gaussian is significantly detected across 97.2% of all the realizations (compared to 46.5% for H.E.S.S.). For $\Gamma = 1$ and $P_0 = 68.9$ ms (upper right panel), the trends are similar, with a minimum $\Delta AIC \sim 28.8$ and a maximum $\Delta AIC \sim 184.0$. A lower proportion of realizations (62.6%) result in a significant secondary Gaussian (compared to 5.9% for H.E.S.S.). For lower $\Gamma = 2$ and $P_0 = 28.3$ ms (lower left panel), the ΔAIC starts at ~ 31.0 and rises to $\Delta AIC \sim 542.5$, with 89.2% of all realizations resulting in a significant secondary Gaussian (compared to 25.6% for H.E.S.S.). For $\Gamma = 2$ and $P_0 = 68.9$ ms (lower right panel), a secondary Gaussian is significant in only 21.5% of all realizations (compared to 0% for H.E.S.S.), and the ΔAIC ranges from $\Delta AIC \sim 4.6$ at $D_0 \sim 1.27 \times 10^{26}$ cm^{2}s^{-1} and $V_{PSR} = 0$ to $\Delta AIC \sim 55.0$ at $V_{PSR} \sim 943.0$ km/s.

When $E_c = 1$ PeV (not shown here), the trends are the same as for the $E_c = 100$ TeV case and there are more parameter combinations for which an exponential cut-off is on average not detected significantly for the best Gaussian model. Additionally, the ΔAIC values are slightly lower. Hence, the conclusions for the CTAO simulations are the same as for H.E.S.S., except that there are significantly more realizations where a secondary Gaussian component is detected, and the identification of the pulsar halo is improved.

Finally, we looked at the power-law spectral indices and exponential cut-offs of the best-fit Gaussian models in Fig. 7.11 and Fig. 7.12, respectively. For the indices (Fig. 7.11), if a cut-off in the spectrum is significant, the corresponding index is reported (which yields a harder index). For the harder component when a secondary Gaussian is found to be significant (middle panel), the simulated P_0 and E_c values have no significant impact on the PL index. In the single and soft component cases (left and right panels), the fitted PL is significantly harder with higher P_0 (younger pulsar), with difference of ~ 0.4 compared to the older case. For $\Gamma = 1$, the fitted PL is significantly harder when E_c is higher. In Fig. 7.12, we show that the impact of the simulated E_c value on the estimated cutoff energy of the power law is more significant for $\Gamma = 1$ than for $\Gamma = 2$, and that P_0 does not significantly impact it at constant Γ and E_c. These results are expected because the age of the pulsar does not affect the γ-ray contribution by the highest energy $e^{-/+}$. For the older pulsar case ($P_0 = 28.3$ ms), the cut-off energy is significantly higher for $\Gamma = 1$ than for $\Gamma = 2$ at constant E_c.

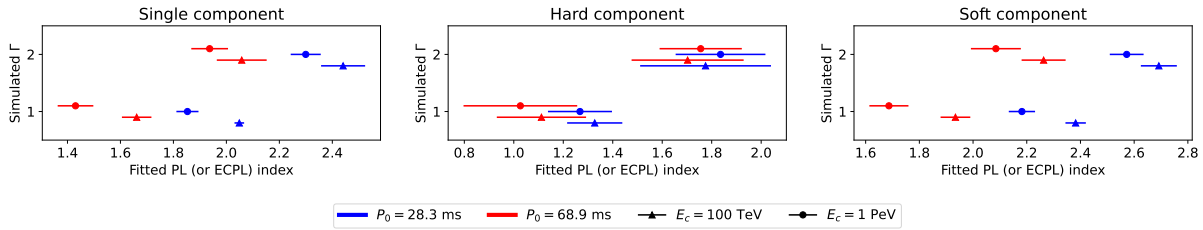

Figure 7.11: **Left:** Mean and standard deviation of the measured power-law indices for realizations where only one Gaussian component is significant. **Middle:** Mean and standard deviation of the measured power-law indices of the hard component when a secondary Gaussian is significant. **Right:** Mean and standard deviation of the measured power-law indices of the soft component when a secondary Gaussian is significant.

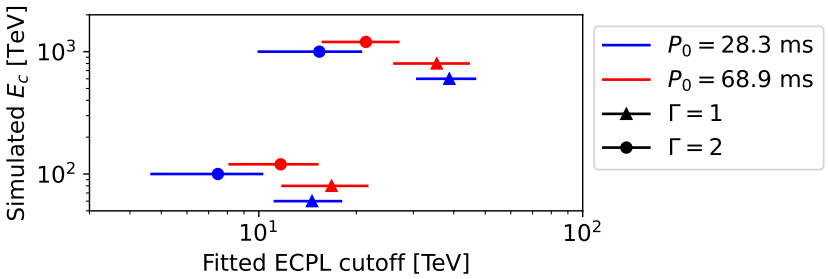

Figure 7.12: Average fitted exponential cut-off of the best-fit Gaussian model across all realizations for a given Γ, P_0 and E_c combination.

7.4 Conclusion

We used a spatially resolved model of escaped $e^{-/+}$ diffusing in the ISM, injected by a middle-aged PWN, to simulate H.E.S.S. and CTAO observations of pulsar halos at a distance of 3 kpc. The assumed pulsar has a present-day period $P = 80$ ms and characteristic age $\tau_c = 100$ kyr, implying a spin-down power $\dot{E} \sim 9.8 \times 10^{35}$ erg/s for a braking index $n = 3$. A parameter space was explored with different values of the diffusion coefficient normalization (D_0 from $\sim 1.3 \times 10^{26}$ cm^2 s^{-1} to $\sim 5 \times 10^{27}$ cm^2 s^{-1} at 100 TeV), pulsar proper motion (V_{PSR} from 0 to $\sim$ 943 km/s) and initial period (an "older" case with $P_0 \sim 28.3$ ms and a "younger" case with $P_0 \sim 68.9$ ms). Different parameters of the $e^{-/+}$ injection spectrum were considered, with an injection index $\Gamma = 1$ and 2, and an injection cut-off energy $E_c = 100$ TeV and 1 PeV. We characterized the different possible morphologies and photon spectra of the source with H.E.S.S and CTAO.

The results show that the emission morphology can be highly asymmetric in the "older" case for a proper motion $\gtrsim 400$ km/s and a low diffusion coefficient normalization on the order of 10^{26} cm^2 s^{-1}. However, in real data, one would expect less asymmetry, because the distribution of known pulsars' transverse velocity peaks between $300-400$ km/s (and $V_{PSR} \sim 1000$ represents rare cases). Less asymmetry is also expected if the diffusion coefficient normalization of the majority of halos is similar to that of the Geminga and Monogem halos, on the order of 10^{27} cm^2 s^{-1}. Further, the majority of the identified and candidate PWNe in H.E.S.S. data lie at a distance higher than 3 kpc, which would also reduce the asymmetry with the sources appearing more compact and fainter.

In the "older" pulsar case, with a harder injection index $\Gamma = 1$, a secondary Gaussian is detected in 46.5% of all the realizations with H.E.S.S., and for a softer $\Gamma = 2$, this occurs in 25.6% of all the realizations. The occurrence rate of detecting a secondary Gaussian is comparably negligible for the "younger" case. The detection of a secondary Gaussian with CTAO occurs in more than $\sim 90\%$ of all realizations for the "older" case, and is not negligible for the "younger" case.

For the "older" case, H.E.S.S. can some times discriminate between a pulsar halo and 2D Gaussian $\times$ PL model, while this occurs for nearly the entire parameter space with CTAO. A caveat is that the identification of the halo is expected to be more difficult given the higher distances of detected PWNe in H.E.S.S. data, and in this study we used a simple PL spectrum for the Gaussian model, while curved models such as a log-parabola or the inclusion of an exponential cut-off could better reproduce the halo's spectrum, drastically reducing the ΔAIC in favor of the halo. This is currently a work in progress.

We also note that a model of the interstellar emission is not included in the simulations. It is expected to reduce the significance of the simulated source and our ability to

characterize it. Source confusion is expected to occur, particularly for more diffuse halos. The softer relic component of $e^{-/+}$ can be drowned out by the interstellar emission. Eckner et al. (2023) estimated at least a 20% impact on the detection sensitivity of halos due to the interstellar emission. Its implementation in our study is currently a work in progress.

It is noteworthy that for simulated halo parameters that are roughly similar (e.g. $D_0 \sim 4.9 \times 10^{27}$ cm^2 s^{-1}, $V_{PSR} = 0$, $P_0 \sim 28.3$ ms, $\Gamma = 2$) to those of HESS J1831−098 and PSR J1831−0952, which has a present-day period of 67 ms and a characteristic age of 128 kyr, the ΔAIC is similar to the one found in the data analysis of Chap. 6. If the astrophysical scenario of the source is truly that of a pulsar halo powered by PSR J1831−0952, the ΔAIC with CTAO could be nearly 10 times higher than the one found in this work.

In upcoming IACT catalogs, such as the second H.E.S.S. Galactic Plane Survey (2HGPS) or the CTA Galactic Plane Survey (CGPS), sources detected with a softer secondary Gaussian component or with asymmetric components could hint at the presence of two distinct particle populations (with different ages and energies). Sources characterized by multiple components would merit re-investigation to pursue pulsar halos in the Galaxy, particularly with a template-based approach and ideally in joint analyses using data from different γ-ray experiments (IACTs and Direct EAS detectors in tandem).

Conclusion and prospects

The halos around middle-aged pulsars open a window to study the late stages of pulsar wind nebula evolution, to constrain particle escape from pulsar wind nebulae, and to constrain their contribution to the local electron and positron cosmic-ray spectra. Extending the size and diversity of the population of known pulsar halos can help understand the conditions favoring the emergence of the pulsar halo phenomenon. H.E.S.S., an Imaging Atmospheric Cherenkov Telescope with access to the inner Galaxy, is well suited to conduct deep observations of pulsar halos which probably lie in different environments than the current known and candidate population. Recently developed analysis methods (such as 3D analyses) are likely much better suited to the study of pulsar halos, and revisiting the H.E.S.S. data on plausible pulsar halo candidates is warranted.

In this work, we proposed a template approach to constraining particle transport in halos with H.E.S.S. data, conducted a search for pulsar halo candidates in the H.E.S.S. Galactic Plane Survey, applied the template method to a suitable candidate in H.E.S.S., and explored the detectability and identifiability of halos with H.E.S.S. and CTAO using observation simulations.

We adopted a model of particle transport that was used in the literature to describe the spectrum and morphology of the Geminga and Monogem pulsar halos (e.g. Albert et al. 2024). It describes the inverse Compton emission from electrons and positrons continuously injected by a pulsar wind nebula of negligible size into the interstellar medium, cooling through synchrotron and inverse Compton scattering as they diffuse away from the pulsar. The model predicts that in the H.E.S.S. energy band, the γ-ray emission is highly impacted by the pulsar's true age, both spatially and spectrally, due to the contribution by relic electrons and positrons which have been cooling throughout the pulsar's evolution. Thus, the proper motion is predicted to introduce some asymmetry in the H.E.S.S. energy band if the pulsar is old and close enough. The main contribution to the inverse Compton emission is the up-scattered infrared and far-infrared photons from dust, while the inverse Compton emission observed by HAWC (and LHAASO's Kilometer Squared Array) is pre-dominantly due to up-scattered Cosmic Microwave Background photons. We created templates of the γ-ray emission morphology and spectrum that can be fitted to H.E.S.S. data with Gammapy and provide best-fit values of physical parameters such as the diffusion coefficient normalization, the pulsar's proper motion, the initial period, the injection index and the injection cut-off energy.

We searched for halo candidates in the H.E.S.S. Galactic Plane Survey (HGPS) by looking for spatial coincidences with energetic middle-aged pulsars and HGPS components that fall within a loosely defined criterion. This search resulted in 12 known H.E.S.S. sources and 8 source candidates (the so-called "Discarded" components of the H.E.S.S. Galactic Plane Survey) that are spatially coincident with such pulsars. 4 of the 7 halo candidates that are visible to LHAASO have a plausible counterpart which we show as having a consistent morphology and photon spectrum. The pulsar halo candidates have

on average a shorter period than those of Geminga and Monogem, which is expected since γ-ray emission in H.E.S.S. data is easier to detect towards farther pulsars due to the instrument's field of view, requiring that these pulsars be more powerful. Additionally, we highlighted 12 middle-aged energetic pulsars farther than 1 kpc in the H.E.S.S. Galactic Plane Survey coverage that have less than 40 hours of observations. If these pulsars develop a halo, most of them could potentially be detectable by CTAO according to the study of Eckner et al. (2023). Additionally, 4 of them are spatially coincident with LHAASO sources. Thus, additional H.E.S.S. observation time towards these pulsars could result in the detection of new pulsar wind nebulae or pulsar halos. The pulsar halo candidates cited in this thesis could warrant being re-analyzed in H.E.S.S. data with more statistics and the 3D template-based approach as conducted for HESS J1831−098, a plausible pulsar halo candidate.

HESS J1831−098 is well reproduced by the halo template model with the pulsar PSR J1831−0952. The halo template model, however, is not significantly preferred over a simple 2D Gaussian morphology and power law spectrum. The fitted diffusion coefficient was found to be similar to that of the Geminga and Monogem halos (Albert et al. 2024), and the particle injection index significantly softer. We found a 30 TeV lower limit on the injection cut-off energy at the 1σ level. The addition of the proper motion was not significant, improving the likelihood by $\sim 2.1\sigma$. The energy density averaged over the source's 68% containment extension is on the order of that of the interstellar medium, which is higher than the values estimated for the Geminga and Monogem halos in Giacinti et al. (2020). HESS J1831−098's spectrum and morphology are well consistent with very plausible HAWC and 1LHAASO counterparts. We also tested a scenario in which another, less energetic pulsar in the region PSR J1831−0941 powers the halo, showing that the required injection efficiency of electrons and positrons is compatible with 100%, making a halo scenario involving this pulsar less plausible than in the PSR J1831−0952 case. More tests are required however, as it is possible that lower assumed values of the injection cut-off energy yield lower injection efficiencies.

Finally, we simulated observations of a pulsar halo with different model parameters at 3 kpc from Earth using H.E.S.S. and CTAO instrument response functions. 3D Analyses of the simulated datasets were conducted, wherein the halo templates and a model of 2D Gaussians with power law spectra are fitted and compared to each other. The analyses revealed a highly asymmetric morphology when the proper motion is high enough and the pulsar is old enough. The pulsar halo is most significant, and most distinguishable from a model containing simple 2D Gaussian components when it is older and when the electron and positron injection spectrum has a harder index. A secondary Gaussian component is most frequently detected in this scenario as well, due to the presence of two prominent lepton populations of different age and energy. Distinguishing between a pulsar halo and 2D Gaussian morphology becomes more difficult in the H.E.S.S. simulations when the diffusion coefficient normalization is higher due to the reduced surface brightness of the source. The ΔAIC scores are roughly 10 times higher in the CTAO simulations, drastically favoring the halo template fit over that of the model containing 2D Gaussian components. The interstellar emission is expected to be impactful on the simulated halo's significance, and this is currently under investigation.

In the short term, the continued development of H.E.S.S. - HAWC joint data analysis methods, which are already available in Gammapy, may help improve constraints on middle-aged pulsar-powered sources. The analysis of HESS J1831−098 can already be improved by including HAWC data in a joint-analysis, with access to a higher energy

range crucial to reduce parameter degeneracy in the pulsar halo template approach. The HAWC counterpart of HESS J1831−098, 3HWC J1831−095, is possibly significant up to 100 TeV. This should break the degeneracy of the halo model with respect to the electron and positron injection efficiency, which acts as a normalization, and the pulsar's true age, which governs the contribution of relic electrons and positrons below ~ 10 TeV.

In the future, the CTAO Galactic Plane Survey will likely significantly increase the population of PWNe in VHE astronomy (Abe et al. 2024) and will be more suitable to detect extended sources such as pulsar halos due to its larger field of view compared to H.E.S.S. CTAO will help close the gap between IACT and Direct EAS detector pulsar halo populations, with Geminga and Monogem-like halos possibly detectable at a distance of 3 kpc with a moderate amount of exposure (which is not the case for H.E.S.S.). In the long term, the Southern Wide-Field Gamma-ray Observatory (SWGO), could unveil a new population of halos in the southern hemisphere. These instruments in tandem will enrich the known population by increasing the diversity of PWNe/pulsar halo populations in terms of their Galactic environments and associated pulsar properties, and may help identify defining trends to discriminate between the populations of PWNe and pulsar halos.

Bibliography

Aab, A., Abreu, P., Aglietta, M., et al. 2020, Phys. Rev. D, 102, 062005

Abbasi, R. U., Abu-Zayyad, T., Allen, M., et al. 2008, Phys. Rev. Lett., 100, 101101

Abdalla, H., Aharonian, F., Ait Benkhali, F., et al. 2021, The Astrophysical Journal, 917, 6

Abdollahi, S., Acero, F., Ackermann, M., et al. 2020, The Astrophysical Journal Supplement Series, 247, 33

Abe, S., Abhir, J., Abhishek, A., et al. 2024, Journal of Cosmology and Astroparticle Physics, 2024, 081

Abeysekara, A., Alfaro, R., Alvarez, C., et al. 2013, Astroparticle Physics, 50-52, 26

Abeysekara, A. U., Albert, A., Alfaro, R., et al. 2018, Nature, 562, 82

Abeysekara, A. U., Albert, A., Alfaro, R., et al. 2017, Science, 358, 911

Abraham, J., Aglietta, M., Aguirre, I., et al. 2004, Nuclear Instruments and Methods in Physics Research Section A: Accelerators, Spectrometers, Detectors and Associated Equipment, 523, 50

Accardo, L., Aguilar, M., Aisa, D., et al. 2014, Phys. Rev. Lett., 113, 121101

Acero, Aharonian, F., Akhperjanian, A. G., et al. 2010, Astronomy and Astrophysics, 516, A62

Acero, F., Bernete, J., Biederbeck, N., et al. 2024, Gammapy v1.2: Python toolbox for gamma-ray astronomy, URL: https://doi.org/10.5281/zenodo.10726484

Ackermann, M., Ajello, M., Allafort, A., et al. 2011, Science, 334, 1103

Ackermann, M., Ajello, M., Atwood, W. B., et al. 2012, The Astrophysical Journal, 750, 3

Aguilar, M., Alberti, G., Alpat, B., et al. 2013, Phys. Rev. Lett., 110, 141102

Aguilar, M., Ali Cavasonza, L., Ambrosi, G., et al. 2016, Phys. Rev. Lett., 117, 231102

Aharonian, F., Akhperjanian, A. G., Bazer-Bachi, A. R., et al. 2006, Astronomy and Astrophysics, 460, 743

Aharonian, F., An, Q., Axikegu, et al. 2021, Phys. Rev. Lett., 126, 241103

Aharonian, F., An, Q., Axikegu, et al. 2021, Chinese Physics C, 45, 025002

Aharonian, F., Ashkar, H., Backes, M., et al. 2026, arXiv e-prints, arXiv:2602.14640

Aharonian, F., Ashkar, H., Backes, M., et al. 2022, Astronomy and Astrophysics, 666, A124

Aharonian, F., Benkhali, F. A., Aschersleben, J., et al. 2023, Nature Astronomy, 7, 1341

Aharonian, F., Benkhali, F. A., Aschersleben, J., et al. 2024, Phys. Rev. Lett., 133, 221001

Aharonian, F., Yang, R., & de Oña Wilhelmi, E. 2019, Nature Astronomy, 3, 561

Albert, A., Alfaro, R., Alvarez, C., et al. 2024, The Astrophysical Journal, 974, 246

Albert, A., Alfaro, R., Alvarez, C., et al. 2020, The Astrophysical Journal, 905, 76

Albert, A., Alfaro, R., Arteaga-Velázquez, J. C., et al. 2023, The Astrophysical Journal Letters, 944, L29

Amato, E. & Recchia, S. 2024, La Rivista del Nuovo Cimento, 47, 399

Ansoldi, S., Antonelli, L. A., Antoranz, P., et al. 2016, Astronomy and Astrophysics, 585, A133

Apel, W., Arteaga-Velázquez, J., Bekk, K., et al. 2013, Astroparticle Physics, 47, 54

Becherini, Y., Djannati-Ataï, A., Marandon, V., Punch, M., & Pita, S. 2011, Astroparticle Physics, 34, 858

Becker Tjus, J. & Merten, L. 2020, Physics Reports, 872, 1

Blumenthal, G. R. & Gould, R. J. 1970, Rev. Mod. Phys., 42, 237

Brinkmann, W., Aschenbach, B., & Kawai, N. 1996, Astronomy and Astrophysics, 312, 306

Bucciantini, N., Arons, J., & Amato, E. 2010, Monthly Notices of the Royal Astronomical Society, 410, 381

Cao, Z., Aharonian, F., An, Q., et al. 2024a, Chinese Physics C, 48, 065001

Cao, Z., Aharonian, F., An, Q., et al. 2024b, The Astrophysical Journal Supplement Series, 271, 25

Cao, Z., Aharonian, F., Axikegu, et al. 2025, Science China Physics, Mechanics, and Astronomy, 68, 279504

Carrigan, S., Hinton, J. A., Hofmann, W., et al. 2008, in International Cosmic Ray Conference, Vol. 2, International Cosmic Ray Conference, 659–662

Cash, W. 1979, Astrophysical Journal, 228, 939

Cavanaugh, J. E. & Neath, A. A. 2019, WIREs Computational Statistics, 11, e1460

Chambéry, P., Gallant, Y., Jardin-Blicq, A., et al. 2024, in 7th Heidelberg International Symposium on High-Energy Gamma-Ray Astronomy, 135

Chang, J., Ambrosi, G., An, Q., et al. 2017, Astroparticle Physics, 95, 6

Clark, G. W., Garmire, G. P., & Kraushaar, W. L. 1968, , 153, L203

Coleman, A. 2020, PoS, ICRC2019, 225

Collins, T., Rowell, G., Einecke, S., et al. 2024, Monthly Notices of the Royal Astronomical Society, 528, 2749

Cristofari, P. 2021, Universe, 7

CTAO & Consortium, C. T. A. 2021, CTAO Instrument Response Functions - prod5 version v0.1, URL: https://doi.org/10.5281/zenodo.5499840

Dame, T. M., Hartmann, D., & Thaddeus, P. 2001, The Astrophysical Journal, 547, 792

de Naurois, M. 2012, Accreditation to supervise research, Université Pierre et Marie Curie - Paris VI

de Oña Wilhelmi, E., López-Coto, R., Amato, E., & Aharonian, F. 2022, The Astrophysical Journal Letters, 930, L2

Delahaye, T., Lavalle, J., Lineros, R., Donato, F., & Fornengo, N. 2010, Astronomy and Astrophysics, 524, A51

Devin, J., Lemière, A., Streil, K., Terrier, R., & van Eldik, C. 2025, arXiv e-prints, arXiv:2507.00132

Donath, A., Terrier, R., Remy, Q., et al. 2023, Astronomy and Astrophysics, 678, A157

Eckner, C., Vodeb, V., Martin, P., Zaharijas, G., & Calore, F. 2023, Monthly Notices of the Royal Astronomical Society, 521, 3793

Evoli, C. 2025, The Cosmic-Ray Energy Spectrum, URL: https://doi.org/10.5281/zenodo.14635074

Evoli, C., Morlino, G., Blasi, P., & Aloisio, R. 2020, Phys. Rev. D, 101, 023013

Fang, K., Bi, X.-J., & Yin, P.-F. 2019, Monthly Notices of the Royal Astronomical Society, 488, 4074

Fang, K., Bi, X.-J., Yin, P.-F., & Yuan, Q. 2018, The Astrophysical Journal, 863, 30

Fang, K., Xi, S.-Q., Bao, L.-Z., Bi, X.-J., & Chen, E.-S. 2022, Phys. Rev. D, 106, 123017

Faucher-Giguère, C.-A. & Kaspi, V. M. 2006, The Astrophysical Journal, 643, 332

Fenu, F. & Pierre Auger Collaboration. 2017, in International Cosmic Ray Conference, Vol. 301, 35th International Cosmic Ray Conference (ICRC2017), 486

Fletcher, R. & Powell, M. J. D. 1963, The Computer Journal, 6, 163

Gabici, S., Evoli, C., Gaggero, D., et al. 2019, International Journal of Modern Physics D, 28, 1930022

Gaisser, T. K., Engel, R., & Resconi, E. 2016, Cosmic Rays and Particle Physics, 2nd edn. (Cambridge University Press)

Gaug, M., Fegan, S., Mitchell, A. M. W., et al. 2019, The Astrophysical Journal Supplement Series, 243, 11

Gelfand, J. D., Slane, P. O., & Zhang, W. 2009, The Astrophysical Journal, 703, 2051

Genzel, R., Eisenhauer, F., & Gillessen, S. 2010, Rev. Mod. Phys., 82, 3121

Giacinti, G., Mitchell, A. M. W., López-Coto, R., et al. 2020, Astronomy and Astrophysics, 636, A113

Gonthier, P. L., Ouellette, M. S., Berrier, J., O'Brien, S., & Harding, A. K. 2002, The Astrophysical Journal, 565, 482

Greisen, K. 1956, Progress in Cosmic Ray Physics, 3, 1

Halpern, J. P. & Ruderman, M. 1993, Astrophysical Journal, 415, 286

Hayakawa, S. 1952, Progress of Theoretical Physics, 8, 571

Heitler, W. 1954, Quantum theory of radiation (Oxford University Press)

Hermsen, W. 1983, Space Science Reviews, 36, 61

H.E.S.S. Collaboration. 2018a, Astronomy and Astrophysics, 612, A8

H.E.S.S. Collaboration. 2018b, Astronomy and Astrophysics, 612, A9

H.E.S.S. Collaboration. 2018c, Astronomy and Astrophysics, 612, A7

H.E.S.S. Collaboration. 2018d, Astronomy and Astrophysics, 612, A1

H.E.S.S. Collaboration. 2018e, Astronomy and Astrophysics, 612, A6

H.E.S.S. Collaboration. 2018f, Astronomy and Astrophysics, 612, A2

H.E.S.S. Collaboration. 2019a, Astronomy and Astrophysics, 627, A100

H.E.S.S. Collaboration. 2019b, Astronomy and Astrophysics, 621, A116

H.E.S.S. Collaboration. 2023a, Astronomy and Astrophysics, 673, A148

H.E.S.S. Collaboration. 2023b, Astronomy and Astrophysics, 672, A103

H.E.S.S. Collaboration. 2024a, Science, 383, 402

H.E.S.S. Collaboration. 2024b, Astronomy and Astrophysics, 686, A149

H.E.S.S. Collaboration, Abramowski, A., Aharonian, F., et al. 2015, Astronomy and Astrophysics, 574, A27

Hobbs, G., Faulkner, A., Stairs, I. H., et al. 2004, Monthly Notices of the Royal Astronomical Society, 352, 1439

Hobbs, G., Lorimer, D. R., Lyne, A. G., & Kramer, M. 2005, Monthly Notices of the Royal Astronomical Society, 360, 974

Hobbs, G., Lorimer, D. R., Lyne, A. G., & Kramer, M. 2005, Monthly Notices of the Royal Astronomical Society, 360, 974

Jackson, J. M., Rathborne, J. M., Shah, R. Y., et al. 2006, The Astrophysical Journal Supplement Series, 163, 145

James, F. & Roos, M. 1975, Computer Physics Communications, 10, 343

Jansson, R. & Farrar, G. R. 2012, The Astrophysical Journal Letters, 761, L11

Kafexhiu, E., Aharonian, F., Taylor, A. M., & Vila, G. S. 2014, Phys. Rev. D, 90, 123014

Khangulyan, D., Aharonian, F. A., & Kelner, S. R. 2014, Astrophysical Journal, 783, 100

Khelifi, B., Djannati-Ataï, A., Jouvin, L., et al. 2015, in PoS, Vol. ICRC2015, The Hague, Netherlands, 837

Kraichnan, R. H. 1965, The Physics of Fluids, 8, 1385

LHAASO Collaboration. 2021, Science, 373, 425

LHAASO Collaboration. 2024, Science Bulletin, 69, 449

Lhaaso Collaboration, Cao, Z., Aharonian, F., et al. 2025, National Science Review, 12, nwaf496

Liu, R.-Y., Yan, H., & Zhang, H. 2019, Phys. Rev. Lett., 123, 221103

Lorimer, D. R. & Kramer, M. 2004, Handbook of Pulsar Astronomy, Vol. 4 (Cambridge University Press)

Lu, F.-W., Zhu, B.-T., Hu, W., & Zhang, L. 2022, Monthly Notices of the Royal Astronomical Society, 518, 3949

Manchester, R. N., Hobbs, G. B., Teoh, A., & Hobbs, M. 2005, The Astronomical Journal, 129, 1993

Martin, P., de Guillebon, L., Collard, E., et al. 2024, Astronomy and Astrophysics, 690, A116

Martin, P., Marcowith, Alexandre, & Tibaldo, Luigi. 2022, Astronomy and Astrophysics, 665, A132

Moderski, R., Sikora, M., Coppi, P. S., & Aharonian, F. 2005, Monthly Notices of the Royal Astronomical Society, 363, 954

Mohrmann, L., Specovius, A., Tiziani, D., et al. 2019, Astronomy and Astrophysics, 632, A72

Parsons, R. & Hinton, J. 2014, Astroparticle Physics, 56, 26

Pavlov, G. G., Bhattacharyya, S., & Zavlin, V. E. 2010, The Astrophysical Journal, 715, 66

Planck Collaboration. 2011, Astronomy and Astrophysics, 536, A19

Ponti, G., Terrier, R., Goldwurm, A., Belanger, G., & Trap, G. 2010, The Astrophysical Journal, 714, 732

Popescu, C. C., Yang, R., Tuffs, R. J., et al. 2017, Monthly Notices of the Royal Astronomical Society, 470, 2539

Posselt, B., Pavlov, G. G., Slane, P. O., et al. 2017, The Astrophysical Journal, 835, 66

Pétri, J. 2012, Monthly Notices of the Royal Astronomical Society, 424, 2023

Regeard, M., Arache, D.-A., & Léa, D. 2025, PoS, ICRC2025, 820

Riviere, C., Fleischhack, H., & Sandoval, A. 2017, The Astronomer's Telegram, 10941, 1

Ruszkowski, M. & Pfrommer, C. 2023, The Astronomy and Astrophysics Review, 31, 4

Rybicki, G. B. & Lightman, A. P. 1979, Radiative processes in astrophysics (John Wiley and Sons, Ltd)

Seo, E. S., Ahn, H. S., Beatty, J. J., et al. 2004, Advances in Space Research, 33, 1777

Shapiro, S. L. & Teukolsky, S. A. 1983, Black holes, white dwarfs and neutron stars. The physics of compact objects (John Wiley and Sons, Ltd)

Sheidaei, Djannati-Ataï, & Gast. 2011, in International Cosmic Ray Conference, Vol. 7, International Cosmic Ray Conference, 244

Siemiginowska, A., Burke, D., Günther, H. M., et al. 2024, The Astrophysical Journal Supplement Series, 274, 43

Smith, A. J. 2005, in International Cosmic Ray Conference, Vol. 10, 29th International Cosmic Ray Conference (ICRC29), Volume 10, ed. B. S. Acharya, S. Gupta, P. Jagadeesan, A. Jain, S. Karthikeyan, S. Morris, & S. Tonwar, 227

Su, M., Slatyer, T. R., & Finkbeiner, D. P. 2010, The Astrophysical Journal, 724, 1044

Syrovatskii, S. I. 1959, Soviet Astronomy, 3, 22

Tang, X. & Piran, T. 2019, Monthly Notices of the Royal Astronomical Society, 484, 3491

Tibaldo, L., Gaggero, D., & Martin, P. 2021, Universe, 7

Torii, S. 2007, Nuclear Physics B - Proceedings Supplements, 166, 43, proceedings of the Third International Conference on Particle and Fundamental Physics in Space

Tsuboi, M., Handa, T., & Ukita, N. 1999, The Astrophysical Journal Supplement Series, 120, 1

Turner, J. D., Stappers, B. W., Carli, E., et al. 2024, Monthly Notices of the Royal Astronomical Society, 531, 3579

Uchiyama, Y., Funk, S., Katagiri, H., et al. 2012, The Astrophysical Journal Letters, 749, L35

Vincent, P. 2005, in International Cosmic Ray Conference, Vol. 5, 29th International Cosmic Ray Conference (ICRC29), Volume 5, ed. B. S. Acharya, S. Gupta, P. Jagadeesan, A. Jain, S. Karthikeyan, S. Morris, & S. Tonwar, 163

Wach, T. & Mitchell, A. M. W. 2025, arXiv e-prints, arXiv:2510.02802

Wach, T., Mitchell, A., & Mohrmann, L. 2024, Astronomy and Astrophysics, 690, A250

Weekes, T. C., Cawley, M. F., Fegan, D. J., et al. 1989, Astrophysical Journal, 342, 379

Wilks, S. S. 1938, The Annals of Mathematical Statistics, 9, 60

Xian, Y., Yu, H., Zhou, L., & Fang, J. 2026, The Astrophysical Journal, 997, 213

Yao, J. M., Manchester, R. N., & Wang, N. 2017, Astrophysical Journal, 835, 29

Zabalza, V. 2015, in International Cosmic Ray Conference, Vol. 34, 34th International Cosmic Ray Conference (ICRC2015), 922

Zhang, Y., Liu, R.-Y., Chen, S. Z., & Wang, X.-Y. 2021, The Astrophysical Journal, 922, 130

Thesis summary (French version)

L'astronomie en rayons γ sonde le ciel en photons dans la gamme d'énergie du MeV au PeV, qui comprend le signal électromagnétique émis par les particules chargées relativistes galactiques et extra-galactiques dans leur accélérateurs et lors de leur propagation. Dans la Voie Lactée, l'accélération de ces particules a lieu dans des chocs associés aux objets stellaires, des évènements de reconnection magnétique et des collisions entre vents. Ces particules se propagent dans le milieu interstellaire (MIS), interagissant avec les noyaux du gaz interstellaire, les champs de photons produits par les étoiles et la poussière interstellaire, le Fond Diffus Cosmologique (CMB, Cosmic Microwave Background) et le champ magnétique galactique. Les particules chargées relativistes baignant la Voie Lactée sont appelées "rayons cosmiques" (RC).

Les RC interagissent avec le milieu ambiant et produisent des rayonnements électromagnétiques. L'émission synchrotron est le rayonnement cyclotron focalisé produit par des particules chargées ultra-relativistes dans un champ magnétique, qui peut être observé du domaine radio jusqu'au MeV, principalement dû aux électrons et positrons car la fréquence de gyration des protons est plus faible. La diffusion Compton est le processus dans lequel un photon incident est diffusé par un électron. Si l'électron est relativiste, il perd de l'énergie dans le référentiel de l'observateur. On appelle cela la diffusion Compton inverse (ICS, inverse Compton scattering), qui peut être observée jusqu'au PeV dû aux électrons et positrons interagissant avec les champs de rayonnement des étoiles, de la poussière, et du CMB. Les charges accélérées dans le champ coulombien d'un noyau émettent du rayonnement bremsstrahlung (émission de freinage), qui peut être observé du domaine radio jusqu'aux rayons γ, principalement dû à des leptons à cause de la masse supérieure des protons. Les collisions inélastiques de hadrons (par exemple entre les rayons cosmiques et les noyaux du milieu interstellaire) produisent des pions neutres et chargés en proportions approximativement égales. Les pions neutres de désintègrent en deux photons, et le spectre observé est caractérisé par une bosse à ~ 280 MeV.

Les électrons et positrons cosmiques subissent des pertes d'énergie à des échelles de temps beaucoup plus courtes que les RC hadroniques, et ceux mesurés sur Terre sont donc produits par des accélérateurs proches. Ainsi, le flux local d'électrons et positrons cosmiques implique que la ou les source(s) doivent être situées à moins de $\sim$1 kpc. L'abondance des électrons relative à celle des positrons indique que ces premiers sont des particules primaires, car il est attendu que les électrons et positrons secondaires, produits par la spallation des RC lors de leur propagation dans le MIS, aient des abondances similaires. Une augmentation de la fraction de positrons est observée dans les données AMS-02 à partir de ~ 10 GeV, et peut être expliquée comme étant due à des sources de positrons primaires (comme les nébuleuses de vent de pulsar) et/ou à la signature d'interactions de matière noire dans le halo galactique. Ce résultat est appelé "l'excès de positrons". Ainsi, contraindre la population d'accélérateurs proches comme les nébuleuses de vent de pulsar présente un grand intérêt.

Les gerbes atmosphériques sont des cascades de réactions initiées lors de l'incidence d'un photon γ ou d'un RC sur l'atmosphère terrestre. Les rayons γ dans l'atmosphère terrestre initient une production de paires $e^{-/+}$ en interagissant avec les champs coulombiens des noyaux. Les paires produites interagissent à leur tour avec les champs coulombiens des noyaux pour produire des rayons γ par rayonnement de freinage. D'une manière similaire, des gerbes sont produites par les RC hadroniques entrant dans l'atmosphère. Celles-ci aboutissent à la création de pions neutres et chargés qui se désintègrent en rayons γ, muons et $e^{-/+}$ secondaires.

Les RC sont déviés par le champ magnétique galactique avant leur arrivée sur Terre. L'étude des sources de RC nécessite donc notamment l'observation du signal électromagnétique qu'ils émettent dans leurs accélérateurs. Dans la gamme d'énergie des photons du TeV au PeV, les observations sont effectuées au sol pour assurer les surfaces de détection nécessaires à des mesures précises du flux de photons. Cela peut impliquer la détection du signal Tcherenkov émis par les particules produites dans les gerbes induites par des rayons γ entrant dans l'atmosphère terrestre. Les télescopes à imagerie Tcherenkov atmosphérique (IACT, Imaging Atmospheric Cherenkov Telescope) reposent sur la détection de la gerbe en utilisant des caméras UV-optiques. La direction et l'énergie du photon primaire sont reconstruites par les images du signal Tcherenkov produit par les particules de la gerbe atmosphérique. Bien que le champ de vue de ces instruments soit limité à quelques degrés, ils possèdent la meilleure résolution angulaire en astronomie γ (quelques minutes d'arc), et couvrent la gamme d'énergie de 0.1 à 100 TeV, aussi connue comme la gamme de très haute énergie (VHE, Very High Energy). Dans cette gamme, le signal des sources astrophysiques est souvent dominant par rapport au signal de l'émission interstellaire à grande échelle produite par les RC dans le plan galactique. Ces observatoires sont ainsi adaptés pour des analyses détaillées des sources. Dans les deux dernières décennies, les IACT ont montré qu'une grande diversité de sources sont des émetteurs efficaces de rayons γ VHE, comme les pulsars et leurs nébuleuses, les restes de supernova, les amas stellaires massifs, les systèmes binaires et les noyaux actifs de galaxies. L'expérience H.E.S.S. a une situation unique dans l'hémisphère Sud et fournit une vue détaillée des régions intérieures de la Galaxie. Le catalogue du relevé du plan galactique par H.E.S.S. (HGPS, H.E.S.S. Galactic Plane Survey) contient 78 sources à des latitudes galactiques $|b| \leq 3°$, dont 28 qui sont identifiées comme étant les contreparties de nébuleuses de vent de pulsar, de restes de supernova, ou les deux (i.e. de systèmes composites).

Les étoiles massives subissent un effondrement de coeur à la fin de leur vie, en éjectant la majorité de leur enveloppe stellaire et en créant un objet compact, qui peut être une étoile à neutrons en rotation rapide: un pulsar. Les pulsars jeunes produisent une nébuleuse dans laquelle les électrons et les positrons sont confinés dans le champ magnétique de la nébuleuse, qui provient du pulsar. Ces nébuleuses de vent de pulsar (PWNe, pulsar wind nebulae) constituent une catégorie importante de sources γ et contibuent potentiellement de manière importante au spectre local des positrons cosmiques. Les électrons et positrons s'étant échappés des pulsars d'âge moyen ($\gtrsim 40$ kyr), détectés aux VHE, permettent d'étudier l'échappement de particules de leur PWNe et les étapes tardives de leur évolution. Ce phénomène est appelé "halo de pulsar". Les halos des pulsars d'âge moyen permettent de contraindre la contribution des PWNe au flux local d'électrons et de positrons. Seul un petit nombre de sources aux très hautes énergies sont proposées comme étant des halos identifiés ou candidats, et la distinction entre PWN et halo de pulsar n'est pas évidente dans les données aux VHE. Etendre le nombre et la

diversité de la population de halos de pulsar connue permettrait de mieux comprendre les conditions favorisant leur formation. Dans cette thèse, nous étudions ces halos de pulsars avec les données de H.E.S.S., une expérience de télescopes à imagerie Tcherenkov atmosphérique.

En 2017, les données de HAWC ont révélé deux structures en rayons γ très étendues autour des pulsars de Geminga (PSR J0633+1746) et de Monogem (PSR B0656+15) dans la gamme de 8 à 40 TeV. L'émission autour de chaque pulsar s'étend sur plusieurs degrés dans le ciel. Ces pulsars sont moyennement évolués, avec un âge caractéristique de 342 kyr pour Geminga et 110 kyr pour Monogem. Le pulsar de Geminga, un pulsar silencieux en radio détecté dans les gammes d'énergie des rayons X et du GeV, est entouré par une nébuleuse observée en rayons X notamment par l'observatoire Chandra avec une extension de quelques minutes d'arc. Ainsi, étant donnée la distance entre la Terre et le pulsar de 250 pc, l'émission aux VHE trace le transport d'$e^{-/+}$ à une échelle plus grande ($\sim$ 20 pc) que celle des rayons X ($\lesssim$ 1 pc). Cette différence importante de taille est due aux échelles de temps de pertes d'énergies différentes, de sorte que la composante de rayons X trace une population d'$e^{-/+}$ confinée et plus jeune que la population responsable de l'émission aux VHE par l'ICS. Les âges des pulsars de Geminga et de Monogem sont significativement plus grands que ceux de la majorité des PWNe détectées aux TeV, et il est possible que les pulsars aient quitté leurs restes de supernova (SNR, supernova remnant), sachant que le pulsar de Geminga à traversé une distance de $\sim$ 70 pc depuis sa naissance. Ces caractéristiques justifient la distinction entre PWN et halo de pulsar.

Au long de cette thèse, nous adoptons un modèle fréquemment utilisé des halos de pulsars, qui reproduit adéquatement les caractéristiques de la morphologie et du spectre de l'émission γ autour des pulsars de Geminga et de Monogem dans les données HAWC. Les $e^{-/+}$ produits dans la magnétosphère du pulsar, qui sont ré-accélérés au choc entre le vent de pulsar et la nébuleuse synchrotron, diffusent le long des lignes de champ magnétique dans la PWN, où le processus dominant de transport des particules est l'advection alimentée par la rotation du pulsar. Ultimement, ces particules s'échappent de la PWN dans le MIS et diffusent le long des lignes de champ magnétique du MIS. Le halo émerge pendant les étapes tardives de l'évolution du système pulsar-PWN-SNR, quand l'échappement des particules est favorisé par la perturbation de la PWN due à son interaction avec le SNR, ou car le pulsar a quitté le SNR à cause de la vitesse de "kick" dont il a hérité suite à l'asymétrie de la supernova, et forme une nébuleuse à choc en arc.

Dans ce modèle, les $e^{-/+}$ sont injectés de manière continue par une PWN de taille négligeable par rapport à l'extension de l'émission aux VHE par ICS, et ils diffusent dans le MIS. Le MIS est caractérisé par un coefficient de diffusion supposé isotrope et homogène, un champ magnétique uniforme, et les champs de rayonnement cibles du ICS. Le modèle prédit que dans la gamme de H.E.S.S., l'émission γ est fortement impactée morphologiquement et spectralement par l'âge du pulsar, dû à la contribution des $e^{-/+}$ reliques qui se refroidissent (i.e. qui perdent de l'énergie) tout au long de l'évolution du pulsar. Ainsi, le mouvement propre du pulsar introduit une asymétrie dans la gamme de H.E.S.S., s'il est suffisamment âgé et proche. Cette asymétrie se manifeste comme une structure allongée qui est visible aux énergies les plus basses car produite par des $e^{-/+}$ reliques. La contribution principale à l'émission ICS provient du rayonnement infrarouge de la poussière, tandis que dans la gamme de HAWC, il s'agit du CMB.

Nous utilisons ce modèle pour créer des "templates" spectro-morphologiques de halos de pulsar pour plusieurs valeurs de la normalisation du coefficient de diffusion à 100 TeV, la période initiale du pulsar, l'indice du spectre d'injection de $e^{-/+}$, leur effi-

cacité d'injection et la vitesse transverse du pulsar. Les "templates" sont utilisés pour créer des modèles dans la librairie Gammapy pour l'analyse spectro-morphologique des données de H.E.S.S. (et des IACT en général).

Nous cherchons des candidats de halo de pulsar parmi les composantes du HGPS à travers leur coïncidence spatiale avec des pulsars d'âge moyen, après avoir rejeté les sources H.E.S.S. identifiées comme ayant une origine astrophysique différente d'un halo de pulsar. Nous avons construit une liste de 20 sources du HGPS qui méritent potentiellement d'être ré-étudiées avec des analyses spectro-morphologiques dédiées. De plus, nous trouvons 4 associations plausibles entre candidat de halo du HGPS, pulsar d'âge moyen et composante détectée par l'experience LHAASO aux ultra hautes énergies (UHE), qui sont compatibles morphologiquement et spectralement dans la gamme des VHE aux UHE. Les candidats de halo du HGPS sont généralement plus jeunes que les halos candidats ou identifiés proposés HAWC et LHAASO. Nous mettons en évidence 13 pulsars d'âge moyen suffisamment lointains et puissants sans coïncidence spatiale avec une composante du HGPS, qui pourraient potentiellement avoir un halo ou une PWN détectable avec davantage d'heures d'observations.

Cette recherche a motivé l'étude spectro-morphologique d'un candidat halo du HGPS, HESS J1831−098, en utilisant les "templates" de halo et en supposant que le halo est produit par l'un des pulsars énergétiques PSR J1831−0952 ou PSR J1831−0941 coïncidant avec la région d'émission aux VHE.

L'émission γ est bien décrite par un modèle de halo de pulsar alimenté par PSR J1831 −0952, bien que le modèle ne soit pas significativement préféré par rapport à un modèle simple de morphologie gaussienne à deux dimensions et un spectre de loi de puissance. La valeur estimée de la normalisation du coefficient de diffusion dans le halo de HESS J1831 −098 est statistiquement compatible avec celles qui ont été trouvées par HAWC dans le cas de Geminga et Monogem. L'efficacité d'injection estimée est plausible pour une source alimentée par un pulsar, mais nous trouvons une contrainte faible avec $\eta \sim 3 - 20\%$ à cause de la corrélation entre ce paramètre et la période initiale du pulsar, qui paramétrise l'âge du pulsar. Cela est dû au fait que la source n'est pas significative au-delà de 10 TeV dans les données H.E.S.S. Nous estimons un indice spectral d'injection des $e^{-/+}$ significativement plus mou ($\Gamma \sim 2$) que celui de Geminga et Monogem mesuré par HAWC ($\Gamma \sim 1$). L'inclusion de la vitesse propre dans le modèle n'est pas significative, améliorant la vraisemblance par seulement $\sim 2.1\sigma$ (avec deux degrés de liberté). D'autre part, nous déterminons une limite inférieure avec un niveau de confiance de 68% sur l'énergie de coupure de l'injection de 30 TeV. Quand l'énergie de coupure est supposée de 1 PeV, HESS J1831−098 est compatible morphologiquement et spectralement avec les possibles contreparties UHE 1LHAASO J1831−1007u* et 3HWC J1831−095. Nous étudions également le scenario où le pulsar moins énergétique PSR J1831−0941 produit le halo. Les résultats préliminaires suggèrent que ce pulsar pourrait ne pas être suffisamment puissant pour produire l'émission γ, nécessitant une efficacité d'injection possiblement supérieure à 100%.

Ces modèles de halo ont ensuite été utilisés pour simuler des observations avec H.E.S.S. et le futur Cherenkov Telescope Array Observatory (CTAO), afin d'évaluer la capacité de ces expériences à détecter et identifier les halos. Le pulsar est supposé avoir une période actuelle de 80 ms, un âge caractéristique de 100 kyr et une distance de 3 kpc. Un espace de paramètres a été exploré, avec plusieurs valeurs de la normalisation du coefficient de diffusion (D_0 de $\sim 1.3 \times 10^{26}$ cm^2 s^{-1} à $\sim 5 \times 10^{27}$ cm^2 s^{-1} à 100 TeV), de la vitesse transverse du pulsar (V_{PSR} de 0 à ~ 943 km/s) et de la période initiale du

pulsar (un cas "âgé" avec $P_0 \sim 28.3$ ms et un cas "jeune" avec $P_0 \sim 68.9$ ms). Différents paramètres du spectre d'injection sont considérés, avec $\Gamma = 1$ ou 2 et l'énergie de coupure de l'injection $E_c = 100$ TeV ou 1 PeV. Ainsi, nous examinons 120 différentes combinaisons de paramètres du modèle. Pour chaque combinaison, nous effectuons 160 réalisations de la simulation. Dans chaque réalisation, une analyse spectro-morphologique est effectuée, en ajustant le modèle de "templates" de halo en premier temps, et un modèle contenant des gaussiennes 2D avec des spectres en loi de puissance en deuxième temps. La préférence statistique entre le modèle de halo et celui de gaussiennes est déterminée avec le Critère d'Information d'Akaike en calculant le ΔAIC.

Les résultats montrent que la morphologie peut être fortement asymétrique dans le cas du pulsar "âgé" avec une vitesse propre $\gtrsim 400$ km/s et une normalisation faible du coefficient de diffusion de l'ordre de 10^{26} cm^2 s^{-1}. Cependant, dans les données réelles, nous pouvons nous attendre à moins d'asymétrie, car les vitesses transverses des pulsars connus ont une moyenne entre $300 - 400$ km/s et les cas avec $V_{PSR} \sim 1000$ km/s sont rares. L'asymétrie devrait aussi être moindre si le coefficient de diffusion des halos est plus similaire à ceux de Geminga et de Monogem (de l'ordre de 10^{27} cm^2 s^{-1}). De plus, la majorité des PWNe identifiées et candidates dans les données H.E.S.S. se trouvent à une distance plus grande que 3 kpc en moyenne, ce qui réduirait la détectabilité de l'asymétrie car la source serait plus compacte.

Dans le cas "âgé", avec un indice d'injection dur $\Gamma = 1$, une gaussienne secondaire est détectée dans 46.5% des réalisations avec H.E.S.S., et pour $\Gamma = 2$, c'est le cas dans 25.6% des réalisations. La fréquence de détection d'une gaussienne secondaire est relativement négligeable pour le cas "jeune". La détection d'une gaussienne secondaire avec CTAO a lieu dans plus de $\sim 90\%$ dans le cas "âgé" et n'est pas négligeable dans le cas "jeune".

D'autre part, dans le cas "âgé", H.E.S.S. arrive parfois à discriminer entre un halo et une gaussienne 2D avec un spectre en loi de puissance, alors que cela est le cas pour la majorité de l'espace des paramètres explorés avec CTAO. Toutefois, l'identification des halos devrait être plus difficile étant donné les distances des PWNe détectées dans les données H.E.S.S. D'autre part, nous utilisons dans notre étude une simple loi de puissance pour le spectre des composantes gaussiennes, alors que des spectres avec courbure comme une parabole logarithmique ou l'inclusion d'une coupure reproduiraient mieux le spectre simulé du halo, ce qui réduirait le ΔAIC en faveur du modèle de halo ajusté.

L'émission interstellaire à grande échelle n'est pas incluse dans cette étude. Il est attendu que celle-ci réduise la significativité de la source simulée et notre capacité à la caractériser. De plus, de par la confusion de sources pour les halos plus diffus, la composante plus étendue et ayant le spectre le plus mou de $e^{-/+}$ pourrait être noyée par l'émission interstellaire.

Notons que, pour un halo simulé avec des paramètres similaires à ceux de HESS J1831 −098 et PSR J1831−0952 (qui a une période actuelle de 67 ms et un âge caractéristique de 128 kyr) qui résultent de notre analyse de données précédente (e.g. $D_0 \sim 4.9 \times 10^{27}$ cm^2 s^{-1}, $V_{PSR} = 0$, $P_0 \sim 28.3$ ms, $\Gamma = 2$), nous retrouvons dans les simulations un ΔAIC similaire à ce que nous retrouvons dans l'analyse des données sur HESS J1831−098. Si le scénario astrophysique à l'origine de HESS J1831−098 est réellement un halo de pulsar alimenté par PSR J1831−0952, le ΔAIC avec CTAO pourrait être ~ 10 fois plus important.

Dans les futurs relevés du plan galactique avec H.E.S.S. (2HGPS) ou CTAO, les sources détectées avec une gaussienne secondaire au spectre plus mou ou avec une composante asymétrique pourraient pointer vers l'existence de deux populations distinctes de

$e^{-/+}$ (avec des âges et énergies différents). Ainsi, les sources caractérisées par plusieurs composantes pourraient être ré-étudiées pour trouver des halos de pulsars dans la Galaxie, particulièrement avec une approche basée sur des "templates" et idéalement avec des analyses conjointes de données de différentes expériences de rayons γ (IACT et détecteurs directs de gerbes en tandem).

À court terme, la poursuite du développement des méthodes d'analyses conjointes H.E.S.S. et HAWC, qui sont déjà disponibles dans la librairie Gammapy, pourra améliorer les contraintes sur les sources alimentées par des pulsars d'âges moyens. L'analyse de HESS J1831−098 pourrait déjà bénéficier de l'inclusion des données HAWC dans une analyse conjointe, l'accès à une gamme d'énergie plus haute étant crucial pour réduire la corrélation entre les paramètres du modèle de halo. La contrepartie HAWC de HESS J1831−098 étant possiblement significative jusqu'à 100 TeV, cela permettrait de rompre la dégénérescence du modèle entre l'efficacité d'injection, qui joue le rôle de normalisation, et l'âge du pulsar, qui gouverne la contribution des $e^{-/+}$ reliques à des énergies en-dessous de ~ 10 TeV.

Dans le futur, le relevé du plan galactique avec CTAO améliorera significativement la population de PWNe dans l'astronomie γ aux VHE et sera plus approprié pour la détection de sources étendues comme les halos. CTAO réduira l'écart des populations de PWNe et de halos entre les IACTs et les détecteurs directs de gerbes, avec des halos similaires à ceux de Geminga et Monogem possiblement détectables à des distances de 3 kpc avec un temps d'exposition raisonnable (ce qui n'est pas le cas avec H.E.S.S.). Dans le long terme, le Southern Wide-field Gamma-ray Observatory (SWGO) pourrait révéler une nouvelle population de halos de pulsars dans l'hémisphère Sud. Ces instruments en tandem enrichiraient la population connue en augmentant la diversité de PWNe/halos de pulsar en termes d'environnements galactiques et de propriétés de pulsars qui leur sont associés, et pourraient aider à définir des tendances observationnelles afin de mieux séparer les populations des PWNe et des halos.

Appendix: HESS J1831−098

Results with the CO template

Fig. A.1 shows the fitted parameter values of all source components and their 68% confidence intervals when modeling the diffuse Galactic plane emission using the Planck Collaboration (2011) Dust template, shown in blue, and when using the Dame et al. (2001) CO template, shown in orange. The final two rows show the fitted values of the pulsar halo model powered by PSR J1831−0952 with and without the proper motion. We find that all parameters are statistically consistent across both the dust and CO template cases.

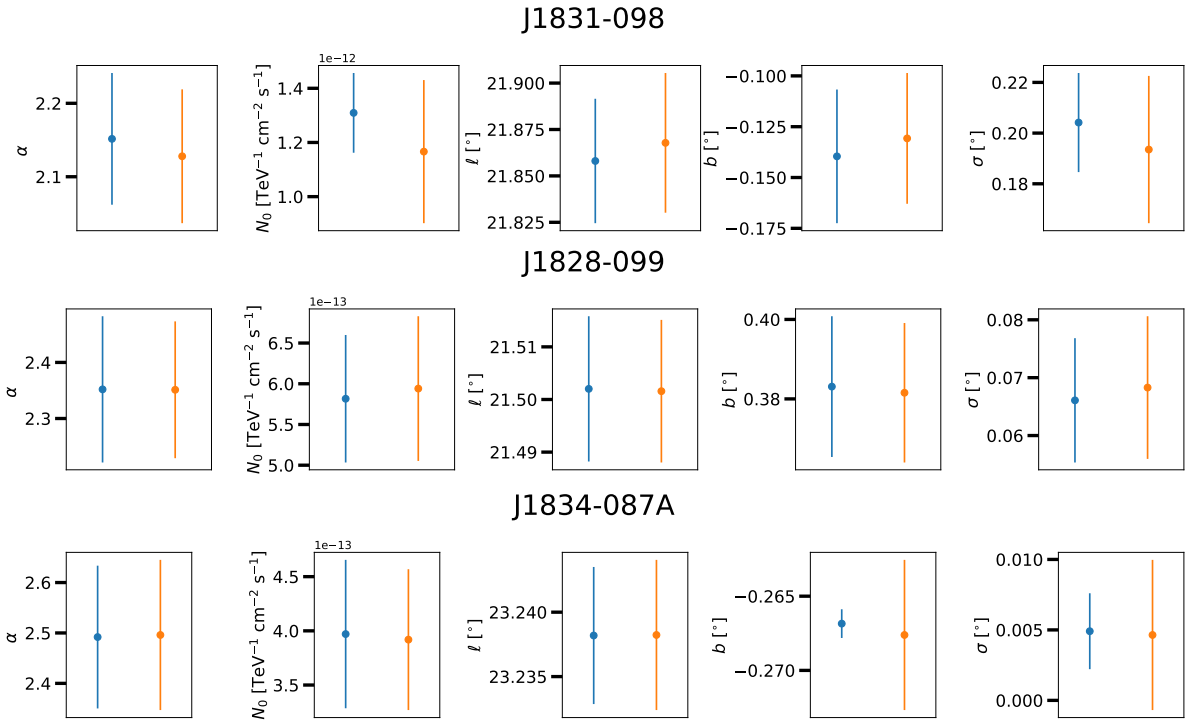

Figure A.1: Fitted parameters of each source component and their 68% confidence intervals when modeling the diffuse Galactic plane emission using the Planck Collaboration (2011) Dust template (blue) vs. when using the Dame et al. (2001) CO template (orange). **From top to bottom:** HESS J1831−098, HESS J1828−099 and HESS J1834−087A (continued).

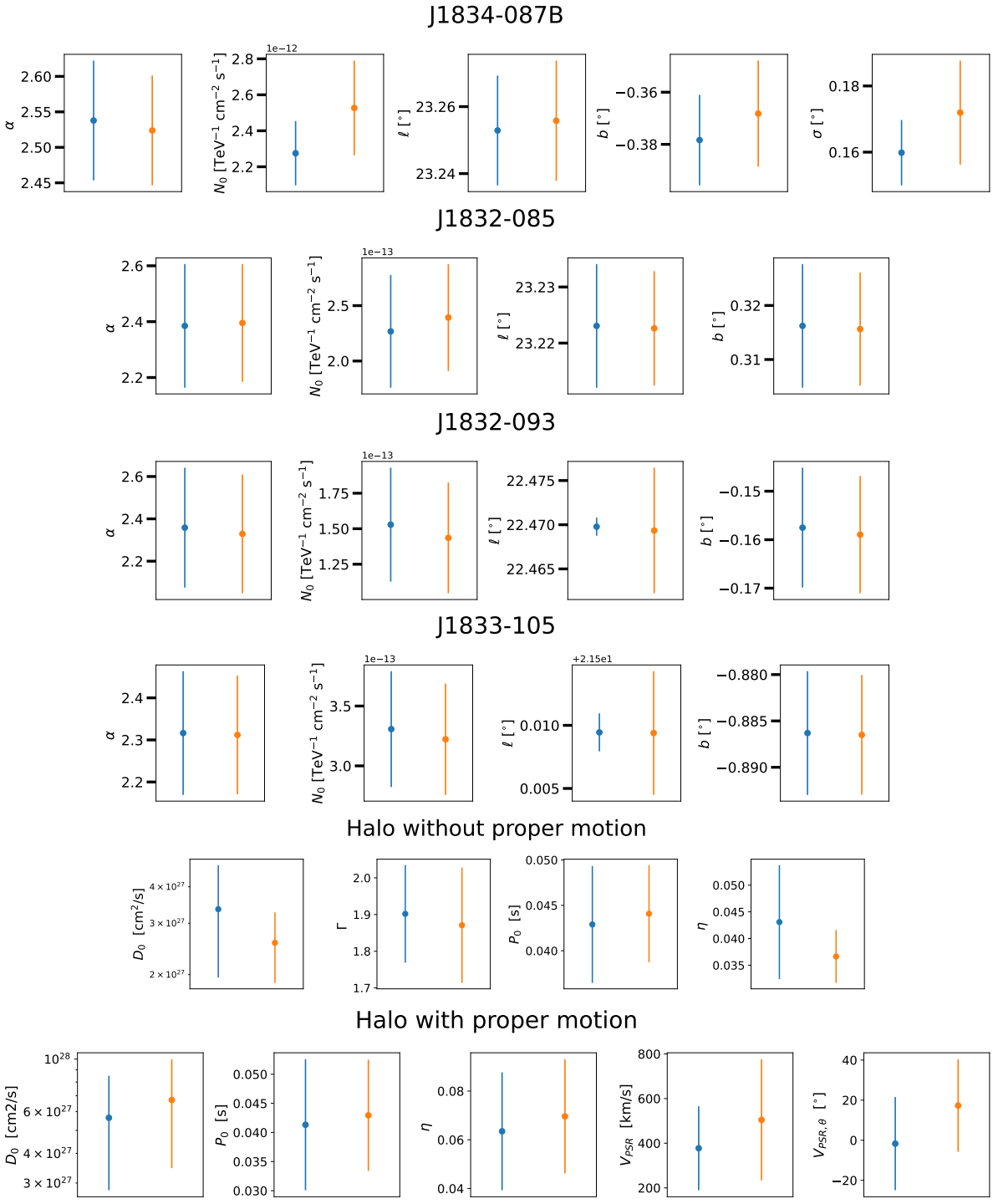

Figure A.1 (continued): **From top to bottom:** HESS J1834−087B, HESS J1832−085, HESS J1832−093, HESS J1833−105, HESS J1831−098 when modeled as a pulsar halo without proper motion and HESS J1831−098 when modeled as a pulsar halo with proper motion (powered by PSR J1831−0952).

Background re-normalization values

Table A.1 shows the values of the piece-wise normalization and tilt of the residual hadronic CR background model for all assumed models of HESS J1831−0952: A 2D Gaussian ×PL, a pulsar halo powered by PSR J1831−0952 (with or without proper motion) or a pulsar halo powered by PSR J1831−0941 (with proper motion). All the fitted values are statistically consistent across all cases.

Energy [TeV]	2D Gaussian ×PL	PSR J1831−0952	PSR J1831−0952 ($V_{PSR} \neq 0$)	PSR J1831−0941 ($V_{PSR} \neq 0$)
0.5	0.77 ± 0.01	0.77 ± 0.01	0.77 ± 0.01	0.77 ± 0.01
0.66	1.21 ± 0.01	1.21 ± 0.01	1.21 ± 0.01	1.21 ± 0.01
0.87	0.85 ± 0.01	0.85 ± 0.01	0.85 ± 0.01	0.85 ± 0.01
1.15	1.16 ± 0.01	1.16 ± 0.01	1.16 ± 0.01	1.16 ± 0.01
1.52	0.85 ± 0.01	0.85 ± 0.01	0.85 ± 0.01	0.85 ± 0.01
2.01	0.94 ± 0.02	0.94 ± 0.02	0.94 ± 0.02	0.94 ± 0.02
2.66	1.07 ± 0.02	1.07 ± 0.02	1.07 ± 0.02	1.07 ± 0.02
3.52	0.95 ± 0.02	0.95 ± 0.02	0.95 ± 0.02	0.95 ± 0.02
4.65	1.04 ± 0.03	1.04 ± 0.03	1.04 ± 0.03	1.04 ± 0.03
6.15	1.01 ± 0.03	1.01 ± 0.03	1.02 ± 0.03	1.02 ± 0.04
[8.13; 100]	0.99 ± 0.02	0.99 ± 0.02	0.99 ± 0.02	0.99 ± 0.02
Tilt				
[8.13; 100]	0.06 ± 0.04	0.05 ± 0.04	0.05 ± 0.04	0.04 ± 0.04

Table A.1: Parameters of the residual hadronic CR background model re-normalization using a piece-wise normalized PL from 0.5 to 8.13 TeV and a normalized PL from 8.13 to 100 TeV. The first section of the table represents the normalization values, while the second section represents the tilt values for the normalized PL. Each column represents the assumed model for HESS J1831−098.

Significance of modeling point-like sources with 2D Gaussians

Table A.2 shows the ΔTS between a point-like spatial assumption (the null hypothesis) and a 2D Gaussian spatial assumption (the test hypothesis) for the following sources in the field of view: HESS J1833−105, HESS J1832−093, HESS J1832−085 and HESS J1834−087 A. In the analysis, HESS J1834−087 A was modeled with a 2D Gaussian spatially following the HGPS model, however this choice had no statistically significant impact on the fitted parameters of HESS J1831−098 (the source of interest), nor HESS J1834−087 B. We conclude that these four components are not significantly extended in the data. We note that for HESS J1833−105, HESS J1832−093 and HESS J1832−085, the spatial parameters of other sources in the field of view were spatially frozen during the fit of the test hypothesis due to convergence failures.

Source component	ΔTS
HESS J1833−105†	0.24
HESS J1832−093†	0.23
HESS J1832−085†	0.23
HESS J1834−087 A	0.21

Table A.2: Likelihood improvement when modeling assumed point-like source components with 2D Gaussians. The null hypothesis is the point-like assumption, and the test hypothesis is the 2D Gaussian assumption. In the main analysis, HESS J1834−087 A was assumed to be extended. †: Other source components were spatially frozen during the fit of the null hypothesis due to failed convergence otherwise.

Detection significance of all sources

The detection significance of all sources in the field of view is shown in Table A.3. The significance of HESS J1832−093 is particularly low, however this source is significant in both the HAP-HD ImPACT cross-check analysis (6.0σ) and in the HGPS (6.8σ). Thus, the source component was kept in the model used in our main analysis. The reason for this discrepancy could be due to a difference in exposure (there are 20 more observation runs included in the cross-check analysis than in the main analysis), and/or the better angular resolution of HAP-HD ImPACT.

Source component	Significance
HESS J1831−098	7.7σ
HESS J1828−099	6.6σ
HESS J1833−105	7.8σ
HESS J1832−093	3.2σ
HESS J1832−085	4.2σ
HESS J1834−087 A	4.7σ
HESS J1834−087 B†	12.3σ

Table A.3: Detection significance of all source components in the field of view. †: Null hypothesis TS computed with HESS J1834−087 A's spatial parameters frozen.

HESS J1831−098 significance maps in different energy bands

The significance maps of HESS J1831−098 (i.e. having subtracted all other model components from the data) in different energy bands are shown in Fig. A.2, where the fitted model components' position and extension (similarly to Fig. 6.5) and the two pulsars' positions are also shown. The 3σ and 4σ levels are shown as black contours. The source is clearly most significant in the 1.53-10.74 TeV band. An energy-dependent model cannot be inferred from the data due to a lack of statistics.

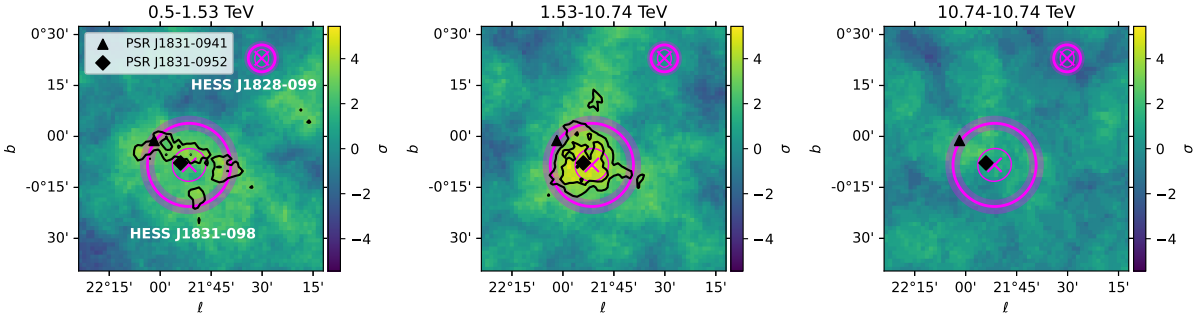

Figure A.2: Significance maps after subtracting all fitted model components except HESS J1831−098 in different energy bins, with a correlation radius of 0.15°. The contours represent the 3σ and 4σ levels. The magenta bands represent the 68% confidence interval on the extensions, and the magenta circles the 95% confidence interval on the positions shown with crosses.

Significance of a spectral curvature

Different assumptions on the spectral shape of HESS J1831−098 were tested. The results are shown in Table A.4. $E_{c,\mathrm{ECPL}}$ corresponds to the cut-off energy in the exponential cut-off factor of the power law, and we may only derive a lower limit for this parameter. The log-parabola (LP) model is expressed as:

$$\phi(E) = N_0 \left(\frac{E}{E_0}\right)^{-\alpha_{\mathrm{LP}} - \beta_{\mathrm{LP}} \log\left(\frac{E}{E_0}\right)} \tag{1}$$

In the spectral LP case, all sources except for HESS J1831−098 and HESS J1828−099 were spatially frozen during the fit due to convergence failures otherwise. The addition of curvature to the spectral model is not statistically significant. Fig. A.3 shows the fitted spectra in the ECPL and LP case compared with the HAWC and LHAASO sources in the region (for comparison, the PL spectrum can be seen in Fig. 6.12). These results indicate that no significant curvature is detected in the spectrum.

Parameter	PL	ECPL	LP†
N_0	$(1.31 \pm 0.15) \times 10^{-12}$	$(1.34 \pm 0.28) \times 10^{-12}$	$(1.35 \pm 0.28) \times 10^{-12}$
α	2.15 ± 0.09	2.05 ± 0.14	-
α_{LP}	-	-	2.0 ± 0.14
β_{LP}	-	-	0.073 ± 0.06
$E_{c,\mathrm{ECPL}}$ [TeV]	-	$45.45^{+\infty}_{-26.22}$	-
σ [°]	$0.204^{+0.034}_{-0.030}$	0.204 ± 0.03	0.205 ± 0.03
ℓ [°]	21.86 ± 0.03	21.86 ± 0.04	21.86 ± 0.04
b [°]	-0.14 ± 0.03	-0.14 ± 0.03	-0.14 ± 0.03
ΔTS vs. PL	0	0.27	0.32

Table A.4: N_0 is in units of TeV^{-1} cm^{-2} s^{-1}. σ represents the radial extension of the 2D Gaussian. †: All source components except for HESS J1831−098 and HESS J1828−099 were spatially frozen during the fit due to convergence failures otherwise.

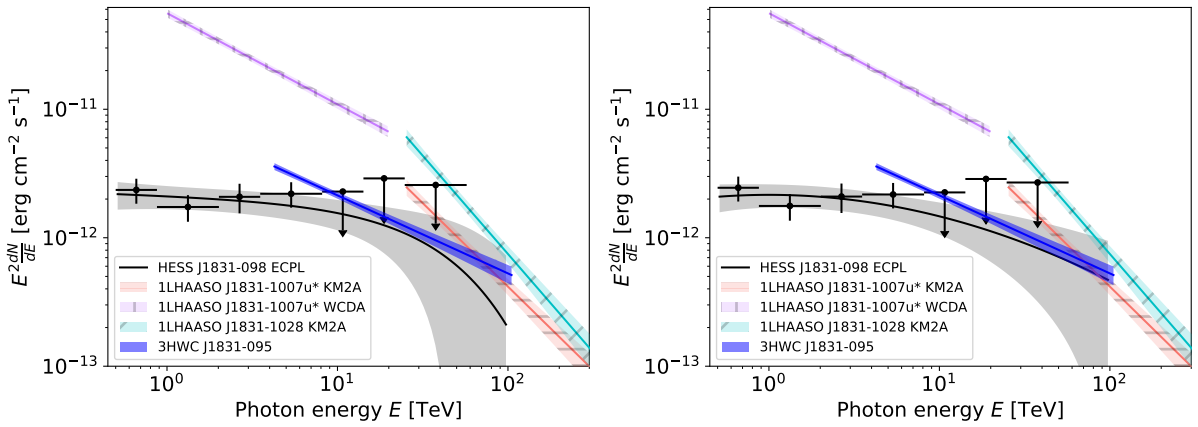

Figure A.3: Fit photon SED and derived flux points of the pulsar halo model, the 1LHAASO components and 3HWC J1831-095. The shaded bands and the vertical bars represent the 1σ uncertainty. The upper limits are given at the 2σ level. **Left:** Exponentially cut-off PL spectrum. **Right:** Log-parabola spectrum.

Anti-correlation between HESS J1831−098 and HESS J1828−099

The 68% confidence intervals on the extension are larger than those estimated through uncertainty propagation due to an anti-correlation between the extensions of HESS J1831−098 and the nearby extended HESS J1828−099. This correlation is shown in Fig. A.4. The top left panel shows the 2D confidence contours obtained by scanning over the extensions of HESS J1828−099 shown as the vertical axis and HESS J1831−098 shown as the horizontal axis. The 1σ and 1.5σ levels are shown. The cyan solid lines represent the 68% C.I. estimated with uncertainty propagation, and the dashed lines those estimated with the likelihood scan shown in Fig. 6.7. This investigation was prompted by the finding that HESS J1831−098's extension can only be shown to be compatible with the HAP-HD cross-check analysis if the 68% C.I. was computed correctly using a likelihood scan. The anti-correlation with HESS J1828−099 is more pronounced in HAP-HD as shown in the top right panel of Fig. A.4. The bottom panel shows a comparison of the confidence contours between HAP-FR in red and HAP-HD in blue.

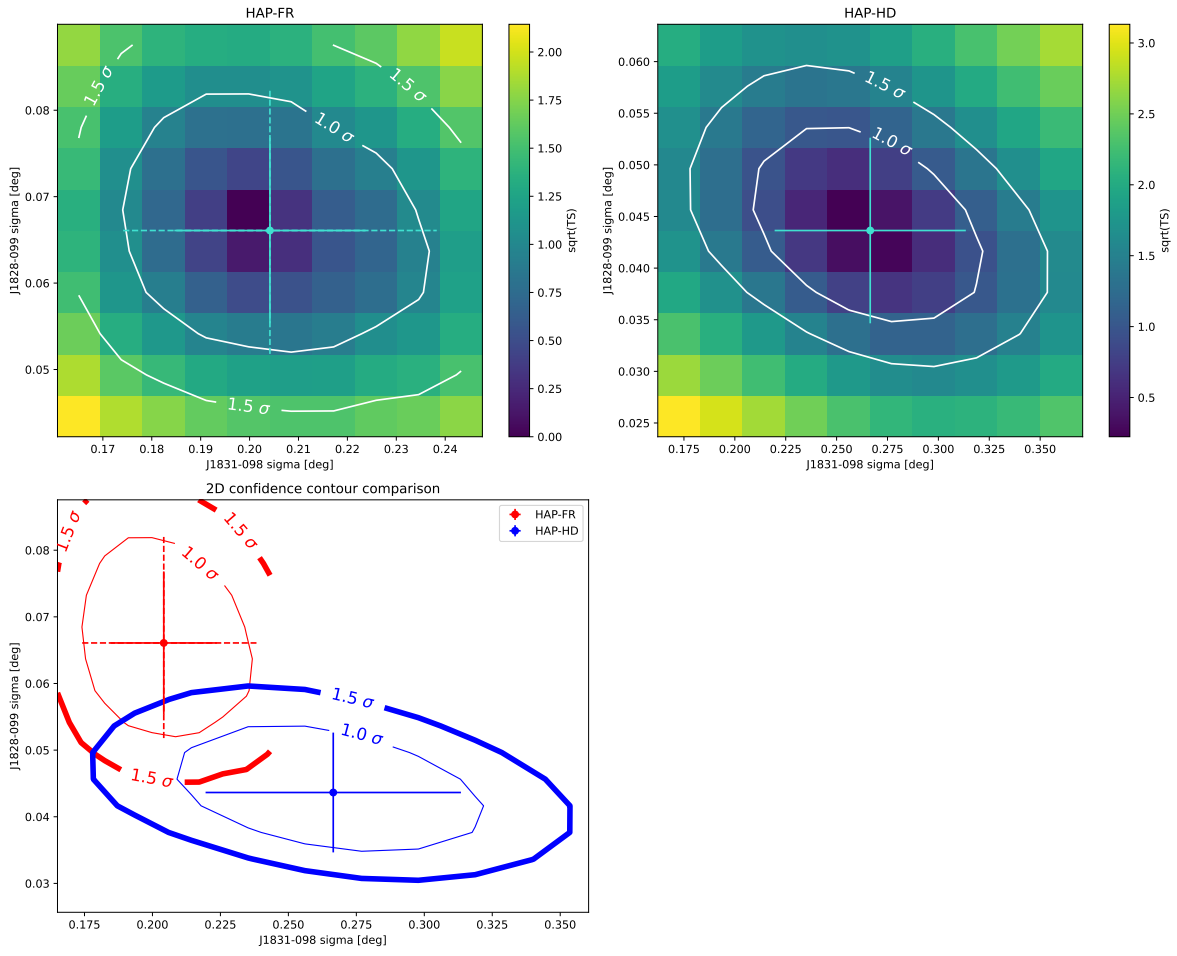

Figure A.4: **Top left:** 2D confidence contours of the extensions of HESS J1828−099 (y-axis) and HESS J1831−098 (x-axis) in the main analysis (HAP-FR). The cyan solid lines represent the 1σ errors computed from uncertainty propagation, while the dashed cyan lines represent the 1σ errors computed from the likelihood scans (cf. Fig. 6.7 in the original manuscript). The 1.5σ and 1σ levels are shown in white. **Top right:** Same figure but from the cross-check analysis with HAP-HD. **Bottom:** Comparison of the confidence contours between HAP-FR and HAP-HD.

Predicted counts by the diffuse Galactic plane emission model

For the middle region illustrated in Fig. 6.11, Fig. A.5 shows the contribution in predicted counts by the large-scale diffuse emission model, when the Planck Collaboration (2011) dust template is assumed, compared to the predicted background model counts and the total counts.

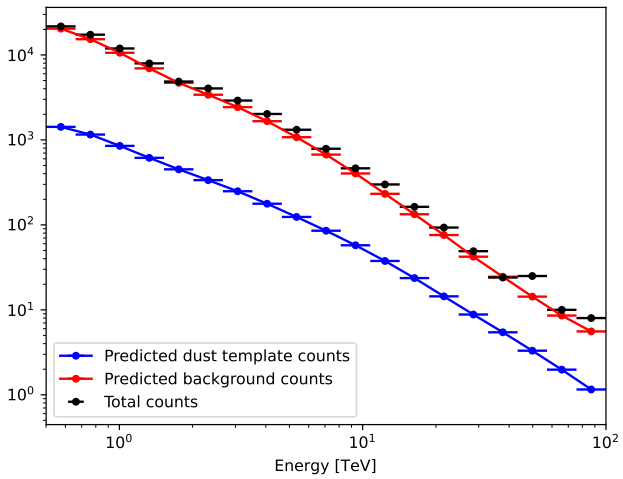

Figure A.5: Total counts (black), predicted counts from the Planck Collaboration (2011) dust template (blue) and predicted background counts (red) as a function of reconstructed energy, in the middle rectangular region shown in the top left panel of Fig. 6.11.

All fitted parameters when HESS J1831−098 is modeled using the pulsar halo templates

The fitted components of all model components are shown in Tables A.5, A.6 and A.7, for all the tested pulsar halo cases. The fitted parameters are statistically consistent.

Component	N_0	α	σ [°]	ℓ [°]	b [°]
J1828−099	$(5.55 \pm 0.79) \times 10^{-13}$	2.35 ± 0.13	0.064 ± 0.011	21.50 ± 0.01	0.38 ± 0.02
J1833−105	$(3.29 \pm 0.48) \times 10^{-13}$	2.32 ± 0.15	-	21.509 ± 0.005	-0.89 ± 0.01
J1832−093	$(1.45 \pm 0.40) \times 10^{-13}$	2.35 ± 0.30	-	22.470 ± 0.004	-0.16 ± 0.01
J1832−085	$(2.29 \pm 0.51) \times 10^{-13}$	2.38 ± 0.22	-	23.22 ± 0.01	0.32 ± 0.01
J1834−087 A	$(3.96 \pm 0.58) \times 10^{-13}$	2.49 ± 0.15	0.005 ± 0.003	23.24 ± 0.01	-0.267 ± 0.009
J1834−087 B	$(2.34 \pm 0.23) \times 10^{-12}$	2.53 ± 0.08	0.162 ± 0.012	23.25 ± 0.02	-0.38 ± 0.02
Dust template	$(2.84 \pm 0.31) \times 10^{-11}$	2.44 ± 0.04	-	-	-

Table A.5: Best-fit spatial and spectral parameters of the components included in the model (with the reference energy E_0 fixed to 1 TeV). HESS J1831−098 is modeled as a pulsar halo powered by PSR J1831−0952 without proper motion. N_0 is in units of TeV^{-1} cm^{-2} s^{-1}. σ represents the radial extension of the 2D Gaussian components.

Component	N_0	α	σ [°]	ℓ [°]	b [°]
J1828−099	$(4.86 \pm 1.01) \times 10^{-13}$	2.35 ± 0.14	0.056 ± 0.014	21.50 ± 0.01	0.39 ± 0.02
J1833−105	$(3.21 \pm 0.48) \times 10^{-13}$	2.31 ± 0.15	-	21.509 ± 0.004	-0.89 ± 0.01
J1832−093	$(1.56 \pm 0.41) \times 10^{-13}$	2.37 ± 0.30	-	22.470 ± 0.007	-0.16 ± 0.01
J1832−085	$(2.33 \pm 0.51) \times 10^{-13}$	2.39 ± 0.22	-	23.22 ± 0.01	0.32 ± 0.01
J1834−087 A	$(3.95 \pm 0.58) \times 10^{-13}$	2.49 ± 0.16	0.005 ± 0.003	23.24 ± 0.01	-0.268 ± 0.009
J1834−087 B	$(2.45 \pm 0.25) \times 10^{-12}$	2.53 ± 0.08	0.167 ± 0.014	23.25 ± 0.02	-0.37 ± 0.02
Dust template	$(2.71 \pm 0.28) \times 10^{-11}$	2.44 ± 0.05	-	-	-

Table A.6: Same as Table A.5 but with the proper motion included in the halo model.

Component	N_0	α	σ [°]	ℓ [°]	b [°]
J1828−099	$(5.70 \pm 0.83) \times 10^{-13}$	2.36 ± 0.13	0.065 ± 0.011	21.50 ± 0.01	0.38 ± 0.02
J1833−105	$(3.24 \pm 0.48) \times 10^{-13}$	2.32 ± 0.15	-	21.509 ± 0.004	-0.89 ± 0.01
J1832−093	$(1.57 \pm 0.40) \times 10^{-13}$	2.37 ± 0.30	-	22.470 ± 0.007	-0.16 ± 0.01
J1832−085	$(2.29 \pm 0.51) \times 10^{-13}$	2.38 ± 0.22	-	23.22 ± 0.01	0.32 ± 0.01
J1834−087 A	$(3.96 \pm 0.58) \times 10^{-13}$	2.49 ± 0.15	0.005 ± 0.003	23.24 ± 0.01	-0.267 ± 0.001
J1834−087 B	$(2.35 \pm 0.27) \times 10^{-12}$	2.53 ± 0.08	0.163 ± 0.014	23.25 ± 0.02	-0.38 ± 0.02
Dust template	$(2.84 \pm 0.31) \times 10^{-11}$	2.44 ± 0.04	-	-	-

Table A.7: Same as Table A.5 but HESS J1831−098 is modeled as a pulsar halo powered by PSR J1831−0941 with proper motion.

Predicted radial surface brightness

Fig. A.6 shows the predicted surface brightness profiles (in the 0.5-100 TeV range) convolved with the PSF, for the halo model (powered by PSR J1831−0952 with no proper motion) and the 2D Gaussian×PL model. The predicted surface brightness convolved with the PSF for the halo model is shown in red, along with an envelope representing the 68% confidence interval. For the Gaussian, the predicted surface brightness profile convolved with the PSF is shown in blue, along with an envelope representing the 68% confidence interval. The data points (in black) were extracted in concentric annuli centered on the pulsar's position (PSR J1831−0952) in an energy bin 0.5-100 TeV, and the vertical bars represent the 1σ statistical uncertainty. The data points are extracted assuming a PL spectrum with spectral index $\alpha = 2$. The horizontal axis represents the angular distance from the pulsar's position in degrees. This figure shows that we may not have enough statistics to discriminate between a Gaussian profile or a pulsar halo-like profile for the source, which would explain the low $\Delta AIC \sim 2.1$ between both hypotheses. We note that the Gaussian profile's envelope in Fig. A.6 was computed using uncertainty propagation and not through a likelihood scan as is done for the halo profile.

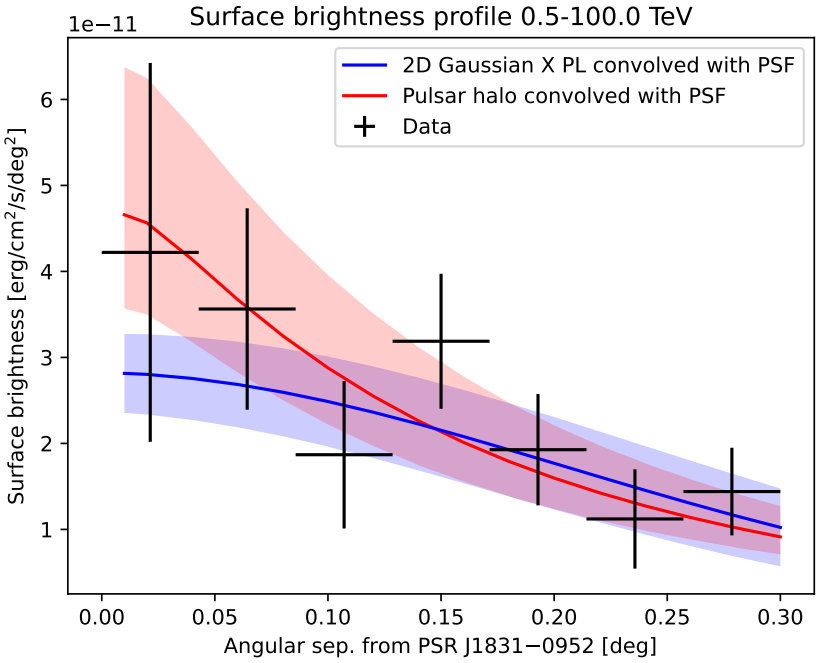

Figure A.6: Model-predicted surface brightness profiles (0.5-100 TeV) as a function of the angular distance from the position of PSR J1831−0952, convolved with the PSF. The halo model's profile is shown in red, and the 2D Gaussian×PL model's profile is shown in blue. The envelope represents the 68% confidence interval. The halo profile's envelope was computed using a likelihood scan, while the Gaussian's envelope was computed through uncertainty propagation. The data points are extracted in concentric annuli centered on the pulsar's position, assuming a PL with spectral index $\alpha = 2$. The vertical bars represent the 1σ statistical uncertainty.